Electronic properties of interfaces produced by silicon wafer hydrophilic bonding

Von der Fakultät für Mathematik, Naturwissenschaften und Informatik
der Brandenburgischen Technischen Universität Cottbus

zur Erlangung des akademischen Grades

Doktor der Naturwissenschaften
(Dr. rer. nat.)

genehmigte Dissertation

vorgelegt von

Magister in Physik
Maxim Trushin
geboren am 18. März 1981 in Samarkand, Uzbekistan

Gutachter: Prof. Dr. rer. nat. habil. Jürgen Reif

Gutachter: Prof. Dr. sc. nat. Martin Kittler

Gutachter: Prof. Dr. Oleg Vyvenko

Tag der mündlichen Prüfung: 15 Juli 2011

Contents

Introduction.

Like human defects, those of crystals come in a seemingly endless variety, many dreary and depressing, and a few fascinating.
N. Ashcroft & N. Mermin.

Silicon now is the leading material in the areas of microelectronic and photovoltaic applications. The electronic chip industry of the present days produces complex circuitry, boasting over one billion components in a single processor with the size of an individual transistor (gate length) going down to *20 nm* [Intel roadmap 2009]. However, in recent years some concerns about the evolution of this industry have been raised which are related with the fundamental materials and processing aspects [Pavesi 2003]. Currently used interconnects based on Cu wiring will cause serious problems in future such as complexity of their architecture (more than 10 layers of metal levels), non-acceptable delay in signal propagation, heat penalty, signal latency and crosstalk etc., in case of further reduction in dimensions and increasing in the density of metal lines.

A possible solution to these problems is looked for in optics: on-chip optical interconnects are able to overcome these problems and will be essential for future integrated circuits [Pavesi 2003] [Jalali 2008]. Many key photonic components compatible with CMOS-technology have been already demonstrated, as for example optical waveguides [Pavesi 2003], electro-optical modulator [Oehme 2006], fast and sensitive Ge detector [Liu 2004]. However, an appropriate light emitter, also compatible with CMOS-technology, is still lacking. Different approaches for such light emitters have been suggested, among them intra-atomic optical transitions in Er atoms in Er-doped Si [Zheng 1994], luminescence of β-$FeSi_2$ precipitates in Si [Lourenco 2003] and optical transitions in SiGe quantum cascade structures [Zakharov 2003].

Another promising conception of silicon-based light emitting diode (LED) was proposed exploiting the dislocation-related luminescence band of *1,5 μm* wavelength [Kveder 2005]. Silicon is transparent in that wavelength range, thus the optical waveguides and modulators prepared on silicon can be utilized for on-chip signal transmission. Moreover, wavelength of about *1,5 μm* coincides with the transparency window of the optical fibres used in the telecommunication [Kartalopoulos 2000], making therefore this kind of silicon LED more attractive for industrial applications.

Photovoltaic solar energy market also shows an explosive growth during the last decades. Growth rates well above the long-term average of 15% could be realized and both politicians and PV module producers foresee growth scenarios in excess of 25% in the next few years [Schönecker 2004]. Multicrystalline (mc-) silicon now is the most widely used material for solar cell application, which meets both the low cost production and

satisfactory efficiency. However, mc-Si has serious disadvantages compared with the considerable perfection achieved in single crystalline silicon. The efficiency of multicrystalline solar cells is limited by grain boundaries, and – more significantly – by the high density of dislocations in many grains and metal impurities that segregated at these structural defects.

Thus, as one can see, dislocations in silicon may be attributed both to "beneficial" and to "detrimental" types of defects depending on the application domain. These results have evidenced the barest necessity of a deeper knowledge about the dislocation related gap states, with a particular emphasis to the relation between the radiative and non-radiative electronic transitions at dislocation-induced gap states.

Aim of the work

Aim of the present work is to investigate the electrical properties of dislocation networks in Si, by means of the junction spectroscopy experimental techniques. Dislocation networks (DN) produced by direct bonding of silicon wafers, attract now an increasing interest due to their potential application in microelectronics as all-Si light emitter and as a perfect conductor (for review see [Kittler 2007]), but also as a model object for studying the electronic properties of dislocations and grain boundaries (GB) in silicon [Bengtsson 1992], which is of substantial interest for the semiconductor technology and for photovoltaics. The choice of the junction spectroscopy as the main method for the investigations was determined by its high sensitivity and informativity with respect to the characterization of the electrically active defects in silicon. Issuing from the major goal of this work, the following particular tasks can be specified:

- exploration of the defect states introduced by dislocation networks of different microstructure;
- establishing the correlation between the optical, electrical and structural properties of dislocations;
- specification and characterisation of the dislocation-related defect levels participating in the radiative recombination. Leaving alone the great importance of developing a light emitting device compatible with modern silicon technology, the determination of origin of dislocation-related luminescence in silicon was a challenging question for a quarter of century;
- investigations of the electrical field impact on the carrier emission from the dislocation-related states;

- description of the current-voltage and capacitance-voltage dependences in the investigated structures consisting of two potential barriers – one due to Schottky diode and another one – due to charged dislocation network.

Outline of the Thesis

The thesis is consisted of nine Chapters. There follows an outline of these chapters.

Chapter 1 provides a brief description of Schottky diode theory as well as an overview of experimental methods capacitance-voltage (CV), current-voltage (IV), Deep Level Transient Spectroscopy (DLTS) and Isothermal Spectroscopy (ITS) applied for the investigations.

In Chapter 2 some necessary background about the theory of dislocations in Si along with the review of what is currently known about the electronic properties of dislocations in silicon and dislocation-related luminescence are presented.

Chapter 3 reports the general information concerning direct wafer bonding procedure and the main properties of the resulted dislocation networks.

Chapter 4 presents the description of the investigated samples and some details concerning the capacitance spectrometer used in this work.

Chapter 5 represents the comparative description of the investigation results of electrical, optical and structural properties of dislocation networks in all four bonded samples studied here. General considerations establishing the levels participating in the radiative recombination and, as a result, the optimal dislocation network geometry for the maximal luminescence intensity are also presented in this Chapter.

In Chapter 6 the results of CV and IV measurements are described, which allowed to construct an energy band diagram of Schottky diode / DN double barrier structure and to define the charge state (donor / acceptor) of the revealed defect states.

Chapter 7 acquaints with the results of the investigations of electric field influence on the emission process from the DN-related levels.

In Chapter 8 the results of theoretical calculations explaining the observed electric field influence are presented and the possible origins of the shallow DN-related states are discussed.

And the final Chapter 9 reports the summary and conclusions for the whole work.

Chapter 1
Fundamentals of the experimental methods used.

One of the reasons why semiconductors are so functional for device application is that their electronic properties can be modified in the wide ranges by the incorporation of small amount of impurities or other kinds of defects (vacancies and interstitials, dislocations and internal interfaces). However, while one type of defects can make a semiconductor useful for fabricating a device, another type of defects can provoke undesirable effects which cease the device performance. The quantity of defects necessary to change the properties of a semiconductor is often considerably less than one atom per million host atoms. As a result, our abilities to control the device parameters in practice are often determined whether we can control the amount, parameters and nature of the defects introduced into a semiconductor.

In an effort to characterize the defect traps presented in a semiconductor, one would prefer a technique that is sensitive, rapid, and straightforward to analyze. Such a technique should be able to distinguish between majority- and minority-carrier traps and should provide information about the concentrations, energy levels, and capture rates of these traps. In addition, one would prefer such a technique to be spectroscopic in the sense that the signals due to different traps be resolved from one another and to be reproducible in position when plotted against a single variable. In order to be useful as a survey technique, it should also provide a possibility of measuring the traps distribution over a wide range of depths.

In 1974 D. V. Lang has introduced a new technique, which he called deep-level transient spectroscopy (DLTS), capable to fulfil all of the above requirements [Lang 1974]. This technique utilizes the capacitance of an abrupt *p-n* junction or Schottky diode as a probe to monitor the changes in the charge state of the defects, thus providing the information about all electrically active defects (which introduce an allowed states inside semiconductor band gap), including both radiative and nonradiative centres. In the following, the basic concepts of this technique are reviewed and the expressions / equations needed to analyze the obtained spectra are presented.

1.1 Metal-semiconductor contact and Schottky diode.

Let us consider the n-type semiconductor with an electron affinity χ_s and a metal with the work function ϕ_m, defined respectively as the energies required to remove the electron from the semiconductor conduction band edge E_C and metal Fermi level E_{Fm} to the vacuum level E_0. Suppose now the $\phi_m > \chi_s$ metal and n-type semiconductor are brought together to form an ideal metal-semiconductor (MS) contact. Here ideal means that where is no interface (oxide) layer between the metal and semiconductor, no adsorbed impurities at the MS interface and no interdiffusion of metal and semiconductor atoms. In thermal equilibrium, the Fermi levels of both materials must be coincident and this results in a band diagram for the interface shown in Fig. 1.1. As the vacuum level E_0 at the interface is also the same for both materials, so there must be a step between the Fermi level of metal and conduction band of semiconductor. This is known as the barrier height and is given by

$$\phi_b = \phi_m - \chi_s \tag{1.1}$$

The resulting band bending excludes free electrons from semiconductor in the vicinity of the contact leaving a distribution of the fixed positive charge due to ionized donors. The edge of this "depletion region" x_d is where the bands become flat again and the associated electric field is zero. In the metal a neutralizing negative charge in the form of free electrons is accumulated over the distance x_m from the interface, which is free carrier screening length in metal. Since the electron concentration in metal is much higher than the doping level of semiconductor, $x_m << x_d$ could be assumed, as well as that the potential difference across the metal at the contact V_m is negligibly small compared to that of semiconductor V_s, see Fig. 1.1. Thus, the total zero bias band bending, or built-in voltage, could therefore be written as [Blood 1992]

$$eV_b \approx eV_s = \phi_b - (E_C - E_F) \tag{1.2}$$

where ϕ_b is defined by Eq. 1.1. This kind of MS contact represent itself a rectifying contact which is known also as Schottky diode, named after German physicist Walter H. Schottky.

Application of a forward bias voltage (i.e. 'plus' on the metal side) reduces the barrier seen by electrons in the semiconductor, so a net flow of electrons from semiconductor to metal appears. On the other hand, application of a reverse bias voltage raises the barrier height, thus blocking the electrons flow from semiconductor to metal. As opposed to the rectifying MS contact, an ohmic MS contact exists: resistance of such kind of contact should be much smaller than both bulk resistance of semiconductor as well as be independent on the applied bias. In order to obtain the ohmic metal / n-type semiconductor contact, one should take such a metal for which $\phi_m < \chi_s$ holds true.

Parallel arguments could be applied to an ideal MS contact formed by a metal and p-type semiconductor as well, however the reverse condition $\phi_m < \chi_s$ is needed here to obtain the rectifying contact and $\phi_m > \chi_s$, respectively, to obtain the ohmic one. The sign of the forward and reverse bias voltages also would be reversed as compared with n-type semiconductor.

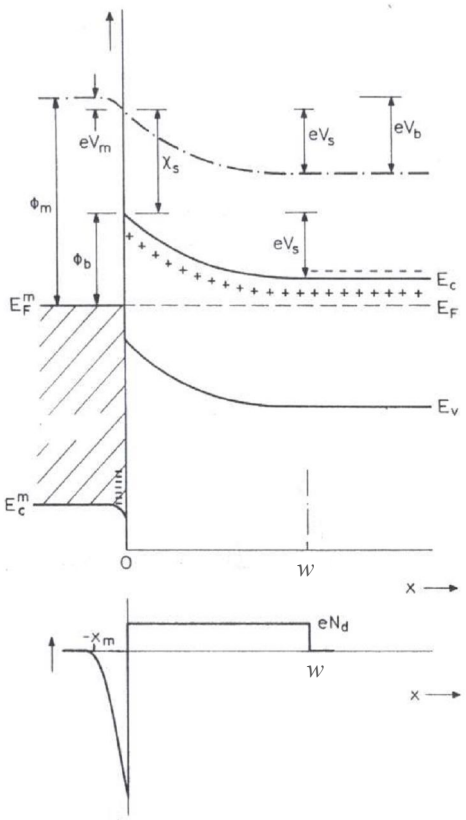

Figure 1.1. Energy-band diagram of rectifying MS contact in thermal equilibrium and the associated charge density profile for uniformly doped semiconductor (After [Blood 1992]).

Depletion region depth w (another definition – space charge region depth or simply SCR depth), electric field $F(x)$ and electrostatic potential $V(x)$ inside the depletion region, can be calculated from the charge density $\rho(x)$ using Poisson's equation. The electrostatic potential at any point is given by (ε is dielectric permittivity)

$$\frac{d^2V}{dx^2} = -\frac{1}{\varepsilon}\rho(x) \tag{1.3}$$

First integration of Eq 1.3 will give the expression for the electric field distribution inside the SCR. Thus, for the semiconductor with uniform doping level N_d one can write

$$\frac{dV}{dx} = -F(x) = \frac{eN_d}{\varepsilon}(w-x) \tag{1.4}$$

and, after the second integration, the electrostatic potential received as

$$V(x) = \frac{eN_d}{2\varepsilon}(w-x)^2 \tag{1.5}$$

for $0 \le x \le w$. Then, the SCR depth will be equal to

$$w = \sqrt{\frac{2\varepsilon}{eN_d}V} \tag{1.6}$$

Under equilibrium conditions the potential drop across the depletion region is V_b, thus $V=V_b$ at $x=0$. In general cases, when external bias is applied, the band bending V is the sum of the built-in voltage and applied bias $V=V_b+V_a$.

Depletion layer is associated with the capacitance related with fix positive charge of the ionized donors. When the bias is increased by the small increment ΔV the depletion layer width increases as well (Eq. 1.6) causing the increase in a fixed charge per unit area ΔQ so one can define a differential capacitance associated with the depletion region as

$$C = A\frac{dQ}{dV} \tag{1.7}$$

where A is the diode area. The expression for the fixed charge stored in the depletion region could be written as $Q=ewN_d$ (this expression is known as "depletion approximation", however in some special case the influence of the free carrier tail penetrating into the SCR should be taken into account [Blood 1992]), then the differentiation gives the depletion layer capacitance

$$C = A\sqrt{\varepsilon\frac{eN_d}{2V}} \tag{1.8}$$

Combining Eq. 1.8 with Eq. 1.6, an important expression for depletion layer capacitance will be obtained

$$C = \frac{\varepsilon A}{w} \tag{1.9}$$

This is identical to the expression for the capacitance of plane capacitor. But unlike the true plane capacitor, where the charge Q varies linearly with V and the linear capacitance $C=Q/V$ is constant, in the depletion region of Schottky diode fixed charge varies with applied bias as $Q \sim V^{1/2}$, so fixed linear capacitance cannot be defined, but only a differential one (Eq. 1.8) and this capacitance decreases with increasing of reverse voltage as $V^{-1/2}$.

- ***CV characteristics***

The measurement of Schottky diode capacitance as a function of applied reverse bias is a routine method for evaluating of the doping profile $N_d(x)$ and a built-in voltage V_b. By rewriting of Eq. 1.8 in the form like

$$\frac{1}{C^2} = \frac{2}{eN_D\varepsilon A^2}V = \frac{2}{eN_D\varepsilon A^2}(V_b + V_a) \tag{1.10}$$

it becomes clear, that the slope of a $1/C^2$ vs V plot is proportional to N_d^{-1}, whereas the extrapolated intersection with the bias axis occurs in the point equal to $-V_b$.

- ***IV characteristics***

Electrical current through the *n*-type Schottky diode is defined mainly by the electron flow from the semiconductor into the metal. The reverse bias hole diffusion current and the recombination-generation current associated with carrier generation in the depletion region are typically negligible. Reflecting the fact that minority carriers play an insignificant role in determination of the IV characteristics, Schottky diodes are often said to be a "majority carrier device".

The current resulting from majority carrier injection over the potential barrier is referred as the thermionic emission current [Bethe 1942]. Total current I flowing through the diode is the difference of the current flowing from the bulk of semiconductor into the metal I_1 and the current flowing from the metal into the semiconductor I_1. In the equilibrium currents I_1 and I_2 are equal, thus the total current is zero $I= I_1 -I_2=0$. However, when the forward bias is applied, thus reducing the barrier height for the electrons flowing from semiconductor into the metal, the I_1 current will increase, whereas the current I_2 will remain the same. The total current at an arbitrary applied bias is given by [Sze, 1981]

$$I = I_s(e^{eV/kT} - 1) \tag{1.11}$$

where I_s is the saturation current and it is equal to

$$I_s = A^* T^2 e^{-\phi_b/kT} \tag{1.12}$$

Equation 1.11 clearly shows that for forward biases greater than a few kT/e, the exponent term becomes dominant and $I \to I_s e^{eV/kT}$. Whereas for reverse bias greater than a few kT/e, the exponential term becomes negligible and the current is predicted to saturate at $I=-I_s$, i.e. the reverse current of a Schottky diode which depends on potential barrier ϕ_b (Eq. 1.1), temperature T and the effective Richardson's constant A^* [Sze, 1981].

1.2 Details and principles of DLTS method.

- ***Carrier capture and emission. Point-defect analysis.***

The occupation of a defect level E_t in the upper half of band gap (n-type semiconductor) is determined by capture and emission of electrons from/to the conduction band. The occupation degree, f, of the level is given to by the ratio of the density of the levels n_t occupied by electrons and the total trap density N_t, $f = n_t/N_t$. For the simplest case of a point defect the following rate equation describes the time-dependent change of occupation of the defect:

$$\frac{\partial f}{\partial t} = c_n(1-f) - e_n f \tag{1.13}$$

where e_n is the emission rate of the electrons and c_n is the capture rate which is equal to

$$c_n = \sigma_n \langle v_n \rangle n \tag{1.14}$$

with σ_n being the capture cross section for the electrons, $\langle v_n \rangle$ mean thermal velocity and n density of the free electrons in the conduction band. For the thermal emission of the electrons from the defect level, Shockley-Read theory gives the following expression

$$e_n = \sigma_n \langle v_n \rangle N_c \exp(-\frac{E_C - E_t}{kT}) \tag{1.15}$$

where N_c is the effective density of states in the conduction band. Further, knowing the expression for thermal velocity $\langle v_n \rangle = \sqrt{\frac{3kT}{m^*}}$ and the density of states $N_c = 2M_C \left(\frac{2\pi m^* kT}{h^2} \right)^{\frac{3}{2}}$ (where M_c is the number of conduction band minima), and if the temperature-dependent capture cross section will be allowed for in the form $\sigma(T) = \sigma_\infty \exp(-\frac{\Delta E_\sigma}{kT})$, Eq.1.15 could be rewritten to give the temperature dependence of $e_n(T)$ as [Blood 1992]

$$e_n(T) = \gamma T^2 \sigma_{na} \exp(-\frac{E_{na}}{kT}) \tag{1.16}$$

where constant $\gamma = 2\sqrt{3} M_C (2\pi)^{\frac{3}{2}} k^2 m^* h^{-3}$. Therefore, a plot of $\ln(e_n / T^2)$ as a function of $1/kT$ is a straight line with the slope coefficient equal to activation energy E_{na} and cut-off value – pre-exponential factor defined by σ_{na}. However, activation energy E_{na} obtained in such a way does not correspond to the energy level of the trap in band gap directly. From the thermodynamic point of view, the energy of the defect level is defined as the variation of the chemical potential, i.e. Gibbs free energy G, needed to create the ionized defect and the free carrier at constant temperature. As the change in Gibbs free energy $\Delta G(T)$ is related to the associated changes in ionization enthalpy (ΔH) and entropy (ΔS) by the thermodynamic identity $\Delta G(T) = \Delta H - T\Delta S$, the activation energy in Eq. 1.16 would correspond then to $E_{na} = \Delta H + \Delta E_\sigma$, and the effective capture cross section $\sigma_{na} = \frac{g_0}{g_1} \sigma_\infty \exp(\frac{\Delta S}{k})$ would correspond to the value extrapolated to $T=\infty$ and modified by degeneracy ratio.

Nevertheless, the plot of $\ln(e_n / T^2)$ versus $1/kT$ is often called the "trap signature" and, although E_{na} and σ_{na} cannot be immediately interpreted in terms of an energy level and capture cross section, their values can be used to characterize a trap in terms of its signature defined by Eq. 1.16. These values of E_{na} and σ_{na} are used to catalogue traps found in various materials.

- ***Schottky diode with single uniformly distributed electron trap level.***

Let us now consider Schottky diode made on the n-type semiconductor with doping density N_d and containing single trap level in the upper part of band gap with the

concentration $N_t < N_d$, see Fig. 1.1. All traps, which are lying below the Fermi level (at $x>x_2$) are filled with electrons (Fig. 1.2A). When a large reverse bias U_r is applied producing the depletion up to the depth $x=w$ (Fig. 1.2B), free electrons are rapidly swept out from this region into the bulk by strong electric field (Eq. 1.4). Traps in the region $x < x_1$ (Fig. 1.2B) have now $E_t > E_F$ so their capture rate is very small and traps which were initially full ($x>x_2$) relax by electron emission alone. Thus the solution of detailed balance equation Eq. 1.13 with boundary conditions $n_t(0) = N_t$ and $e_n > c_n$ will be

$$n_t(t) = N_t \exp(-e_n t) \tag{1.17}$$

In the region $x > x_1$, $c_n > e_n$ and the traps remain occupied and we regard this transition to occur abruptly at $x=x_1$ where $E_t=E_F$, so we define $x_1=w-\lambda$. Here the transition distance λ, for band bending of (E_F-E_t) is given by [Blood 1992]

$$\lambda = \left\{ \frac{2\varepsilon}{eN_d}(E_F - E_t \right\}^{1/2} \tag{1.18}$$

When the bias is switched back to zero again, then all the traps have been emptied during the high reverse bias period refill by the electron capture, i.e. $c_n > e_n$. So, the solution of Eq. 1.13 for the filling process will be

$$n_t(t) = N_t\{1 - \exp(-c_n t)\} \tag{1.19}$$

For a large reverse bias such that $\lambda << w$, the time dependent net space charge density during the emission process can be written (for a donor-like trap):

$$\rho(t) = e\{N_d + N_t - n_t(t)\} \tag{1.20}$$

so, from Eq. 1.8 with the charge density (eN_d) replaced by $\rho(t)$ the time dependent capacitance at constant bias is

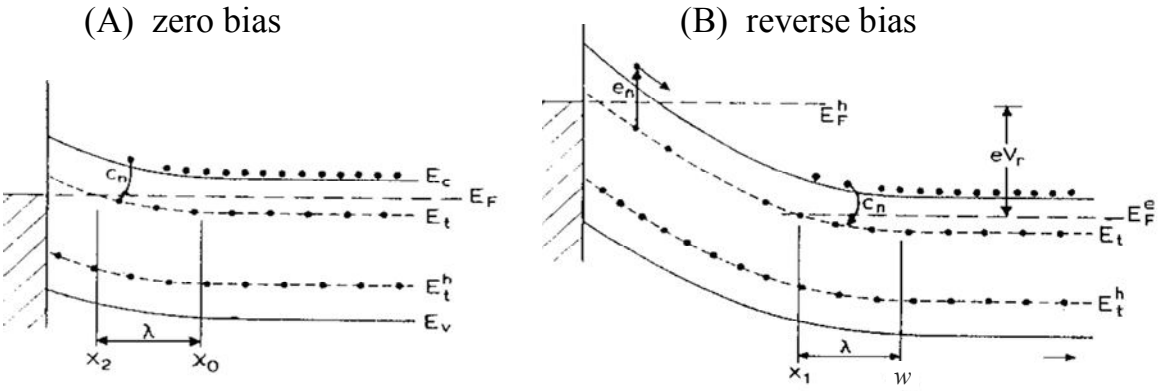

Figure 1.2. Band diagram of the Schottky barrir on n-type material containing an electron trap E_t under (A) zero applied bias when the depletion depth is x_0 and (B) high reverse bias when the depletion depth is w. E^e_F and E^h_F are the quasi-Fermi levels for electrons and holes, respectively. Note, that only the occupation of the electron trap could be varied by filling pulse (After [Blood 1992]).

$$C(t) = C(\infty)\left\{1 - \frac{n_t(t)}{N_d + N_t}\right\}^{\frac{1}{2}} \tag{1.21}$$

where the final capacitance ($n_t(\infty)=0$) is

$$C(\infty) = A\left\{\frac{\varepsilon\varepsilon_0 e(N_d + N_t)}{2}\right\}^{\frac{1}{2}} V^{\frac{1}{2}} \tag{1.22}$$

The square root term in the expression for C(t) can be expanded and when N_t, $n_t << N_d$ the change in capacitance $\Delta C(t)=C(t)-C(\infty)$ can be rewritten using Eq. 1.17

$$\frac{\Delta C(t)}{C(\infty)} = \frac{C(t) - C(\infty)}{C(\infty)} = -\frac{n_t(t)}{2N_d} = -\frac{N_t}{2N_d}\exp(-e_p t) \tag{1.23}$$

and the capacitance increases exponentially with time as carriers are emitted from the trap. This is the main equation used as the basis of DLTS technique. It shows that the time constant of the capacitance transient gives the thermal emission rate and the amplitude of the transient $\Delta C/C(\infty)$ is equal to $N_t/2N_d$, giving a measure of trap concentration. Please note that just the same equation with the same sign one will also obtain for acceptor-like trap ($\rho_a(t)=e\{N_d - n_t(t)\}$ instead of Eq. 1.20) located in the upper part of band gap.

However, it is necessary to realize, that while Eq. 1.23 indicates the basic principles of capacitance transient method, it applies only in rather restricted circumstances. It was assumed that all traps were filled prior to the emission process: this may not be true if the capture cross section is very small. It was also assumed that the emission process occurs over complete depletion region, and ignored the transition region λ and the fact that the traps in the region (w-λ) are never emptied. For more detailed analysis see [Blood 1992].

- ***Correlation procedure.***

Lang in his pioneer work in 1974 [Lang 1974] has suggested to use a dual-gated signal averager in order to determine the emission time constant $\tau_e = 1/e_n$ of capacitance transient. However in the present work, DLTS spectrometer utilizing the "lock-in" detection method was used, since both signal-to-noise ratio and the resolution ability are higher when using lock-in integrator. The principle of this method is shown in Fig. 1.3.

Sequence of the filling pulses of the voltage U_p and duration t_p is applied to the Schottky diode to fill the traps (Fig. 1.3A), and capacitance relaxation after the restoration of high reverse bias U_r is monitored and recorded by fast-response capacitance meter when the sample temperature is slowly varied. A series of the typical capacitance transients for a majority-carrier trap at various temperatures is shown schematically in Fig. 1.3B. According to Eq. 1.16 and 1.23, the emission rate is very small for low temperatures but

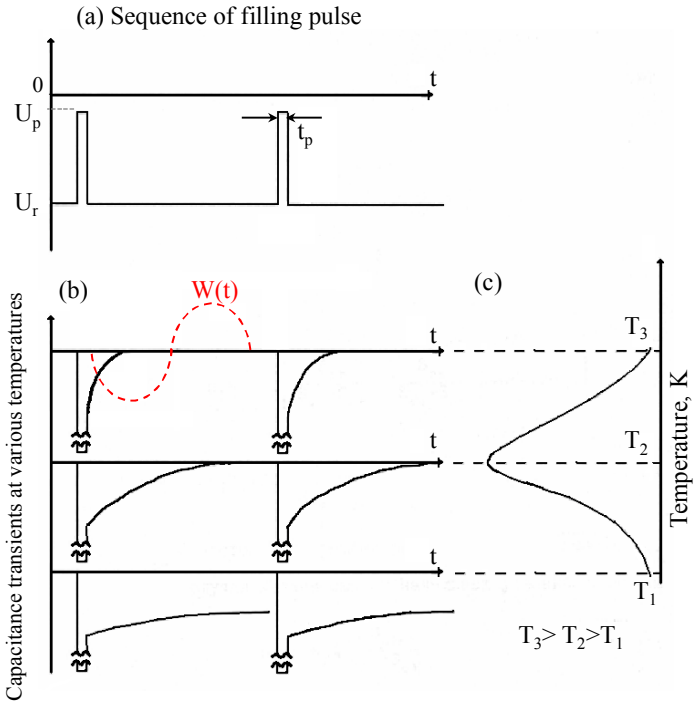

Figure 1.3. (A) Sequence of filling pulses applied to the Schottky diode; (B) Variations of the capacitance relaxations with the increasing of the temperature; (C) Signal as obtained at the output of the lock-in detector.

becomes more rapid as the temperature increases; thus the capacitance relaxations tend to be rather slow at low temperature, but they become faster with temperature growth.

Then, at every particular temperature, lock-in detector multiplies the capacitance transients $\Delta C \cdot exp(-e_n t)$, where ΔC is the relaxation amplitude, with the correlation function $W(t)$ and integrates it over a specified time. In our example the correlation function is *sin*-like function $W(t)=sin(2\pi t/T_C)$ of the period width T_C, which is also called "rate window"; thus the mean value of the capacitance transient signal for one period T_C will be

$$S(T) = \frac{1}{T_C}\int_0^{T_C} \Delta C(t) W(t) dt = \frac{\Delta C}{T_C}\int_0^{T_C} \exp(-e_n t)\sin(\frac{2\pi t}{T_C})dt = \\ = \frac{\Delta C \cdot 2\pi}{(2\pi)^2 + (e_n T_C)^2}[1 - \exp(-e_n T_C)] \qquad (1.24)$$

As one can see, the integral with *sin-like* weighting function can be solved analytically. However, weighting function should not necessary by only *sin-like*, in general this function could be of the any shape satisfying the following condition

$$\frac{1}{T_C}\int_0^{T_C} W(t) dt = 0 \qquad (1.25)$$

The most commonly used functions are *sin/cos*-like, *meander*, *etc*. (see for review [Istratov 1997]). As a result, measured temperature dependence of lock-in output signal *S(T)* (so-called tempscan DLTS signal) goes through the maximum when the emission rate of

carriers from the trap equals to the rate window period, see Fig. 1.3C. The magnitude of the obtained DLTS peak is proportional to the deep level concentration N_t (Eq. 1.23). Temperature position T_{max} of the obtained peak depends on the exact shape of the weighting function W(t) and its period T_C, as well as on the trap parameters – activation energy and capture cross section.

At the maximum position of this temscan signal the emission time constant τ_n of the transient can be calculated by differentiating *S(T)* with respect to *T* and setting the result equal to zero. For the considered case of *sin*-like weighting function, maximum on *S(T)* dependences will appear when $\tau_e \cong 0,4T_C$. By recoding several *S(T)* curves with different rate window periods T_C, one obtains different temperatures at which the particular DLTS peak appears. Thus, having a set of the emission rate and corresponding temperature pairs $\tau_e(T_{max})$, a semi-log dependence of $\ln(e_n/T^2)$ versus $1/kT$ (Arrhenius plot) can be plotted (Eq. 1.16), which allows for the deduction of desired traps parameters E_{na} and σ_{na}.

1.3 Isothermal spectroscopy (ITS) method.

This method is similar to DLTS one and uses the same correlation procedure (Eq. 1.24 and Fig. 1.3) but the measurements are performed at the constant temperature under the gradually increasing rate window period T_C, see Fig. 1.4. Similar to tempscan (DLTS), allows a periodwidthscan (ITS) the time constant τ_e of the emission process determination: at the position of ITS maximum the period rate window period T_C fits best to the emission time constant τ_e. And of course, the magnitude of the ITS peak is proportional the concentration of the level causing the transient. In order to derive the trap parameters E_{na} and σ_{na}, one should measure a set of ITS peaks at different temperatures and plot respectively the $\ln(e_n/T^2)$ vs $1/kT$ dependence. The measurement temperature(s) should be selected that way, to make the time constant τ_e of determined defect level at the relevant temperature fall approximately in the middle the usable time interval of our transient recorder for time-dependent measurements.

ITS method is especially suited for the determination of electrical field-dependent emission, what will be just the case of the samples studied here (see Chapter 7).

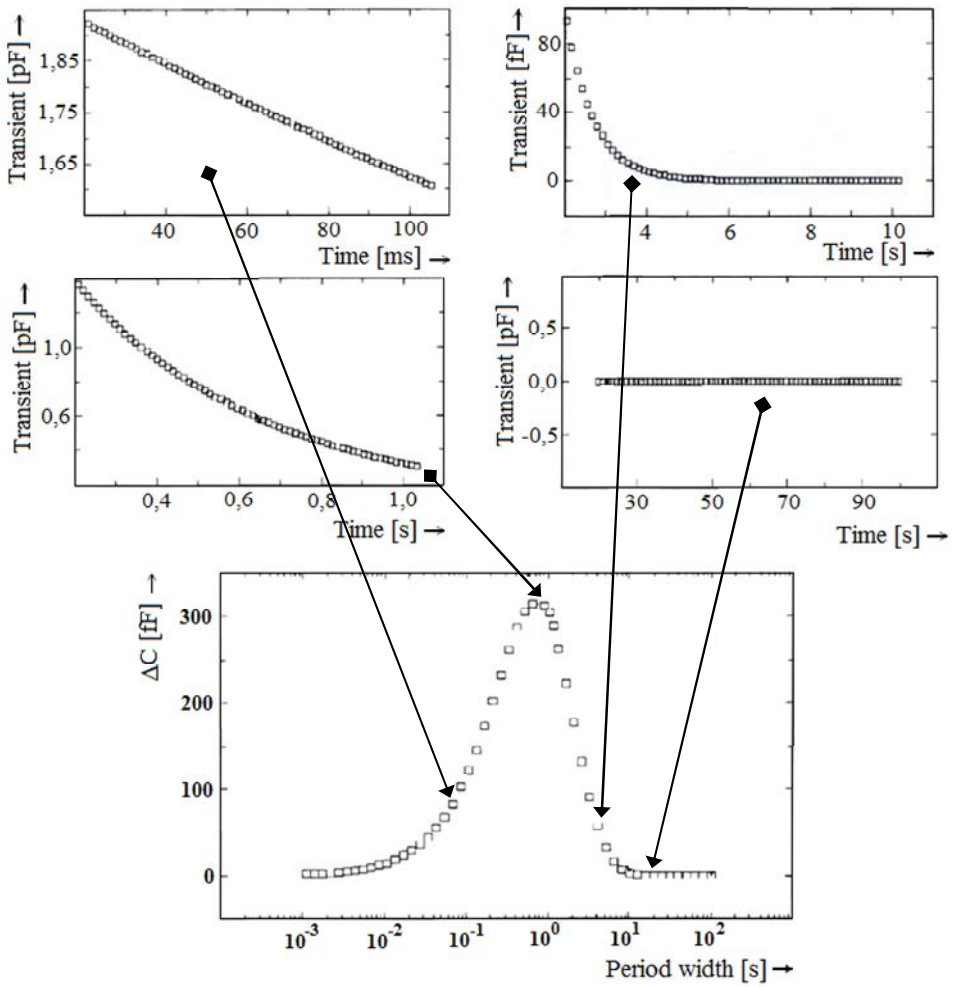

Figure 1.4. Capacitance transients recorded during different period widths and the resulted ITS peak.

1.4 Summary for Chapter 1.

For the summary, the advantages of the DLTS technique can be listed. From the technical point of view, the biggest advantage of DLTS is that the measurements of quite fast signal, capacitance transients, have been transformed into the slow measurements of the tempscan signal. This gives user plenty of time for averaging the signal using various signal integrators just beyond the correlator.

From the scientific point of view, DLTS method represents a big advance over many other techniques for study of defect states because of the following properties:

a) This type of measurement possesses a very high sensitivity – values of $N_t/N_d \approx 10^{-4}$ can be easily achieved.

b) In general the response of the trap is determined by more than one process (Eq. 1.13): in a depletion region capture process is suppressed, so that thermal emission can be observed in isolation.
c) Varying the values of the reverse bias U_b and pulse voltage U_p, trap profile could be derived. By changing the filling pulse duration t_p, capture kinetics could be monitored.
d) Using the optical excitation methods, minority carrier traps could be studied as well (so-called MCTS method – Minority Carrier Transient Spectroscopy).

Chapter 2
Electronic properties of dislocations in silicon.

The question *why* metals could be plastically deformed, and *why* the plastic deformation properties could be changed to a very large degree by forging (and *magic?*) without changing their chemical composition, was for our ancestor a great mystery during thousands of years since the Bronze Age was taken to begin about 3000 years BC in the Ancient Near East.

No explanation was offered before the first suggestions of dislocations were provided by observation in the 19th century that the plastic deformation of metals proceeded by the formation of the slip bands or slip packets, wherein one portion of the specimen sheared with respect to another. Initially the interpretation of this phenomenon was obscure but with the discovery that metals were crystalline, it was appreciated that such slip must represent the shearing of one portion of a crystal with respect to another upon a rational crystal plane. Volterra ([Volterra 1907], note the year – 1907, even 'crystals' haven't been discovered yet) and others, notably Love [Love 1927], in treating the elastic behaviour homogeneous isotropic media considered the elastic properties of a cut deformed cylinder – Volterra construction. Some of deformation operation clearly corresponds to slip, and some of the resulting configurations correspond to dislocations. However, the relation of the work of elasticians to crystalline slip remained unnoticed until the late 1930s, after dislocation have been postulated as crystalline defects.

In 1934 Taylor [Taylor 1934], Orowan [Orowan 1934] and Polanyi [Polanyi 1934] introduced independently the concept of crystal dislocation. This concept allowed a complete understanding the basic scientific principle governing the metallurgy - the plasticity of metals. But it was very soon recognized that in semiconductors the most interesting and important effects of dislocations result from electronic states which they

introduce into the band gap of semiconductors, whereby playing a very specific role in semiconductor crystals suitable for electronics use.

In 1952 with the one and a half page communiqué entitled "Plastic deformation of germanium and silicon" written by Gallagher [Gallagher 1952] from General Electric, in which author announced that he had succeeded in achieving plastic deformation of germanium and silicon crystals at elevated temperatures and that the growth of germanium resistivity upon deformation and decreasing of the photo-injected carriers lifetime were observed – the era of intensive investigations of dislocations in semiconductors began. However, in spite of almost 60 years of efforts, dislocations still possess many unexplained features and unopened secrets.

2.1 Structure of Dislocations in Si.

In material science, **dislocations** are line defects, which keep the lattice translation symmetry along their line directions, but destroy it in radial direction. One cannot establish 1:1-relation between the lattice sites of a crystal containing a dislocation and of a perfect crystal. By counting the number of lattice sites on a loop drawn around the dislocation line and comparing it with that of an identical loop in the perfect crystal, one may determine the fundamental quantity defining the dislocation – Burgers vector $\vec{b}$ and its direction relative to the dislocation line.

Silicon crystallises in the diamond structure, whose Braivais lattice is face centred cubic (*fcc*), but unlike *fcc* metals silicon has a basis of two atoms. In *fcc* crystal structures, the dislocation lines are along [110] directions and a lattice translation vector, i.e. the smallest "perfect" Burgers vector, has the form *a/2[110]*. There are two types of dislocations with perfect Burgers vector: one is a pure screw dislocation (Burgers vector is parallel to the dislocation line) and the other is a 60° dislocations (i.e. with the angle between dislocation line and Burgers vector is of 60°). In *fcc* crystals the main slip planes, which are normal to both, the Burgers vector and the dislocation line, are the (111) planes. Since the diamond crystal structure consists of two *fcc* sub-lattices, displaced by the vector *a[¼ ¼ ¼]* from each other, two possible types of (111) planes exist, namely shuffle- and glide-plane, as shown in Fig. 2.1. The dislocations of the two sets have different core structure and dangling bonds configurations. At present it is widely accepted that in silicon most of dislocations generated at a temperature more than 700°C by either macroscopic or microscopic plastic deformation are of the glide set [Schröter 2002a].

Perfect dislocations of a glide set can dissociate into (Shockley) partial dislocations with smaller Burgers vectors which are not translation vectors of the *fcc*-lattice [Shockley 1953]. A perfect 60° dislocation splits into one 90° and one 30° partial (see Fig. 2.1) preserving the total Burgers vector according to

$$\vec{b}_{60^0} \rightarrow \vec{b}_{30^0} + \vec{b}_{90^0}$$

$$\frac{a}{2}<110>\rightarrow\frac{a}{6}<121>+\frac{a}{6}<21\bar{1}> \qquad (2.1)$$

Whereas a perfect screw dislocation dissociates into two 30°-partials with different Burgers vector directions. In both cases, the partials bound a low-energy stacking fault defect (i.e. stacking faults and dislocations are unambiguously linked), which is a planar defect corresponding to errors in the stacking sequence in the (111) direction, as it is shown in Fig. 2.1. This type of dissociation into two partials reduces the strain energy associated with the dislocation. The size of the stacking fault is determined by the balance of the $1/r$ repulsion between the partials, with the constant attractive force resulting from the formation of the stacking fault. In silicon the width of the stacking fault separating the two partials in a dissociated dislocation is about 40 Å for the screw dislocation and 65 Å for the 60° dislocation [Wessel 1977].

According to further theoretical calculations [Veth 1984] [Lodge 1989], core reconstruction of the partial dislocations is energetically favourable. As partials of the glide set have a core lying between the narrowly spaced (111)-planes, dangling bonds in its core that also lie in the (111) glide plan may disappear by bond reconstruction (i. e. dangling bonds at neighbouring atoms form covalent bonds with each other). When the partial belong to the shuffle set, its core lies between the widely spaced (111)-planes, the dangling bonds of the core are normal to the glide plane and cannot reconstruct.

As it was established, the dislocation related deep states in the indirect band gap of Si are associated with core configuration of threefold (i.e. dangling bond) and fivefold co-ordination, but missing for cores with four-fold co-ordination [Alexander 2000]. Hence, the reconstructed four-fold cores of 30°- and 90°- partials would not introduce deep

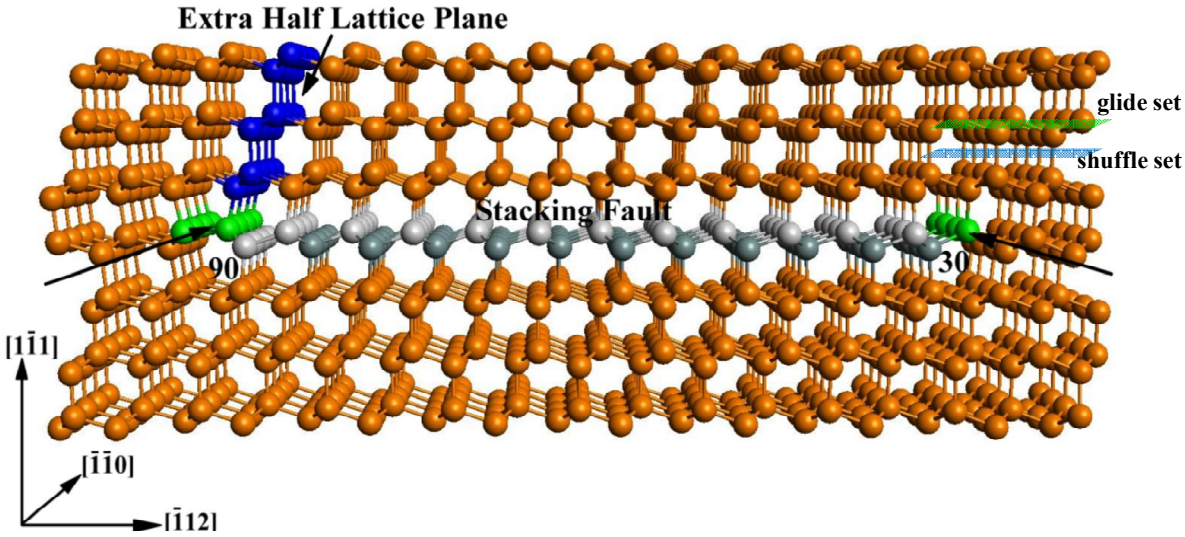

Figure 2.1. Dissociated 60° glide-set dislocation. A stacking fault (SF) ribbon (plane of gray and white atoms) is bound by the two partials. The cores (green) of the 30° and the 90° partial are reconstructed. The extra half plane at the 90° partial is indicated by the blue atoms (after [Koch 2002]).

electronic states in Si band gap. Nevertheless, they can have deep localised electronic states due to: (i) core defects (reconstruction solitons, jogs, etc.) (ii) impurity atoms segregated inside the dislocation core or in the strained region around the dislocation.

One should also note that when moving dislocations meet each other, they could react producing more complicated constructions. For example, when two 60° glide set dislocations with the same line direction in [110] moving in two different glide planes meet each other they can form a new, Lomer type of dislocation, which is not mobile and have a core structure and electronic properties very much different from 60° and screw dislocations [Kveder 2008a].

- ***Dislocations sources in silicon***

Dislocations always exist in poly- and multi-crystalline Si, whereas as-grown CZ or FZ wafers are usually dislocation-free. There are several reasons for existence of dislocations in Si:

• 'Macroscopic' strain (for example, due to thermal gradients).

• 'Microscopic' strain around precipitates (for example, punch-out dislocations produced by oxide precipitates).

• 'Small angle' grain boundaries (see Chapter 3).

• 'Grown-in dislocations' from hetero-interfaces (misfit dislocations on Si/Si_xGe_{1-x} heterostructures)

• Dislocation as product of point defect clustering (dislocation loops formed by implantation of Si ions and subsequent anneal).

2.2 Dislocation-related shallow 1D-bands.

Theory predicts the existence of relatively shallow dislocation-related bands associated with the strong lattice deformation (strain field) around dislocation [Winter 1978]. An empty one-dimensional (1D) band $E_C - E_{De}$ and the occupied one $E_V + E_{Dh}$ have been shown to split off from the conduction band and valence band edge, respectively (Fig. 2.2). These 1D bands are inherent properties of dislocations and stretching along the whole dislocation line, so the dislocations can be considered as native "quantum wires" inside the crystalline solids. Position and properties of shallow 1D-bands depend strongly on the strain field around the dislocation, thus on the particular dislocation type and geometry. According to the theoretical calculations of Farvacque et al. [Farvacque 2001] the electron binding energies are expected to be *49 meV* and *41 meV* for screw and for 60° dislocation, whereas the binding energies for holes - *47 meV* and *37 meV*, respectively. Experimentally obtained values will be discussed in the following paragraphs.

The density of states of a 1D electron system has a minimum at the centre and $1/\sqrt{E}$ -singularities at the band edges (arising from the translation symmetry in one

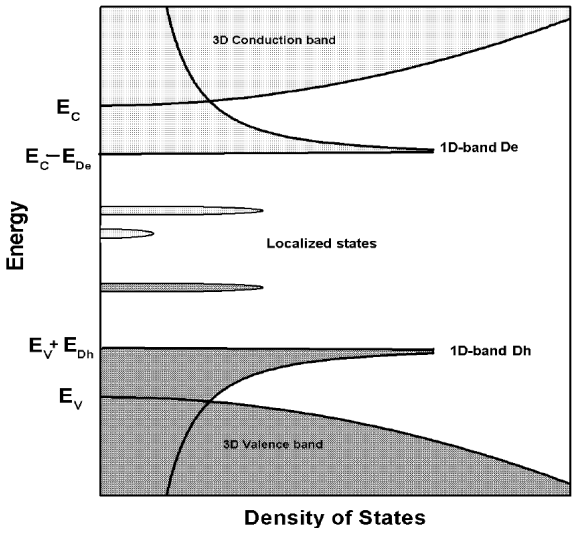

Figure 2.2. Energy diagram for a glide 60° dislocation in Si. Regular segments of the dislocation produce shallow 1D-bands, while some defects and irregularities at the dislocation can produce deep localized states (after [Kveder 2008a]).

direction), that is much different from the 3D-band where it is zero at band edges, increasing as $\sqrt{E}$ (see Fig. 2.2). However, with increasing core defect concentration the wave function in 1D-bands, extending along the dislocation line, becomes more and more localized smoothing the $1/\sqrt{E}$ singularities in density of states at the energy edges of 1D-bands.

1D systems are expected to have extremely high mobility: carriers captured into shallow states can diffuse along the dislocation line for a long distance without recombination [Sakaki 1980]. However, perturbations by point defects or other reasons producing abrupt changes in the 1D band structure could impede high electron mobility.

- ***Shallow stacking fault states.***

It has been shown in earlier investigations [Mattheiss 1981] [Marklund 1981], that infinite intrinsic stacking fault in Si generates two degenerated bands of shallow states with the sharp maximum at the Brillouin zone centre (Γ-point) and that these bands split and bend rapidly into the valence band when leaving the Brillouin zone centre. These bands are occupied and localized near the stacking fault plane in real space.

In more detailed investigation by Lehto [Lehto 1997], the finite stacking faults and the influence of the stacking fault width on the electronic states in band gap have been studied using the super-cell computational method. It was found, that the positions of shallow states inside the band gap depend significantly on the stacking fault size: when the partials come closer together, lager overlap of the partials strain fields "pushes" the shallow states deeper into the band, however without changing their shallow character. This is seen in Fig. 2.3, where the energy of the fault shallow states as a function of the number of atoms in the computational unit cell is presented (stacking fault width is proportional to square root of the number of atoms in the unit cell).

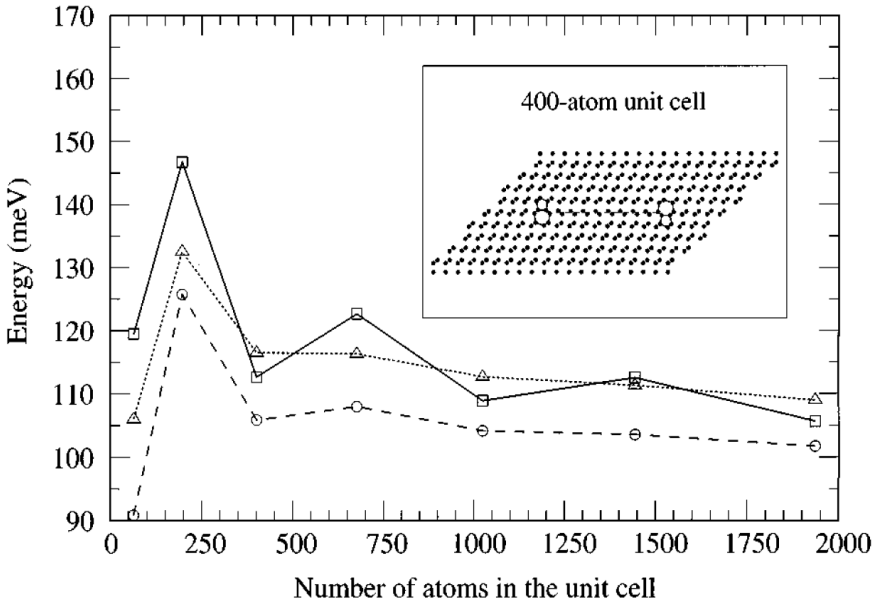

Figure 2.3. The energy of the fault state of an intrinsic stacking fault bounded by two 90° partials (such choice was necessary to keep the sum of Burgers vectors equal to zero inside the computation cell) as a function of the number of atoms in the unit cell. The square root of the number of atoms is proportional to the width of the stacking fault: stacking fault width of about 13 Å corresponds to the smallest cell and of about 70 Å to the 1936-atom cell. The atomic structure is determined by the Keating model (squares and solid line), the bond-charge model (triangles and dotted line), and the anharmonic bond-charge model (circles and dashed line). The valence band maximum (E_V) of the ideal structure is at *zero eV*. The inset shows a 400-atom unit cell used in the calculation (after [Lehto 1997]).

The alternation in energy is due to the fact that the cells with 64, 400, 1024, and 1936 atoms are rotationally symmetric about the centre of the cell, while the cell with 196, 676, and 1444 atoms are inversionally symmetric about the cell centre and the energy tends to be somewhat lower in the rotationally symmetric cells than in the inversionally symmetric ones. Generally, the energy of fault states with the increasing of the distance between the partials (when width goes to infinity) should converge to the value E_v*+75 meV*, corresponding to the infinite stacking fault, but the convergence appeared to be rather slow. In the case of a bounded intrinsic stacking fault with equilibrium width of 60 Å, the shallow state is localized close to E_v*+100 meV*.

2.3 Electrical charge associated with dislocations.

The dislocation-related states can be occupied with electrons in n-type Si (or holes in p-type Si) forming a negative (positive) line charge Q. To keep space charge neutrality the negatively charged dislocation line in *n*-Si is surrounded with a cylinder of ionized (i.e. positively charged) donor atoms, the so-called Read cylinder. In the opposite case of p-

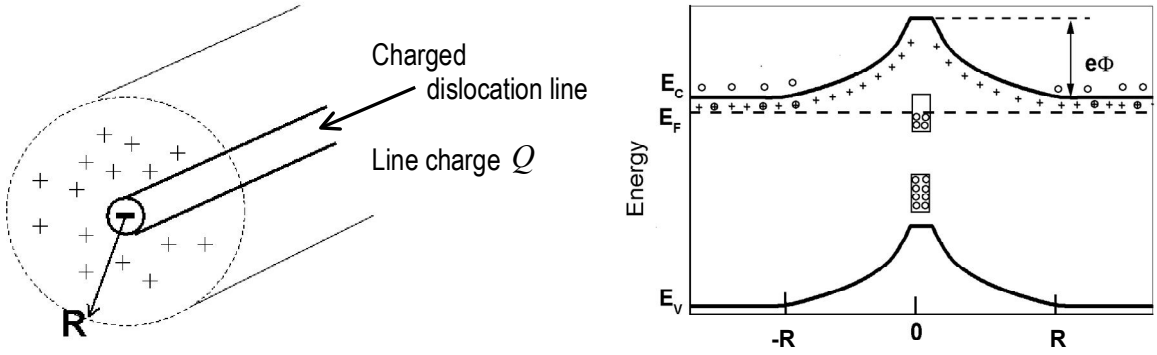

Figure 2.4. Illustration of the Coulomb barrier appearing around a dislocation due to its line charge caused by electrons captured to the dislocation-related states (after [Kveder 2008a]).

type Si the dislocations form positively charged lines surrounded with ionized (negatively charged) acceptors. Such a structure results in the bending of conduction and valence bands in the vicinity of dislocation, i.e. in the appearance of so-called Coulomb barrier $e\Phi$ around the dislocation, which is associated with the presence of the electric field. This is demonstrated schematically in Fig. 2.4 for n-type Si.

The radius of the Read cylinder (i.e. screening radius R of the electric field around the dislocation) is given by:

$$R = \sqrt{\frac{eN_{tot}}{\pi eN_d}} \ , \tag{2.2}$$

where N_{tot} is total dislocation charge per unit length (a concentration of electrons or holes captured to all dislocation energy states), N_d is a concentration of shallow donors (or acceptors) in the sample and e is an elementary charge. The exact calculation of barrier $e\Phi$ is a difficult problem (for details see [Schroter 2002a]), but in many cases it can be approximated by simple formula:

$$e\Phi \approx e^2 N_{tot}\left(\ln[{N_{tot}}^{3/2}/(\pi N_d)^{1/2}]-0.5\right)/\varepsilon \, . \tag{2.3}$$

The dislocation line charge $Q=eN_{tot}$ has major influence on the barrier height and, hence, on the electric field around the dislocations. Typically, the average electric field $E = \Phi / R$ may reach the values around 10^4 *V/cm*. This electric field attracts the minority carriers, thus leading to the enhanced recombination when minority carriers captured at the dislocation recombine trough the deep states in the band gap (as a rule – related with the impurity atoms segregated at dislocation). One should also note that due to the shallow character of strain-induced 1D bands, their wave functions are radially extended and coupled to deep levels of point defects located at or close to dislocations. Whereby, 1D shallow states may strongly affect the recombination rate and the lifetime of minority charge carriers in Si, see [Kveder 2001] for details.

2.4 Experimental observation of dislocation-related localized states.

- ***Particularities of DLTS analysis of dislocations in Si.***

Deep level transient spectroscopy (DLTS) has been initially developed as a powerful experimental tool to investigate the electrically active point defects in semiconductors and their parameters determination (see [Lang, 1974] and Chapter 2). Nevertheless, this method was widely used to study the defects introduced by plastic deformation as well [Kveder, 1982] [Patel, 1979] [Omling, 1985] [Kisielowski, 1991].

However, one should be very careful when using this method to study the dislocation-related defects (i.e. spatially extended defects) since several problems must be considered:

A) First of all, dislocation in Si may be associated not with a single level inside the band gap, but with a density of states or levels $N_D(E)$ where $E_1 \geq E \geq E_2$, see Fig. 2.5. Emission rate and capture rate will be dependent on the level position E_i within that range, so that $\Delta C(t)$ becomes non-exponential during emission, which gives broadened DLTS peaks (i.e. broader than the DLTS peak of point-like defects arising at the similar temperature, which follows the Eq. 1.16 and 1.17). Moreover, owing to the DLTS peak broadening, the concentration of the traps as derived from Eq. 1.23 deduced for point-like defects could be underestimated.

It is possible to specify two different types of extended defects states relative to their internal equilibration time Γ_i, which is the time needed to establish electronic equilibrium at the defect: (i) "band-like" states with $\Gamma_i \ll \tau_e, \tau_c$ (emission and capture time constant) and (ii) "localised" states with $\Gamma_i \gg \tau_e, \tau_c$. As a result, for the band-like states because of the fast inter-level transition rate, emission to the conduction band occurs mainly from the upper filled level(s); whereas the localised states almost exclusively exchange their charge carriers with conduction band or valence band. Criteria to distinguish between band-like and localised levels by measuring dependence of DLTS spectra on capture time duration t_p have been developed by Schröter et al. [Schröter 1995]. Localised behaviour was established for the most of defects observed in the plastically deformed samples (see following paragraphs), whereas band-like behaviour – for the centres related with $NiSi_2$ and Cu_3Si precipitates [Schröter 2002a].

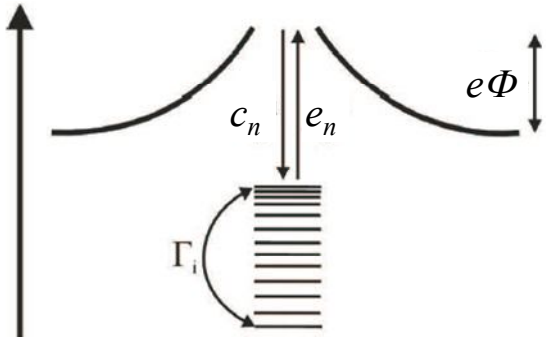

Figure 2.5. Electron transitions between conduction band and dislocation states. Capture c_n and emission e_n rates are affected by the barrier δE_C. Γ_i is the internal equilibration time of electron exchange between the dislocation states (after [Schröter 2002a]).

B) Another particular property of the DLTS peaks due to the dislocation-related defects is the logarithmic dependence of DLTS line amplitude on filling pulse duration t_p. Accounting the Coulomb potential barrier around the dislocation (Eq. 2.3), detailed balance equation for the point defects (Eq. 1.13) could be rewritten for dislocation-related defects (without consideration of dislocation levels distribution $N_D(E)$) as

$$\frac{\partial f}{\partial t} = c_n \exp\left(-\frac{e\Phi}{kT}\right)(1-f) - e_n f \qquad (2.4)$$

Thus, barrier $e\Phi$ around the dislocation slows down further capturing of free electrons to the dislocation approximately by the factor $exp(-e\Phi/k_BT)$ and finally limits the total equilibrium occupation of dislocation states. This results in a logarithmic dependence of number of captured carriers on the filling time t_p, i.e. $\Delta C_{max} \sim ln(t_p)$, while for point defects this dependence is exponential (see [Alexander 1991] and reference therein). So, the observation of logarithmic dependence of DLTS line amplitude on t_p indicates that this DLTS line corresponds to states localized at dislocation (or other extended defect). It is accepted that due to Coulomb barrier $e\Phi$ around the dislocations, the total density N_{tot} of electrons (or holes) captured to the dislocation per unit length usually cannot exceed $N_{tot} = \sim 2*10^6\ cm^{-1}$ even if the total number of states N_{DD} per unit length at the dislocation is much larger than this value [Kveder 2008a].

C) Dislocations are extended defects and consequently they can change their charge state within wide limits. The Coulomb interaction among charges confined at the dislocation causes a shift of the dislocation level with respect to the Fermi level: this local band bending induces a change in the positions of the energy levels during filling and emptying of the traps. Moreover, dislocation strain field may also cause an effective shift of point defect levels relative to the silicon band edge [Schröter 2002a].

Despite these difficulties extensive DLTS investigations of plastically deformed Si samples (PDS) have yield quite lot of comprehensive data about dislocation electrical

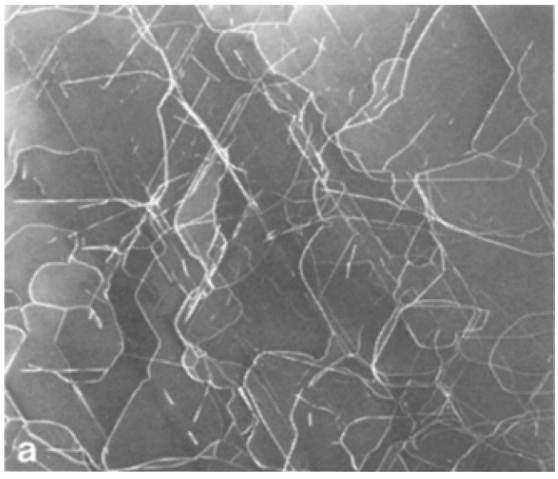

Figure 2.6. TEM micrograph (*8,5* x *7 μm*) of the dislocations in the Si sample deformed at 650 °C with resolved shear stress $\tau = 30\ MPa$, deformation time $t_d=40\ min$, shear strain $\varepsilon=1.5\%$. Deformation density is $\sim 10^9$ cm^{-2} (after [Sauer 1985]).

properties. It should be however mentioned, that plastic deformation performed as usual at temperatures 600-900 °C introduces fairly randomized dislocations mix regarding dislocation types, directions and degree of contaminations (see example in Fig. 2.6), so that the interpretation of the obtained results becomes an intricate task. Dislocation density in the plastically deformed samples prepared for DLTS study usually not exceeds a few 10^8 $cm^{-1.}$ In the following, the short review concerning the most prominent findings is presented.

- ***Dislocation-related lines in n-type Si.***

Extensive work on plastically deformed *n*-type Si have led to the identification of four traps, labelled according to Omling et al [Omling 1985] as A (E_C *–0,19 eV*), B (E_C – *0,3 eV*), C (E_C – *0,37...0,43 eV)* and D (E_C – *0,54eV*) traps, whose intensities and corresponding DLTS peaks parameters (broadening) are strongly dependent on deformation and annealing procedures. As an example, Fig. 2.7 shows a typical DLTS spectrum measured on n-Si deformed at 750°C to a dislocation density N_D of about ~10^4 cm^{-2} [Cavalcoli 1997]. These levels are frequently observed in the as-deformed samples when dislocations have been introduced at T<800°C and were investigated by many groups of scientist [Kveder 1982] [Omling 1985] [Kisielowski 1991].

All these lines revealed characteristic feature of deep localized states at extended defects [Schröter 1995] [Schröter 2002b], namely the logarithmic dependence of the signal amplitude on pulse duration t_p. Moreover, they were identified as acceptors [Omling 1985] [Kveder 2008a], thus showing general agreement with the results of Hall measurements which have found the reduction of the initial doping in n- and p-type material after the plastic deformation [Bondarenko 1980].

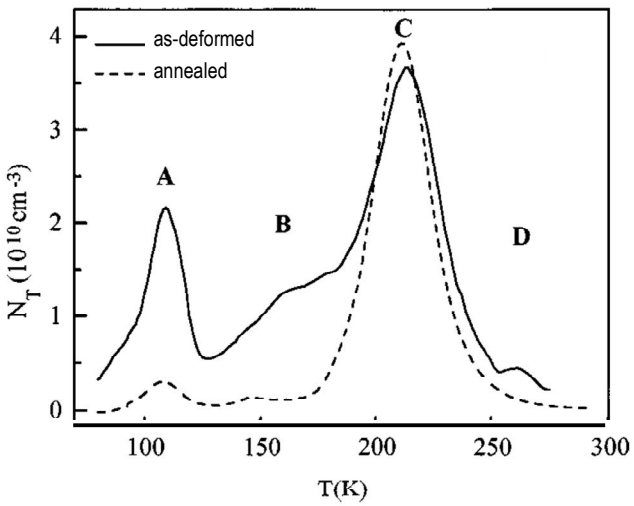

Figure 2.7. Deep-level transient spectroscopy spectra of a plastically deformed n-type Si sample before (solid line) and after (dashed line) annealing at *850 °C* for *1h* in forming gas (after [Cavalcoli 1997]).

Consensus of opinion exists concerning the annealing behaviour of these lines (see [Schröter 2002a] and references therein): defects A, B and D are thermally unstable and disappear completely after annealing at 850-900°C, giving rise to a more pronounced C-peak which survives after annealing (Fig. 2.7). That C-line is really connected with dislocations has been concluded from the comparison of the C-defect density and the dislocation density measured by EBIC and TEM. A linear relation has been found for dislocation densities ranging from $7*10^6$ cm^{-2} to $1,5*10^9$ cm^{-2} (see [Schröter 2002a] and references therein).

Other levels, namely - A, B and D didn't reveal direct correlation with the dislocation density. Thus, traps *A* and *B* because of their thermal instability were identified with point-defect clusters related in some way to dislocations motion [Omling 1985] [Cavalcoli 1997] that located close to, or inside, the dislocation core thus feeling the influence of Coulomb potential barrier, showing therefore a logarithmic filling dependence. Whereas D-line was attributed to the dangling bonds at dislocations, which are always observed in the as-deformed samples by the electron-paramagnetic resonance (EPR) technique and which disappear during thermal annealing via bond reconstruction [Omling 1985]. It should be also pointed out, that the total concentration of all detected traps (as estimated from the numerical simulations of DLTS peaks shapes) is much lower than the expected density of the dangling bonds in the core of the un-reconstructed dislocations, thus confirming the reconstructed geometry of dislocations in Si.

- ***C-line properties***

For the C-line it was clearly shown, that its shape (broadening) depends strongly on the sample preparation conditions. Possible explanation of this phenomenon was suggested by Knobloch et al [Knobloch 2003]. Applying DLTS and Scanning-DLTS methods to study the misfit dislocations in $Si/Si_{0,98}Ge_{0,2}$-heterostructures grown by chemical vapour deposition, authors have shown that *C* line is absent for the case of clean misfit dislocations. However, it was also found that intentional contamination by gold provokes the appearance of *C*-line with its magnitude and shape being strongly dependent on the degree of contamination. Specifically, contamination degree affects drastically the broadening of the *C*-line, i.e. energy distribution of the dislocation-related states: *C*-line was found to be sharp in sample with little degree of contamination but it became symmetrically or asymmetrically broadened in the sample with higher contamination level.

Basis on the obtained results, it was supposed that in case of weak contamination degree, the impurities accommodate mainly in the dislocation core, giving rise to a sharp distribution of levels (i.e. non-broadened DLTS peak) that could differ significantly from the level of isolated atoms of the same species because of dislocation strain field impact. It was also supposed that this "core level" formed by Au atoms accommodated in the dislocation core might exhibit similar properties for different metallic impurities. With

increasing of the contamination level, impurities become collected in the cloud around the dislocation that extends *1–2 nm* from the core, thus generating a broad distribution of levels that range between core-like levels and levels of isolated impurity atoms. As a result, it was concluded that the *C*-line generally consists of a distribution of levels, presumably caused by point defects/impurities, whose width is influenced mainly by the amount of contamination rather than by particular type of impurity.

Another important hint about the origin of the localised states (levels) responsible for *C*-line has been obtained by Kononchuk et al [Kononchuk 1996] and Kveder et al. [Kveder 2008b]. In the experiments of Kononchuk et al the density of dislocations N_D and the path L_D the dislocations have moved were controlled by variation of stress and deformation time. In FZ-samples standard set of 4 peaks appeared only after the prolonged deformation time of several hours which corresponds to the pathway length $L_D \geq 500\ \mu m$. Whereas in Cz-samples all 4 dislocation related peaks became clearly visible already after the shortest pathway ($\sim 30\mu m$). Moreover, it was found that the weak DLTS spectrum on FZ-sample (after the medium deformation time) has been developed towards the normal one after additionally annealing for several hours or after intentional copper contamination.

To explain their findings, Kononchuk et al. suggested that during the dislocations motion or additional annealing, electrically active centres are forming in the dislocation vicinity and that these centres contain as the main component oxygen or intrinsic point defect or both. As created, these centres provoke the increase of dislocation recombination activity, which for the clean and uncontaminated dislocations in Si seems to be extremely low in accordance with theoretical predictions. On the other hand, in the set of separate experiments it was shown, that the presence of various metallic contaminants in Si, despite of their thousand times lower concentration than oxygen, can drastically accelerate the oxygen-related complexes formation (examples for iron-oxygen interaction in Si could be found in [Shen 1996], [Trushin 2009]); this model, supposing the catalytic action of metallic impurities, can alternatively explain the similarity of dislocation-related DLTS spectra observed in the different samples prepared at different conditions.

In the experiments of Kveder et al. [Kveder 2008b] it was additionally specified, that when the dislocations were forced to move with a high velocity of *10μm/min*, the shape of DLTS spectrum has been changed drastically: strong D-line appeared whereas C-line instead – decreased considerably. The following explanation was suggested: when dislocations are moving slowly, they collect impurities responsible for *C*-like traps and the corresponding DLTS signal increases with dislocation travelling distance. However, if one forces the dislocations to move with a high velocity, the impurity atoms cannot follow dislocations anymore so that the dislocations loose nearly all impurity atoms accumulated before. Contrariwise, some intrinsic core defects can be generated during fast dislocation motion. Increased intensity of the D-line, which was subscribed to the dangling bonds in the core of dislocations, confirms this suggestion.

So, it could be stated at the moment, that in dislocated n-type Si samples 4 deep traps were frequently detected and among them: traps A and B were identified with point-defect clusters related in some way to dislocation motion, trap(s) C – with the point defects/impurities located in the dislocation core and in the clouds around (probably related with oxygen) and trap D – with the dangling bonds in the dislocation core. However, no DLTS peak due to shallow 1D centres was detected in PDS or Si/Si_xGe_{1-x} hetero-structures.

- ***Dislocation-related lines in p-type Si.***

The most prominent DLTS line in plastically deformed p-type silicon is so-called *F*-line located around $E_V+0,33\ eV$ [Schröter 2002a], see Fig. 2.8 left. This trap has been discovered by Kimerling and Patel in 1979 [Kimerling 1979] and its properties were studied later in the works of [Lemke 1981] [Ono 1985] [Kisielowski 1991]. The filling characteristics of this line were found to be logarithmic, thus confirming that *F*-line is caused by deep localized states at extended defects. Lemke found that the amplitude of the *F*-line is proportional to the dislocation density, at least for the range of 10^6-$10^7\ cm^{-1}$. However, in the work of Castaldini et al [Castaldini 2005a] this line was also observed in the sample containing nano-sized oxide precipitates but not dislocations. It was then suggested that *F*-line may be associated with an impurities located in the strain field of extended defects – either dislocations or oxygen precipitates.

Partly controversial results exist concerning its annealing behaviour: high temperature stability of *F*-line has been observed in [Kimerling 1979] and [Kveder 1982], but Ono and Sumino [Ono 1985] reported the disappearance of F-line after 900°C annealing whereas Kisielowski et al. [Kisielowski 1991] – that the annealing has reduced the spectra to a broad unresolved band in p-type material.

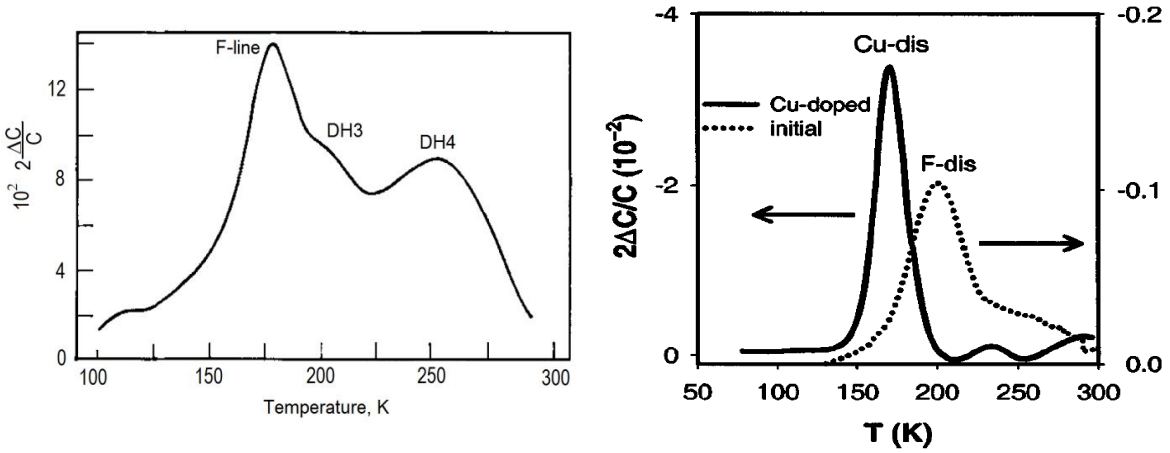

Figure 2.8. Left – DLTS spectrum of as-deformed p-type Si sample (after [Kveder 1982]). Right - DLTS spectra of *p*-type Si/SiGe/Si structures taken from as-grown (dotted line) and contaminated samples (solid line). The DLTS peak observed in the as-grown sample is marked as *F-dis*. The new DLTS peak arising after copper contamination is marked as *Cu-dis* (after [Vyvenko 2004]).

Posterior work of Cavalcoli et al [Cavalcoli 2008] casts some light into this question. It was found that *F*-line is stable only in the presence of rather high oxygen concentration, namely it is thermally stable in Cz-samples but anneals out in FZ-Si. It was supposed, that oxide precipitates (OP) or other kinds of oxygen-related defects when located at the dislocations can increase the thermal stability of the *F*-line defects, as the presence of OPs would impede the considerable rearrangement of the point defects in the dislocation vicinity. Moreover, modifications of the oxygen-related defect sizes and configuration in the dislocations cores and clouds during the post-deformation annealing were supposed to be responsible for the variations of the DLTS peak shape (broadening) before and after annealing [Cavalcoli 2008].

Among the traps which do not survive upon annealing, the following could be mentioned: trap at $E_V+0,21\ eV$ (H0.21 trap in [Kisielowski 1991]), trap close to $E_V+0,4\ eV$ (H0.39 trap described in [Kisielowski 1991], trap T4 in [Castaldini 2005a] and DH3 trap in [Kveder 1982]) and trap at $E_V+0,5\ eV$ (H0.49 trap described in [Kisielowski 1991], DH0,56 trap in [Ono 1985] and DH4 trap in [Kveder1982]), see Fig. 2.8 left. As the origin of these traps the deformation-induced point defects or point defect clusters as well as the dislocation debris were suggested.

Very interesting results were obtained on the misfit dislocations of *p*-type $Si/Si_{0.98}Ge_{0.02}/Si$ hetero-structures by Vyvenko et al. [Vyvenko 2004] and [Vyvenko 2005]. In contrast to the results of Knobloch et al [Knobloch 2003] who did not reveal any DLTS signal on the uncontaminated misfit dislocations in n-type Si, on the as-grown (noncontaminated) *p*-type $Si/Si_{0.98}Ge_{0.02}$ /Si sample a dislocation-related hole-trap level designated as *F-dis* with activation enthalpy $E_a \sim 0,2\ eV$ and capture cross section $\sigma \sim 10^{-18}\ cm^2$ was detected [Vyvenko 2004]. Unfortunately no information about the dislocation densities was reported in this article as well as in the work of Knobloch et al. [Knobloch 2003]; thus it is hard to tell at the moment what could be the reason for such different behaviour of misfit dislocations in n- and p-type materials.

Using the obtained values of activation enthalpy and capture cross section, the shape of the peak could be fitted well by using a nonbroadened single-level model (i.e. by plotting the Eq. 1.24 with known parameters E_{na} and σ_{na} as a function of temperature). No evidences of other dislocation-related traps with similar parameters were reported in the literature before. Moreover, the refilling behaviour of the *F-dis* peak in the as-grown sample was found to be of the band-like character, thus the origin of this peak cannot be explained with the impurity cloud model [Vyvenko 2005]. As the possible origin of *F-dis* trap, the theoretically predicted hole bound states at the stacking fault ribbon of a splitted dislocation were suggested. Contamination with a low level of copper (5 ppb) gave rise to the appearance of another dislocation-related defect level *Cu-dis* with $E_a \sim 0,32\ eV$, whereas the *F-dis* line disappeared completely, see Fig. 2.8 right. This level arising after the copper contamination has not been described in the literature for investigations of copper-related defects in perfect silicon. On the other hand, activation energy of this trap is

rather similar to that of the dislocation-related *F-line*. One should also note that in the previous works elevated temperatures were used for introduction of dislocations at which the diffusivity of copper is high enough to cause an unintentional co-introduction by this (or other) impurity.

Thus, similar to the dislocation-related traps in n-type Si samples, particular evidences regarding the influence of oxygen [Cavalcoli 2008] and copper [Vyvenko 2004] impurities onto the electrical activity of dislocations in p-type Si were found as well.

2.5 Experimental observations of the shallow 1D bands.

The first experimental confirmation of the 1D-band existence came from the measurements of microwave conductivity caused by motion of electrons and holes captured to 1D-bands E_{De} and E_{Dh} [Kveder, 1985] [Brohl, 1990] [Bazhenov, 1993]. The observed nearly temperature-independent microwave (continuous-wave) conductivity at the temperatures lower than the freezing-out temperature of the doping impurities (T<20K) in the samples with dislocations, which exceeds that in the un-deformed samples by more than order of magnitude, has been attributed to the motion of captured electrons on 1D bands. Additionally, it was shown that the continuous-wave anisotropy follows the respective dislocation structure anisotropy closely, thus confirming the one-dimensional nature of dislocation conductions.

Even more convincing and comprehensive data about dislocation 1D-bands associated with 60° and with Lomer dislocations were obtained from the measurements of so-called "electric-dipole spin resonance" (EDSR) [Kveder 1989] [Wattenbach 1990] [Kveder 1997]. Resonance singularity, called EDSR, appears in the sample dielectric permittivity $\varepsilon = \varepsilon' + i\varepsilon''$ when the sample with dislocations is subjected to the alternating microwave electric field E_ω with a frequency ω in a static magnetic field. In the un-perturbed high-symmetrical silicon crystal the EDSR signal is absent. However, the local symmetry of dislocation core is lower than of Si-crystal, thus EDSR signal can be very large for electrons in dislocation 1D-bands. It was shown that for specially prepared straight dislocations the length of electron localization in 1D-band along the dislocation may exceed *300-500 nm* even at $T < 5\ K$ and that it can vary strongly depending on dislocation prehistory determinative for the core defects concentration [Kveder 1995a].

From the temperature dependences of microwave conductivity in plastically deformed n- and p-type Si crystals, location of the 1D band for holes $E_{Dh} - E_V \approx 70\ meV$ and electrons $E_C - E_{De} \approx 80\ meV$ have been obtained [Brohl 1989]. Quite similar results for the energy positions of the 1D-bands E_{De} and E_{Dh} were derived for straight 60° dislocations from photoexcitation spectrum of the EDSR signal [Kveder 1995a]. It was concluded that the energy depths of the edges of 1D-bands are nearly the same for both 1D-bands, namely, $E_C - E_{De} \approx E_{Dh} - E_V \approx 80\text{-}85\ meV$.

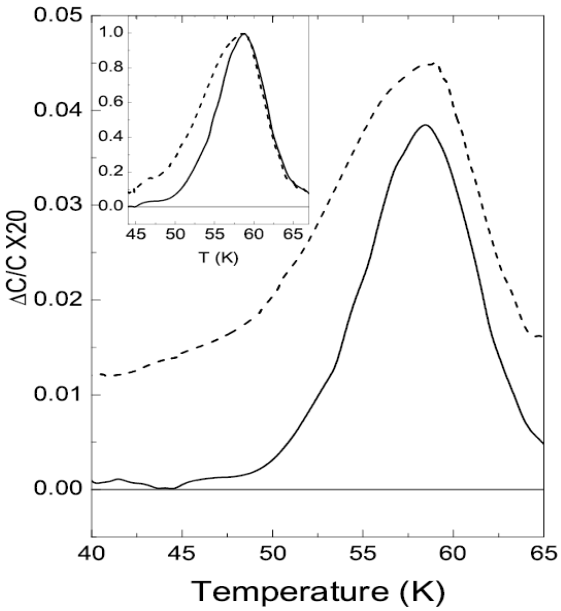

Figure 2.9. DLTS spectra showing the peak ascribed to the E_{Dh} band, measured with filling pulse width t_p = *1 ms* (solid line) and *10 ms* (dashed line). In the inset the signals normalized to the peak amplitudes are reported (after [Castaldini 2005b]).

Notwithstanding of these theoretical calculations and experimental confirmations of the dislocation shallow 1D-bands existence, all attempts to detect them by DLTS technique – specially designed to study the electrically active defects in semiconductors – were unsuccessful, and only deep dislocation related states have been observed. The following explanation was suggested: due to the high electric field in the depletion region of Schottky diode, electrons captured to 1D-band can quickly leave the depletion region just by drift along dislocation line without being thermally excited into the 3D conduction or valence band [Kveder 1995b]. The first clear experimental observation of these shallow states by DLTS was carried out by Castaldini et al [Castaldini, 2005b]. In that work, p-type Si samples containing a very regular array of parallel 60° dislocations were under investigation. At first, no DLTS signal due to shallow dislocation related states was observed on the sample containing clean non-perturbed dislocations. However, after additional annealing (at 800 ^{0}C for 24 h in argon) corresponding DLTS peak appeared, see Fig. 2.9. Activation enthalpy of about *70 meV* and capture cross section $\sim 10^{15}$ *cm*^{2} were derived for this peak, thus showing general agreement with the values obtained from EDSR and microwave conductivity measurements. Capture kinetics revealed the localized behaviour of the observed trap. Appearance of the desired DLTS peak in the annealed sample was explained by supposition that during post-deformation annealing oxygen, segregated at dislocations, has destructed the initially ideal non-perturbed dislocations structure, thereby reduced the probability of carrier diffusion along the dislocation, thus making the emission process from 1D shallow states detectable by DLTS.

As one can see, all experimentally derived values of the shallow 1D bands energy appeared to be somewhat higher than that predicted theoretically for the “perfect” 60° and screw dislocations [Farvacque 2001] (see paragraph 2.2). Evidently, 1D bands of the dissociated dislocations – dominating in Si – are lying deeper inside band gap.

2.6 Optical properties of dislocations in Si.

The dislocation-related luminescence consists of four broadened lines (or bands), denoted as D1, D2, D3 and D4, whose maxima are located at *0,81*, *0,875*, *0,93* and *1,0 eV*, respectively. For the first time these lines have been reported by Drozdov et al. in 1976 [Drozdov 1976]. Typical photoluminescence spectra measured at T = 4 K in sample with dislocations density of $3*10^8$ cm^{-2} and its variations with temperature are presented in Fig. 2.10. The relative intensities of D1, D2 and D3, D4 lines depend on the dislocation density and geometry and can vary strongly in different samples. Usually, at low dislocation density N_D lines D3, D4 dominate, while at high N_D the D1 and D2 lines become dominating. Note, that radiative recombination via D-centres is much faster than direct E_V-E_C transition – no band-to-band emission at *1,1 eV* is visible in Fig. 2.10.

The polarization of the D-lines emission and their response to uniaxial stress has been utilized to establish their relations to the dislocations. Lines D1 and D2 on the one hand, and lines D3 and D4 on the other, show the similar shifts under uniaxial stress and therefore have been grouped as pairs, D1/D2 and D3/D4 [Sauer 1985]. From the polarization measurements [Weber 1994] the E-vector of the light for lines D3/D4 was found to be in the glide plane of dislocations and is strongly correlated with the direction of the dislocation Burgers vector. These findings firmly point to the dislocations as radiative centres for D3/D4 lines. For the D1/D2 the situation is more complicated, but still the E-vector is related to the dislocation glide plane, being perpendicular to it. That means that D1/D2 lines are associated with the dislocations in some way, but not with point defects or impurity atoms randomly distributed in a bulk. Additionally, Suezawa and Sumino [Suezawa 1983a] confirmed in a high temperature annealing experiments that dislocations themselves are active as recombination centres. They concluded also that dangling bonds at the dislocation core are not responsible for radiative recombination processes.

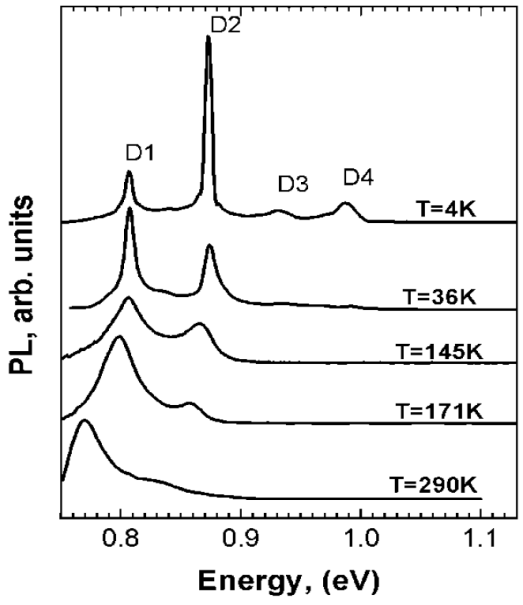

Figure 2.10. Typical dislocation-related luminescence consisting of 4 bands and its variations with temperature as measured on p-type FZ-Si with a dislocation density $N_D \approx (3\text{-}5)*10^8\ cm^{-1}$. The spectra are normalized to their integral intensity. Please note the absence of the band-to-band luminescence at *1,1 eV* (after [Kveder 2005]).

Investigations performed on multi-crystalline Si allowed to study the relation between the intensity of different D bands radiation from dislocations. As the local density of the dislocations varies in this material from point to point, one can expect also variations in the intensity of the D lines. Profiles of the intensity of the D lines were measured over a distance of a few *mm*. The intensity ratio of D4/D3 was found to be nearly constant. On the contrary, the D2/D1 ratio scattered strongly [Arguirov 2007]. This observation confirms that the lines D3 and D4 are of the same origin, while the relationship between D1 and D2 lines is questionable. Based on the temperature dependence of the D1 and D2 line intensities, these lines were attributed to the same defect centre being in different states [Sauer 1985].

- ***Origin of D4 and D3 luminescence bands.***

Origin of D3/D4 lines is considered to be quite well understood now. First of all, from the good coincidence between the energy of D4 line and the energy transition between shallow 1D bands E_{De} and E_{Dh}, it was suggested that the D4 line corresponds to direct radiative recombination of electrons in 1D band E_{De} with holes in 1D band E_{Dh}. And that the D3 line is a TO-phonon replica of D4 line [Weronek 1992]. However, in different samples the ratio between D3 and D4 intensities could be variable, because the probability of electron–phonon interaction depends on the length of a straight dislocation segments.

Another very important experiments for clarification of the nature of D4/D3 lines were related with studying of the influence of so-called low temperature / high stress (LTHSD) plastic deformation on the energy position of D4, D3 lines [Sauer 1985] [Sauer 1986]. This deformation procedure is able to create the set of straighten 60° dislocation with a large deviation of the staking fault width *d* between 30° and 90° partials from its equilibrium value $d_0 \sim 5nm$ (the reason for this is that the glide forces acting to this two partials and their mobility are different). Obviously, change in the distance *d* between two partials should result in a change of the total strain field and therefore, similar to the theoretical calculations of Lehto [Lehto, 1997] (Fig. 2.3) for stacking fault states, one can expect deeper positions of 1D bands E_{De}, E_{Dh} for dislocations with smaller *d*. Hence, one may expect that the change of *d* would result in a shift of the energetical position of D3/D4 luminescence lines as well.

That was directly proven by Sauer et al. [Sauer 1985] [Sauer 1986] and the shift of the D4 and D3 energy positions towards the lower energies was indeed observed for the smaller distances *d* between the partial dislocations, thus confirming that D3 and D4 line "families" originate from recombination processes at straight segments of 60° dislocations. It was also specified by Lelikov et al. [Lelikov 1992], that the luminescence source of D4 line in a dissociated 60° dislocation is a 90° partial Shockley dislocation (due to deeper 1D bands), while the potential of a 30° partial acts as a disturbance.

Weber and Alonso [Weber 1990] have investigated the dislocation-related luminescence in the epitaxial-grown $Si_{1-x}Ge_x$- layers in the range from $x=0$ to $x=1$. From the variations of the D4 line positions with x, authors have suggested, that this line represents the annihilation of an exciton bound to the dislocation core by a deeply bound electron and a weakly bound hole.

- ***properties of D1/D2 luminescence lines.***

Contrary to D3/D4, the exact origin of D1 and D2 luminescence is still not really understood. However, it could be stated at the moment that D1 is not a phonon replica of D2 line [Arguirov 2007]. According to the literature, impurity atoms in the dislocation core [Higgs 1993], dislocation jogs [Watson 1998], segments of dislocations of special types (like Lomer dislocations [Rebane 1990]) appearing due to dislocation reactions, multi-vacancy and/or self-interstitial clusters trapped in the core [Jones 2000] were suggested as candidates for the D1 and D2 lines origin. However, the prevalence of the D-band luminescence seen in very different samples with different impurity contamination levels raises a doubt that metal impurities are primarily responsible for D1 and D2 luminescence. An important fact, which should be taken into account when selecting a model, is that D1 and D2 lines usually dominate the luminescence spectra in the samples where dislocations could interact with each other.

Detailed investigation on the characteristics of cathodoluminescence (CL) maps from Si crystals with various configurations of dislocations was performed by Sekiguchi and Sumino [Sekiguchi 1996]. It was definitely shown that D1 and D2 luminescence appears dominantly in the regions where plural dislocations slip planes intersect each other, whereas strong D3 and D4 luminescence was detected along the slip lines. It supports the idea that D1 and D2 lines originate from the reaction products of dislocations, such as jogs or Lomer-Cottrell dislocation segments.

Steinman et al. [Steinman 1999] studied the photoluminescence spectra of partially relaxed epitaxial Si/Si_xGe_{1-x} structures containing different densities of interfacial misfit dislocations so as to specify the defects responsible for the dislocation PL lines. As a result, D1 and D2 lines were ascribed to the products of dislocation reactions in the intersection sites of the misfit dislocation network, whereas D4 line – to the extended straight segments of misfit dislocations. It was supposed that the rise in linear density of the defects at dislocations should cause the decrease of the D4 line intensity and the increase of the D1 and D2 line intensities. Thus, conclusions of Steinman et al. correlate well with the inference of Sekiguchi and Sumino [Sekiguchi 1996] as well as with earlier suppositions [Suezawa 1983b] [Sauer 1986] [Izotov 1987] that D3/D4 lines result from carrier recombination on the straight segments of dislocations whereas D1/D2 lines are rather due to the products of dislocation reactions.

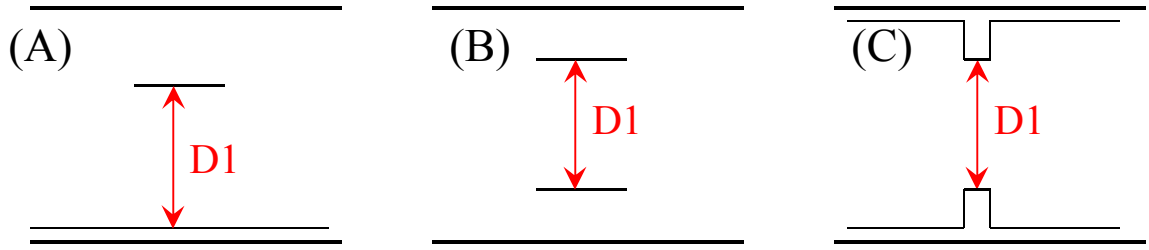

Figure 2.11. Suggested energy schemes of D1 radiative recombination, see text for details (after [Kveder 2005]).

However the question, which still puzzles everyone, is related with the identification of the exact levels inside the Si band gap participating in the radiative D1 and D2 transitions. It is rather firmly accepted now that D1 luminescence proceeds as an optical transition between two levels inside the band gap rather than between the conductive or valence band and a defect level [Kveder 1995b]. Temperature dependence of D1 energy (Fig. 2.10) follows quiet well the temperature dependence of Si band gap as $E_g(T)$-*0,362 eV*, where $E_g(T)$ is the energy gap of silicon at temperature T. If it is assumed that the D1 band originates from the optical transitions between two localized energy states of energies E_V+E_{D1h} and $E_C - E_{D1e}$, then $E_{D1h}+E_{D1e}$ should be about *362 meV*. Several possible energy schemes of D1 radiative recombination (Fig. 2.11) were suggested [Kveder 2005]:

(A) – Model (A) assumes that one of the D1 levels (E_{D1e} or E_{D1h}) is shallow – about *7–10 meV*. This was proposed in [Suezawa 1983b] to explain the very small (*7-10 meV*) activation energy for the temperature dependencies of the PL-amplitude at $T < 70–100$ *K*. Then the second level should be quite deep – nearly *0,3 eV,* see Fig. 2.11A. This model of the D1 recombination between deep and shallow levels was also supported in the work of Kittler et al [Kittler 2009]. Authors revealed two values of activation energies on their temperature dependence of optimal current (density through the diode containing the dislocations) corresponding to the highest D1 intensity: E_a *~0,09 eV* at $T < 220K$ and E_a *~0,29 eV* at $T > 220K$, i.e. the values which appeared to be very close to the predicted ones.

One may suggest that *C*-line (*F*-line) is just the sought-for deep level. However, these lines were related with the point defects/impurities located in the dislocation core and in the clouds and not with the dislocation intersections. Moreover, it was shown that the magnitude of *C*-line (*F*-line) can be drastically reduced by the passivation treatments (Al gettering and hydrogen plasma annealing), whereas the intensity of D1 line – quite the contrary – is enhanced after the passivation [Kveder 2008a].

(B) – Model (B) assumes more symmetric positioning of D1 levels E_{D1e} and E_{D1h} with respect to the middle of the band gap, so that their depth becomes of about *0,18 eV,* see Fig. 2.11B.

(C) – Model (C) is similar to model (B), but in addition it is supposed that D1 levels E_{D1h} and E_{D1e} have a strong coupling with 1D energy bands E_{De} and E_{Dh} (Fig. 2.11C), existing at regular parts of reconstructed 60° dislocations. In this model electron from D1 centre can be thermally activated to 1D band (instead of valence or conductive band) and then diffuse quickly along this 1D band out of the space charge region [Kveder 2001].

Notwithstanding numerous experiments carried out during more than a quarter of century of investigation, the exact origin and even a scheme of optical transitions for D1/D2 luminescence are not known precisely and none of many models advanced for these luminescence lines has been universally accepted.

2.7 Summary for Chapter 2.

The dislocation radiation consists of four lines D1–D4. D3 and D4 are generated by transition between one-dimensional dislocation bands on 60° dislocations. In comparison to D3 and D4, the origin of D1 and D2 is less clear, but it they are most probably caused by the interaction of dislocations. At the same time, among all dislocation luminescence lines, the D1 line is most interesting for practical applications. It has a convenient wavelength of about *1,55 μm*, i.e. at the wavelengths corresponding to the low absorption in fibber glass, and it survives up to higher temperature, than the other lines (see Fig. 2.10). However, up to now no one succeeds in finding out a one-to-one correspondence between the electrical levels registered with capacitance spectroscopy technique and the levels involved in optical transition.

Meanwhile, DLTS revealed two levels surviving high-temperature annealing, one in the upper part of band gap, another in the lower. And there are two models exist explaining the origin of these levels: (i) segregation of metal impurities in the dislocations core and in the clouds around [Knobloch 2003] and (ii) oxygen-related defects also in the cores and clouds, probably including some metal atoms as well or metal serving as preferable nucleation place for oxygen [Kononchuk 1996]. Neither of two seems to be involved in radiative D1 luminescence.

The quantum efficiency of luminescence in silicon is limited mainly by competing with non-radiative recombination at deep level defects. This implies that further deeper knowledge of dislocation related gap states, with a particular emphasis to their efficiency as radiative or nonradiative recombination centres and on the effectiveness of carrier confinement at dislocation related shallow bands, could help to increase the D1 luminescence efficiency near room temperature.

Chapter 3
Dislocation networks produced by silicon wafer direct bonding.

For practical exploiting of the dislocation's unique properties in microelectronic devices [Kittler 2007] an appropriate technology for well-controllable and reproducible fabrication of dislocations regarding their structure, electrical and optical properties, location, state of decoration with impurities, etc., being of course compatible with CMOS technology – is required. Evidently, that macroscopic plastic deformation is unable to satisfy these demands, hence this method is not acceptable for practical applications in microelectronics.

As a result, another methods for well-controllable dislocations fabrication were developed, such as dislocation loops formed by implantation of Si ions and subsequent anneal [Hoang 2007], misfit interfacial dislocations on epitaxial $Si/Si_{1-x}Ge_x$ heterostructures, regular dislocation networks (DN) produced by silicon wafer direct bonding method. Among these methods in particular the last one – silicon wafer direct bonding – seems to be the most promising for practical application, since the DN properties could be adjusted in the wide ranges by bonding conditions and further processing. Moreover, in combination with generally applied pattern formation and dry etching processes, dislocation networks can be produced in strictly defined area in order of several square microns (see for example [Ishikawa 2006]).

3.1 Details of semiconductor wafer direct bonding technique.

As a result of application of silicon wafer direct bonding method, a regular dislocation network with the pre-defined parameters (dislocation type and density) located strictly at the bonding interface which could be, in turn, positioned at the desired depth under the sample, is produced. Detailed descriptions of this procedure could be found in a set of previous publication – see for example [Reiche 1997] [Reiche 2008] and references therein, whereas here only a short description concerning the general points of the method will be considered.

Semiconductor wafer bonding generally refers to a process where two mirror-polished wafers with a high degree of flatness, parallelism and smoothness adhere to each other at room temperature without application of any macroscopic gluing layer or external forces. Also, wafers surfaces should be necessary clean, i.e. free of particulate, organic, and metallic contaminations. This is important because the surface cleanliness has a direct influence on the both structural and electrical properties of the bonding interface as well as on the resulting electrical properties of the bonded material. After cleaning an activation of the surfaces is required prior to bonding.

Then, the two mating wafers are brought together face to face in air at room temperature. The top wafer will be floating on the other due to the presence of a thin cushion of air between both wafers. When an external pressure is applied in order to push out the intermediate air, a bond is allowed to be formed by surface attraction forces between the wafers. The most important for wafer bonding are the following forces:

a) capillary force,

b) electrostatic force initiated by Coulomb interaction between charged objects or from the contact potential between two surfaces caused by differences in the local energy states and electron work functions,

c) van der Waals force resulting from the interaction between instantaneous dipole moments of atoms,

d) solid bridging caused by impurites, and

e) hydrogen bonding between OH groups as the separation between the surfaces becomes small.

Measurements on silicon microstructures revealed that capillary forces dominate, whereas electrostatic forces, van der Waals forces, and hydrogen bonding are of about one order of magnitude lower. However, all these forces act only over short ranges and depend on the specific surface conditions, most important of them is the surface roughness, but also the chemistry of species on the silicon surfaces plays a definite role.

As usual, silicon surfaces are covered with the thin oxide layer under room temperature conditions. Thus, two different bonding methods could be distinguished:

- hydrophobic wafer bonding, when the oxide layer from silicon surfaces is removed by HF solution or plasma etching, and
- hydrophilic wafer bonding, when the oxidized wafers are bonded to each other.

Let's now consider either of methods in more details.

3.2 Hydrophobic wafer bonding.

The removing of the surface oxide result, as in the case of natural bicrystals, that two silicon lattices are in direct contact during the bonding procedure. As a result of high-temperature annealing, weak attractive forces (capillary and others) are transformed into Si-Si covalent bonds. Moreover, dislocation network forms at the bonding interface as a result of the misorientation between the wafers in order to match both crystal lattices. Though some authors reported the appearance of dislocation network already after the bonding at room temperature [Plößl 1999], it is however more probable to expect the dislocation network formation only after a subsequent annealing at temperatures above 800°C [Reznicek 2002] [Reznicek 2003], since the boundary is unrelaxed after bonding at room temperature and relaxation occurs because of energetical reasons at higher temperatures only [Schober 1970].

The structure of the created dislocation network depends strongly on the misorientation angles. For instance, bonding of Si (100) wafers cause a Σ1 (100) small-angle grain boundary (GB) characterized by a square-like mesh of screw dislocations expected from theory [Bollmann 1970]. These dislocations are formed by the rotational misfit (twist) between both crystal lattices, see Fig. 3.1A, C. Between the meshes the Si atoms form an ideal and non-perturbed lattice with unstretched covalent Si-Si bonds. There is, however, an additional tilt component caused by the deviation from the [100] axis of the real wafers (miscut), see Fig. 3.1B. The tilt component is compensated by a periodic array of 60^0 dislocations (see TEM image in Fig. 3.2). Thus, the bonded interface can be considered as an artificial grain boundary in Si.

The formation of the dislocation network is a self-organized process. Furthermore, since the dislocation network in the bonded samples appears only at the interface, it may be considered as two-dimensional (2D) structure. The spacing D between the dislocations composing the DN depends on the angle of misorientation α between the both wafers. It can be approximated by the simple relation

$$D_{TW} = \frac{A}{2\sqrt{2}\cdot\sin\left(\frac{\alpha_{TW}}{2}\right)} \tag{3.1}$$

for the square mesh of screw dislocations (screw dislocation network). On the other hand, the relation between dislocation distance and tilt angle of the network formed by 60^0 dislocations is described by

$$D_{TI} = \frac{A}{\sqrt{2}\cdot\tan\left(\alpha_{TI}\right)} \ . \tag{3.2}$$

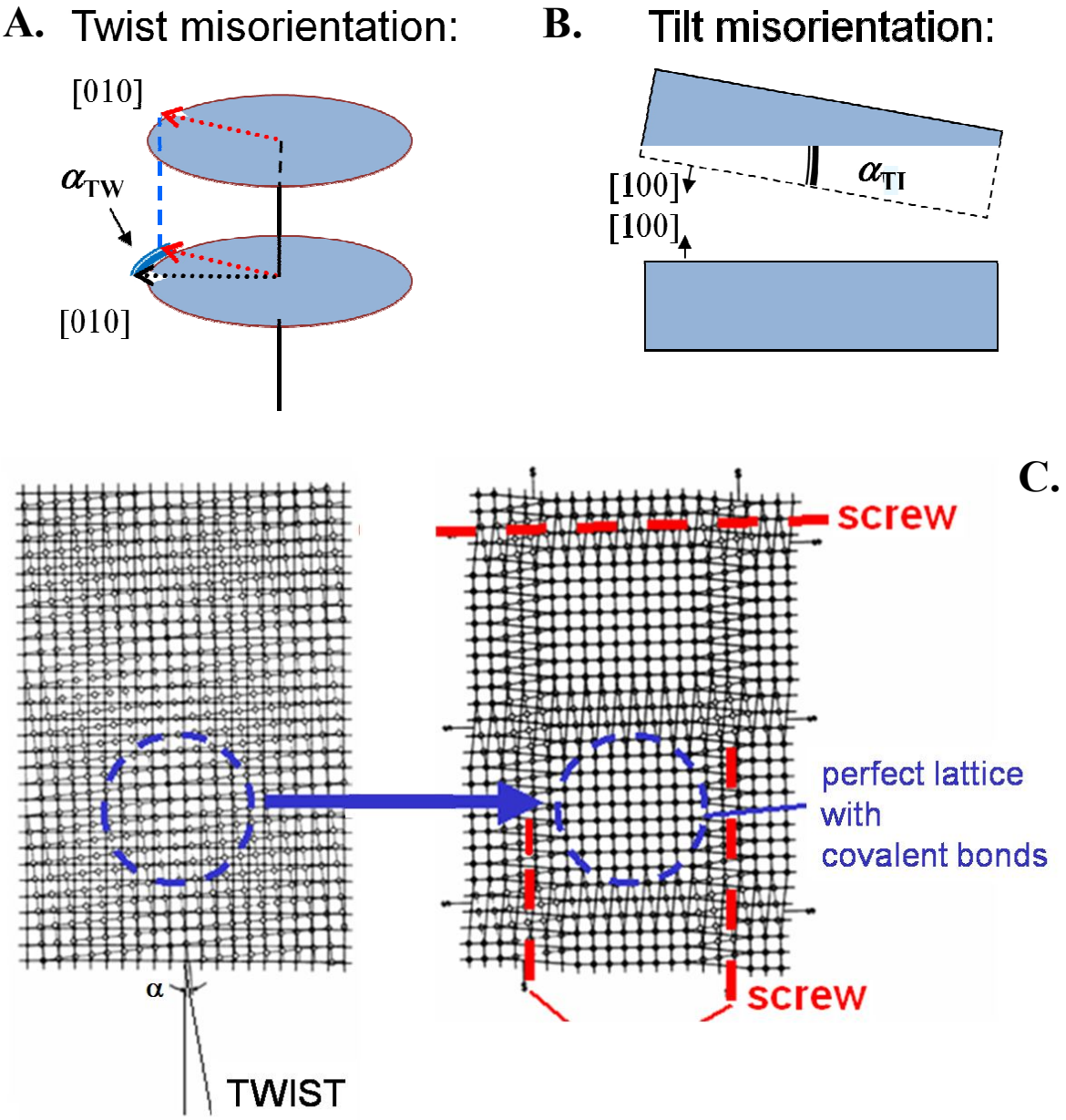

Figure 3.1 Drawing showing schematically (A) twist misorientation between two wafers; (B) tilt misorientation. Front wafers surfaces are of (100) type. Note, that in (B) tilt component is shown only for one (upper) wafer, whereas in general tilt component (i.e. deviation from ideal (100) surface) could exist for both wafers as well. (C) Sketch representing formation of epy-network of twist dislocations at the bonding interface due to the twist misorientation relative to the axis which is normal to the sketch plane. The open circles represent the atoms just above the boundary, the solid circles, the atoms just below. The grains join together continuously except along the two sets of screw dislocations, which form a crossed grid (after [Read 1953]).

In both equations A means the lattice constant (which is $A=0.543nm$ for Si) and α_{TW} and α_{TI} are the angles of twist and tilt misorientation components. Consequently, the distance between the dislocations can be controlled in a wide range by adjusting corresponding angles. For example, according to Eq. 3.1 the spacing between dislocations is $D \sim 10\ nm$ for a misorientation of about 2° and $D \sim 1\ \mu m$ for a very small misorientation of only 0.02°. However, at very small twist and tilt angles $\alpha \sim 0.001^0$ dislocation network was not observed. Instead of it, segments of individual dislocations of different geometries were found [Wilhelm 2008].

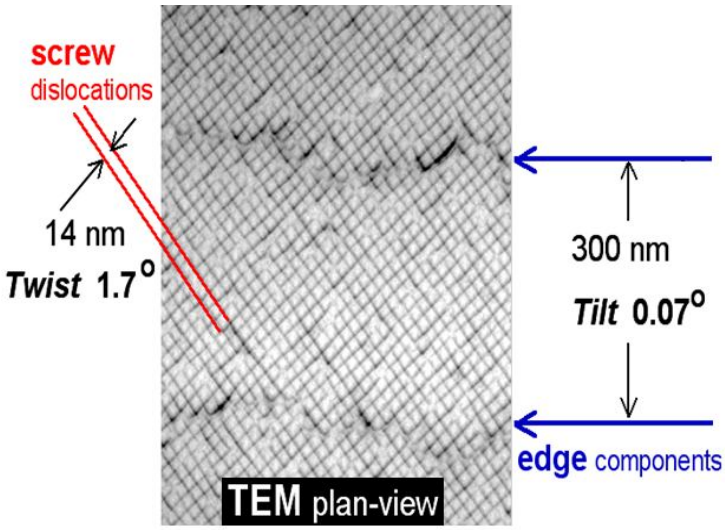

Figure 3.2 Plan-view TEM image of the dislocation network in a hydrophobically bonded Si(100)/Si(100) interface. Screw dislocations form a network having square-like meshes and are caused by the twist misoerintation angle $\alpha_{TW} = 1,7^0$, which corresponds to the interdislocation distance $D=14\ nm$. The network is superimposed by an array of 60^0 dislocations produced by the tilt component of $\alpha_{TI} = 0,07^0$, which gives $D \sim 300\ nm$.

Twist component can be controlled rather easily and with high precision, what allows us to vary the screw dislocation density rather precisely and in a wide range. However, there are definite problems with the controlling of tilt misorientation. Special efforts should be taken to prevent the formation of tilt misorientation component, i.e. the array of periodical 60^0 dislocations, see for example [Fournel 2002]. But even more care is needed to prepare the DN with the pre-defined non-zero tilt component. As usual, tilt misorientation component appears as a result of non-uniformity of wafers polishing (so-called miscut of the initial wafer surfaces), see Fig. 3.1B, being, therefore, weakly controlled as compared with the twist angle α_{TW}.

Unfortunately, hydrophobic Si surfaces appeared to be not stable and very susceptible to contamination. Even when bonding procedure occurs under vacuum condition, it is very difficult to achieve oxygen-free bonded interface. Indeed, a

considerable density of oxide precipitates (up to ~5*10^{10} cm^{-2}) non-uniformly distributed along the bonded interface was detected by TEM in the samples prepared by hydrophobic wafer bonding method [Mchedlidze 2008]. Whereas the oxide precipitates, being positively charged in silicon, can alter significantly the own height of the potential barrier along the DN; thus the inhomogeneity in the oxide precipitates distribution will lead to the appearance of electrical inhomogeneities at the bonding interface [Trushin 2011a], whereby complicating significantly the measurements itself as well as the interpretation of the obtained experimental results [Mchedlidze 2009].

- ***Thinning of the top layer***

Since the bonding process assumes that wafers of a finite thickness are involved (which is about *900 nm* for standard wafers having a diameter of *300 mm*), the bonded interface appeared to be several hundred microns below the surface. Therefore, additional post-bonding thinning procedures are required to adjust the generated dislocation network in a defined depth below the surface. This can be done either by a combination of mechanical grinding and polishing (CMP) processes, if depths of a few micrometers are required, or, if a depth of the dislocations network only of a few nanometers is needed, by a combination of wafer bonding and hydrogen-induced layer splitting, the so-called smart-cut process [Aspar 1997], see Fig. 3.3.

For smart-cut process one of the wafers is implanted with hydrogen H^+ or H_2^+ with a dose ≥ 10^{16} at/cm^2 prior to bonding. After the bonding an annealing step follows that results in the formation of hydrogen bubbles located parallel to the bonding interface at the certain depth which could be easily controlled by the implantation energy. The ripening of bubbles causes stress resulting in microcracks and, finally, in the ablation of the top layer. Depending on the implantation energy the thickness of the transferred layer is varied in the range 1 *μm – 100 nm*. A further thinning of the layer – up to less than *10 nm* – can most effectively be done by thermal oxidation and removal of the grown oxide [Rousseau 2002].

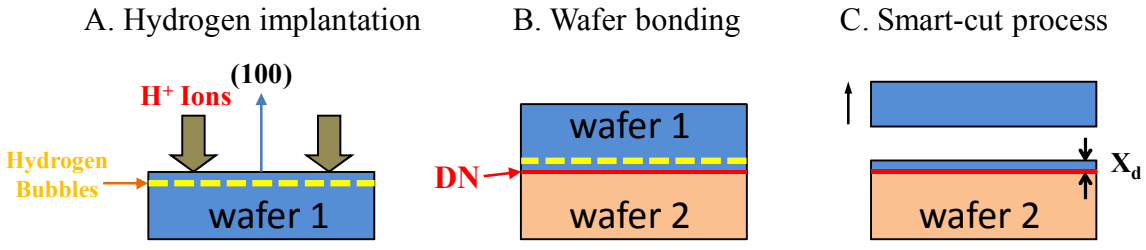

Figure 3.3 Schematic representation of the basic steps of smart-cut process: (A) Implantation of the hydrogen atoms at a dose ≥ 10^{16} cm^{-2}, (B) the implanted wafer is bonded with the untreated wafer and (C) subsequently annealed in order to introduce the layer splitting.

3.3 Hydrophilic wafer bonding.

Hydrophilic bonding implies that Si wafers (or at least one of them) are covered by the oxide layer (native or grown by thermal wet or dry oxidation) before the bonding process. As a consequence – buried oxide layer (BOX) of a certain thickness will be presented at the bonded interface, see Fig. 3.3. Clear, that no dislocations (screw or 60^0) will appear at the interface after such bonding process. But at the same time, hydrophilic bonding is now an established method for the industrial production of advanced substrates (so-called silicon on insulator wafers - SOI) applied as basic material in high-performance device fabrication.

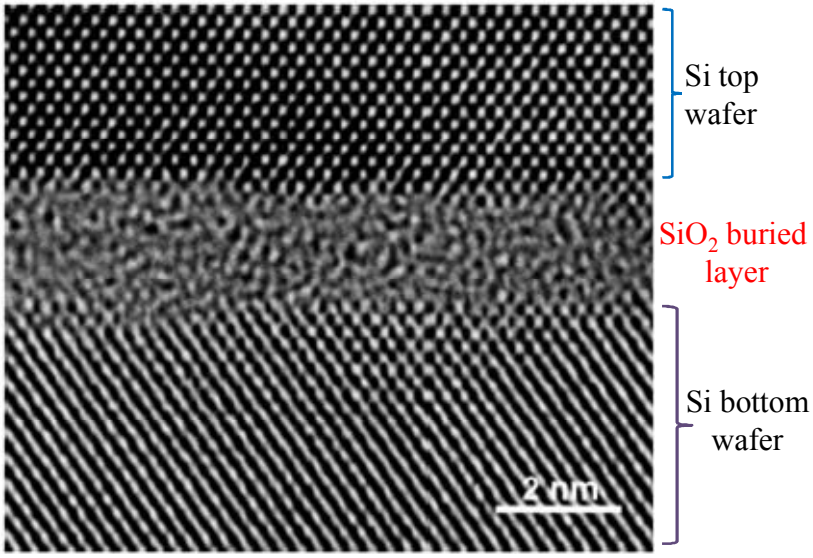

Figure 3.4 Cross-sectional high-resolution TEM image of the interface of hydrophilically bonded wafer pair. Wafers with a native oxide layer on the surfaces were applied (after [Reiche 2008]).

However, it was found that BOX in silicon could be thinned down or dissolved completely (leading to the Si-Si covalent bonds restoration), depending on the desired application (see [Ahn 1989] and references therein), when annealed with proper chosen conditions and temperature. In case of complete BOX dissolution, by analogy with the hydrophobic bonding process, dislocation network appears at the interface due to misorientation of the wafers. And again twist misorientation would be compensated by the screw dislocation network and tilt component – by the periodic array of 60^0 dislocations.

Let us now consider briefly the performance of BOX layer system during the high-temperature annealing at *1100-1200* ^0C in oxygen-free atmosphere, such as pure Ar ambient. Figure 3.5 schematically shows distribution of oxygen in the system. More detailed description of internal dissolution of buried oxide layer could be found in [Kononchuk 2008].

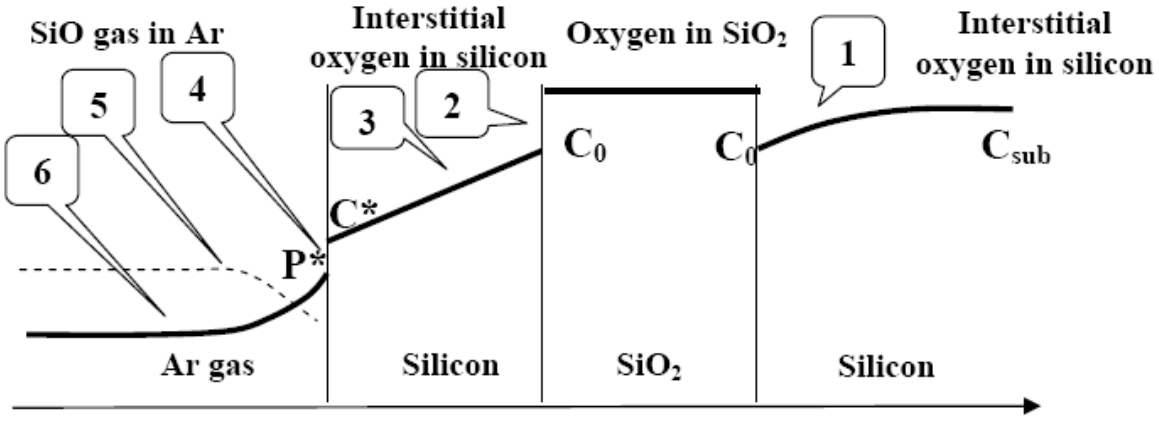

Figure 3.5 Oxygen distribution in hydrophilic bonded wafers during annealing in Ar atmosphere for oxide layer dissolution (after [Kononchuk 2008]).

There are multiple processes, which define oxide dissolution rate:

1. Diffusion of interstitial oxygen O_i from the base wafer, which leads to growth of buried oxide at the BOX/base interface (usually could be neglected)
1. Decomposition of the BOX at the BOX/top Si interface into O_i and Si, which results in Si epitaxial regrowth at the top interface
2. Diffusion of interstitial oxygen through the top Si layer
3. Reaction of O_i with silicon at the top Si surface resulting in volatile SiO gas

$$Si + O_i \rightarrow SiO(g) \qquad (3.3)$$

5. Etching of the top Si layer by residual oxygen contamination in the annealing atmosphere, which competes with the reaction 3.3

$$O_2 + Si \rightarrow SiO_2$$
$$SiO_2 + 2\,Si \rightarrow 2\,SiO(g) \qquad (3.4)$$

6. Gas phase SiO transport through Ar ambient.

In steady-state conditions oxide dissolution rate is determined by the slowest of the mechanisms of the oxygen transport from the oxide. There could be two limiting cases for oxide dissolution. When mass transport through gas ambient is fast, dissolution is limited by interstitial oxygen diffusion through the top Si layer and the dissolution rate is inversely proportional to the top Si wafer thickness. According to the experimental observations [Kononchuk 2008], for successful dissolution of BOX layer and Si-Si covalent bonds re-appearance, the top Si layer thickness should not exceed *~400 nm* (molecular beam epitaxy could be used for the build-up of the upper Si layer if the deeper position of DN is required). In another case of gas transport limited regime, the dissolution rate depends only on temperature and local mass transport coefficient. It should be emphasized that the dissolution rate of the BOX does not depend on the BOX thickness or on the base wafer material.

Thus, after the hydrophilic bonding procedure and subsequent oxide-dissolution annealing (typical temperature *1100-1200* ^0C, duration *1-2 h*) in oxygen-free atmosphere, the dislocation network free from the oxide remnants or precipitates is formed at the

bonding interface. Generally speaking, one may also expect that expressions Eq. 3.1 and 3.2 for the spacing D between the screw and 60^0 dislocations in the network would be fulfilled in case of hydrophilically prepared networks, too (however, as it will be shown in the next Chapter, some exceptions are possible).

3.4 Difference between large-angle (LA) and small-angle (SA) grain boundaries.

As it was usually accepted (and described above, see Fig. 3.1C), the twist misorientation around the (001) axis (pure twist GB - see the sketch in Fig. 3.6A) introduces two orthogonal arrays of dislocations which are generally considered as screw-type dislocations. However, one should note, that with the increasing of the twist angle from α_{TW1} to α_{TW2}, not only the distance D between dislocations varies, but also the orientations of the dislocation lines do – as denoted in Fig. 3.6A by vectors $\boldsymbol{v_1}$ ($\boldsymbol{w_1}$) and $\boldsymbol{v_2}$ ($\boldsymbol{w_2}$), respectively (according to 0-lattice theory, $\boldsymbol{v}$=1/4[1+cot(α_{tw}/2), 1-cot(α_{tw}/2), 0] and $\boldsymbol{w}$=1/4[cot(α_{tw}/2)-1, 1+cot(α_{tw}/2), 0] where vectors are expressed in grain **I** coordinates, [Bollman, 1970]). This implies the continuously changing of the atomic configuration around the dislocation lines with the increasing of twist angle α_{TW}.

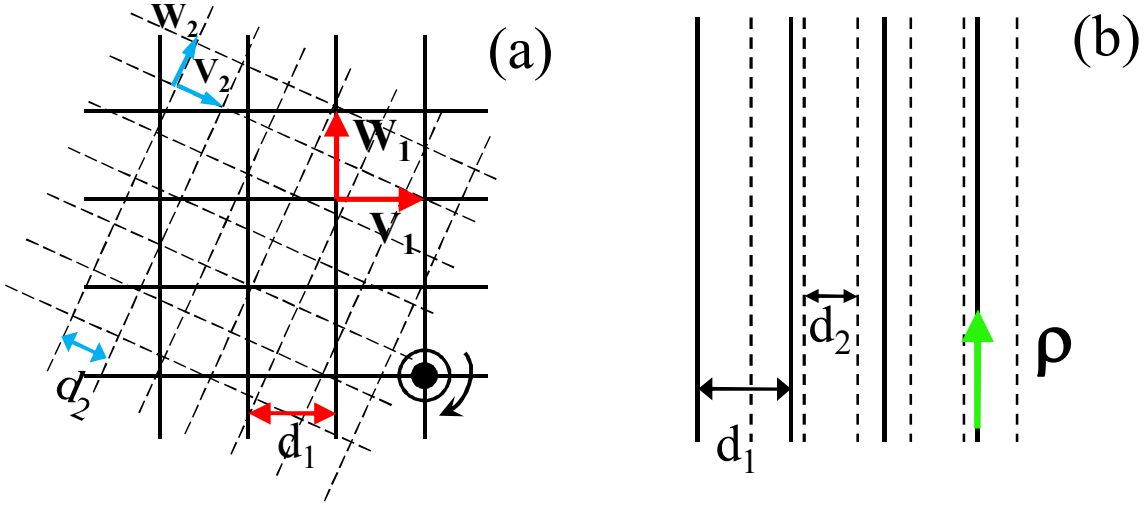

Figure 3.6. Schematical representation the dislocation arrays in (a) pure twist GB and (b) pure tilt GB. In each scheme the arrays corresponding to two different misorientations are represented (full lines: misorientation 1, dashed lines: misorientation 2). (a) For twist GB, the interface is composed of two orthogonal dislocation arrays perpendicular to the rotation axis ρ. Both the distance D between dislocations and the orientations $\boldsymbol{v}$ and $\boldsymbol{w}$ of the dislocation lines vary with the increasing of the twist angle from α_{TW1} to α_{TW1}. (b) In case of pure tilt GB, the interface is composed of straight dislocations going parallel to the rotation axis ρ. When the tilt angle α_{TI} varies from α_{TI1} to α_{TI2}, only the distance D between dislocations changes from d_1 to d_1 (after [Rouviere 2000]).

Actually, from an elastic point of view, twist GB should contain screw dislocations for any value of α_{TW}. However, from a crystallographic point of view – as it was noticed by Rouviere et al. [Rouviere 2000], this is not so unambiguously: dislocation lines are stretching out not along <110> directions – as the true screw dislocation in the crystal bulk should be – but along one of the two vectors ***v*** and ***w***. In fact ***v*** **(**respectively, ***w***) is the bisecting of the crystallographic vectors $[110]_I$ and $[110]_{II}$ (respectively, $[1, -1, 0]_I$ and $[1, -1, 0]_{II}$) of the two grains **I** and **II** of the GB. Only in the small-angle twist GBs, lattice surrounding the dislocations can be twisted elastically in such a way that the directions of screw dislocations will locally coincide with any <110> directions of two grains. For the high twist angles this will be not possible because the thickness of the disturbed interface will be too small and the misorientation between crystals too large.

Thus, although the square dislocation network compensating the twist misalignment exists and can be observed by classical two beams and weak beam TEM methods for twist angles up to about 10° [Wilhelm 2008], [Belov 1999] and [Föll] (for higher twist angles α_{TW}, conventional microscopy did not allow to visualize the dislocation mesh), only when α_{TW} is small enough the twist GB will really consist of perfectly screw dislocations, whereas at higher twist angles this network of screw dislocations will be gradually transformed into the network of particular "interfacial" dislocations, which have nothing in common with the "bulk" screw dislocations [Rouviere 2000].

Moreover, in equilibrium situation screw dislocations in Si are split at two 30° partial dislocations, while 60° dislocations – at 30° and 90° partials. The width of the stacking fault in the equilibrium as determined from the theory of elasticity is about *~5 nm* [Sauer 1986]. In case of small-angled GBs, screw dislocations in DN were also found to be split into partials with the stacking faults of the width d_{SF} between them [Belov 1999], [Rouviere 2000]. However, as far as DNs are concerned, one should remember that when α_{TW} increases, the distances between the neighbouring dislocations decrease (Fig. 3.6, Eq. 3.1 and 3.2), consequently, the partials of two adjacent dissociated dislocations become closer; and as they push each other back the stacking fault width d_{SF} becomes smaller than in the equilibrium cases. As it was reported in [Rouviere 2000], the d_{SF} decreases from *3,5 nm* for α_{TW}=0,84º to *2 nm* for higher angle α_{TW}=1,75º and becomes smaller than the detection limit, i.e. *<1 nm*, for $\alpha_{TW}=5^o$.

Thus, the critical twist angle for the transformation of the "screw DN" to the "interfacial DN" was estimated to be in order of $3,5\text{-}5^0$. In the DN produced with twist angle $\leq 3,5^0$, screw dislocations locally coincide with <110> directions in both grains, they are dissociated and produce rough interface as the dissociated dislocations are no longer located in a well-defined interfacial plane but extend into the grains, making the Si/Si interface look ''wavy'' and thick [Rouviere 2000]. Quite the opposite situation with the dislocations in the DN produced with twist angle $\geq 4^0$: dislocations divert from <110> directions to those bisecting the crystallographic vectors of <110> type of both grains, there is no dissociation and the interface looks smooth.

However, this is not the case for the pure tilt (100) grain boundaries, see Fig. 3.6b. The dislocation network in this case is formed by an array of straight 60° dislocations lying parallel to the rotation axis. Consequently, only the distances D between the dislocations vary with the increasing of the tilt misoerintation angle, keeping constant the atomic configurations for the dislocation cores. Hence, no distinction from the bulk 60° dislocations is expected for rather high diapason of tilt angles (till the distance D between the neighbouring dislocations is high enough to prevent the overlapping of their cores).

3.5 Interactions of dislocations composing the DN.

Co-existence of screw and 60^0 dislocations at the bonded interface may cause various dislocation reactions at the intersection points with a third dislocation being involved [Föll 1979] [Benamara 1995] [Akatsu 2004]. An example of such reaction is demonstrated in Fig. 3.7. A 60° dislocation lying along $[\bar{1}10]$ direction with Burgers vector $b = a/2[\bar{1}01]$ intersecting the screw dislocation with Burgers vector b_1 =a/2[110] at the node, both dislocations react to form another 60° dislocation with $b_3 = b_1 + b = a/2[011]$, such that $b^2 + b_1^2 > b_3^2$, thus lowering the line energy of dislocation (since $E_{dis} \sim b^2$, dislocations always tend to have the smallest possible Burgers vector). The low-energy configuration is achieved when the angles between dislocations change to 120° [Benamara 1995]. Before reaction takes place, the 60° dislocation b had an edge component in the plane of the interface. After reaction, both 60° dislocations b and b_3 are characterized by an equal but opposite edge component. The total edge component vanished and is accommodated by the offset of the screw dislocation.

The appearance of both 60° dislocations introduces the frequent displacements of the screw dislocations by about half network spacing $0,5*D_{TW}$ when running along irregularly curved lines of 60° dislocations, since their efficient component in

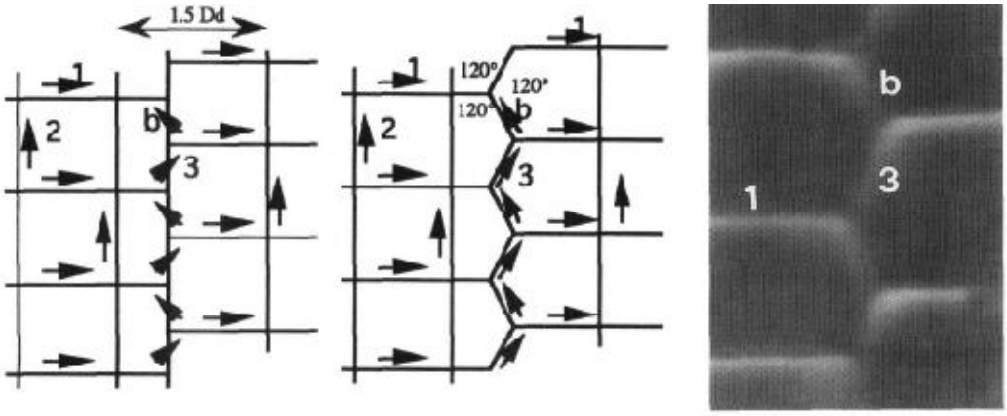

Figure 3.7. Interaction between a 60°-dislocation lying along $[\bar{1}10]$ with Burgers vector b and screw dislocations with Burgers vector b_1 =a/2[110] (after [Benamara 1995]).

compensating the twist misorientation is *a/4[110]*. This is well visible in the plan-view TEM image shown in Fig. 3.7. Please note also, that this kind of dislocation reactions not necessary would occur in case of 60° dislocations and interfacial dislocations interaction, i.e. when the twist angle α_{TW} is higher than critical.

Another dislocation reaction takes place when the tilt angle is close to the twist angle, independent of the degree of the misalignment: a two-dimensional square screw dislocation network does no longer dominate the interface structure, since the density of so-called zigzag reactions increases leading to the formation of hexagonal dislocation meshes which now dominate the dislocation configuration [Akatsu 2004].

Moreover, it was found recently that the DN structure and the particular kinds of dislocation reactions would depend also on the directions of 60° dislocations relative to the screw ones, i.e. if the 60° dislocations are going parallel to one set of screw dislocations or making a certain angle (as in case of Gr-3 sample studied here, see TEM images in Fig. 5.12) [Vdovin 2011] [Isakov 2011].

3.6 Summary for Chapter 3.

A brief overview of the bonding methods used for the controllable creation of the dislocation networks in silicon, of their merits and demerits, was given in this Chapter. For the summary, some advantages of samples with DN – especially in respect to the investigations by means of DLTS method, in comparison with the samples containing randomly distributed dislocations could be listed:

(i) DN is going strictly parallel to the sample surface,

(ii) distance between the DN and the sample surface can be controlled.

(iii) density and the types of dislocation are well defined by the twist and tilt misorientation angles between the bonded wafers.

(iv) as the dislocations on the bonded interface were not moving during their formation, the absence of the defects or defect agglomerates created during the motion of dislocations could be expected (see paragraph 2.4). Moreover, annealing treatment at 1100°C - 1200°C (for BOX dissolution and/or Si-Si bonds restoration) implies that all temperature unstable defect complexes (if any) would be destroyed.

As expected, these could allow straightforwardly interpret DLTS-results and by comparison with the data obtained by other experimental methods, such as photoluminescence (PL) and transmission electron microscopy (TEM), to establish the reliable correspondence between the detected traps and DRL luminescence centres as well as particular element of dislocation network.

Chapter 4
Samples description and experimental details.

In order to respond to the assigned investigation goals and tasks, four bonded samples with different DN structures were prepared. Within each bonding process, the dislocation networks were fabricated under the same process conditions and the only parameter varied was a mutual crystallographic orientation of surfaces between the pair of the bonding wafers. Parameters and details of samples preparation procedure and the resulted samples geometry are presented in this Chapter, together with the description of electrical contacts formation method. For application of junction spectroscopy techniques (CV, IV, DLTS and ITS) a rectifying contact – Schottky diode or p-n junction – should be prepared on the front sample surface, whereas ohmic contact should be prepared on the back sample surface.

Besides, an overview of the particular DLTS spectrometers used in this work will be considered. Each measurements system has its own advantages and disadvantages, which sometimes are even not represented in the manuals. The latter needs additional and thorough researches so as to avoid misinterpretation of the measured results. Just about such unexpected peculiarities will be discussed in the corresponding paragraph of this Chapter.

4.1 Investigated samples.

In the present work, four samples produced by hydrophilic bonding method were under investigations. Samples were prepared by SOITEC Company, Grenoble, France. Initial Si wafers were of p-type with doping level *~1,25*10^{15} cm^{-3}* of boron and (100) surface orientation. Wafers were thermally oxidized before the bonding, and one of two wafers for every particular sample were subjected to the hydrogen ions implantation at the depth of approximately *~170 nm*.

In order to dissolve the buried oxide layer, samples were annealed in pure Ar atmosphere in vertical furnaces, specially designed to reduce residual oxygen gas contamination. Annealing was performed at 1100°C - 1200°C for 2 hours in a high purity surrounding conditions to prevent contamination by transition metals. After the dissolution annealing, bonding interface appeared to be at the depth of *~160nm* going parallel to the front surface. Neither secondary ion mass spectrometry (SIMS) nor transmission electron microscopy (TEM) did reveal the presence of increased oxygen concentration or any kind of oxide precipitates at/near the bonding interface.

Samples differ from each other mainly by the twist misorientation angle between the wafers: α_{twist} is <1°, 3°, 5,9° and 29,9°, respectively, see Table 4.1. As one may note from Table 3.1, samples notations correspond to the approximate values of twist misorientation angles. Additionally, small tilt misorientation component of about 0,5-0,7° was found for all samples, resulting due to uncertainty of wafers polishing. Exact misorientation angles were determined from X-ray diffraction (XRD) (Gr-6 and Gr-30 samples) and transmission electron microscopy (Gr-3 sample; whereas for Gr-1 sample TEM revealed very unusual DN structure, thus making it difficult an evaluations of exact misorientation angles, see Chapter 5 for more details).

Table 4.1. Samples notations and corresponding twist and tilt misorientation angles.

Samples notation	Twist angle α_{twist}	Tilt angle α_{tilt}
Gr-1	<1°	<0,7°
Gr-3	3°	0,75°
Gr-6	5,9°	0,67°
Gr-30	29,9°	0,45°

4.2 Contacts preparation.

In order to produce the Schottky contacts for DLTS measurements, *100 nm*-thick round titanium dots were evaporated on the polished oxide free front surface of all samples. Area of the Ti contacts is $1,4*10^{-2}$ cm^2.

Before Ti evaporation, samples were carefully cleaned in boiling acetone and then in methanol in order to remove organic contaminations from the samples surfaces. Then all samples were etched in the solution of $HF+H_2O=1:10$ for *2 min* in order to remove native oxide layer. This chemical solution is known for the slow etching rate of silicon itself, thus there was no danger to etched-out or somehow destroy the bonded interface. Ti contacts were evaporated immediately after the etching with the minimal possible storage time in open air in order to prevent further SiO_2 regrowth.

Ohmic contacts were prepared by rubbing of InGa eutectic on the rear side of the samples. Schematic structure (cross-section) of the studied bonded samples with DN and electrical contacts is presented in Fig. 4.1.

Such sample structure – Schottky diode (or p-n junction) with DN that is going parallel to the front sample surface at the depths of *0,1-1 μm* – seems to be the most perspective for the future applications in microelectronics, since it enables an effective electron-injection and/or modulation of potential by application of corresponding external bias voltage. Indeed, the promising concepts of *MOS-LED* and a *p-n LED* emitting at *1,5 μm* (D1 line) which are based on a dislocation network formed during direct bonding of Si wafers have been suggested [Kittler 2007].

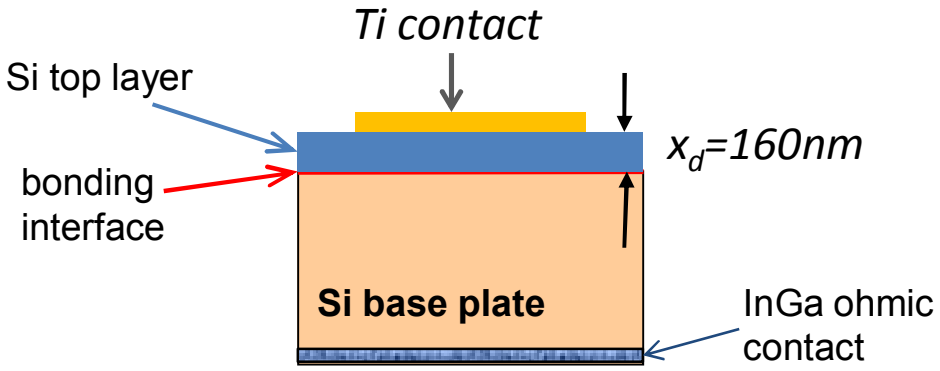

Figure 4.1. Schematic representation of the sample structure with electrical contacts.

4.3 DLTS spectrometers used in the present work.

Most of DLTS measurements in the present work were performed using Accent DL-8000 transient Fourier spectrometer, equipped with the close cycle helium cryostat (Cryophysics) allowing to vary sample temperature from *~10K* to *320K* with temperature increase step better than *0,1K*. System is completely computerized and all electronic hardware is controlled by the CPU.

All electronic components have been designed for two kinds of application needed for correct DLTS measurements: the static measurement of the voltage dependence of sample capacitance and current (*CV* and *IV* measurements) and the time dependent measurement of the capacitance relaxations after switching-off the voltage filling pulse. The Boonton 72b capacitance meter used in the DLTS system fits to both measurement tasks. It can measure capacitance in the range of *0,1 pF -3000 pF* in 4 ranges with the absolute accuracy of *100 fF* and gives the possibility to supply a bias voltage to the sample. Voltage applied to the sample under investigations can be defined within the range of *-20 V* to *+20 V* with resolution of *1mV*, whereas the current flowing through the sample can be measured within the range ±(*1 nA -10 mA*), with resolution *0,1 nA*.

At the beginning of the DLTS measurement, operator should specify the period width T_w in the range *0,2 ms – 4 s* (up to 9 periods T_w simultaneously), during which the capacitance transient will be recorded and then saved in the computer memory. More than 20 correlation functions (*sin*- and *cos*- like, as well as of "double box-car" type [Lang 1974]) with their periods $T_C = T_w$ or (divisible) smaller can be applied to the recorded capacitance transients in order to plot the DLTS spectra (Eq. 1.24 and Fig. 1.3). This gives allows to draw a very detailed Arrhenius plot with large number of points, thus to define the trap parameters E_{na} and σ_{na} precisely.

Unfortunately, this DLTS spectrometer suffers from two grave disadvantages, which were revealed while carrying out the experiments described in this work. First of them is related with very slow filling pulse front time – see Fig. 4.2 left plot. This picture shows two filling pulses with assigned durations t_p=*5 μs* and t_p=*10 μs*, with the same reverse biases U_r= *-6V* and pulse voltages U_p= *0V*. As one can see, filling pulse t_p=*5 μs* even did not reach the assigned pulse voltage *0V*. The shape of t_p=*10 μs* filling pulse is also rather far from the supposed rectangular-like. As a result, all DLTS spectra presented in this work were measured with the filling pulse duration *0,1-1 ms* in order to minimize the effect of slow front time. Verdict – no t_p- dependence could be measured on this DLTS spectrometer.

The second problem is related with the parasitic oscillation occurring during the first *~50 μs* after the filling pulse voltage was applied, see Fig. 4.2 right plot. Obviously, that during such oscillations (especially during 2-3 first of them) the filling pulse voltage is sufficiently higher than was initially assigned. This means that trap profiling measurements

– when reverse bias voltage is kept constant whereas the filling pulse voltage gradually increases – will give wrong results (note, that the time duration of these oscillations is rather large, on order of several μs, which is enough to fill the trap). Oscillations appearing after the filling pulses switching off have no influence on to the measurement process (they could be either filtered or omitted by setting an appropriate delay time).

Thus, in order to perform the trap profiling measurements, SULA DLTS spectrometer, free from the above mentioned disadvantages, was used. However, this spectrometer is not computerized and could work only in the manual mode at the moment. Thus, it is not suited for the full-range DLTS measurements, but still could be used for the trap profiling measurements.

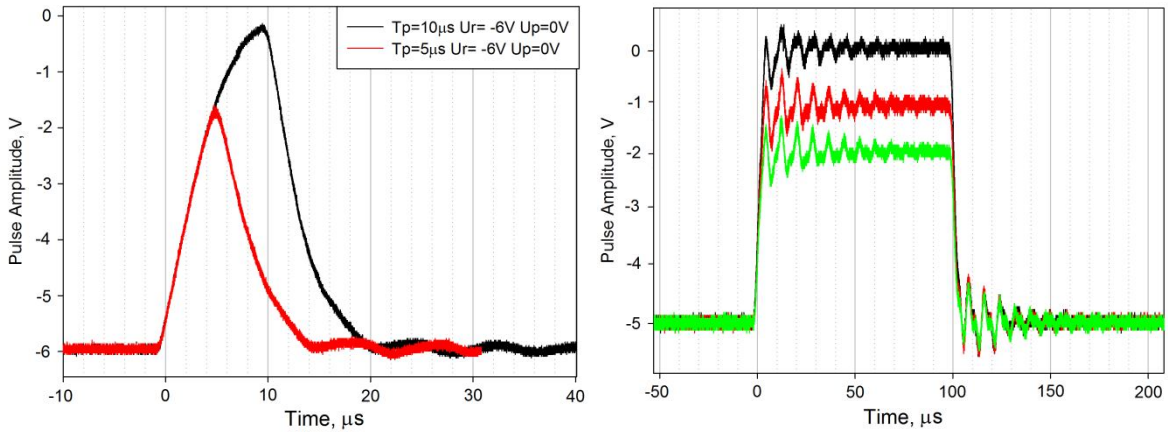

Figure 4.2. Shape of the filling pulses as measured by oscilloscope connected to the sample top biased contact. Left plot: pulse durations t_p=*5 μs* and t_p=*10 μs*, reverse bias U_r= *-6V* and pulse voltage U_p= *0V*. Right plot: pulse durations t_p=*100 μs*, reverse bias U_r= *-5V* and pulse voltages of *0V, -1V* and *-2V*.

4.4 Summary for Chapter 4.

In this Chapter the procedures of samples preparation and formation of electrical contacts essential for junction spectroscopy techniques were considered.

A row of the specific technical problems of Accent DLTS spectrometer, which were revealed while performing the measurements actual for the present work preparation, was also discussed. As a result, it was determined, that Accent DLTS spectrometer is not valid for studying the filling pulse dependence as well as for measurements of traps distribution profiles (at least in the case of DN-related traps studied here), forcing to use another spectrometer (SULA) in order to measure the reliable trap profiles.

Chapter 5
Local electronic states of interfaces between hydrophilically bonded wafers with different misorientation angles.

In spite of rather long history of studying of artificial DNs (or artificial GBs) in Si – first papers are going back to the end of 1970s! – including TEM investigations [Foll 1979], CV & IV measurements [Seager 1979] [Pike 1979], EBIC & CL [Ikeda 2000] [Sekiguchi 2002], PL [Mtchedlidze 2008], no extensive study by DLTS method was done so far (while the preliminary work carried out using GB-DLTS method [Yu 2007] revealed a significant potential of DN structures in the field of investigations of the dislocation-related defect states). Whereas the deeper knowledge about the dislocation related gap states, with a particular emphasis to their efficiency as radiative or nonradiative recombination centres and on the effectiveness of carrier confinement at dislocation related shallow bands are highly needed in order to construct the highly-efficient Si-based LED for on-chip interconnection.

In order to highlight these questions, the experimental investigations by DLTS method concerning the characteristics of defect levels introduced by the dislocation network into the Si band gap and their evolution with the increasing of the twist misoerintation angle α_{tw} in wide range were performed, and the obtained results are reported in this Chapter. Depending on the misoerintation angles, both structural and electro-optical properties of DNs vary significantly, thus giving the possibility to correlate the detected defect states with D1 luminescence centers as well as with the particular structural elements of dislocation network considering all obtained DLTS spectra and the actual PL and TEM results together. As a result of investigations, an optimal bonding processing conditions (geometry) for which the intensity of the D1 luminescence is maximal could be suggested.

5.1. Calculations of the interface trap density from DLTS peaks amplitude in the case of narrow 2D trap distribution.

In order to determine correctly the concentration of the defect states from the magnitude of the DLTS peaks, the proper expression for DLTS spectrum normalization should be formulated. To do this, Poisson equation (see Eq. 1.3)

$$\varepsilon V = \int_0^w \rho(x) x dx \tag{5.1}$$

should be solved taking into account the charge Q_s collected by the DN-related states. As the dislocation network in the investigated samples is located at the depth of only *160 nm* below the sample surface, it will be inside the space charge region at any value of reverse bias voltage (and even at zero bias, as the SCR depth at *0V* is *~700 nm*). Thus, the total charge density $\rho(x)$ inside the SCR will be the sum of the charge of ionized shallow acceptors ρ_A and the charge collected by the interface states ρ_S (traps supposed to be of donor-like character – see Chapter 6 for details, i.e. the sign of the trapped charge ρ_S would be opposite to the charge of ionized shallow acceptors ρ_A)

$$\begin{aligned} &\rho = \rho_A + \rho_s \\ &\rho_A = eN_A \quad 0 < x < w \\ &\rho_s = -Q_s\,\delta(x_d) = -eN_s\delta(x_d) \end{aligned} \quad , \tag{5.2}$$

where N_a is the concentration of shallow acceptors (considered to be uniform), N_s – 2D concentration of DN states, e – electron charge, w – SCR depth and $\delta(x_d)$ is the delta-function expressed as

$$\delta(x_d) = \begin{cases} 1 & when \quad x = x_d \\ 0 & when \quad x \neq x_d \end{cases} . \tag{5.3}$$

Analogous treatment considered previously for the case of a single quantum well (QW) of the width L located at the depth x_{QW} inside the SPR [Debbar 1989] deals – due to the finite QW thickness – with the 3D concentration of the QW states N_{QW} and the charge ρ_{QW} collected by QW thus being equal to $\rho_{QW} = eN_{QW}*L$ (i.e. without using of delta-function like in Eq. 5.2). Whereas the DNs studied here are regarded as 2D defects (see discussion in the previous Chapter 4), thus 2D concentration of DN states N_s and the delta-function $\delta(x_d)$ reflecting the 2D trap distribution should be used in the calculations (Eq. 5.2) to get the proper expression for the interface charge density.

By solving Poisson equation Eq. 5.1 with the charge density given by Eq. 5.2, the total band bending voltage will be

$$\varepsilon V = \frac{eN_A}{2} w^2 - Q_s x_d \ , \tag{5.4}$$

from which the expression for the width of the depletion region containing DN of the charge Q_s at the depth x_d can be expressed as

$$w = \sqrt{\frac{2\varepsilon V + 2Q_s x_d}{eN_A}} \tag{5.5}$$

If the relative change of the DN charge is small - so that $dQ_s << Q_s + \frac{\varepsilon V}{x_d}$, then it could be derived by the differentiation of Eq. 5.5, so that

$$dw = \frac{x_d}{w}\frac{dQ_s}{eN_A} \tag{5.6}$$

Numerically the above-mentioned condition could be estimated as

$$dQ_s << Q_s + \varepsilon V / x_d = e\left(N_S[cm^{-2}] + V * 4 * 10^{11}[cm^{-2}v^{-1}]\right). \tag{5.7}$$

In the following it will be shown that this condition is indeed fulfilled for all investigated samples at any applied biases.

Capacitance transient dC could be expressed then from Eq. 5.6 as

$$\frac{dC}{C} = -\frac{dw}{w} = -\frac{x_d}{w}\frac{dQ_s}{eN_A w}. \tag{5.8}$$

Physical meaning of the Eq. 5.8 could be interpreted as follows: relative capacitance change dC/C is proportional to the ratio of relative change of the DN charge dQ_s to the full charge of all acceptors inside the SCR (eN_A*w) and to the relative depth position of the interface layer. So, from the physical point of view this expression is correct. Keeping in mind that

$$C = \varepsilon A / w$$

Eq. 5.7 could be rewritten as

$$\frac{dC}{C} = -\frac{x_d}{A^2\varepsilon^2}\frac{dQ_s}{eN_A}C^2 \tag{5.9}$$

where ε is the dielectric constant for Si and A – area of the Schottky contact. Thus, the relative change of the total DN charge dQ_s for the case of DN located inside the depletion region of the Schottky contact

$$dQ_s = -\frac{A^2\varepsilon^2}{x_d}eN_A\frac{dC}{C^3} \tag{5.10}$$

turned out to be proportional to the dC/C^3. It means that in order to derive properly the DN trap concentration N_s from the DLTS peak magnitude, the absolute change of capacitance dC should be normalized to C^3-value and not by C as in usual cases for the uniform trap distribution (Eq. 1.23). Similar expression – however falsely overestimated by factor of 2 – was used by Schmalz et al [Schmalz 1996] to calculate the hole density in quantum well structures.

5.2. DLTS spectra of four bonded samples.

Examples of the DLTS spectra of Gr-1, Gr-3, Gr-6 and Gr-30 samples measured with the reverse bias $U_r=1V$ and filling pulse voltage $U_p=-1V$ are presented in Fig. 5.1. Spectra were normalized to C^3-values and recalculated according to Eq. 5.10 to represent the surface trap concentration N_s. Since the DN is located close to the metal / semiconductor interface, all states in the lower half of the band gap are empty even at zero applied bias, implying that the forward-biased filling pulses should be used to refill them.

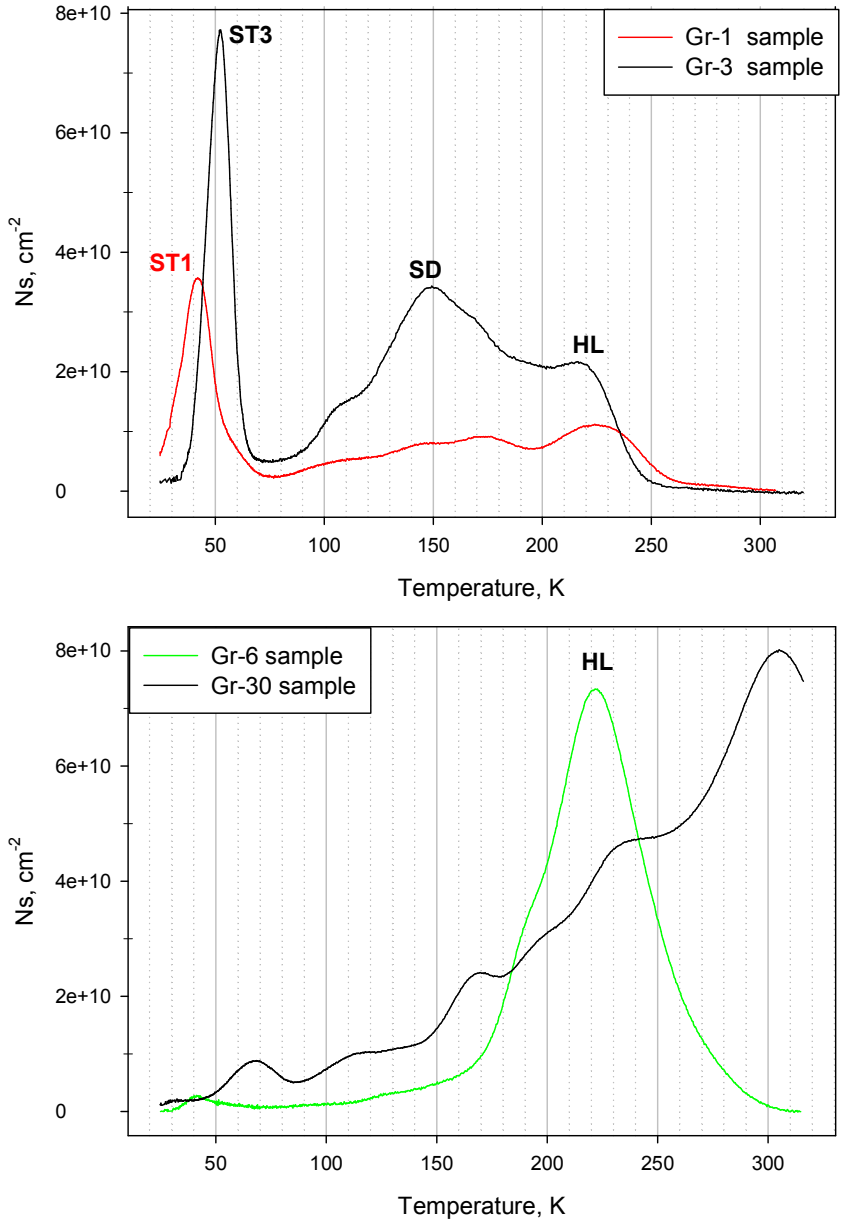

Figure 5.1. DLTS spectra of Gr-1 and Gr-3 sample (upper plot) and Gr-6 and Gr-30 samples (lower plot). DLTS-scan parameters: filling pulse duration t_p=1ms, reverse bias U_r=1V, filling pulse voltage U_p= –1V, rate window T_w=20ms.

Small twist-angle samples Gr-1 and Gr-3 revealed similar features in DLTS spectra (Fig. 5.1, upper plot): a low temperature peak dominating the spectra and a set of unresolved peaks appearing at 90-250K. The magnitude of DLTS peaks in Gr-3 sample is ~2-3 times larger than in Gr-1 sample. Besides, the temperature position of the main peak in Gr-1 sample, labelled as ST1 in Fig. 5.1, is *~10K* lower than that for the main low-temperature peak ST3 in Gr-3 sample.

DLTS spectra of Gr-1 and Gr-3 samples between 90 K and 250 K are composed of a set of at least four peaks with the similar or close temperature positions for both samples. Strong overlapping of these peaks makes impossible an exact determination of the number of the peaks and their concentrations. One should also point out a significant enhancement of the magnitude of the peak marked as SD with the increasing of the twist angle.

DLTS spectra of the large twist-angle samples Gr-6 and Gr-30 differ significantly from those of the low twist-angle samples Gr-1 & Gr-3 (see Fig. 5.1, lower plot). Low-temperature peaks ST1 and ST3 as well as SD peak vanished completely. The main feature of DLTS spectrum of Gr-6 sample is broad unresolved peak HL, located at around 220 K that could be also recognized in the spectra of Gr-1 and Gr-3 samples. A small low-temperature peak at approximately 40K still could be visible on the spectrum, but its concentration is too small to make a detailed comparison with ST1 or ST3 peak.

The spectrum of Gr-30 sample shows a set of strongly overlapped DLTS peaks with their magnitudes continuously growing up to 300 K. Low-temperature peaks are absent on the spectrum of Gr-30 sample. Due to the strong overlapping of the neighbouring DLTS peaks, it is hard to determine the exact concentrations of every particular peak. However, it could be estimated that the total concentrations of the electrically-active defect states in Gr-3 and Gr-30 samples are comparable, while in Gr-1 and Gr-6 samples are 2-3 times lower – see Table 5.1. Looking on the values in Table 5.1 it becomes clear that the inequality 5.7 is indeed fulfilled for all investigated samples.

Table 5.1. Concentration of the shallow traps (appearing at T<60K), summary concentration of the deep traps and total concentration of all (shallow + deep) traps as derived from the magnitude of the corresponding DLTS peaks using Eq. 5.9.

	Gr-1	Gr-3	Gr-6	Gr-30
Shallow states, cm^{-2}	$3{,}7*10^{10}$	$7{,}8*10^{10}$	$0{,}3*10^{10}$	–
Deep states, cm^{-2}	$\sim 4{,}5*10^{10}$	$\sim 9*10^{10}$	$7{,}5*10^{10}$	$\sim 17–20*10^{10}$
Total, cm^{-2}	$\sim 8*10^{10}$	$\sim 17*10^{10}$	$\sim 8*10^{10}$	$\sim 17–20*10^{10}$

5.3. Traps profiling.

Trap profiles were measured at several particular temperatures, corresponding to the main DLTS peaks, by using SULA DLTS spectrometer (reminding – all DLTS spectra were measured on Accent DLTS spectrometer, see Chapter 4). At the selected temperatures and for the fixed reverse bias voltages U_r, the dependences of the DLTS signal on the increasing filling pulse voltages U_p were measured – see examples for ST1 and HL peaks of Gr-1 sample and ST3 and SD peaks of Gr-3 samples, presented in Fig. 5.2. By exceeding some threshold voltage, the corresponding DLTS signal rapidly appears, quickly reaching its steady value. As it is clear from Fig. 5.2, it is necessary to apply the forward filling pulses to reach the steady magnitudes of all DLTS peaks.

Traps density profiles, calculated as the derivative of the obtained dependences of the DLTS signal on the U_p voltage, are presented in Fig. 5.3. For the sake of the accuracy, the curves corresponded to ST1 and ST3 peaks were splined before the application of differentiation procedure (bold lines in Fig. 5.2 and 5.3). Resulting narrow profile peaks – as against to the monotonically-continual trap profiles expected for 3D (bulk) trap distribution or unsaturable-growth profile behaviour typical for the surface states – reflect the "plane-like" (2D) distribution of the traps.

The fact that the profile peaks in Fig. 5.3 for different traps appeared at different values of pulse voltage U_p is explained by different energy positions of particular trap levels inside Si band gap: for the deeper trap the corresponding DLTS signal should appear at smaller filling pulse voltages, just corresponding to the profiles shown in Figs. 5.2 and 5.3. On the other hand, Coulomb repulsive barrier along the DN could also influence the capture process onto the DN states: as this barrier is expected to be higher in Gr-3 sample because of considerably higher total traps concentration (see Table 5.1) – the higher pulse voltage is needed to fill the shallow ST3 traps in this sample as compared with the ST1 shallow traps in Gr-1 sample.

Traps profiles measured on the other two samples – Gr-6 and Gr-30 – also revealed similar property, i.e. the narrow trap distribution. Thus, the following evidences:

-different shapes of the DLTS spectra in the different samples (with the Schottky contacts being prepared at the same time and by the same method)

-absence of somehow similar DLTS peaks on the reference sample without DN

-narrow trap profile peaks typical for 2D trap distribution

testify, that all observed DLTS peaks are directly related with the defect states introduced by the dislocation networks and not by the surface states or unintentional/residual bulk contaminations introduced during samples or contacts preparation. Hence, the observed variations of the DLTS spectra with the increasing of the twist misoerintation angle reflect solely the changes of the DN's microstructure.

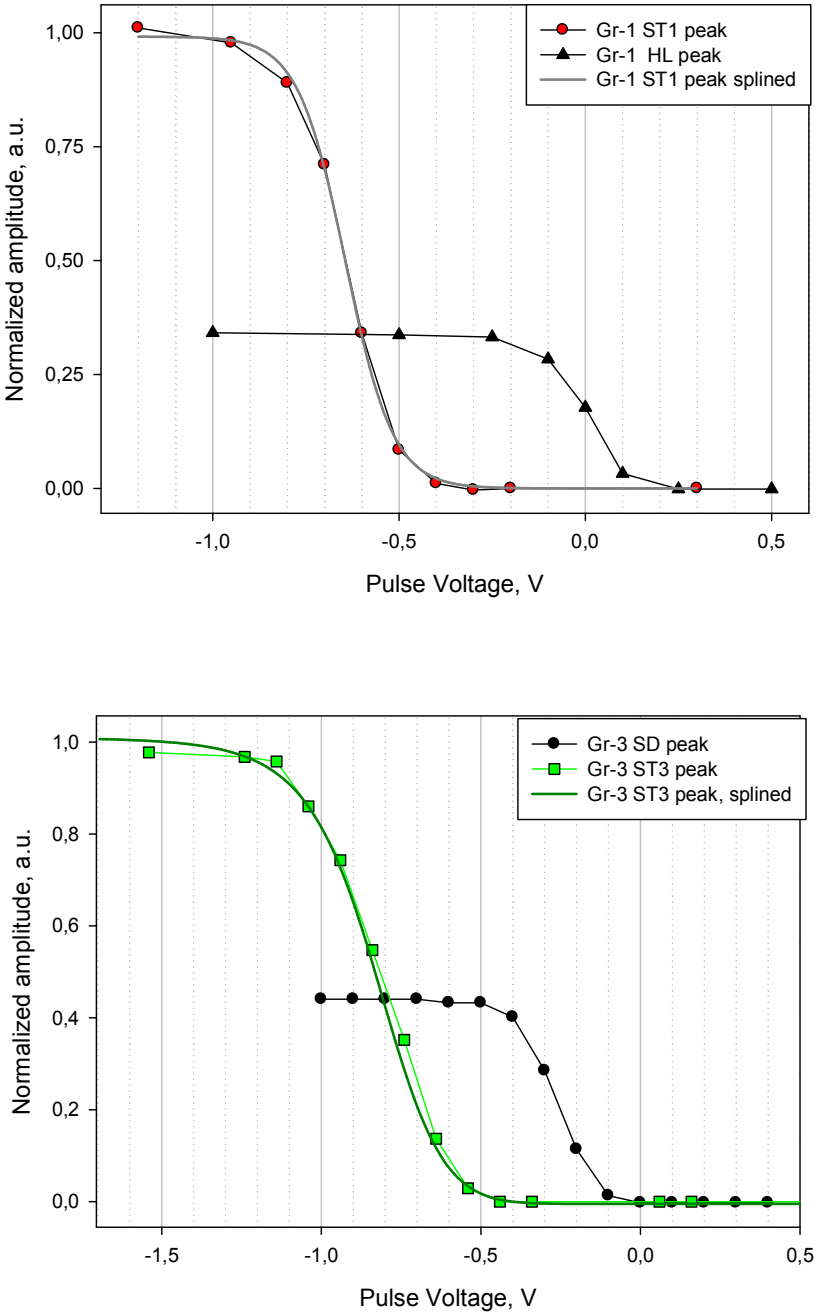

Figure 5.2. Dependences of the DLTS signal on the filling pulse voltage. Upper plot - ST1 and HL peaks in Gr-1 sample; lower plot - ST3 and SD peaks in Gr-3 sample. Measurements parameters: filling pulse duration t_p=1ms, reverse bias U_r=4V, rate window t_w=20ms. Positive pulse voltages correspond to the reverse bias, negative – forward bias.

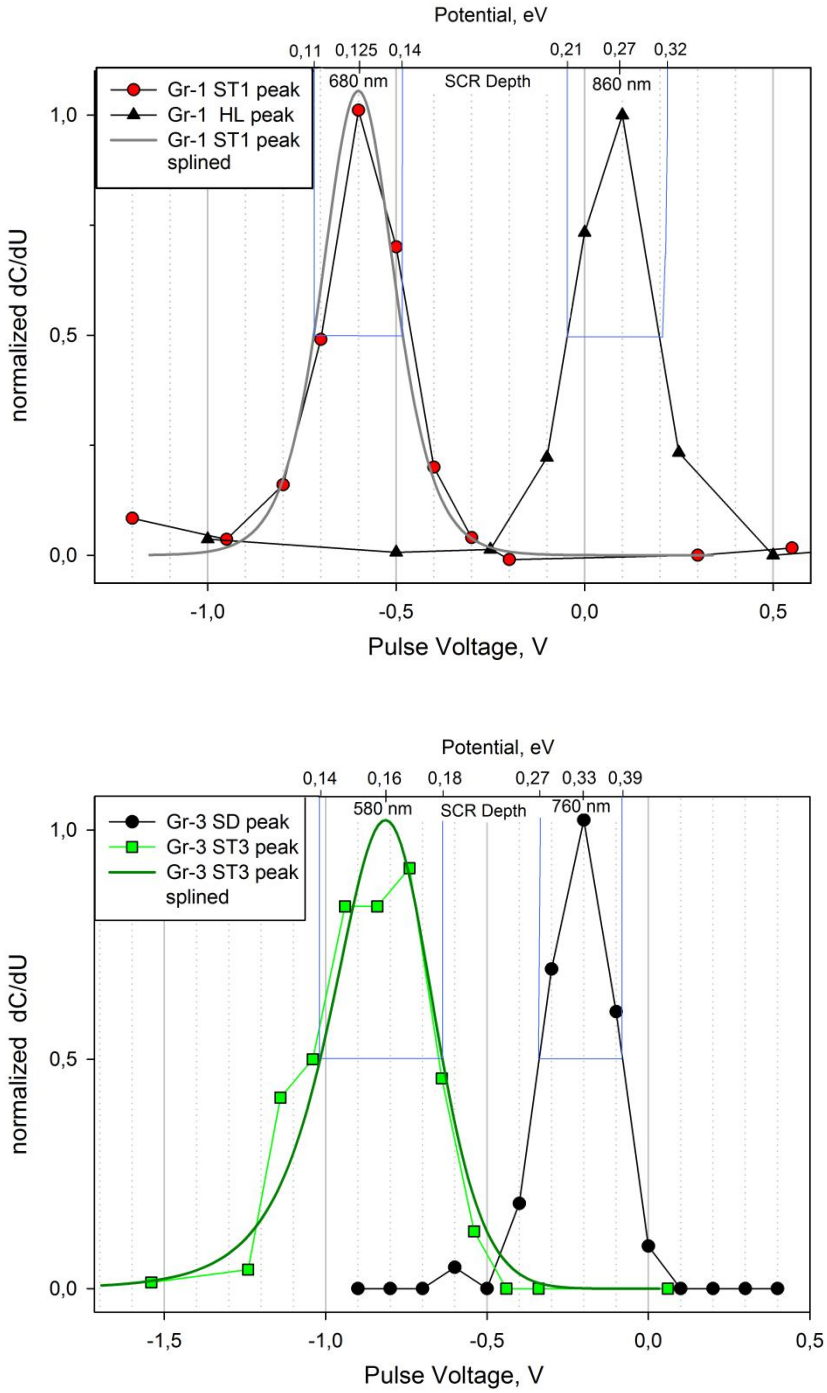

Figure 5.3. Traps density profiles normalized to same magnitudes, as derived from the dependences of DLTS peaks magnitudes on the filling pulse voltage. Upper plot - Gr-1 sample, ST1 and HL peaks; lower plot - Gr-3 sample, ST3 and SD peaks. Potential values and SCR depths on the top of the graphs correspond to the particular temperature of respective DLTS peak appearance. Measurements parameters: filling pulse duration t_p=1ms, reverse bias U_r=4V, rate window T_w=20ms. Positive pulse voltages correspond to the reverse bias, negative – forward bias.

Additionally, the obtained profiles can provide the information concerning whether the traps giving rise to ST1, ST3, SD and HL DLTS peaks are associated with a single level inside the band gap or with the density of states (or levels). Upper scales on the trap profile plots in Fig. 5.3 give the electrostatic potential $V(x_d)$ at the position of DN (Eq. 1.5 with $x=x_d$) for the particular pulse voltages on the lower scales (i.e. for the particular SCR depths w). The depletion layer widths w depicted over the trap profile peaks in Fig. 5.3 were calculated from the stationary capacitance values measured at the corresponding voltage and at the same temperature as the DLTS profiles were.

Variation of electrostatic potential corresponding to the half-width of the trap profile (blue lines in Fig. 5.3) reflects in turn the variation of the defect energy level position relative to the Fermi level position in the neutral region during the filling process of the respective defect level. In case of a single trap level, $V(x_d)$ difference equivalent to the half-width of profile peak should correspond to the full width at half maximum (FWHM) of the Fermi function at a given temperature, i.e. to be in order of $\sim 3,5kT$. The calculated values of $3,5kT$ corresponding to the temperatures of interest and the actual half-widths of the obtained trap profile peaks (according to Fig. 5.3) are collected in Table 5.2, clearly showing that the latter are considerably broader than is expected for the single trap levels. Hence, the revealed defects should be associated with the density of states inside the band gap, what will find a confirmation as the broadened DLTS peaks in the following paragraphs.

In principle, knowing the exact depth position of the DN ($x_d = 0,16\ \mu m$) as well as the SCR depth w corresponding to the profile peak position, it is possible to calculate the energy position of respective defect level following Eq. 1.18

$$E_F - E_t = \frac{eN_A}{2\varepsilon\varepsilon_0}\left(w - x_d\right)^2 . \tag{5.11}$$

However practically, the accuracy of such calculations will be rather low due to established uncertainty in the estimation of the acceptor doping level N_a in the near-surface region ($w < 1\mu m$), see details in paragraph 6.6 (note that in the discussion just above we were interesting in the $V(x_d)$ potential difference rather than in the absolute values, minimizing in such a way errors related with N_a uncertainty).

Table 5.2. Full width at half maximum-values of a Fermi function ($3,5kT$) at corresponding temperatures and of the trap profile peaks shown in Fig. 5.3.

	ST1 peak / 40K	ST3 peak / 55K	SD peak / 150K	HL peak / 220K
$3,5kT$, *meV*	13	17	46	67
FWHM of the profile peak, *meV*	30	40	120	110

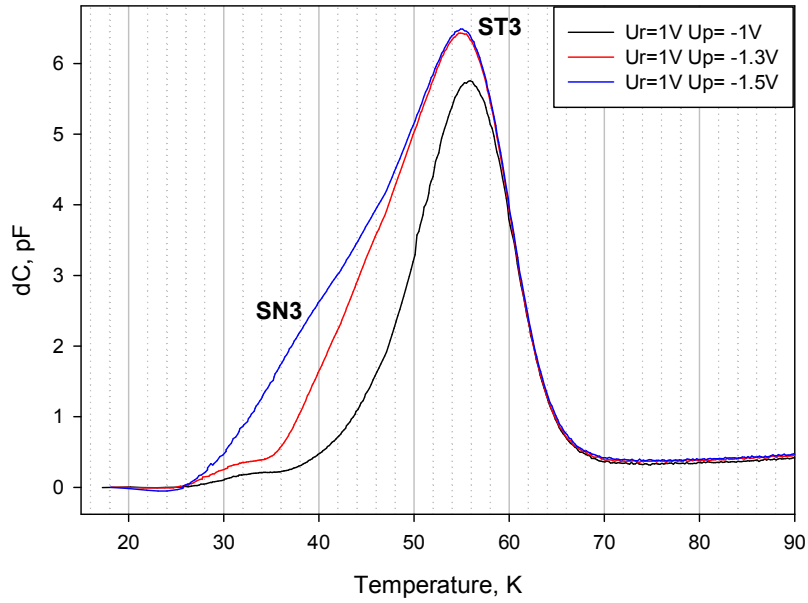

Figure 5.4. DLTS spectra of Gr-3 sample (low-temperature part) measured with different filling pulse voltages U_p, while keeping the reverse bias voltage unchanged. DLTS-scan parameters: filling pulse duration t_p=1ms, reverse bias U_r=*1V*, rate window T_w=20ms, values of the filling pulse voltages are shown in the legend.

Another important conclusion which could be drawn from the trap profiles shown in Fig. 5.2 and 5.3 is that the filling pulse voltage of U_p=*-1V* is practically enough to fill completely the traps located at the bonded interface, thus implying that a complete set of DN-related traps can be detected by DLTS when measured with U_p=*-1V*. Exception – Gr-3 sample, where the further increasing of the filling pulse voltages up to U_p=*-1,5V* leads to the appearance of the DLTS signal due to the trap even shallower than that responsible for the ST3 peak: note the shoulder appearing on the low-temperature side of the ST3 peak, whose magnitude is growing with the filling pulse voltage, without noticeable changes of the ST3 peak height – Fig. 5.4. Second low-temperature signal was denoted as SN3 peak. Details concerning the properties of the second shallow SN3 level will be reported in Chapter 7 (paragraph 7.10) and Chapter 8 (paragraph 8.4).

5.4. Energetic levels and capture cross sections of DN-related hole traps.

In this paragraph mostly the deep traps will be considered, since the shallow ones – ST1 and ST3 – revealed very distinctive features, demanding thereby a separate detailed consideration, which will be performed in Chapter 7.

By plotting DLTS spectra with different periods of the weighting function T_C (rate window period, see explanations in paragraphs 1.2 and 4.3) and subsequent drawing of the

Arrhenius graphs, the main trap parameters – activation energy E_a and capture cross section σ can be determined. Figures 5.5 and 5.6 represent the sets of DLTS spectra of Gr-1 and Gr-3 samples recorded with five different periods of the weighting function. As one can see, no appreciable increase of the DLTS peaks magnitudes occurs with the shifting of the whole spectra towards the higher temperatures (i.e. with the decreasing of the rate window period).

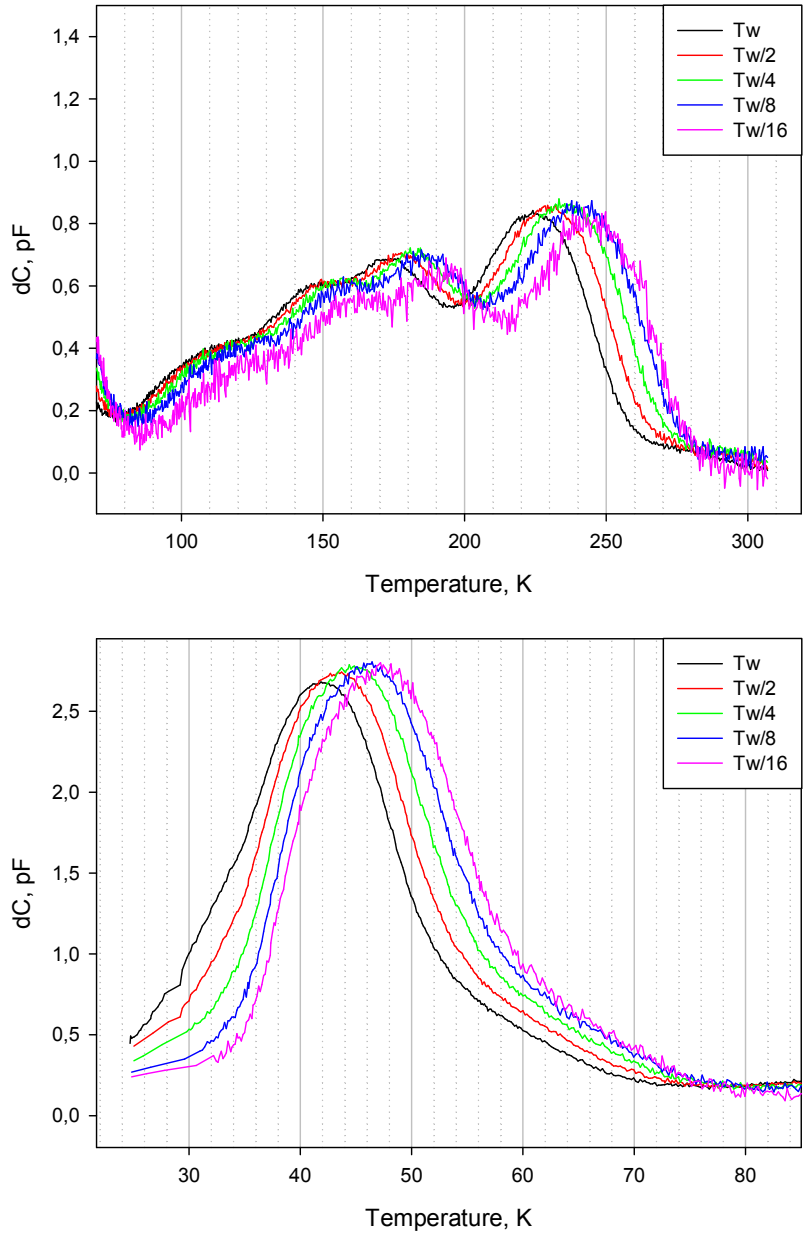

Figure 5.5. DLTS spectra of Gr-1 sample corresponding to five different periods of rate window function T_C (shown in the legend): upper plot – detailed view of deep traps in temperature range 80-270K, lower plot – detailed view of low-temperature ST1 peak. DLTS-scan parameters: reverse bias U_r= 1V, filling pulse voltage U_p= –1V, filling pulse duration t_p=100μs, initial rate window period T_w=20ms.

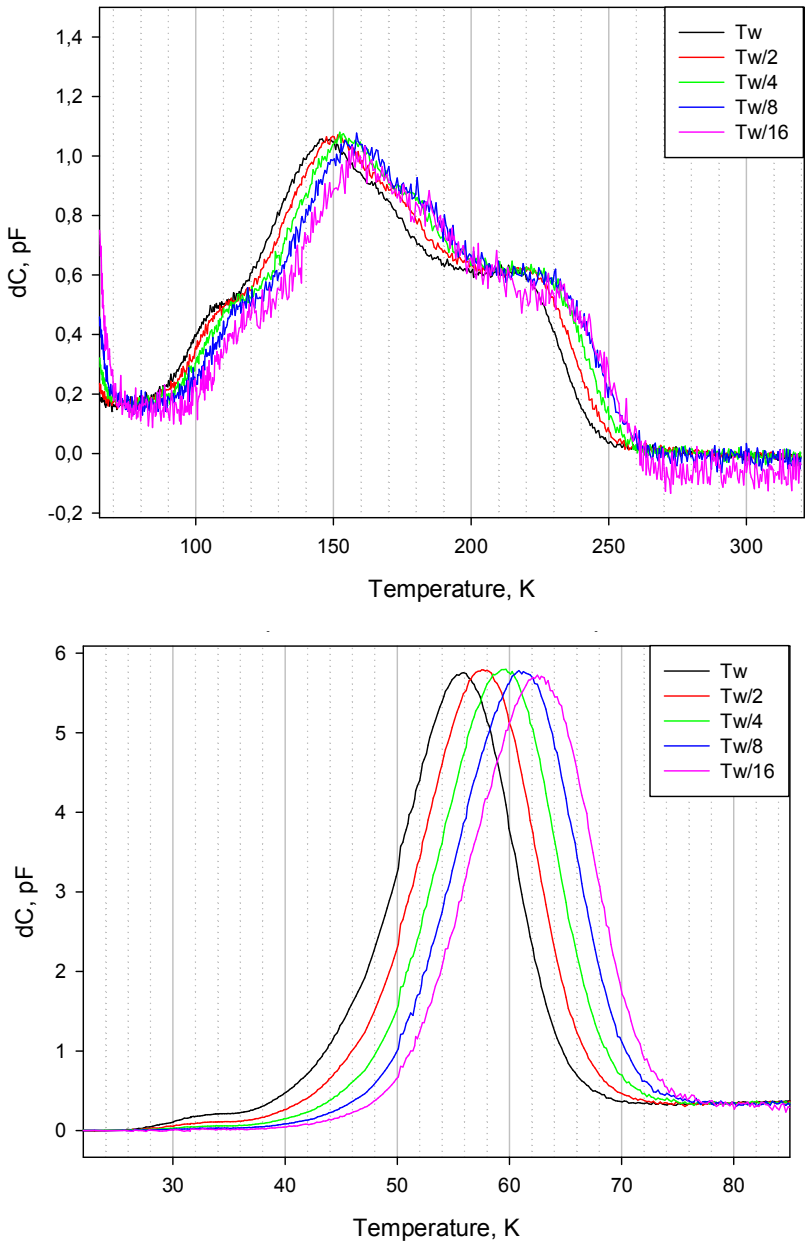

Figure 5.6. DLTS spectra of Gr-3 sample corresponding to five different periods of rate window function T_C (shown in the legend): upper plot – detailed view of DLTS peaks appearing in temperature range 80-270K, lower plot – detailed view of low-temperature ST3 peak. DLTS-scan parameters: reverse bias U_r= 1V, filling pulse voltage U_p= –1V, filling pulse duration t_p=100µs, initial rate window period T_w=20ms.

This could serve as evidence for the following consequences:

- capture cross sections for majority carriers of all revealed traps are temperature independent, i.e. $\sigma_p \neq \sigma_p(T)$ and

- no Gaussian broadening of the DLTS peak takes place (which was usually observed in plastically deformed samples and related with the fluctuations of the densities of dislocations and point defects due to various inhomogeneties caused by deformation) [Omling, 1983],

since both above-mentioned abilities are known to give rise to the considerable growth of the peak height with the decreasing of the rate window period. The absence of Gaussian broadening might be explained by the fact that the dislocation structure in the bonded samples is more regular than that in previously studied plastically deformed samples (PDS).

Arrhenius graphs plotted for the main DLTS peaks detected in the investigated samples are shown in Figs. 5.7 and 5.8. The obtained trap characteristics are summarized in Tables 5.3 and 5.4. DLTS data measured with $U_r=1V$ were used here. The impact of the bias voltage on the hole trap emission parameters will be presented in Chapter 7 and 8. For comparison, the literature data relevant to the hole traps detected in plastically deformed *p*-type Si [Kisielowski 1991] and in uncontaminated *p*-type $Si/Si_{0.98}Ge_{0.02}/Si$ hetero-structures [Vyvenko 2005] are also presented in Fig. 5.7.

From Fig. 5.7 it is clearly visible the coincidence of Arrhenius graphs for the DLTS peaks arising near the temperatures of 150K (SD peak) and 170K for Gr-1 and Gr-3 samples and of 220K (HL peak) for Gr-1, Gr-3 and Gr-6 samples. Somewhat different particular values of E_a and σ (Table 5.3) could be attributed to some uncertainties in the estimation of traps parameters related with the peaks overlapping. It was already pointed out previously, that the direct comparison of the Arrhenius plots represents a more reliable way for the establishing of traps similarity than by using only the E_a and σ pairs [Istratov 1995]. Arrhenius graph for DLTS peak appearing near 106K in the spectrum of Gr-1 sample could not be plotted due to the small magnitude and strong overlapping with high-temperature neighbour. Nevertheless, it is reasonable to suppose that this peak would have the same parameters (E_a and σ pair) as the DLTS peak arising near 106K in the spectrum of Gr-3 sample (see Table 5.3).

On the contrary, no correlations were found between the deep traps detected in Gr-30 sample and those observed in the other three samples with the smaller twist angles – see the comparison represented in Fig. 5.8 and traps parameters listed in Table 5.4.

Thus, it could be concluded that the DLTS peaks composing the spectra of Gr-1 and Gr-3 sample in the temperature diapason between 100 K and 250 K are exactly the same in both samples showing the similar (or very close) traps characteristic parameters. With the increasing of the twist angle up to 6^0 (Gr-6 sample), most of these traps disappeared and only the deepest one among them – HL peak – survives together with the considerable growth of its magnitude. While Gr-30 sample contains considerably different set of defect states, which are not presented in the DLTS spectra of other three samples with smaller twist angles.

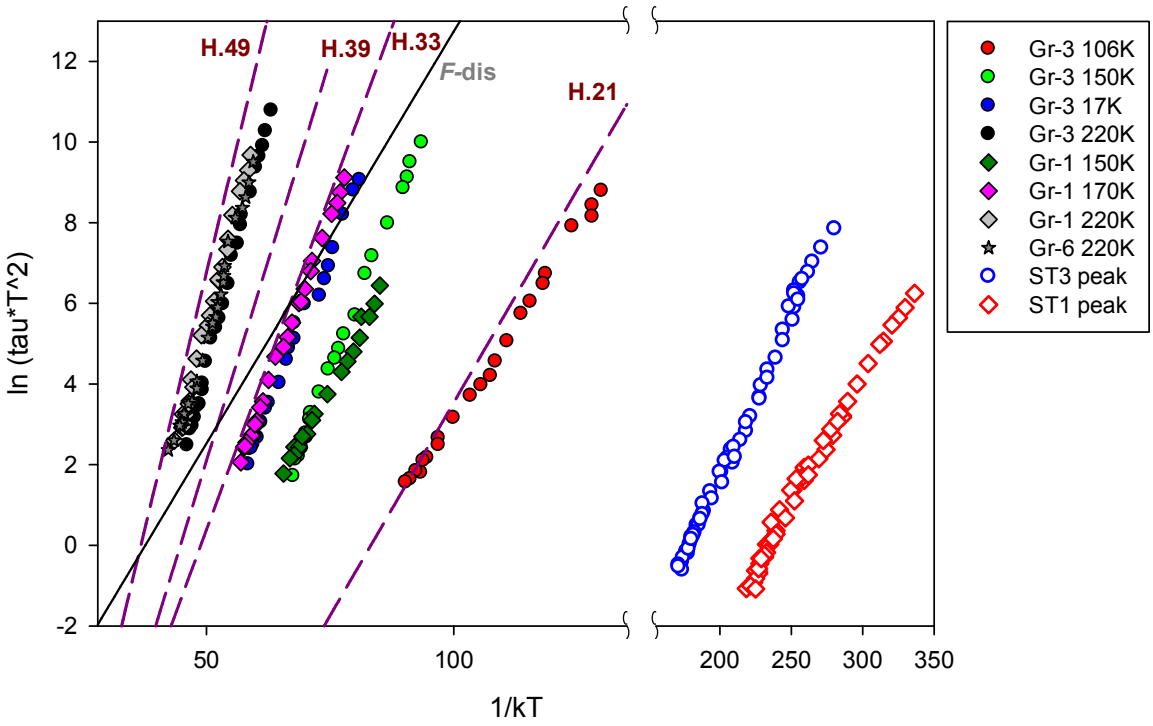

Figure 5.7. Logarithm of T^2-corrected thermal emission time constant τ as a function of reverse temperature for the traps detected in Gr-1 sample (diamonds), Gr-3 sample (circles) and Gr-6 sample (stars), as derived from the sets of DLTS spectra measured with U_r=*1V* and U_p=*-1V*. Curves assignments are shown in the legend. Points are the present experimental data, lines represent previously published results: dashed lines - traps H.21, H.33, H.39 and H.49 according to [Kisielowski 1991], solid black line – *F*-dis trap observed in [Vyvenko 2005].

Comparison with the literature data also revealed a certain correspondence between the traps observed previously in the plastically deformed p-type Si samples (shown as straight dashed lines in Fig. 5.7) with the traps detected in Gr-1 and Gr-3 samples. First of all, Arrhenius plot of the DLTS peak appearing near 170K in the spectra of both Gr-1 and Gr-3 samples is in a satisfactory agreement with that of H0.33 trap [Kisielowski 1991], found in plastically deformed *p*-type Si, known also as *F*-line. This line was attributed to some kind of oxygen-related defects located at (or close to) the dislocations, see the description of *F*-line properties in paragraph 2.4.

Additionally, Arrhenius plot and the temperature position of the *F*-dis peak observed on the *p*-type $Si/Si_{0.98}Ge_{0.02}/Si$ hetero-structures containing the network of clean misfit dislocations (solid black line in Fig.5.7) appeared to be close enough to those of the 170K peak observed in Gr-1 and Gr-3 samples. However, the activation enthalpy and especially capture cross section found for the *F-dis* peak (*0,2 eV* and $10^{-18}\ cm^2$, see [Vyvenko 2004] and [Vyvenko 2005]) differs considerably from the values obtained for the DLTS peak appearing at 170K – see Table 5.3, indicating another origin of that peak.

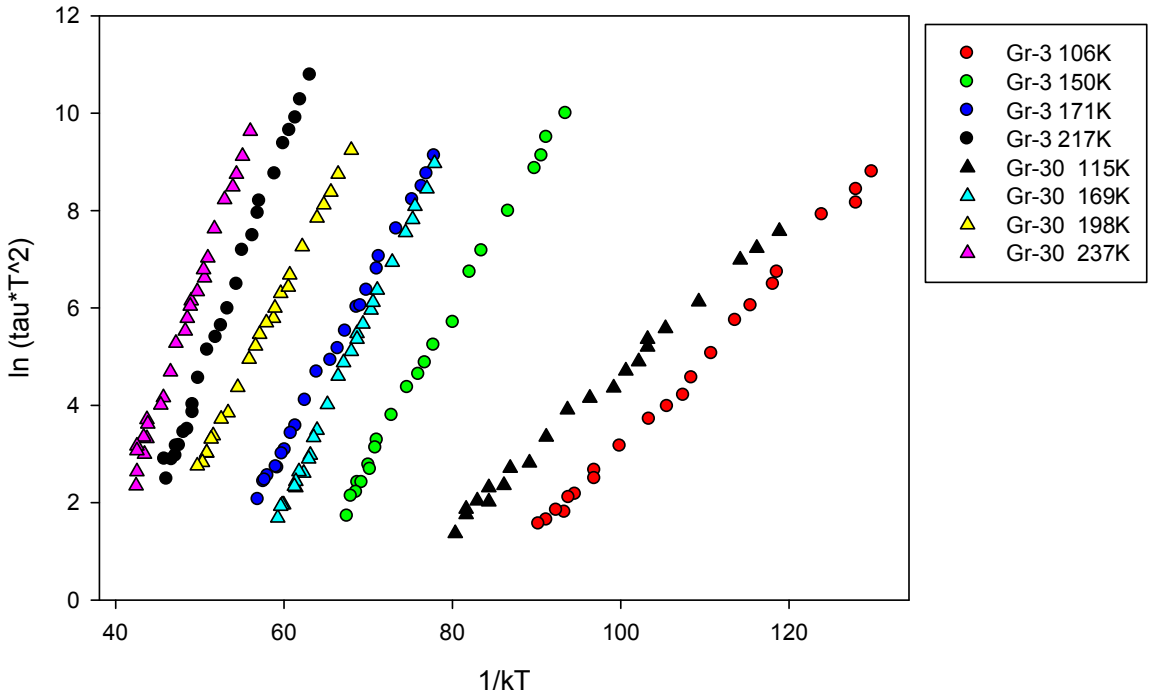

Figure 5.8. Logarithm of T^2-corrected thermal emission time constant τ as a function of reverse temperature for the traps detected in Gr-3 (circles) and Gr-30 sample (triangles), as derived from the sets of DLTS spectra measured with U_r=*1V* and U_p=*-1V*. Curves assignments are shown in the legend.

So, it should be concluded that the origins of the hole trap state corresponding to the 170K DLTS peak differ from that of *F-dis* peak observed on clean misfit dislocations in *p*-type $Si/Si_{0.98}Ge_{0.02}/Si$ hetero-structures.

Close coincidence could be also established between the Arrhenius graphs for the DLTS peak appearing at 106K and for H.21 peak observed by [Kisielowski 1991] in plastically deformed p-Si. Moreover, some correlation could be also observed for the Arrhenius graph of the DLTS peak appearing at 220K (HL peak) and of the H.49 peak observed in plastically deformed samples [Kisielowski 1991]. Unfortunately, much less is known about the origin of H.21 and H.49 lines, only that they appear in moderately-deformed p-type silicon and do not survive upon annealing, see paragraph 2.4.

As for Gr-30 sample, no correlations were found between the traps detected in this sample and those dislocation-related traps observed previously. Discussion about the possible origins of the deep traps observed in four bonded samples studied here will be continued in the following paragraphs 5.9 and 5.12 after the consideration of additional information – DN microscopy-images and PL spectra.

Table 5.3 Labels and characteristics of the traps detected in Gr-1 and Gr-3 samples: E_a – activation enthalpies from the valence band edge, σ – apparent capture cross sections for holes. Small magnitude of the DLTS peak appearing near 106K in the spectrum of Gr-1 sample as also strong overlapping with its neighbour impede the estimation of its parameters. *- activation enthalpies and capture cross sections for the shallow levels ST1 and ST3 in Gr-1 and Gr-3 sample, respectively, as derived from the DLTS spectra measured with reverse bias $U_r=1V$.

	Gr-1 sample		Gr-3 sample	
	E_a, eV	σ, cm^2	E_a, eV	σ, cm^2
ST1 / ST3 peak *	0,062	$7,6*10^{-16}$	0,081	$1,2*10^{-15}$
T=106K	-	-	0,187	$3,0*10^{-15}$
T=150K, SD peak	0,280	$2,8*10^{-14}$	0,310	$1,15*10^{-13}$
T=170K	0,333	$1,1*10^{-14}$	0,300	$2,40*10^{-15}$
T=220K, HL peak	0,482	$7,3*10^{-14}$	0,490	$2,85*10^{-13}$

Table 5.4 Labels and characteristics of the DN-related traps detected in Gr-6 and Gr-30 samples: E_a activation enthalpies from the valence band edge, σ – apparent capture cross sections for holes.

Gr-6 sample, shallow & deep level

	E_a, eV	σ, cm^2
T=40K	~0,07	$8,90*10^{-15}$
T=222K	0,458	$2,85*10^{-14}$

Gr-30 sample, deep levels

	E_a, eV	σ, cm^2
T=68K	0,072	$3,93*10^{-18}$
T=115K	0,159	$3,84*10^{-17}$
T=169K	0,392	$1,27*10^{-12}$
T=198K	0,362	$2,37*10^{-15}$
T=237K	0,507	$7,45*10^{-14}$
T=305K	0,582	$2,75*10^{-15}$

5.5. DLTS peak shape analysis.

Considering the trap profiles in paragraph 5.3, some evidences of broad distribution of states associated with shallow ST1/ST3 as well as with the deep SD and HL traps were obtained. Now it is possible to prove (or instead - disprove) these experimental findings by simulating the shape of DLTS peaks using the standard model developed for point-like

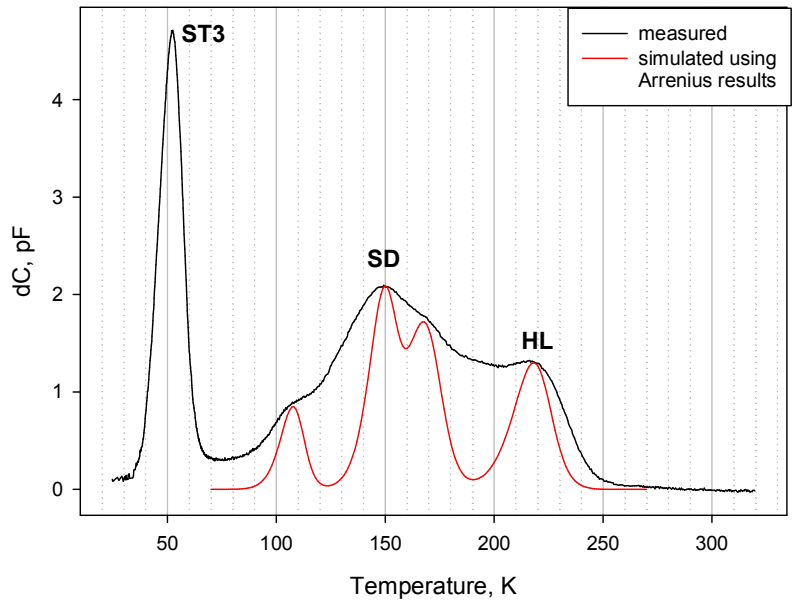

Figure 5.9. Measured DLTS spectrum of Gr-3 sample in comparison with the simulated one. Measurement settings: reverse bias U_r= 1V, filling pulse voltage U_p= –1V, filling pulse duration t_p=100μs, rate window period t_w=20ms.

defects where E_a and σ values derived from the Arrhenius plots stand as known-parameters. Comparing the real and the simulated peaks, the fact of broadening could be definitely established. For *sin*-like weighting function, DLTS signal is defined by the expressions Eq. 1.24 and 1.16. Amplitude of the capacitance transient ΔC (which defines the peak amplitude) would be considered as a free parameter. By adjusting the ΔC parameter, the magnitude of the simulated peak will be brought into correspondence with that of the real DLTS peak.

Simulation results are presented in Fig. 5.9 for the set of deep traps in Gr-3 sample, showing a good correspondence between the temperature positions of real and simulated peaks. A closer look on to the simulated and real DLTS spectra in Fig. 5.9 gives clear evidence that two more peaks – near 130K and 190K – are presented in the set of overlapped peaks at 100-250K, but which are fully concealed by the neighboring peaks of higher magnitudes, making it impossible to plot the Arrhenius graphs for these DLTS peaks. Obviously, these two peaks should be expected in the spectrum of Gr-1 sample, too.

As a result, the fact of broadening can be established firmly for HL peak, whereas for SD and other DLTS peaks the strong overlapping makes it difficult to come to the definite conclusion about the broadening of these peaks and its possible origin (may be this apparent broadening is simply due to strong overlapping of the several closely-spaced DLTS peaks?). However, broadening of the individual low-temperature ST1 and ST3 peaks could be established unambiguously, see Fig. 7.4 in Chapter 7 and the respective discussion.

Discussion and comparison with the results of optical (PL) and structural (TEM) investigations.

Issuing from the obtained DLTS spectra, four bonded samples could be divided into two groups:

- small-angle (SA-samples) samples Gr-1 and Gr-3 with dominating low-temperature peaks ST1 and ST3, respectively, and with similar sets of deep traps, giving rise to the strongly overlapped DLTS peaks in the temperature diapason of 100-250K;
- large-angle (LA-samples) samples Gr-6 and Gr-30 with the dominating high-temperature peaks. Moreover, parameters (E_a and σ pairs) of DN-traps in Gr-30 sample were found to be completely different from those detected in SA-samples.

Specifying, SA-interfaces in Gr-1 and Gr-3 samples introduced mainly shallow levels in Si band gap, while LA-interfaces in Gr-6 and Gr-30 – deep levels. Other main findings are broad distribution of levels associated with DN-related traps and particular correlation between some of deep traps in SA-samples with those observed previously in PDS samples.

In order to ascertain the origin of revealed defect states as well as to establish the relationship between the DN-related states in samples with different twist misorientation angle α_{TW} and dislocation related luminescence (DRL), detailed analysis by means of photoluminescence spectroscopy (PL) and transmission electron microscopy (TEM) methods were carried out. Being considered together, these three methods supply the complex information about the structural, electrical and optical properties of DN in every particular sample. Results of these investigations are reviewed below and the determined correlations with the results of DLTS measurements are discussed.

5.6 PL spectra of the investigated samples.

Samples photoluminescence was measured by T. Mchedlidze. PL was excited be Nd:YVO_4 laser emitting at $\lambda_{EXC}=532\ nm$ with excitation power of *100-200 mW* and the laser beam focused into a spot with the *100 μm* diameter. Results of the PL investigations were discussed in [Mchedlidze 2010] and [Mchedlidze 2011].

PL spectra detected from all 4 bonded samples and for two different measurement temperatures – 300K and 80K – are presented in Fig. 5.10.

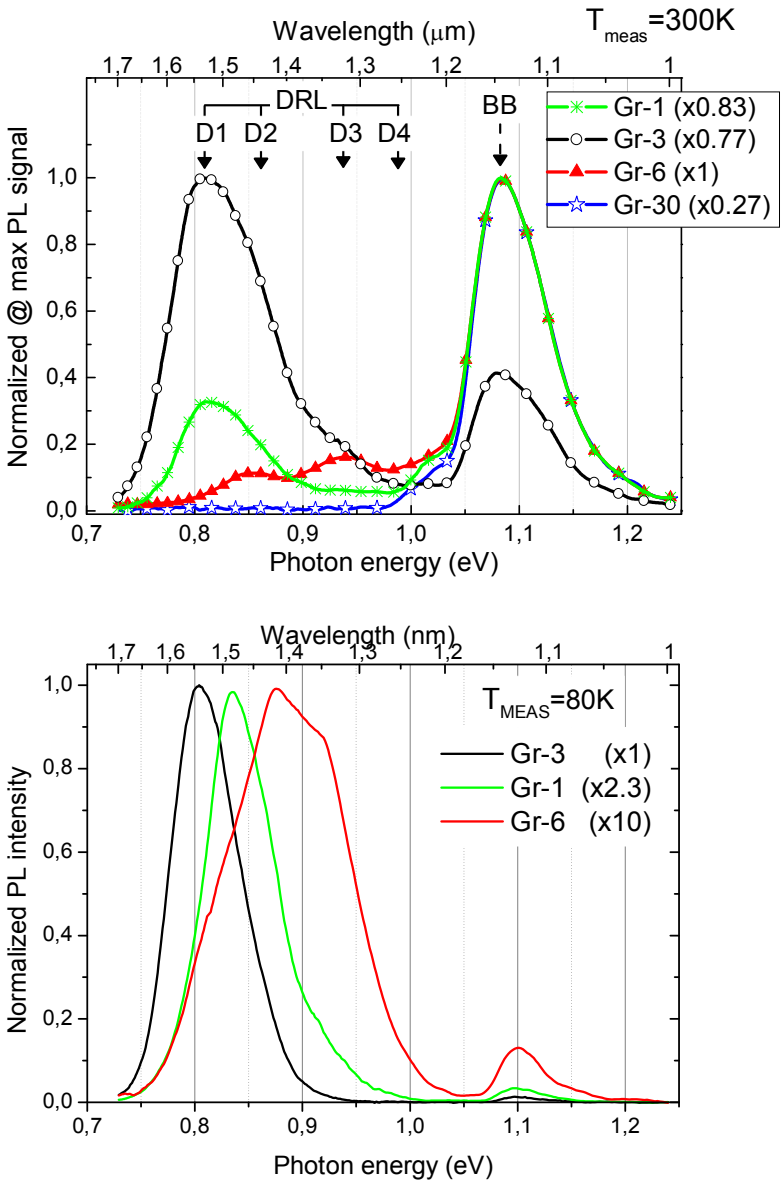

Figure 5.10. PL spectra detected from the 4 bonded samples at 300K (upper plot) and at 80K (lower plot). Excitation power was P_{EXC} =200 mW at 300 K and P_{EXC}=100mW at 80K. Attribution of the curves and normalization coefficients are shown in the legends (after [Mchedlidze 2011]).

As it is visible in Fig. 5.10, the shape and the intensity of DRL peaks depend strongly on the twist misorientation angle between the bonded wafers. The strongest dislocation related luminescence (DRL) spectra consisting mainly of D1 peak at *~0,81 eV* was observed on Gr-3 sample. D1 peak was less intensive in Gr-1 sample and was under detection limit in Gr-6 and Gr-30 samples. Extremely weak DRL consisting from D2 and D3 peaks was found in Gr-6 sample and no DRL signals were observed in Gr-30 sample at T_{MEAS}*=300 K*. Band-to-band (BB) luminescence showed nonmonotonic behaviour as a function of the twist angle. It was found to be the maximal in Gr-30 sample.

Measurement temperature also has a significant influence on the luminescence spectra, see Fig. 5.10 lower plot, leaving however the general trend – highest DRL in Gr-3 sample, lower in Gr-1 and the weakest in Gr-6 sample – unchanged (PL on Gr-30 sample was not measured at 80K). Whereas at T_{MEAS}= 300 K PL spectra of Gr-1 and Gr-3 samples contain similar single broad peak with the maximum at *~0,81 eV*, at lower T_{MEAS}= 80 K the differences in the DRL shape and energy position of the PL peaks in Gr-1 and Gr-3 samples become clearly visible. Previous investigations of various dislocated samples revealed [Mchedlidze 2011], that D1 line position is very sensitive to the particular dislocation morphology and fine structure, so that its energy position may drift slightly near the prescribed position. So, in both Gr-1 and Gr-3 samples at T_{MEAS}= 80 K the main PL line should be D1 line, in spite of *~25meV* difference in energy positions. Obviously, this energy shift reflects the different structure of the DNs in these samples, which, in turn, yield to the different energy position of the dislocation-related bands or levels participating in D1 radiative recombination [Mchedlidze 2011]. Intensity of DRL lines at 80K is considerably higher than BB for any of the samples (as against to T_{MEAS}= 300K where this is the case only for Gr-3 sample), thus implying that the DN is the preferred sink for the light-generated carriers at T_{MEAS}= 80K.

Observed trend for D1 band suggests an existing of the optimal alignment between bonded Si wafers, for which the intensity of D1 line has a maximum, i.e. an optimal density of interface dislocations corresponding to the maximal intensity of D1 line. Since the D1-line from the whole DRL spectrum is the most proper candidate for practical application in all-Si LED, the optimum twist angle of α_{TW} *~3°* could be proposed for the maximal efficiency of DN-based LED [Mchedlidze 2010]. However, in order to specify the optimum tilt misorientation angle – additional information is needed.

5.7 Results of TEM investigations

TEM images were obtained by V. Vdovin at Interdisciplinary Resource Center at Saint-Petersburg State University, Russia (see also [Vdovin 2011]).

Figure 5.11 depicts the TEM images of DN in Gr-1 sample. Structure of DN in this sample appeared to be of unique peculiarities: it consists of uni-directional 60° dislocations of a double-contrast (I set), which are disturbed by the curved 60° dislocations (II set), issuing in the triple dislocation knots formation in the intersection points – see Fig. 5.11a and 5.11b. The interdislocation distance between the straight uni-directional 60° dislocations of the I set is *60 nm,* whereas the period of the curved 60° dislocations of the II set after the averaging across the big area may be estimated approximately as *~ 240 nm*.

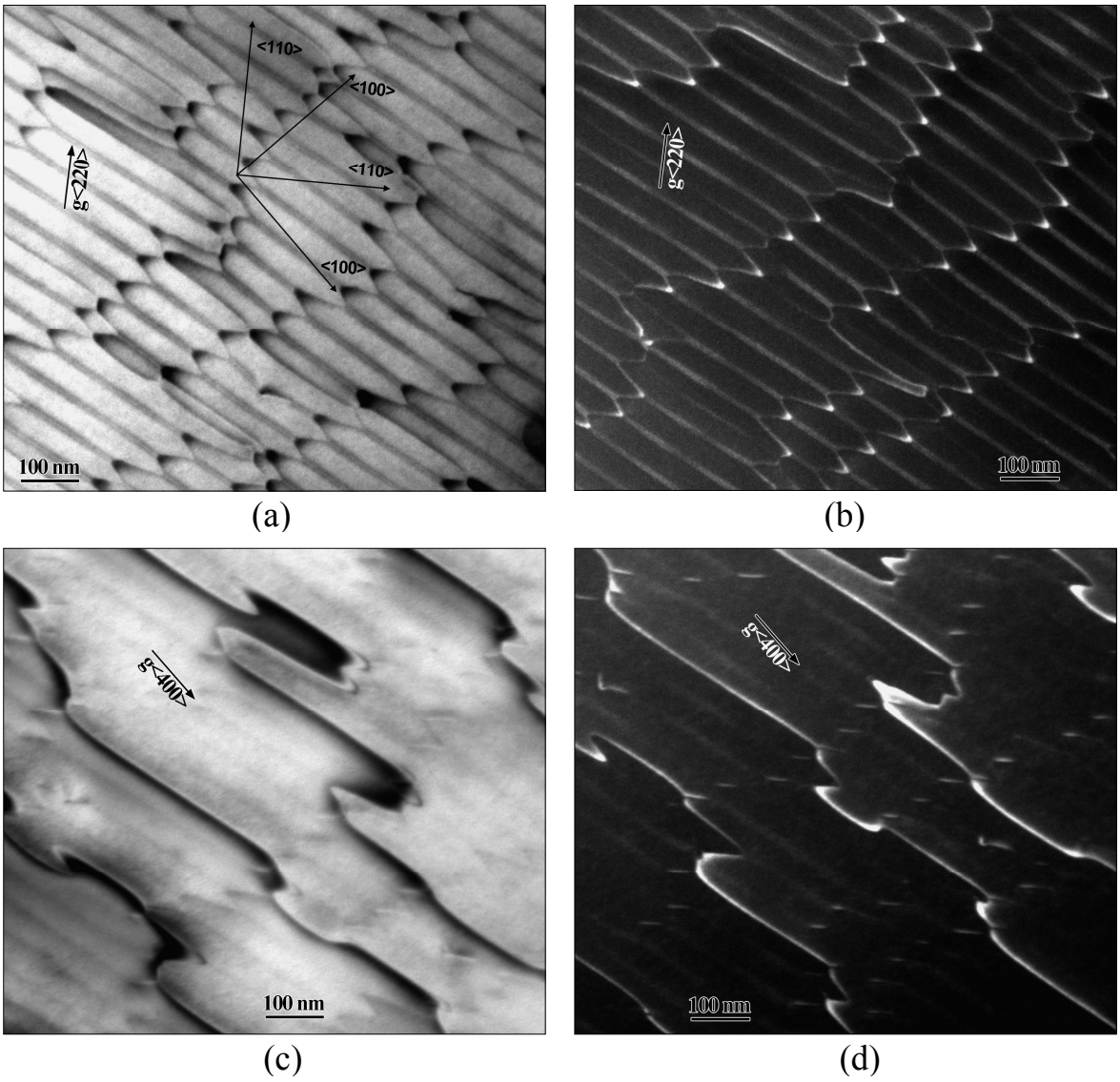

Figure 5.11. TEM images of the DN in Gr-1 sample recorded in two-beam diffraction condition: (a) and (c) – bright-field mode, (c) and (d) – dark-field mode. Particular directions of the diffraction vectors are shown by the arrows (after [Vdovin 2010] and [Trushin 2011b]).

Both sets of 60° dislocation (uni-directional dislocations of a double-contrast and disturbing set of curved dislocations) are vanishing in the ***g***<400> diffraction condition, thus verifying that they are indeed 60° dislocation [Föll]. However, another set of zigzag dislocations with single-contrast becomes clearly recognized at such diffraction conditions in Fig. 5.11c and 5.11d. Exact direction of the Burgers vector for such type of dislocations is unknown yet. The absence of Moiré contrast on the electro-miscroscopical images confirms the small values of misoerintation angles ($\alpha < 1^0$).

Detailed examinations of the contrast behaviour when the Bragg condition didn't met exactly (excitation error $s < 0$ or $s > 0$; kinematical case [Föll]) revealed, that the

dislocations in the triple knots deviate turn-by-turn in both directions relative to the proper DN plane while moving along the curved 60° dislocation line (bright-white segments in Fig. 5.11b). This finding correlates with the results of Rouviere et al [Rouviere 2000], who also did observe the rough and wavy bonded interface with the actual visual width of nearly *5nm* in case of the small twist angles $\alpha_{tw} \leq 1^0$ but of only *~1nm* for the higher twist angle of $\alpha_{tw} \sim 3\text{-}5^0$. Authors have found, that when the dislocations composing the DN are splitted into partials, the resulted dissociated dislocations do not locate in a well-defined interfacial plane anymore but extend into the grains, producing the ‘‘wavy’’ and thick Si/Si interface [Rouviere 2000].

Unfortunately, is not known at the moment whether (and which) the dislocation are dissociated in this sample (as well as the dislocations in Gr-3 sample). Obviously, more detailed TEM investigations including cross-section TEM measurements are needed to establish the fact of dislocations dissociation for sure.

Dislocation structure of Gr-3 sample consists of square network of perfectly straight screw dislocations with the mean interdislocation distances *~7-8 nm* (on the upper image in Fig. 5.12 only one set of screw dislocations is visible due to particular diffraction condition of $\boldsymbol{g}$<220>, while lower STEM image shows both sets) and the curved 60° dislocations that are inclined in average to the screw dislocation lines under the angle of about 30°. Vanishing of the corresponding set of the screw dislocations in one of the <220> reflexion types is a distinctive feature of screw dislocations, allowing to distinguish them from the other types of dislocations [Föll].

Obtained value of interdisclotain distance between the screw dislocations is in a good agreement with the declared twist angle of 3^0. Mean distances between 60° dislocations vary from *30* to *50 nm*, which correspond to the tilt angle of $\alpha_{TI} \sim 0{,}7^0$. Interaction of 60° dislocations with the network of screw dislocations gives rise to the zigzag configuration of the resulting dislocations [Föll 1979] [Akatsu 2004] with the triple dislocation knots in the points of intersections. While the intersections of perfectly straight screw dislocations produce the four-fold dislocation knots.

Thus, DN in Gr-3 sample revealed the typical structure expected for such kind of samples, which has been extensively described in the literature already, namely – square network of screw dislocations which are perturbed by the periodical array of 60° dislocations. Whereas the structure of the DN in Gr-1 sample, consisting mainly of uni-directional 60° dislocations, appeared to be rather unusual. Furthermore, nothing similar was reported in the literature before: instead, bonded samples with similar small twist and tilt misorientation angles were also found to possess the standard network of screw dislocations like that in Gr-3 sample [Rouviere 2000], [Rousseau 2002].

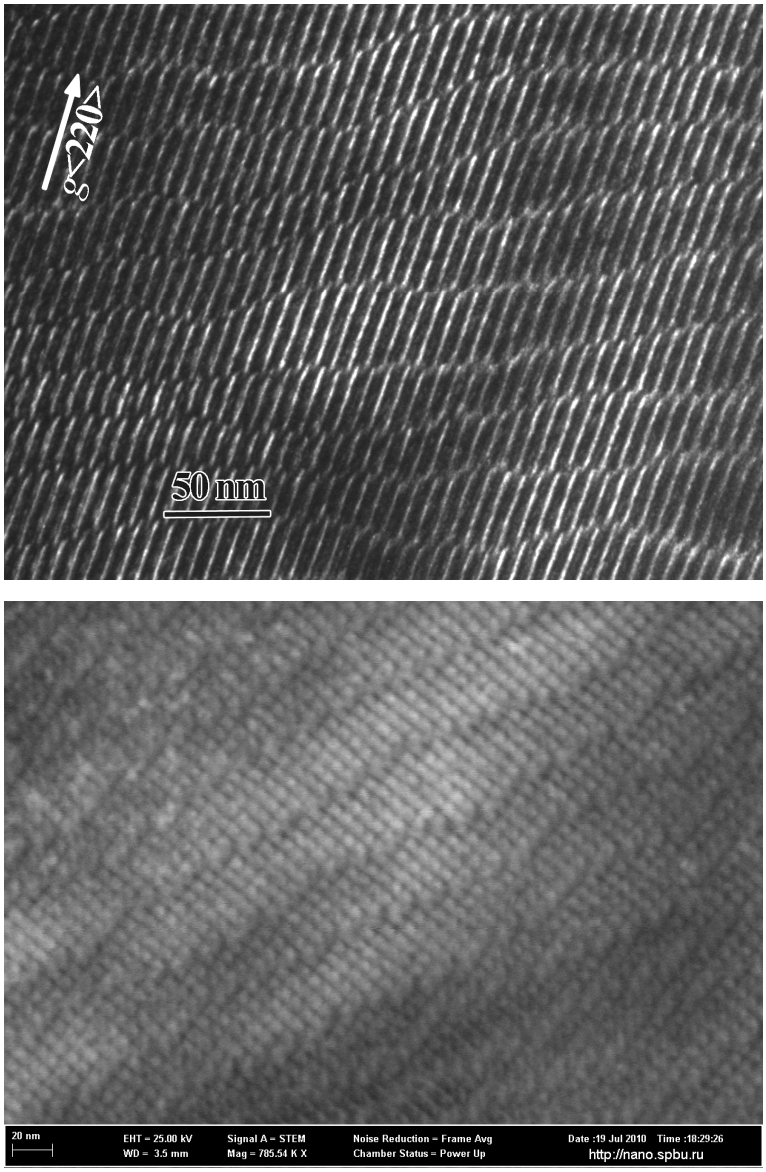

Figure 5.12. TEM images of the DN in Gr-3 sample: upper image – two-beam diffraction condition, dark-field image; lower image – multi-beam condition, STEM image. Particular direction of the diffraction vector in the upper image is shown by the arrow (after [Vdovin 2010] and [Trushin 2011b]).

The reason for such strong deviation of the DN structure in Gr-1 sample from the expected one is unknown yet. But one should remember that all previous TEM investigations were performed on the hydrophobically bonded samples, while in the present work the hydrophylically bonded samples are used. As a hypothesis it could be suggested that the particular process of buried oxide layer dissolution during prolonged annealing at high temperatures (2h at 1200 ^{0}C) and in case of small but nearly equal misoerintation angles (both α_{TW} and α_{TI} are slightly less than 1^0, with the tilt deflection

being performed in the arbitrary direction) would result in a considerably different DN structure. More detailed investigations are needed to clarify this question.

Thus, it follows that the dislocation densities as derived from the twist and tilt misorientation angles according to Eq. 3.1 and 3.2 are not sufficient to describe DN parameters and structure: they could be much more complicated than was expected from the model described in paragraph 3.2.

Table 5.5 represents the values of dislocations density as well as the density of dislocation knots in Gr-1 and Gr-3 samples as derived from the TEM images in Fig. 5.10 and 5.11. These values will be used later for comparison with the traps densities derived from the DLTS spectra.

Table 5.5. Linear density of 60° dislocations D_{60} and square density of triple dislocation knots N_{3x} in Gr-1 and Gr-3 samples.

	D_{60}, cm^{-1}	N_{3x}, cm^{-2}
Gr-1	$1{,}67*10^5$ I set $4{,}5*10^4$ II set $2{,}1*10^5$ total	$1{,}5*10^{10}$
Gr-3	$\sim 2{,}7*10^5$	$7*10^{11}$

TEM-plane images of the DNs in LA-samples Gr-6 and Gr-30 could not be obtained due to resolution limit of conventional diffraction image contrast TEM modus.

5.8 DLTS – PL correlation. Levels participating in D1 transition.

Among three possible models of D1 (and D2) radiative recombination, presented in paragraph 2.6 (Fig. 2.11), the most suitable for the case of investigated samples seems to be just the first one, supposing that the recombination causing D1 luminescence band occurs via two, shallow E_{D1s} and deep E_{D1d}, dislocation-related levels located in the opposite parts of Si band gap. It is obvious to suppose, that shallow levels ST1 and ST3 (which are too shallow to serve as an effective channel for non-radiative recombination therewith) dominating in the DLTS spectra of Gr-1 and Gr-3 samples where significant D1 luminescence was revealed, are just the implied shallow levels E_{D1s} participating in D1 luminescence.

One may however suppose, in the frame of model (C) in Fig. 2.11, that ST1 and ST3 DLTS peaks are due to the hole thermal emission from the deep states into the shallow 1D band, i.e. the activation enthalpies derived from Arrhenius plots for ST1/ST3 peaks (Table 5.3) is equal to $E_a(ST1/ST3) \approx E_{deep} - E_{1D\ band}$. Nonetheless, this is an unlikely scenario, since in such case a peak corresponding to the transition between the deep trap

and valence band with $E_a = E_a(ST1/ST3) + E_{1D\ band}$ should be present on DLTS spectra with the magnitude comparable with that of ST1/ST3 peaks [Isakov 2011], but it is absent. Moreover, in case of hole emission from deep to shallow 1D band and further carrier diffusion along these 1D bands outside of the Schottky contact region, a particular dependence of the low-temperature peaks shape and amplitude on the Schottky contact diameter should be expected, like it was observed previously in case of thin quantum wells [Schmalz 1996]. Such dependence was not revealed for the investigated samples, DLTS spectra measured on Schottky contacts with diameter *1 mm* and *1,4 mm* appeared to be absolutely similar after C^3-normalization.

Additional argument confirming that ST1/ST3 levels participate in D1 luminescence could be found by comparing the ratios of the ST3 and ST1 DLTS peaks magnitudes (concentrations) (see also Table 5.6 for details):

$$\frac{N_S(ST3)}{N_S(ST1)} \approx 2,2$$

and of the intensities of D1 PL bands in Gr-3 and Gr-1 sample (see Fig. 5.14)

$$\frac{D1(ST3)}{D1(ST1)} \approx 2,3 \text{ at } T_{MEAS}= 80K \qquad \text{and} \qquad \frac{D1(ST3)}{D1(ST1)} \approx 2,6 \text{ at } T_{MEAS}= 300K$$

which appeared to be very similar (especially at 80K). However, in spite of such perfect correlation, here the general tendency – the higher ST peak, the more intense D1 band – is most essential, since PL method is not a quantitative method (for example – surface recombination could have a significant but distinct in different samples influence) as well as the concentration derived from DLTS spectra sometimes is not so straightforward as one may expect (broadened DLTS peaks).

Finally, the direct relation of shallow ST levels with D1 luminescence was established in the recent work of Bondarenko et al [Bondarenko 2011], who, by using the pulsed-CL method on the same bonded sample, has found a direct correlation between the rising of ST peak amplitude and D1 band intensity with the increasing of the filling pulse voltage.

Table 5.6. Comparison of the concentrations of deep and shallow traps detected in Gr-1 and Gr-3 samples. Please note, that strong overlapping of the DLTS peaks located at 90-230K complicates the exact determination of their concentrations.

	Gr-1 sample (U_r=*1V*) *10^{10} cm^{-2}	Gr-3 sample (U_r=*1V*) *10^{10} cm^{-2}	ratio Gr-3/Gr-1
ST1/ST3 peak	3,5	7,6	2,2
150K (SD peak)	0,82	3,4	4,1

As it was already noted in paragraph 5.6, D1-lines in Gr-1 and Gr-3 samples at T_{MEAS}= 80K have different energy positions (Fig. 5.10), reflecting in such a way the different structures of DNs in these samples. In general, the positions and the structures of both shallow E_{D1s} and deep E_{D1d} states could depend on the actual structure of the dislocation network, for example – on the density of the dislocation intersection points or length of the unperturbed segments between them. However, if the variations of the energy position of the deep level E_{D1d} would exist inside the band gap with changing of DN structure, the shape of the DRL should vary at 300 K as well [Mchedlidze 2011]. But the shapes and the energy positions of DRL bands in Gr-1 and Gr-3 samples at T_{MEAS}= 300K are the same. Moreover, DLTS measurements revealed equal set of the deep states in Gr-1 and Gr-3 samples in the lower half of band gap (Fig. 5.1 and Arrenius plots in Fig. 5.7); in the same way, the deep states located in the upper part of Si band gap could be supposed to be the same in these two samples.

Thus, the obtained results suggest that only the position of shallow level E_{D1s} changes with α_{TW}. Since the D1 line in Gr-1 sample appears at higher energy position than in Gr-3 sample (*0,83 eV* vs. *0,81 eV*, see Fig. 5.14), the shallow level E_{D1s} in Gr-1 sample should be shallower than in Gr-3, i.e. DLTS peak corresponding to E_{D1s} level in Gr-1 sample should appear at lower temperatures than in Gr-3 one – what correlates exactly with the experimental results, see DLTS spectra in Fig. 5.1 and activation enthalpies in Table 5.3 (but note the more detailed discussion concerning the enthalpies for the shallow ST1/ST3 levels in Chapter 7 !). Whereas broad distribution of states revealed for shallow ST1 and ST3 traps (see Table 5.2) – considering that at T_{MEAS}=300K D1 recombination proceeds through the bottom of shallow ST1 or ST3 band – could be supposed as a reason for the similar energy position of D1 line at 300K.

Thus, all foregoing facts clearly confirm, that the detected ST1 and ST3 shallow levels are involved in the D1 radiative process. However, D1 recombination could also proceed in the reverse way – between the shallow level E_{D1s} in the upper part of band gap and deep level E_{D1d} in the lower part. Indeed, shallow level near the edge of conduction band was detected by MCTS spectroscopy in the similar bonded samples [Isakov 2011]. Considering the expected energy position of the shallow level in the upper part of band gap as *0,06-0,1 eV* and the energy of the D1 transition of *0,81 eV* (*~0,83 eV* in Gr-1 sample), the most suitable candidate for the E_{D1d} level in the lower part of band gap will be the SD level with E_a=*0,28-0,3eV* (see Table 5.3). Which exact recombination path dominate in the investigated samples (and in all other dislocated samples, in general) – between the shallow ST1/ST3 levels in the lower part of band gap and deep level E_{D1d} in the upper part of band gap, or, instead – between the shallow state E_{D1s} in the upper part of band gap and deep SD level in the lower part – is unclear at the moment.

However, as one can see in Table 5.6, the ration of SD peak magnitudes in Gr-3 and Gr-1 samples differs significantly from the ratio of D1-bands in these samples. From one side, we should take in mind that due to the strong overlapping with the neighbouring peaks and possible peak broadening, the exact concentration of SD traps in Gr-1 and Gr-3 samples could not be derived precisely. But from another side, this could be considered as an evidence, that in these samples D1 transition occurs (mainly) via shallow ST1/ST3 levels in the lower part of band gap and deep level E_{D1d} in the upper part of band gap.

5.9 Possible origins of deep traps in SA-samples.

- ***Intersections of dislocations.***

As it was discussed in paragraph 5.3, the observed deep traps are directly related with the defect states introduced by the dislocation networks. These deep traps could be hardly due to external contamination by fast transition metals segregated at DN, since all samples were annealed simultaneously in the furnace specially designed to prevent such kind of contamination (see Chapter 4). They might be caused by the rest impurities presented in the initial wafers and segregated at bonded interface during annealing.

The more intriguing then to detect the same set of deep traps in Gr-1 and Gr-3 samples in spite of completely different DN structures. We have to admit then, that neither the own states of square screw dislocation network presented in Gr-3 sample, nor of straight segments of 60° dislocations in Gr-1 themselves can not be responsible for the detected deep traps, since the straight segments of the uncontaminated dislocations do not introduce the deep levels into the Si band gap (see discussion in Chapter 2). One of the possible explanations of the similarity of the deep levels in these samples might be that the impurities are segregate at the staking faults of splitted dislocation cores like it was assumed in [Vyvenko 2004] [Vyvenko 2005].

Another source might be the special points on the dislocation lines, such as triple dislocations knots (points of intersections of 60° and screw dislocations in Gr-3 sample and of 60° dislocations of I and II set in Gr-1 sample), four-fold dislocation knots (points of intersections of screw dislocations, only in Gr-3 sample), or other products of dislocation reactions (for example - zigzag dislocations). As it was discussed in paragraph 2.6, results of Steinman et al. [Steinman 1999] on the photoluminescence study of epitaxial Si/Si_xGe_{1-x} structures and Sekiguchi and Sumino [Sekiguchi, 1996] on the cathodoluminescence investigations of Si crystals with various configurations of dislocations, infer that D1 and D2 lines originate from the reaction products of dislocations; thus, it could be supposed that in SA-samples the dislocation intersection points are the most probable candidate for

the appearance of the deep level E_{D1d} participating in the D1 radiative transition. The deep level E_{D1d} seems very likely to be the same in Gr-1 and Gr-3 samples. Hence, four-fold dislocation knots must be ruled out from the list of possible candidates for E_{D1d} level, since such kind of knots is absent in Gr-1 sample.

- ***Interstitials and oxygen.***

Several other reasons of the deep traps formation which are not related with the dislocations interaction have to be also considered. During the dissolution of buried oxide layer and DN formation a great number of Si interstitials have to be consumed to replace oxygen with silicon. The interstitials moving towards the bonded interface participate in the rebuilding of the perfect lattice and in the dislocation formation. They, obviously, can partly remain in the interstitial positions, most probably in the tensile-strained regions of dislocations. Hence, clusters containing different number of interstitial Si atoms could grow in a close vicinity of 60° dislocation. In fact, structural defects such as microtwins, stacking-fault-like and rod-like defects caused by self-interstitial incorporation were observed previously by high-resolution TEM (HRTEM) at the interfaces of hydrophilic and hydrophobic bonded wafers even after high-temperature annealing treatments at 1100 °C for 2,5 hours [Reiche 1995].

Self-interstitials agglomerated in clusters and rod-like defects are known to be electrically and optically active in Si, producing multiple defect levels in both halves of Si band gap (see for example [Libertino 2001] [Mchedlidze 2007] and references therein). Theoretical calculations performed by Jones et al [Jones 2000] argue that even small cluster consisting of 4 interstitial atoms would produce a deep donor-like level in the lower part of Si band gap (please note, that in the next chapter deep traps detected in Gr-1 and Gr-3 samples will be identified as donors, too!) and, moreover, is thermally stable enough to survive the high-temperature annealing.

Oxygen-related defects have to be also considered as a further possible origin of the electronic states at DN. This could be concluded from the fact of close relation between the DLTS peak 170K observed in SA-samples and *F*-line found in p-type plastically deformed samples (see Arrhenius plots in Fig. 5.7): according to the experimental observations of Cavalcoli et. al. [Cavalcoli 2008] (see details in Chapter 2), *F*-line defects have a certain relation with oxygen located at or close to the dislocations. Benamara et al. [Benamara 1996] revealed by means of TEM observations of bonded samples with the DN structure similar to that in Gr-3 sample (square network of screw dislocations disturbed by the set of parallel 60° dislocations), that oxygen atoms coalesced more easily at 60° dislocations than at screw ones, forming the faceted oxide precipitates and clusters, and that the total density of the oxide precipitates depends strongly on the 60° dislocation density.

Both interstitial clusters and oxygen-related defects are absent when considering the misfit dislocations in Si/SiGe structures. This is probably the reason, why no deep

levels similar to those observed in the investigated bonded samples were detected in such structures [Vyvenko 2004] [Vyvenko 2005] (however, one should mind much smaller density of misfit dislocation in the cited works). On the other hand, DLTS spectra measured on the natural Σ25 grain boundaries in Si by Broniatowski [Broniatowski 1987], have also revealed the continuous distribution of the GB-states in the range from $E_V+0,2\ eV$ till $E_V+0,6\ eV$, i.e. just in the same energy diapason like in the Gr-1 and Gr-3 samples studied here. Moreover, Broniatowski has noted in his work that electrical activity of GB depends strongly on the thermal history of bicrystals and correlates with the impurities segregated and precipitated at the interface.

As a result, it may be concluded that interstitial clusters and/or some kinds of oxygen-related defects (for-example, embryos of oxide precipitates, which are too small to be detected by TEM or SIMS) stabilized by the strain field of 60° dislocations (being thus able to survive the high-temperature annealing) could give rise to the detected deep traps in SA-samples, except probably SD and HL peak which seem to be related with interaction of dislocations. Some correspondence with the deep levels (Arrhenius plots for H0.21 and 106K peaks, see paragraph 5.4) observed previously in PDS and ascribed to the agglomerates of the deformation-induced point defects could serve as a confirmation of this version. Whereas the mesh of screw dislocations looks less favourable as a place for the interstitials and oxygen-related defects formation because of considerably smaller strain field. Thus, supposing the 60° dislocations in both Gr-1 and Gr-3 sample to be responsible for the formation of the observed deep levels in one or another way, their similarity in Gr-1 and Gr-3 sample becomes clear.

5.10 Correlations of the shallow ST1/ST3 and SD traps concentrations with the total length of 60° dislocations D_{60} and triple knots density N_{3x}.

In Chapter 7 the particular property of ST1 and ST3 shallow levels – field enhanced emission – is described, and the theoretical calculations presented in Chapter 8 give the firm evidences that such an effect could take place only if these shallow levels are related with 60° dislocations. Hence, the concentrations of the shallow ST1/ST3 defects in Gr-1 and Gr-3 samples should correlate somehow with the total length of 60° dislocations in these samples.

The shallow dislocation-related 1D bands (stacking fault states) are inherent properties of dislocations (of intrinsic stacking fault - infinite or bounded by the partials) and stretching along the whole dislocation line (stacking fault stripe), i.e. the density of 1D states should in principle be proportional to the linear dislocation density (the same is true

Table 5.7. Concentrations of ST1 and ST3 traps N_{ST} (Table 5.6) in the ratio with the linear densities of 60° dislocations D_{60} and with the square density of triple dislocation knots N_{3x} in Gr-1 and Gr-3 samples (Table 5.5). Ratios of SD traps concentration N_{SD} to the triple knots density are also presented.

	D_{60}/N_{ST}	N_{ST}/N_{3x}	N_{SD}/N_{3x}
Gr-1	$\frac{2,1*10^5\ cm^{-1}}{3,5*10^{10}\ cm^{-2}} \simeq 60nm$	$\frac{3,5*10^{10}\ cm^{-2}}{1,5*10^{10}\ cm^{-2}} \simeq 2,3$	$\frac{0,82*10^{10}\ cm^{-2}}{1,5*10^{10}\ cm^{-2}} \simeq 0,5$
Gr-3	$\frac{2,7*10^5\ cm^{-1}}{7,6*10^{10}\ cm^{-2}} \simeq 40nm$	$\frac{7,6*10^{10}\ cm^{-2}}{7*10^{11}\ cm^{-2}} \simeq 0,11$	$\frac{3,4*10^{10}\ cm^{-2}}{7*10^{11}\ cm^{-2}} \simeq 0,05$

for the stacking fault shallow states as well). Castaldini et al. [Castaldini 2005b] suggested that 1D bands can be detected by DLTS only if the carrier movement along the dislocation line is disturbed by some defects that hinder fast carrier escape from SCR of Schottky diode (see paragraph 2.5). Authors have also suggested that the defects might appear as the result of oxygen segregation at dislocation. Obviously, the triple dislocation knots along the 60° dislocations could be considered as the disturbing points.

The ratio of the total length of 60° dislocations / ST1 concentration – see Table 5.7, argue, that the holes trapped onto the ST1 traps are spaced along the 60° dislocation at the distances of approximately *60 nm* from each other that corresponds perfectly with the average distance between the triple dislocation knots in Gr-1 sample (see TEM-images in Fig. 5.11). This confirms the supposition, that holes are indeed localised on the dislocation segments between the triple knots. The ratio of ST1 concentration to triple knots densities in Gr-1 sample implies that the one triple knot corresponds to *~2* captured holes, thus confirming the above statement. In Gr-3 sample, holes localisation length appeared to be somewhat smaller than in Gr-1 sample – about *40 nm,* as calculated from the ratio D_{60} / N_{ST3}, see Table 5.7. Looking on the TEM image of DN in Gr-3 sample presented in Fig. 5.12, it could be counted that the segment of 60° dislocation of *40 nm* long contains approximately *9-12* triple knots. Ratio of ST3 concentration to triple knots densities yields one hole per *~10* triple knots, i.e. showing reasonable agreement with the values obtained above.

The estimations of the maximal density of electrons (or holes) which can be captured onto the dislocations, made for plastically deformed samples, give the value of $N_{tot} = \sim 2*10^6\ cm^{-1}$ (see paragraph 3.4), thus corresponding to the minimal distance between the captured carriers of *~5 nm*. In the SA-samples, such distance appears to be ~10 times larger. The reason of the reduced occupation of DN states in GR-3 sample might be the limitation due to electrostatic repulsion among the captured carriers.

As it is follows from Table 5.5, the total length of 60° dislocation in Gr-3 sample is only 1,2-1,5 times higher than that in Gr-1 sample, i.e. D_{60}(Gr-3)/D_{60}(Gr-1) =1,2-1,5. Whereas the magnitude of the ST3 peak in Gr-3 sample is 2,2 times higher than the magnitude of ST1 peak. However, by taking into account that in Gr-3 sample the average distance between the holes captured onto ST3 traps is 1,5 times smaller than the same distance in Gr-1 sample (*40 nm* vs. *60 nm,* as it was just discussed above), this contradistinction can be easily resolved.

N_{SD}/N_{3x} ratios for SD trap is one for 2 triple knots in Gr-1 sample and one for 20 triple knots in Gr-3 sample. In other words, in Gr-1 sample the SD traps (or rather holes captured to this trap) are spaced at the distances of *~100 nm* from each other, whereas in Gr-3 – at the distances of *~75 nm*.

5.11 Traps origin in LA-samples

- ***Gr-6 sample.***

Here we are especially interesting in specifying the changes in the DN structure responsible for the suppression of D1 luminescence intensity and low-temperature DLTS peaks magnitude with the increasing of the twist misorientation angle from 3° to 6° and, finally, disappearance of the DRL and the shallow levels at large twist angles.

Following the model developed by Rouviere et al. [Rouviere 2000] (see paragraph 3.4), twist angle α_{TW}*=5,9°* in Gr-6 sample is higher than critical; thus, the dislocations compensating the twist misalignment in Gr-6 sample are expected to be un-dissociated dislocations of the interfacial type. On the other side, the tilt misorientation of α_{TI}*=0,67°* (which is nearly the same like in Gr-3 sample) should still be compensated by an array of 60° dislocation. In this scheme, the reason for the strong changes of PL and DLTS spectra with the increasing of twist angle from 3^0 to 6^0 can be related with the transformation of the screw dislocations network to the network of the interfacial-type dislocations, which compensates now the twist misalignment. It could be assumed, that the core structure of the un-dissociated interfacial dislocations would be significantly different as compared with the core of common screw dislocations and that the dislocation reactions of 60° dislocations with interfacial dislocations would lead to the completely different atomic configurations (as compared with the interaction of screw and 60° dislocations in Gr-3 sample or reactions of 60° dislocations of I and II sets in Gr-1) which do not create the D1 luminescence centres.

On the other hand, the presence of the dominating D3 line in the PL spectrum of Gr-6 sample (Fig. 5.10) – which has been related with the recombination between the shallow 1D bands on a straight segments of 60° dislocations (see paragraph 2.6), gives the evidence that straight segments of 60° dislocations are indeed presented in the DN of Gr-6 sample. This could mean rather weak interaction between interfacial and 60° dislocations, which anyhow do not lead to the creation of E_{D1d} deep centres participating in the D1 radiative recombination. Note, that the lack of D1 luminescence band correlates with the absence of SD peak in the DLTS spectrum of Gr-6 sample. This gives an additional evidences that SD level in Gr-1 and Gr-3 samples indeed participates in the D1 luminescence and that the lack of D1 band in Gr-6 sample is due to the absence of the required deep levels E_{D1d}.

Note also, that BB luminescence in this sample is the weakest among all 4 samples and simultaneously DRL signal is also very weak. This indicates that the non-radiative recombination – evidently via HL level(s) – dominates in this sample. HL peak is presented in the spectra of three bonded samples – Gr-1, Gr-3 and Gr-6 and its magnitude grows with the twist misorientation angle, thus HL peak could not be assigned to the network of interfacial dislocations alone, as such network is absent in Gr-1 and Gr-3 samples.

As the origin of HL peak one may suppose some kinds of dislocation reactions taking place in all three samples, but the number of which grows with the increasing of the total dislocation density, in other words – with the growth of the dislocation disorder. According to the theoretical calculations of Belov and Scheerschmidt [Belov 1999], the structural disorder could have a considerable impact on the electrical properties of bonded interfaces containing more than one set of dislocations. Large bond-angle and bond-length distortions appearing in the points of dislocations intersection give rise to the formation of the under-coordinated atoms, which are able to introduce the deep levels in Si band gap. Among Gr-1, Gr-3 and Gr-6 samples, the highest structural disorder is expected to be just in Gr-6 sample, hence – the higher concentration of the deep traps provoking the appearance of the unsymmetrical HL peak + its shoulders as well. Alternative version - is that HL peak could be somehow related with the un-dissociated dislocations, which are in small quantities presented also in Gr-1 and Gr-3 samples (for example - zigzag dislocations visible in TEM images of Gr-1 sample in Fig. 5.11c and 5.11d).

Moreover, as a result of interactions of 60° dislocations with interfacial ones the place favourable for segregation of self-interstitials and/or oxygen atoms could be also destroyed, thus causing the disappearance of respective DLTS peaks (such as the peaks near 106K, 170K, etc.).

- ***Gr-30 sample***

Deep levels structure in Gr-30 sample appeared to be completely different than in other three samples with smaller misorientation: DLTS revealed a set of strongly overlapped and continuously growing up to 300K peaks, which do not correlate with those observed in Gr-1, Gr-3 or Gr-6 samples. No hints about the presence of shallow level and DRL luminescence were detected in this sample at all.

Energy distribution of defect states inside Si band gap similar to that observed in Gr-30 sample was also found for the large-angle grain boundaries by McGonigal et. al. [McGonigal 1983], i.e. with continuous growth of the interface-states densities in the lower half of band gap between $E_v+0,3\ eV$ and $E_v+0,5\ eV$. Such distribution was attributed to the defects possessing deep levels in the band gap, formed or segregated due to the large lattice mismatch [McGonigal 1983].

The origins of such phenomenon were clarified in the theoretical work of Kohyama and Yamamoto [Kohyama 1994]. In their work, authors have performed a detailed investigation of the overall features of energies and atomic structures of the twist grain boundaries in Si with different rotation axes and boundary planes – the (111) Σ7, (011) Σ3 and (100) Σ5 twist boundaries. The last one, (100) Σ5 grain boundary which is constructed by $36,9^0$ rotation around <100> axis, corresponds closely to that in Gr-30 sample because of comparable misoerintation angle and similar rotation surface. Of course, the coincident site lattice (CSL) index for the twist angle of 30^0 (Gr-30 sample) will be another than that for angle $36,9^0$ (i.e. Σ=5), nevertheless the main results of Kohyama and Yamamoto should be applicable for Gr-30 sample, too. As a result of these theoretical calculations, very complex configurations with very large interfacial energies and with many coordination defects or very large bond distortions were obtained for the Σ5 (100) twist GB. The large bond distortions generate a lot of empty deep states in the band gap – just what was observed by DLTS in Gr-30 sample.

These complex features of the Σ5 (100) twist GB were explained in [Kohyama 1994] by the morphology of an ideal (100) surface. In the ideal (100) surface, respective surface atoms contain two dangling bonds pointing to different directions, in contrast to one dangling bond per surface atom in the ideal (111) and (110) surfaces. This causes a much higher density of dangling bonds per surface area and increases the difficulty in constructing of stable configuration with as many dangling bonds being reconstructed as possible, resulting therefore in the large interfacial energies. As a result, no stable structural units without large bond distortions or coordination defects (i.e. with the small interfacial energy) are possible to construct for such twist GBs (in general – for all twist GB in Si). This was supposed by Kohyama and Yamamototo be the reason why twist GB's are so seldom found in polycrystalline semiconductors, as compared with the tilt GBs, for which the stable configurations could be easily constructed. Thus, in order to model

correctly the behaviour of typical GB in Si, bonded samples with tilt interfaces should be used (or with small twist misorientation at least) so as to guarantee the higher correspondence with the natural GBs in Si.

Strong BB luminescence in Gr-30 sample could be then explained in the following way: in spite of a high concentration of various deep levels in this sample, due to their narrow planar distribution along the bonding interface, they are unable to reduce considerably the band-to-band luminescence, which is a bulk property and originates from the whole excitation volume (which extends up to the depths of *~0,7 μm* below the sample surface when using the PL laser emitting at λ_{EXC}=532 nm). In other samples, dislocation-induced attractive potential for minority carriers (see paragraph 3.3) increases the probability for light-generated electrons to reach the DN and to recombine there radiatively giving rise to the appearance of DRL bands or non-radiatively via deep levels, thus leading to the suppression of BB intensity. Absence of DRL bands in the PL spectrum of Gr-30 sample argues that no "classical" dislocations (with Burgers vector of **b**=1/2<110> type) exist at the bonding interface in this sample. As a result, lack of classical dislocations in Gr-30 sample means no attractive potential for electrons; hence, the non-radiative recombination rate on the deep states located at the DN would be low, whereas the BB luminescence occurring in the bulk – strong.

5.12. Summary for Chapter 5.

- Electrical properties of dislocation networks with different twist misorientation angles, produced by hydrophilic bonding method, have been studied by means of DLTS technique. The evolution of the characteristic DN-related traps with the increasing of α_{TW} angle was traced for the first time.

- It was found, that shallow levels are dominating in the DLTS spectra of Gr-1 and Gr-3 samples with small twist misorientation angles, whereas deep levels – in the spectra of Gr-6 and Gr-30 samples prepared with higher twist misorientation. However, SA-samples also revealed quite high concentration of the deep levels which seem to be related rather with the interstitial (and may be oxygen) complexes in the dislocation vicinity formed during BOX dissolution than directly with dislocations or products of their reactions. Obviously, the appearance of such deep levels is inseparably linked with the technological essence of the hydrophilic wafer bonding method. Comparison with the samples prepared by hydrophobic bonding method with the similar misorientation angles may help to clarify this question. Deep levels in LA-samples were supposed to be due to

the high structural disorder in these samples caused by strong twist misalignment, resulting in large bond distortions and coordination defects creation at the bonding interface.

- Detected shallow levels ST1 and ST3 in SA-samples are the levels participating in the D1 recombination process and the intensity of D1 band follows the magnitude of the corresponding DLTS peaks, reaching the maximum in Gr-3 sample. Thus, it may be supposed that ST1/ST3 traps are related with the shallow dislocation 1D bands or stacking fault shallow states. Obviously, higher measurement statistics on the different bonded samples with various DN structure involving MCTS measurements are needed to establish the shallow levels origin unambiguously.

- It was also concluded, that D1 luminescence band originates most probably from the intersection points (triple dislocation knots) along the 60° dislocations, while the network of screw dislocations and the four-fold knots seem to have no direct influence onto D1 luminescence. Higher D1 band in Gr-3 sample is related then with the higher density of 60° dislocations which are more frequently disturbed by the triple knots in this sample (but note – due to Coulomb repulsion not every knot will participate in the luminescence, so there is no linear dependence of D1 intensity on the triple knot density). Thus, for higher D1 luminescence both densities are important – the linear density of 60° dislocations and the number of disturbing points on them, i.e. – number of triple knots.

Nevertheless – the indirect influence of the screw dislocation network on D1 band intensity in Gr-3 sample is also possible: screw dislocation may supply additional carriers along their 1D bands for the radiative recombination at the points of intersection with 60° dislocations. Additional clarifications are needed to establish the real form of screw dislocations influence on the D1 luminescence.

- Critical twist angle α^*_{TW} dividing the "SA-sample" behavior (with dominating shallow levels and strong D1 band) from "LA-samples" behavior (dominating deep traps and weak or absent DRL) seems to be close to $3{,}5^0$-4^0 and is related with the transformation of the screw dislocation network to the network of interfacial-type dislocation. Obviously, the interaction of interfacial dislocations with 60° dislocations does not create deep E_{D1d} centers needed for D1 radiative recombination. Thus, the optimal twist misorientation angle of about $\sim 3^0$-$3{,}5^0$ for the maximal D1 luminescence could be suggested, whereas the optimal tilt angle needs further elaboration. Also, passivation treatments for suppression the non-radiative recombination channels should be applied for further increasing of D1 intensity.

Chapter 6
Capacitance-voltage and current-voltage characteristics of Gr-1 and Gr-3 samples

For complete description of the energy-band structure and electrical properties of such a complicated structure as Schottky diode with the DN located inside its space charge region, it is necessary to consider the samples capacitance-voltage (CV) and current-voltage (IV) characteristics with care. They can provide the primary information about the doping (acceptor) profiles N_a that was already used to calculate the trap density from DLTS data in previous chapter as well as the evidences concerning DN-charge and its variations with measurement conditions (such as temperature and traps occupation). Moreover, since such kind of structure – Schottky diode with the DN located close enough to its front surface – is accounted as the most perspective one for the future applications in microelectronics (see paragraph 4.2), all information about the influence of the DN-charge on the current- and capacitance-voltage properties, on the profile of the electrostatic potential is of a great importance. As the samples Gr-1 and Gr-3 revealed the strongest D1 luminescence line, the main attention will be focused on these two samples.

Thus, in this Chapter the results of capacitance-voltage and current-voltage measurements are presented and discussed, with the main efforts devoted to the definition of charge state of the observed DLTS traps (donors/acceptors), verification of the trap concentration derived from the DLTS method in the previous chapter and to the construction of the energy-band diagram appropriate for the description of the investigated samples.

6.1. Interface charge definition from the CV measurements.

Traps concentration derived from the magnitudes of the DLTS peaks by using Eq. 5.15 could be understated. The reasons for that could be different: barrier along the DN preventing the holes capture, broadened and overlapped DLTS peaks or some other reasons, for example – the lateral holes diffusion along the DN without thermoemission into the valence band like this was observed in case of thin quantum wells [Schmalz 1996]. However, there is a way to confirm/disprove the results obtained from DLTS by performing a set of CV (and IV) measurements at different temperatures varying the initial traps occupation condition.

- Measurement temperature 300K

Figure 6.1 illustrates the CV curves for the bonded Gr-1 and Gr-3 samples, which were measured at temperature of 300K. Capacitance of the Gr-3 sample appeared to be somewhat higher than the capacitance of Gr-1 sample, especially at small reverse bias voltages $U_r < 3\ V$. Rapid decrease of the capacitance just after application of the forward bias voltage corresponds to the appearing of high forward current through the diodes resulting in the wrong measurement of the capacitance.

$1/C^2$ curves for Gr-1 and Gr-3 sample, as derived from the capacitance-voltage plots depicted in the upper plot Fig. 6.1, are going nearly parallel with the voltage shift of $\Delta U \sim 0{,}22\ V$ between them, see the lower plot in Fig. 6.1. Whereas $1/C^2$ curve of Gr-3 sample is going rather straight at reverse bias voltages above $0{,}1\ V$, the corresponding curve of Gr-1 sample revealed a particular bending-down of the $1/C^2$ curve for the reverse biases lower than $\sim 0{,}5\ V$. Usually, such bending-down of $1/C^2$ curve indicates a decrease of acceptor concentration in the near surface region.

CV curves measured at 300K revealed no details or features which could be related with the presence of DN (capacitance steps or kinks) since under reverse biasing at room temperature all traps in the lower part of band gap are empty due to high rate of carriers thermoemission. Whereas with the decreasing of the measurement temperatures T_{MEAS} DN-related traps would become frozen out, i.e. filled with holes.

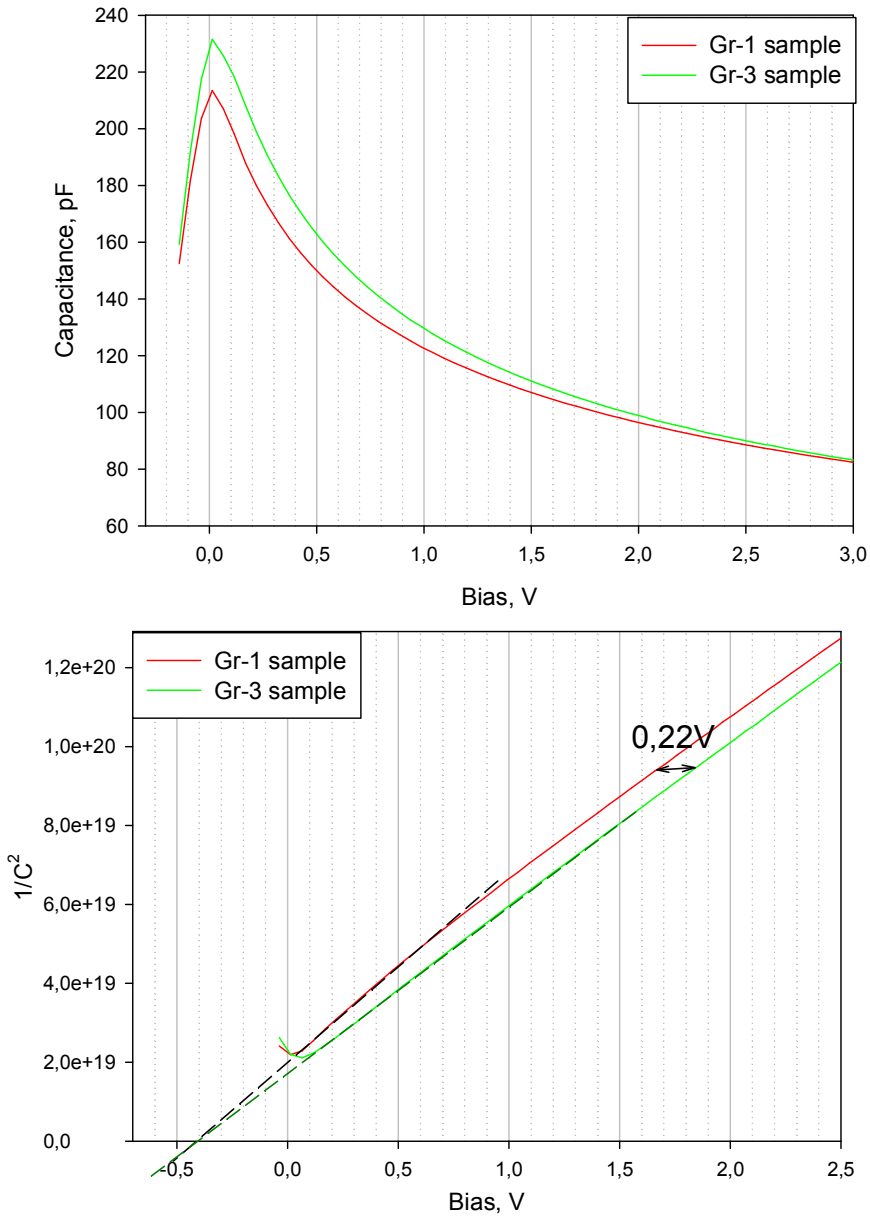

Figure 6.1. CV (upper plot) and $1/C^2$ (lower plot) curves of Gr-1 and Gr-3 samples measured at temperature 300K. Line assignments are shown in legends.

- Measurement temperature 80K

After cooling the sample from 300K to 80K under high reverse bias (U_r=*20V* in our case), all of the deep traps are empty (empty deep traps condition). As the holes emission rate from the deep traps responsible for DLTS peaks above 100K is very low at 80K, the holes would not leave these traps after their filling at sufficient forward bias voltages even after repeated application of high reverse bias at 80K. All the subsequent CV curves measured at 80K afterwards, correspond then to the situation when the deep traps are filled with holes (filled deep traps condition), while the shallower traps ST1 and ST3 remain

empty at T_{MEAS}=80K under application of reverse bias voltages. Results of such measurements are presented in Fig. 6.2 and 6.3.

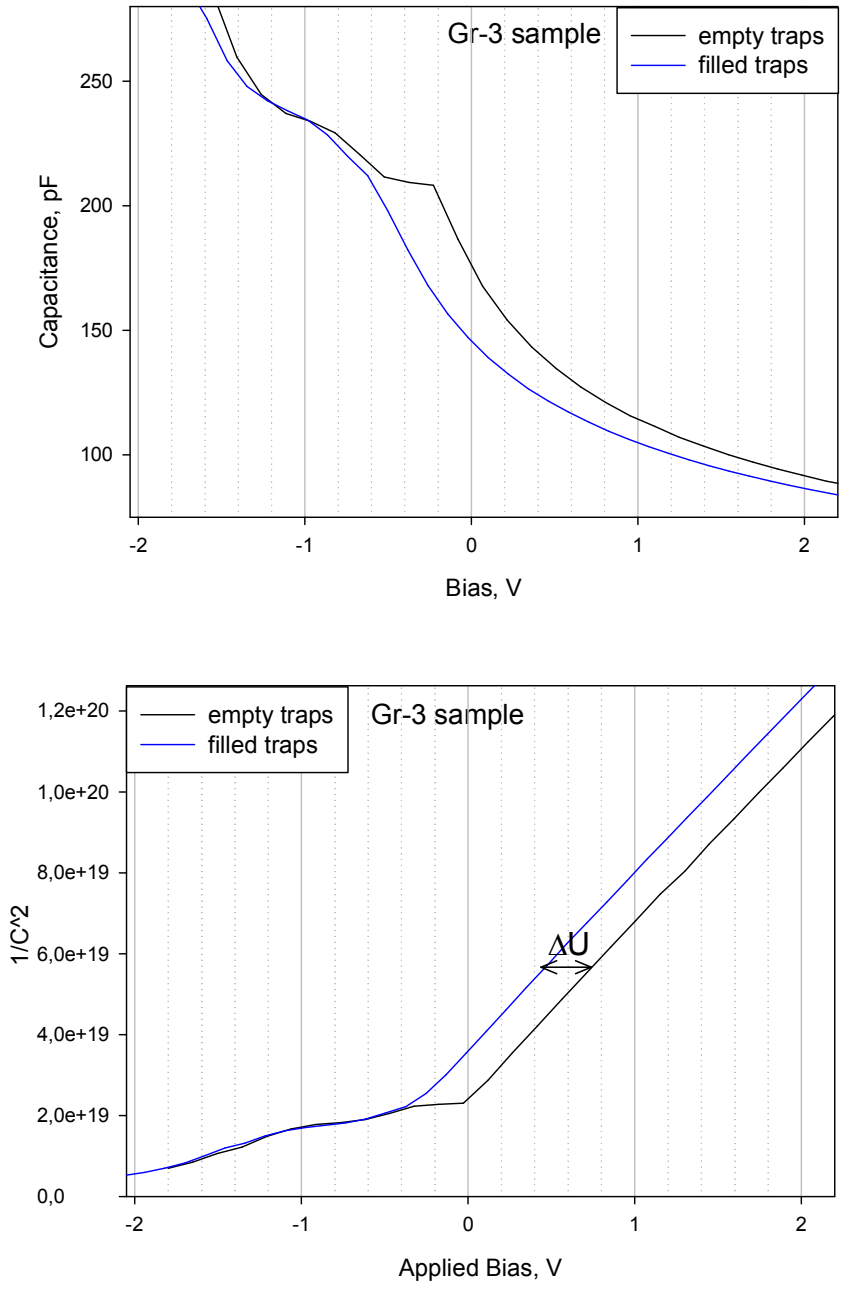

Figure 6.2. CV and $1/C^2$ curves of Gr-3 sample measured at 80K after cooling with a high reverse bias i.e. with empty traps and afterwards, then the traps become filled.

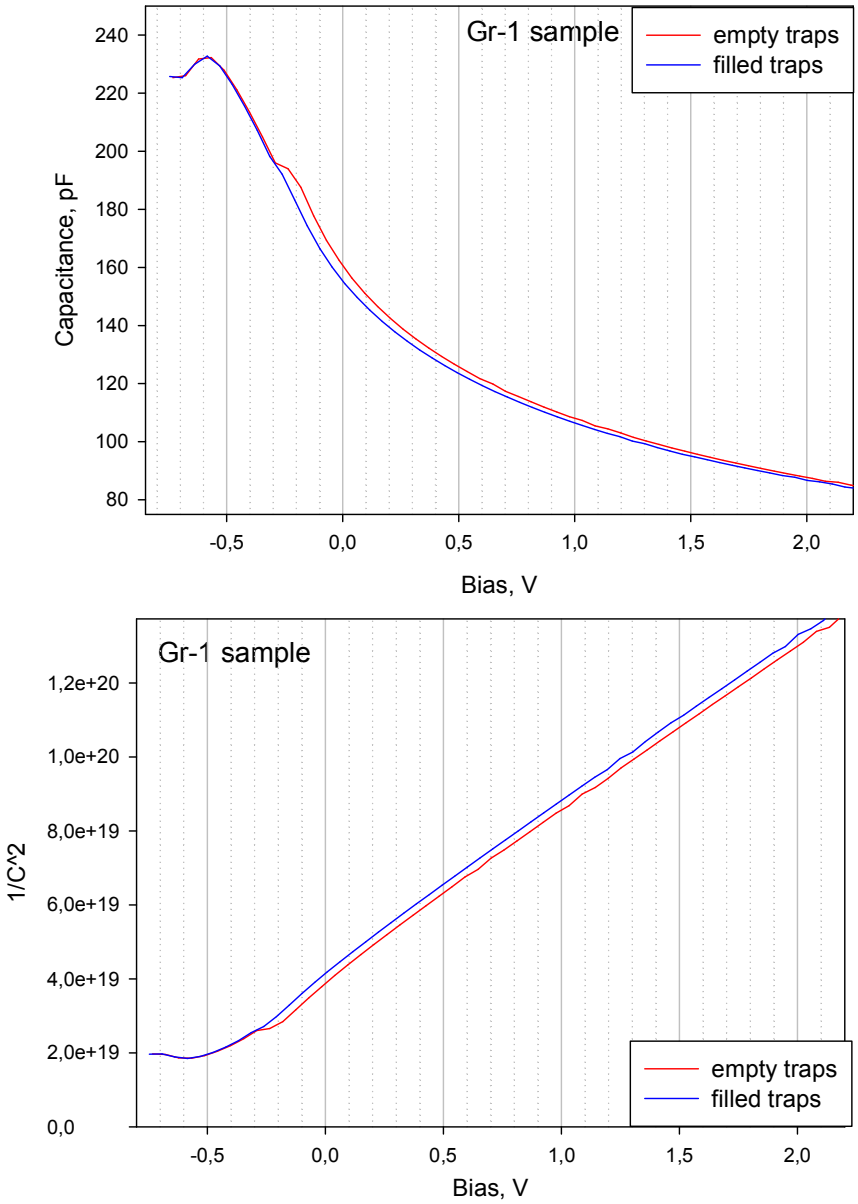

Figure 6.3. CV and $1/C^2$ curves of Gr-1 sample measured at 80K after cooling with a high reverse bias when the deep traps were empty and afterwards, then the traps became filled. Note the much smaller capacitance increase and the shorter length of the capacitance step in comparison with those in Gr-3 sample.

A clear difference between CV curves of Gr-3 sample measured at 80K with the deep traps being filled and empty can be seen in Fig. 6.2. First CV curve corresponding to the case of empty deep traps revealed higher capacitances as compared with the CV curve measured afterwards when the deep traps were filled. $1/C^2$ curves corresponding to these two CV curves are going parallel with the voltage shift of $\Delta U \sim 0,25V$ between them (Fig. 6.2, down). Additionally, a capacitance step appeared in the range of forward bias voltages

of *-0,1...-0,6 V*, which is absent on the CV curve measured with filled deep traps. At the forward biases higher than *-0,6 V* capacitances of both CV curves for the cases of empty and of filled deep traps become nearly equal, showing a second capacitance step at *-0,9...-1,3 V* followed by the rapid capacitance growth.

Similar features were observed for Gr-1 sample as well. Namely – slightly higher capacitance and the appearance of the small capacitance kink at *-0,3 V* in case of biased cooling, see Fig. 6.3. After this kink, at higher forward voltages, CV curves in Fig. 6.3 coincide, reaching the second capacitance kink at *-0,6 V*. The voltage shift between the $1/C^2$ curves (which are also going parallel) is only $\Delta U \sim 0{,}1$ *V*. Weaker effects as compared with Gr-3 sample should be related with the smaller traps concentration in Gr-1 sample.

Thus, the obtained results suggest, that the first capacitance step/kink appearing on the CV curves corresponding to the case of empty deep traps in the range of forward bias voltages of *-0,1...-0,6 V* for Gr-3 sample and *-0,3V* for Gr-1, respectively, reflects the pinning of the Fermi level with DN-related deep states during the process of the majority carriers capturing by these deep traps. As for the second capacitance step at *-0,9...-1,3 V* for Gr-3 sample and *-0,6 V* for Gr-1 sample which are visible at both CV curves (with empty and with filled deep traps) – probably it corresponds to the situation, when the potential barrier along DN determines the SCR width (rather than a distribution of shallow acceptors), see details in paragraph 6.3.

Higher capacitance values in case of empty traps indeed should be expected as the result of an increase of effective diffusion voltage that can be quantified with the help of Eq. 5.5

$$C = \frac{\varepsilon A}{w} = A\sqrt{\frac{e\varepsilon N_A}{2V + 2Q_s x_d/\varepsilon}} \tag{6.1}$$

$$\frac{1}{C^2} = \frac{2}{Ae\varepsilon N_A}\left(V + (Q_{s0} + \Delta Q_s)x_d/\varepsilon\right) = \frac{2}{Ae\varepsilon N_A}\left(V + Q_{s0}x_d/\varepsilon + \Delta U\right) \tag{6.2}$$
$$\Delta U = \Delta Q_s x_d/\varepsilon$$

where Q_{s0} is the interface charge when the deep traps are empty and ΔQ_s is the increase of the interface charge due to filling of the deep traps. Thus $1/C^2$ curves should shift towards the lower voltages with the appearance of an additional DN charge ΔQ_s, as this happens for the case of the CV curves measured at 80K from forward to reverse biases. Note that this does not provide any information about the ground state of the deep traps, i.e. whether they are donors or acceptors.

The concentrations of all deep traps N_{deep} can be calculated from the voltage shift ΔU between the corresponding $1/C^2$ curves measured with empty and filled traps as

$$N_{deep} = \frac{\Delta U \varepsilon}{e x_d}. \tag{6.3}$$

Table 6.1. Comparison of the trap concentrations derived from the voltage shift between the $1/C^2$ curves corresponding to the empty and filled traps (Eq. 6.3, deep traps) and from the voltage increment corresponding to the capacitance step location (Eq. 6.4, shallow traps) with the respective concentrations obtained from the DLTS spectra measured with the filling pulse voltage U_p=*-1,0V* (see Table 5.1).

		ΔU	N_s * 10^{11} cm^{-2}, CV data	Σ N_s * 10^{11} cm^{-2}, DLTS data
Deep traps (from Eq. 6.3)	Gr-1, 80K	0,1 *V*	0,4	0,37
	Gr-3, 80K	0,25 *V*	1	0,9...1
Shallow traps (from Eq. 6.4)	Gr-1, 40K	0,55 *V* *C=220 pF*	0,55	0,45
	Gr-3, 40K	0,85 *V* *C=260 pF*	1	0,8

The values of the voltage shift ΔU used for the calculations together with the direct results of calculations are presented in the Table 6.1, where the values of the traps concentrations derived from the magnitudes of corresponding DLTS peaks (Fig. 5.1 and Table 5.1) are also shown for comparison. A good correlation between the deep trap concentrations derived by two different ways was found.

- Measurement temperature 40K

Similar set of experiments with biased cooling could not be performed to define the density of the shallow traps ST1 and ST3 since even at the measurement temperatures of 35-40K the hole emission rate exceeds well the rate window of CV measurement that is the inverse time of the CV curve acquisition. Further lowering of the temperature was impossible due to the freezing out of the main shallow boron acceptors.

CV curves of Gr-1 and Gr-3 samples measured at T_{MEAS}=40K revealed similar features, namely “double capacitance step” appearing in the particular region of the forward bias voltages and a strong capacitance growth following the capacitance step, see Fig. 6.4. Obviously, these steps should be related with the Fermi level pinning by the shallow states in Gr-1 and Gr-3 sample. Note, that trap density profiles for ST1 and ST3 traps revealed their maxima at *-0,6 V* and *-0,8 V*, respectively (see Fig. 5.3), thus showing a reasonable agreement with the voltages corresponding to the appearance of the capacitance step on the CV curves of Gr-1 and Gr-3 samples. This serves as a confirmation that these capacitance steps are due to the Fermi-level pinning during the capturing process onto the ST1 and ST3 shallow traps.

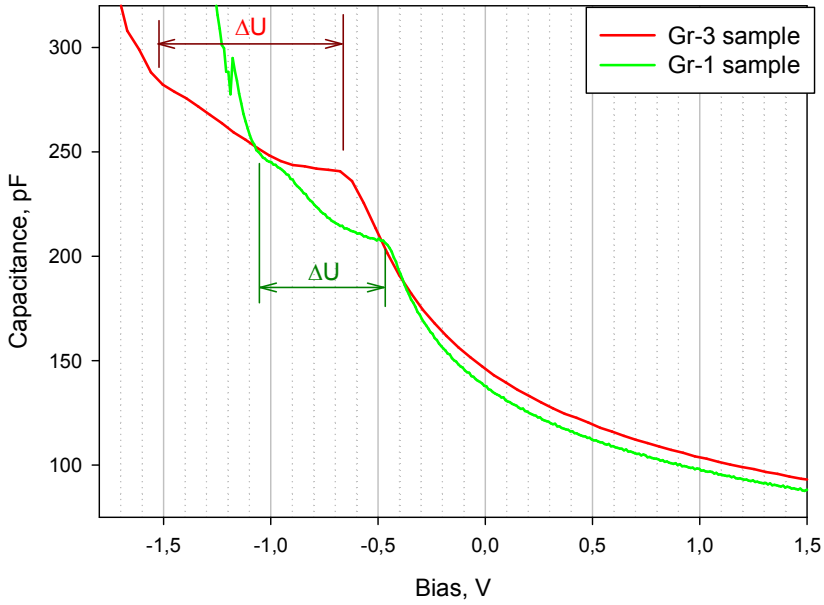

Figure 6.4. CV curves of Gr-1 and Gr-3 samples measured at temperature 40K.

In such a case, the two-dimensional concentration of the shallow states can be estimated from the voltage difference ΔU corresponding to the nearly constant capacitance region (Fig. 6.4) according to the relation proposed by [Kreher 1993] [Schmalz 1996]

$$N_{shallow} = \frac{C \cdot \Delta U}{eA} \tag{6.4}$$

where A is the diode area and C is the (averaged) value of the capacitance step. Equation 6.4 is based on the fact that when the SCR width is nearly constant, then the total charge changes are defined by the changes of the charge at the interface. Calculated in this way concentrations $N_{shallow}$ in Gr-1 and Gr-3 samples are also presented in Table 6.1.

Concentration of the shallow traps in derived from Eq. 6.4 appeared to be ~20% higher than that derived from DLTS. Probably, the shallow trap concentrations derived from DLTS are underestimated because of corresponding peaks broadening (Table 5.2), whereas the results obtained from CV curves are closer to the real values. On the other hand, this difference may partly reflect the concentration of the second shallow trap SN3 in Gr-3 sample, which becomes visible when measuring DLTS spectra with the higher filling pulse voltage U_p=*-1,5V*, see Fig. 5.4 (second shallower level was detected in Gr-1sample as well, see details in Chapter 7).

6.2. Peculiarities of Gr-1 & Gr-3 sample IV characteristics and their correlations with the CV curves.

Figure 6.5 represents the current-voltage characteristics of Gr-1, Gr-3 samples as well as of the reference sample without DN measured at 300K.

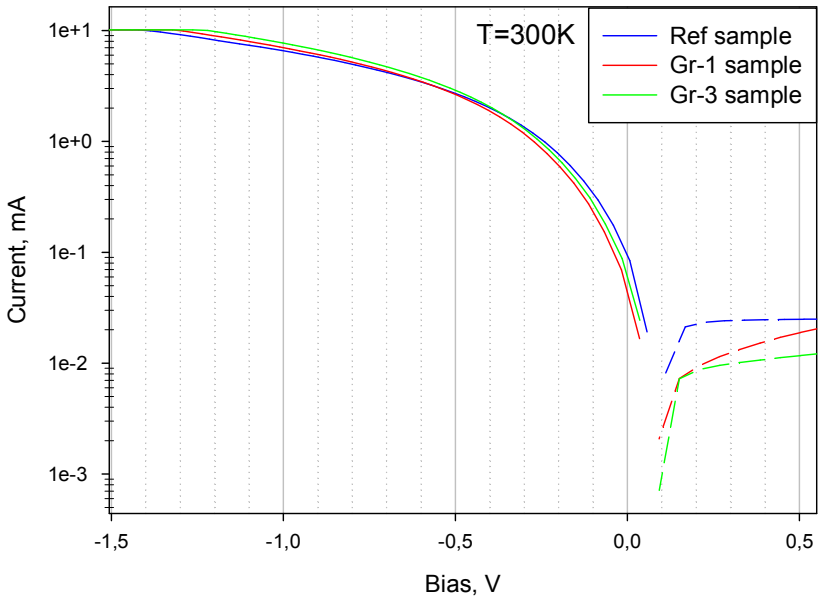

Figure 6.5. IV characteristics of Gr-1 and Gr-3 bonded samples and of the reference sample without DN, as measured at 300K.

All three samples revealed the similar IV curves irrespective of the presence and properties of DN: forward currents through the diodes appear at the same voltages of *~0V* and reach practically the same value at large forward voltages. Evidently, that at T_{MEAS}= *300K* DN has no significant effects on both IV and CV characteristics.

At lower temperatures of 80K and 40K the difference between the current-voltage characteristic of the bonded samples and of Ref one becomes clearly visible, see Fig. 6.6. Whereas the Schottky diode on the reference sample becomes open at the rather small forward bias voltage of 0...*-0,1 V* at both temperatures of *80K* and *40K* (i.e. at nearly the same voltages as at T_{MEAS}= 300K), a significant shift of IV curves toward the larger voltages which depends much on measurement temperature and DN structure was revealed for both bonded samples. For Gr-1 sample the current starts to be detectable at forward bias voltages $\geq$*-0,2V* at T_{MEAS}= *80K* and $\geq$*-0,6V* at T_{MEAS}= *40K* while for Gr-3 sample with a higher DN-related traps density the correspondent values are *-0,4V* at T_{MEAS}= *80K* and *-0,9V* at T_{MEAS}= *40K*.

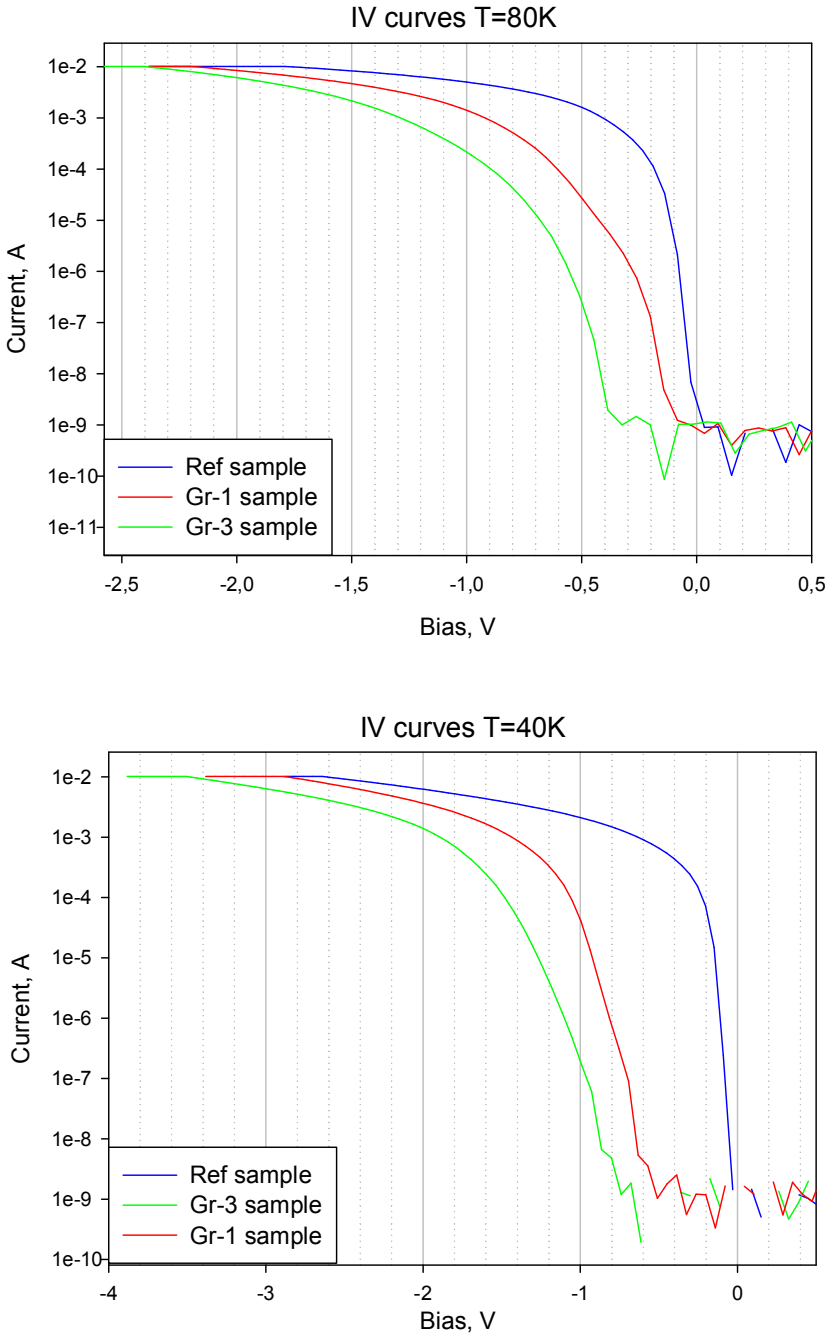

Figure 6.6. IV characteristics of Gr-1 and Gr-3 bonded samples and of the reference one, measured at T_{MEAS}= *80 K* (upper plot) and T_{MEAS}= *40 K* (lower plot).

- Comparisons of CV and IV characteristics of Gr-1 and Gr-3 samples measured at 40K.

Figure 6.7 shows the direct comparison of the CV curves of Gr-1 and Gr-3 samples measured at 40K with the IV curves measured at the same temperature. According to our experimental observations, reliable capacitance values on our Boonton capacitance meter could be measured up to the forward current values of *~0,1 mA* that corresponds in Fig. 6.7 to the forward bias voltage ranges up to *-1,5 V* for Gr-3 sample and up to *-1,1 V* for Gr-1 (thus enabling the correct determination of the SCR depths corresponding to the half-widths of the trap profile peaks depicted in Fig. 5.3 of Chapter 5). Whereas the subsequent capacitance growth at higher forward biases (U_f>*-1,5 V* for Gr-3 and U_f>*-1,1 V* for Gr-1) is related with the incorrect functioning of capacitance meter when the high current is flowing through the diode.

Capacitance steps visible on the CV curves of Gr-1 and Gr-3 samples at 40K occur when no (measurable) current is flowing through the diode (1st step) and when the current has already appeared but still not reached the critical value (2nd step), so they indeed should be considered as being related with the peculiarities of samples electrical structure and not with the artefacts of the measurements, justifying the application of Eq. 6.4 for $N_{shallow}$ calculations.

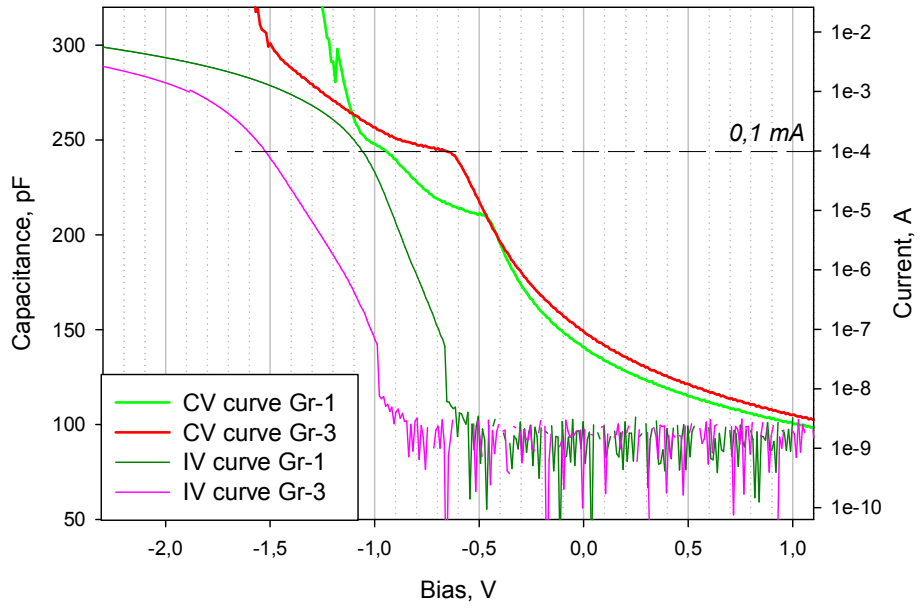

Figure 6.7. CV and IV curves of Gr-1 and Gr-3 sample measured at 40K as represented on the one plot. Steps on the CV curves correspond to those parts of the IV curves where the forward current is absent or where it starts to grow but still doesn't reach the steady value of *~0,1mA*.

Thus, considering the "double capacitance step" on the CV curves of both SA-samples, it is reasonably to suppose that the second step (see Fig. 6.7) is caused by the pinning of Fermi level by the second shallow states like SN3 in Gr-3 sample visible in Fig. 5.4 (and SN1 traps in Gr-1 sample, see Chapter 7 for details). This version correlates with the supposition made in the previous paragraph that the higher $N_{shallow}$ concentration derived from CV measurements (as compared with $N_{shallow}$ derived from DLTS spectrum) is probably due to the participation of the second (shallowest) levels. Another reason of the appearance of particular "kink" between the 1st and the 2nd step might be the bending of the quasi-Fermi level at the DN defect states position – see the theoretical works of G. Pike [Pike 1979] and [Pike 1984].

6.3. Energy-band diagram for Gr-1 and Gr-3 samples.

Evidently, that such an effect of the forward current appearance at considerably higher forward bias voltages as compare with the reference diode (retardation of the diode opening in case of bonded samples) means the presence of an additional potential barrier due to non-compensated positive charge in the near surface region of the bonded samples, which limits the forward current through the diode. The amount of this positive charge depends strongly on the measurement temperature – being at T_{MEAS}= *40K* higher than at *80K*, and on the DN structure (trap density) – being higher in Gr-3 sample than in Gr-1.

Figure 6.8a shows the band diagram of the bonded sample with the DN inside the SCR at zero reverse bias and at temperature 80K. As it was pointed out previously, at temperature of 80K all traps giving rise to the set of overlapped DLTS peaks appearing at 100-250K are frozen out, thus giving rise to the increasing of DN charge as it is evident from the decreasing of sample capacitance (CV curves corresponding to the filled deep traps in Fig. 6.2-6.3). Consequently, the process of the freezing out of deep states should lead to the appearance of the non-compensated positive charge at the DN and to the potential barrier along the DN φ_{DN}, thus making the total height of potential barrier φ_S at the metal / semiconductor interface in bonded samples higher, than the corresponding Schottky diode barrier φ_b in the Ref sample without DN, where it is defined simply by Eq. 1.1 (at zero applied bias).

At all reverse biases as well as at zero bias potential barrier φ_S is higher than the barrier along the DN φ_{DN} – this situation is shown in Fig. 6.8a. With the increasing of the forward bias voltage, barrier φ_S at the metal / semiconductor interface decreases and becomes lower than the DN barrier φ_{DN}, as it is depicted in Fig. 6.8b.

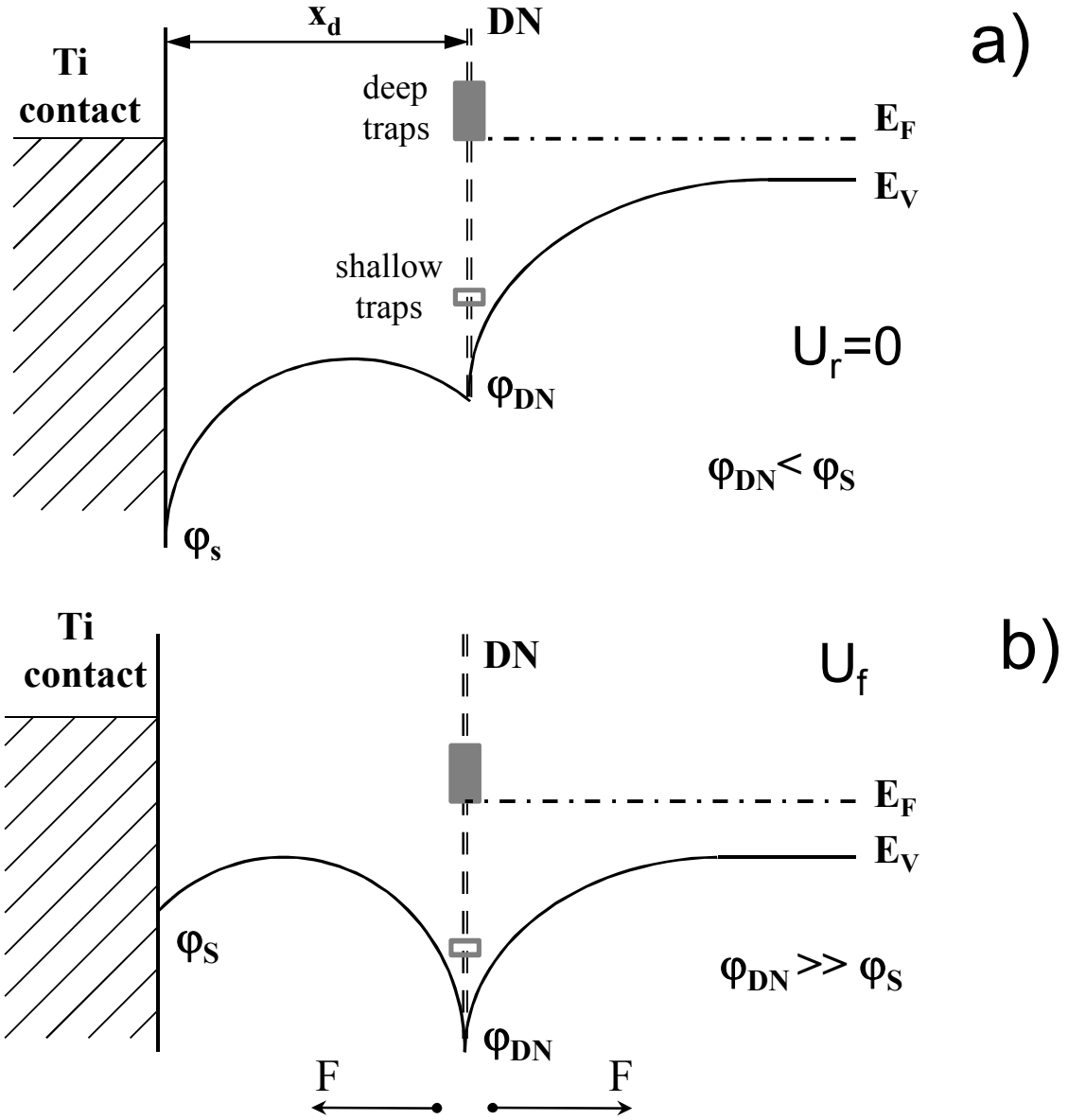

Figure 6.8. Band diagrams of the p-type Schottky diode with the DN lying inside the SCR at the distance of x_d from the surface (a) at *0V* or at small reverse bias, (b) at forward forward bias voltage (less than crytical voltage U_f corresponding to the appearance of the direct current through the diode). In the last case the inversion of the electrical field direction *F* in the layer between the sample front surface and DN is expected.

Hence, the current flow in the interval of forward bias voltages from ~0V and till approximately the forward voltage U_f – which corresponds to the appearance of the forward current (at T_{MEAS}=80K $U_f \approx$ -0,2V and $U_f \approx$ -0,45V for Gr-1 and Gr-3 sample, respectively – see Fig. 6.6), is defined just by the DN-barrier barrier φ_{DN}. Moreover, the inversion of the electric field is expected in the situation depicted in Fig. 6.8b (when

$\varphi_S < \varphi_{DN}$) in the near surface region between the sample front surface and DN. The effect of electrical field inversion was indeed observed experimentally by measuring the CV and IV curves under illumination at T_{MEAS}=80K [Bondarenko 2009] [Trushin 2011a].

As long as the DN barrier φ_{DN} is high – no current will flow through the diode. With the increasing of the forward applied bias, the barrier for holes diffusing from the bulk of semiconductor towards the metal contact will decrease leading to the correspondent increase of the direct current through the diode. Finally, at higher forward biases, the barrier φ_{DN} will disappear completely and the forward current will be defined by the resistance of the back ohmic contact. Obviously, the higher traps density in Gr-3 sample produces higher DN barrier φ_{DN} than in Gr-1 sample and the higher forward bias voltage is needed to overcome this barrier, as it is clearly visible by comparison of the IV curves of Gr-1 and Gr-3 samples shown in Fig. 6.6.

At lower temperature of 40K shallow states are not frozen out completely (just as it was discussed previously in paragraph 6.1), but when the corresponding forward bias is applied, they could be filled with holes, giving rise to a strong pinning of Fermi level at the defect states which is observed as long capacitance step on the CV curves measured at 40K, see Fig. 6.4.

It is also interesting to note, that the IV characteristics of Gr-30 samples (but not of Gr-6 one) appeared to be similar like those of the Ref sample both at T_{MEAS}= *80K* and at *40K*, thus confirming the lack of the positive charge at the DN in this sample, hence – the attractive potential for electrons as well, just as it was supposed in the paragraph 5.11.

6.4. Calculations of the electric current.

Let's now consider the currents flowing through such structure consisting of two potential barriers, one due to Schottky diode and another one – due to charged DN located inside the depletion region of Schottky diode, in more details. Using the thermionic emission theory, the current density through the DN interface can be expressed as [Pike 1979]

$$J_{DN} = A_1 e^{-\varphi_{DN}} (1 - e^{-U_1}), \tag{6.5}$$

whereas the current flowing through the metal / semiconductor interface is equal to (Eq. 1.11)

$$J_{diode} = A_2 e^{-\varphi_s} (e^{U_2} - 1) = A_2 e^{-\varphi_s} (e^{U - U_1} - 1), \tag{6.6}$$

where

$$U = U_1 + U_2 . \tag{6.7}$$

Here U means the total voltage applied to the whole structure, U_1 and U_2 – portions of applied voltage which drop on the bonded interface and on the metal / semiconductor interface, respectively; A_1 and A_2 – constants, accounting the Richardson constant, temperature and the effective areas of the DN-interface and of the Schottky contact; potential barriers φ_S and φ_{DN} (see Fig. 6.8) are expressed in the kT units. From the condition of the generality (equality) of the currents flowing through the DN- and metal / semiconductor interfaces, the following expression for the determination of U_1 voltage can be written

$$e^{-\varphi_{DN}}(1-e^{-U_1}) = \frac{A_2}{A_1} e^{-\varphi_s}(e^{U-U_1}-1), \tag{6.8}$$

and

$$e^{-U_1} = \frac{\frac{A_2}{A_1} e^{-\varphi_s+\varphi_{DN}} + 1}{\frac{A_2}{A_1} e^{-\varphi_s+\varphi_{DN}+U} + 1}. \tag{6.9}$$

Then, the resulting current through the structure will be equal to

$$J_{diode} = A_2 e^{-\varphi_s}\left(\frac{A_2/A_1\, e^{-\varphi_s+\varphi_{DN}+U} + e^{U}}{A_2/A_1\, e^{-\varphi_s+\varphi_{DN}+U} + 1} - 1\right). \tag{6.10}$$

Here the ratios A_2/A_1 reflect only the difference in the effective areas of the DN-interface and of the Schottky contact. As a result, this will lead to the increasing of the effective barrier height by $kT\ln(A_2/A_1)$, giving rise to the small shift of the IV curve as a whole.

From Eq. 6.10 it could be easily shown now, that at small forward biases, when $-\varphi_s + \varphi_{DN} + U_f < 0$ (i.e. when $\varphi_{DN} < \varphi_s - U_f$, case of Fig. 6.8a), the current through the whole structure

$$J = A_2 e^{-\varphi_s + U_f} \tag{6.11}$$

is described by the simple expression for the forward-biased Schottky diode (see Eq. 1.11 and 1.12 and corresponding comments). Whereas at higher forward biases ($-\varphi_s + \varphi_{DN} + U_f > 0$, i.e. $\varphi_{DN} > \varphi_s - U_f$ case of Fig. 6.8b), the current through the structure is limited by the DN barrier height φ_{DN} according to

$$J = A_1 e^{-\varphi_{DN}}. \tag{6.12}$$

Generally speaking, knowing the dependence of φ_{DN} on applied bias, it would be possible to get the full equation describing the current flowing in the investigated structure consisting of two potential barriers. Further details on this respect will be considered in paragraph 6.5.

6.5. Estimations of the trap concentrations from the IV characteristics.

- Ideality factor.

So-called ideality factor of the Schottky diode or simply 'factor *n*' could help to determine the variations of the barrier height with the increasing of forward applied bias in the investigated samples with Schottky diode / dislocation network double barrier structure (Fig. 6.8). According to the theory of an ideal Schottky diodes [Sze 1981], the expression for the current density when the forward bias voltage is applied (when $U>3kT/e$) is looking like as (compare with Eq. 1.11 and 1.12)

$$J = A^* T^2 \exp\left(-\frac{e(\varphi_b - U)}{kT}\right), \tag{6.13}$$

where A^* is Richardson constant, φ_b is the barrier height and U – applied forward bias. It could be simplified to give the following expression

$$J \cong A^* \exp\left(\frac{eU}{nkT}\right), \tag{6.14}$$

where n – is the diode ideality factor, which is defined as

$$n \equiv \frac{e}{kT}\frac{\partial U}{\partial \ln J} = \frac{1}{1+\frac{\partial \varphi}{\partial U}+\frac{kT}{e}\frac{\partial \ln A^*}{\partial U}} \simeq \frac{1}{1+\frac{\partial \varphi}{\partial U}}. \tag{6.15}$$

For the measurements temperature of 40K the kT/e factor will be very small, hence the third term in the denominator could be neglected. Factor n for an ideal Schottky diode made on silicon wafer should be close to *1* [Sze 1981]. However, in practical situations (without special surface treatments), ideality factor could be somewhat larger. Usually, this is related with an inadvertent interface layer presented on the semiconductor surface (usually, a kind of oxide layer), which interface states could communicate with the metal and/or with the semiconductor (see the detailed analysis done by Fonash [Fonash 1983]). Nevertheless, Eq. 6.15 can satisfactorily describe the modifications of the barrier height with the applied forward bias.

Ideality factors of both bonded samples and of the reference one recalculated from the IV curves measured at 40K (Fig. 6.6) according to the Eq. 6.15 are shown in Fig. 6.9 together with the CV curves and resistance-voltage (R-V) dependences (calculated by differentiation of just the same IV curves) also fitted for the temperature of 40K. By the example of the Schottky diode on Ref sample, the typical dependence of n-factor on the applied bias could be considered. Under the reverse bias in the ideal case the reverse current doesn't depend on the applied reverse bias, hence the derivative $\partial U/\partial \ln J = 0$ (moreover, for the investigated samples the values of the reverse current at 40K are under the detection limit of the amperemeter used).

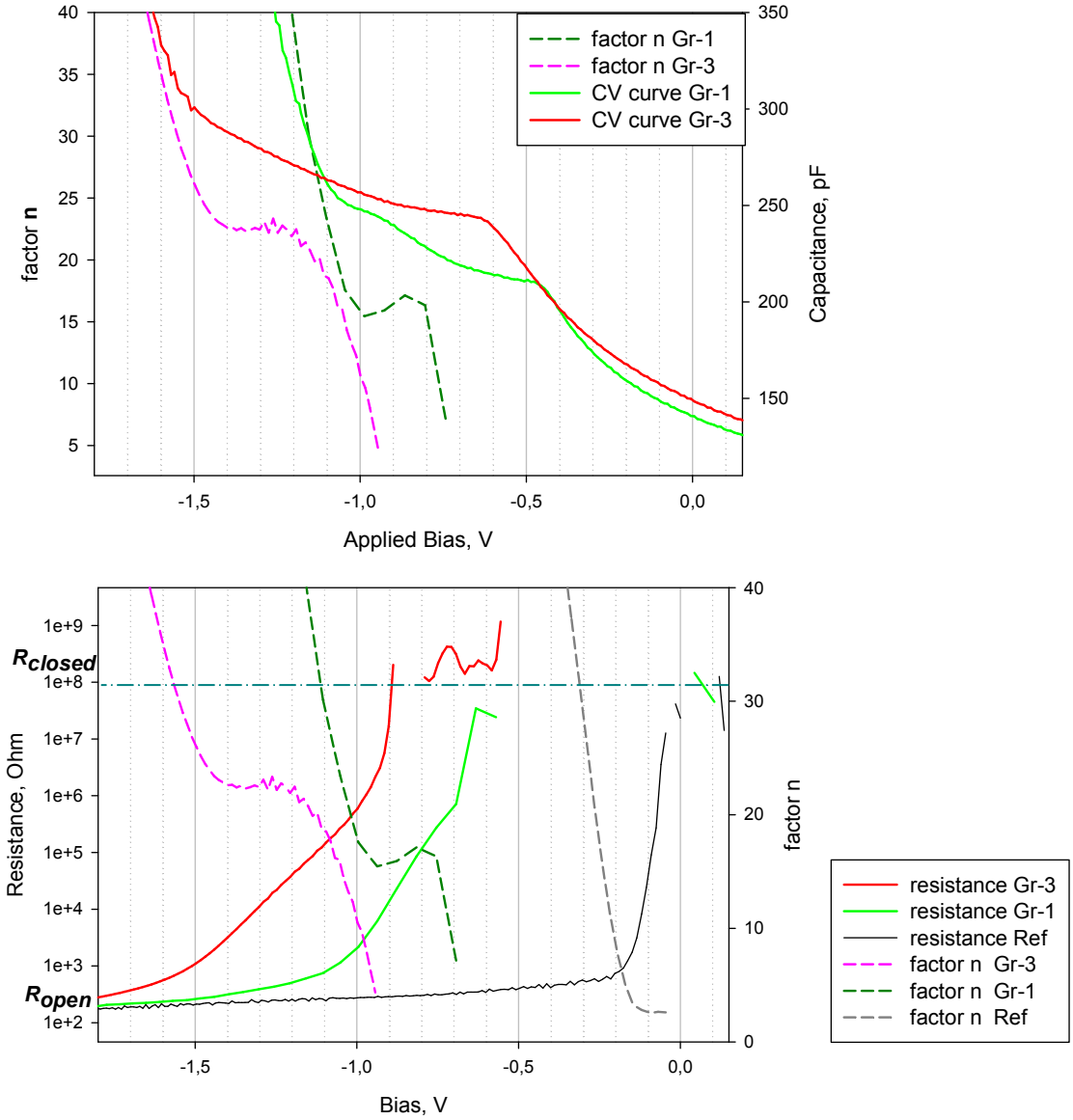

Figure 6.9. Upper plot - factor *n* of Gr-1 and Gr-3 samples as a function of applied bias, plotted together with the CV curves, lower plot – with the samples resistances *R=dU/dI*. All plots are related to the measurement temperature T_{MEAS}= 40K. In the lower plot the corresponding dependences for the Ref sample are also presented for comparison.

Short region of constant ideality factor appearing on the corresponding dependence for the Ref diode at the small forward bias voltages of *-0,05...-0,15 V* determines directly the value of the ideality factor as *n~2,5*. This value is rather typical for the Schottky diodes made on p-type Si wafers due to the higher concentration of interface states expected for p-type Si as compared with n-type Si wafers (whereas the Schottky diodes made on n-type Si wafers usually show the *n*-factor values closer to the theoretically predicted one [Fonash 1983]). Subsequent strong *n*-factor growth at the higher forward voltages U_f *>-0,15 V*

means that the forward current flowing through the diode is defined by the sample series resistance now (i.e., by the resistance of the back ohmic contact) – see the comparison of factor *n* and R-V dependences of the Ref sample shown in Fig. 6.9.

Both bonded samples revealed the similar character of factor *n* vs. applied bias dependences, which however appeared to be completely different from the *n*-factor dependence on the Ref sample. After the first rise of an ideality factor taking place at forward voltages of *-0,7 V...-0,75 V* for Gr-1 and of *-0,95 V...-1,2 V* for Gr-3 sample, the small maximum could be recognised on the respective curves at *-0,8 V* for Gr-1 and at *-1,25 V* for Gr-3 sample. Subsequent plateau-like region of the constant *n*-factor values correlates well with the appearance of the second half of "double capacitance step" on the CV curves of Gr-1 and Gr-3 samples and with the region of a "stretched" decreasing of samples resistance: note, that in case of bonded samples – as compared with the Ref one – considerably higher voltage increment is needed to reduce the sample resistance towards the value attributed to the open diode condition R_{open}. This should be attributed to the presence of DN and the potential barrier V_{DN} which determines the current through the structure (Fig. 6.8 and Eq. 6.12).

Following rapid *n*-factor growth at the forward bias voltages $U_f \geq$*-1 V* for Gr-1 sample and $U_f \geq$*-1,5 V* for Gr-3 one, similar to the case of the reference sample, means that the diodes on Gr-1 and Gr-3 samples are in the open state now, i.e. that the samples resistances have reached (or close to) their steady state values of the opened diode R_{open} and that the capacitance is measured improperly now – see the correlation of the strong capacitance growth after the second capacitance step with the rapid growth on the *n*-factor dependences in Fig. 6.9.

- calculations of shallow traps concentrations from ideality factor.

Considering Eq. 6.12 for the current flowing through the double-barrier structure at high enough forward biases ($\varphi_{DN} > \varphi_s - U_f$ case of Fig. 6.8b), the current derivative by the applied bias can be written as

$$\frac{dJ}{dU} = -A_1 e^{-V_{DN}} \frac{e}{kT}\frac{dV_{DN}}{dU} = \frac{eJ}{kT}\frac{dV_{DN}}{dU}$$
$$\frac{d\ln J}{dU} = \frac{e}{kT}\frac{dV_{DN}}{dU} \qquad (6.16)$$

Electrostatic potential V_{DN} at the position of DN can be received following Eq. 1.5 as

$$V_{DN} = \frac{eN_A}{2\varepsilon}(x_d - w)^2 \ , \qquad (6.17)$$

whereas the SCR depth *w* containing the DN with N_s shallow states at the depth x_d could be expressed as a function of applied bias *U* in the following way (see Eq. 5.5)

$$w(U) = \sqrt{\frac{2(\varepsilon U + V_b + eN_s x_d f)}{eN_A}} \ , \tag{6.18}$$

where f represents the Fermi function describing the filling process of the shallow states

$$f = \frac{1}{1 + \exp((V_{DN} - E_t + E_F)/kT)} \tag{6.19}$$

Built-in voltage V_b in the Eq.6.18 includes also the charge of the completely filled deep interface states $V_b = V_{b-Schottky} + eN_{deep}x_d$. Combining Eq. 6.17, 6.18 and 6.19, the derivative of the potential V_{DN} on the applied bias can be calculated as

$$\begin{aligned} &\frac{dV_{DN}}{dU} = \frac{eN_A}{\varepsilon}(w - x_d)\frac{dw}{du} = \\ &= \frac{eN_A}{\varepsilon}(1 - x_d / w)\frac{\varepsilon + eN_s x_d \, df/dU}{eN_A} = (1 - x_d / w)(1 + eN_s x_d \frac{df}{\varepsilon dU}) \end{aligned} \ . \tag{6.20}$$

By-turn, the derivative of the Fermi filling function f will be given by

$$\frac{df}{dU} = \frac{-e\exp(V_{DN} - E_t + E_F)}{kT\left(1 + \exp(V_{DN} - E_t + E_F)\right)^2}\frac{dV_{DN}}{dU} = \frac{-e}{kT}(1 - f)f\frac{dV_{DN}}{dU} \ . \tag{6.21}$$

This equation implies that the charge trapped on the shallow states can follow the increment of the applied bias dU. Substituting Eq. 6.21 into Eq. 6.20, the final expression for derivative of the potential V_{DN} can be written as

$$\frac{dV_{DN}}{dU} = \frac{1 - x_d / w}{1 + x_d \frac{e^2 N_s}{\varepsilon kT}(1 - f)f(1 - x_d / w)} \tag{6.22}$$

Thus, combining the Eq. 6.15, 6.16 and 6.22, the expression for ideality factor n will be given by

$$n = \frac{e}{kT}\left(\frac{d\ln J}{dU}\right)^{-1} = \left(\frac{dV_{DN}}{dU}\right)^{-1} = \frac{w}{w - x_d} + x_d \frac{e^2 N_s}{\varepsilon kT}(1 - f)f \ . \tag{6.23}$$

Since the first term in Eq. 6.23 is in order of unity, the dependence of the n-factor on the applied bias would be defined by the $(1–f)f$ term, which has a maximum when the filling level is $f=0,5$. Obviously, just this dependence of the ideality factor on the filling level f is responsible for the small maximum visible on the experimental factor n curves.

Density of shallow states can be estimated from the factor n value corresponding to the maximum position on the experimental curves Fig. 6.9 as

$$N_{shallow} = \frac{\varepsilon kT(n-1)}{e^2 x_d (1-f) f} = \frac{3,4*10^8}{0,256*(1-0,5)*0,5}(n-1) \simeq$$
$$\simeq 5\times 10^9 (n-1) \quad (cm^{-2}) \qquad (6.24)$$

For Gr-1 sample with $n=16$ Eq. 6.24 gives the concentration of shallow DN-related states as $N_{sh}(Gr\text{-}1) \approx 0,7*10^{11}$ cm^{-2}, whereas for Gr-3 sample with $n=24$ traps concentration is equal to $N_{sh}(Gr\text{-}3) \approx 1,15*10^{11}$ cm^{-2}. Obtained concentrations correlate rather well with those derived from DLTS and CV measurements (see Table 6.1), though being slightly larger. Probably, this discrepancy is due to some simplifications used while deducing the Eq. 6.24, such as the neglecting of Fermi level dependence on the applied bias in Eq. 6.19 (according to [Pike 1979], [Pike 1984] Fermi level at GB may increase slightly – in order of kT value – relative to the E_V band) and consideration of the first term in Eq. 6.23 simply as unity.

6.6. Acceptor profiles in the near surface region.

-acceptor profiles at 300K and 80K

Acceptor profiles in Gr-1 and Gr-3 samples as derived from the CV curves measured at 300K (Fig. 6.1) and at 80K from the second CV curves (filled deep traps Fig. 6.2 and 6.3) are presented in Fig. 6.10.

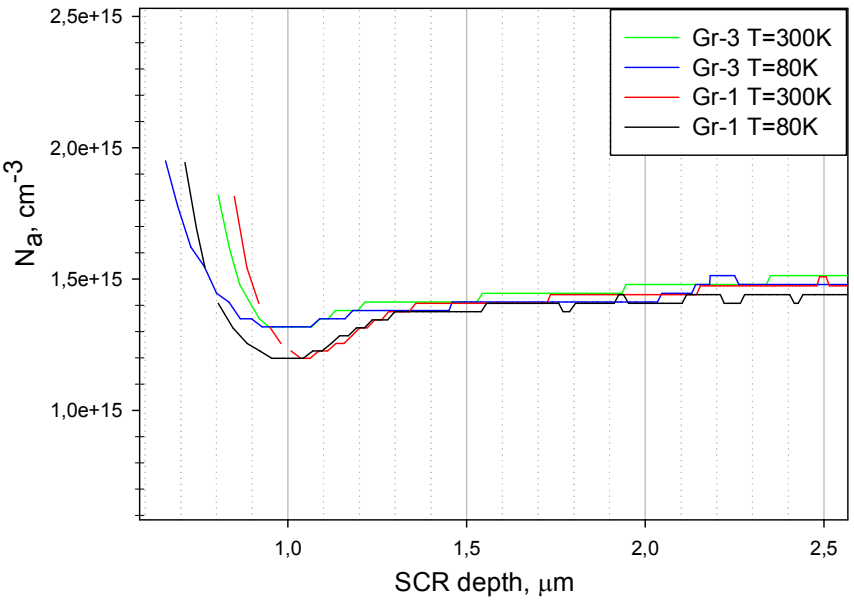

Figure 6.10. Acceptor profiles $N_A(w)$ in Gr-1 and Gr-3 sample as derived from the CV curves measured at 300K and 80K.

The question which should be answered now is whether this N_a lowering indeed due to doping inhomogeneities or due to the artificial effects similar to those observed on the dopant profiles of the samples with the thin quantum well lying parallel to the front surface. Namely, CV measurements performed on the samples containing a single quantum well (well thickness in the order of one Debye length) revealed an acceptor peak in the doping profile at the position of the well which is accompanied by depletion valleys at either side [Tittelbach-Helmrich 1993]. The bonded interface in the investigated samples is similar to thin quantum wells in the ability of charge accumulation, while it does not introduce a band offset. As the depth position of DN in the investigated samples is only $x_d=0,16\ \mu m$, there is no chance to see profile peak, but the observed lowering of the acceptor concentration could be considered as a depletion valley at the bulk side of DN.

It was shown in [Tittelbach-Helmrich 1993], that the temperature dependence of the dopant profiles could help to distinguish between the features in the *CV* doping profiles which are due to doping effects and those which are due to the band offset: the depletion valleys become more pronounced at lower temperatures, while the profile determined by the real lowering of the doping concentration should remain invariable. Comparison of apparent doping profiles of Gr-1 and Gr-3 samples as obtained from CV measurements at 300K and 80K (as also at lower temperature of 40K, as it will be shown later) revealed the invariability of acceptor lowering in the near surface region on the measurement temperature – see Fig. 6.10. Hence, indeed the acceptor lowering occurs in the near surface region of the investigated samples and this is not the artificial effect.

Chemical etching before the Schottky contacts preparation could not be the reason for such acceptor lowering because of two reasons: firstly, no etching solutions capable to introduce a noticeable amount of hydrogen ions H^+ into the near surface regions of the investigated samples were used (see details of contacts preparation in Chapter 4) and secondly, as the Schottky contacts for all bonded samples were prepared simultaneously applying the same chemical treatments, then the similar acceptor profiles in the both Gr-1 and Gr-3 samples would be expected. Hence, another mechanism of acceptor lowering should be proposed for Gr-1 and Gr-3 bonded samples.

Lowering of the acceptor concentration in these samples may be a result of the long-time annealing (BOX dissolution annealing 1200^0C for 2h), which could have led to the boron out-diffusion. On the other side, it was reported previously about the considerable increment of phosphorus [Dimitrakis 1997] and boron [Nagai 1992] concentration near the bonded interface in the n- and p-type Si bonded samples, respectively. Analogous process could have take place in the investigated samples as well. There is no the full clarity at the moment about the exact origin of this phenomena, obviously, additional measurements are needed to clarify this question.

-acceptor profiles at 40K

"Double step" structures on the CV curves of Gr-1 and Gr-3 samples measured at 40K (Fig. 6.4) led to the appearance of a "double peak" construction on the acceptor doping profiles, recalculated from these CV curves, see Fig. 6.11.

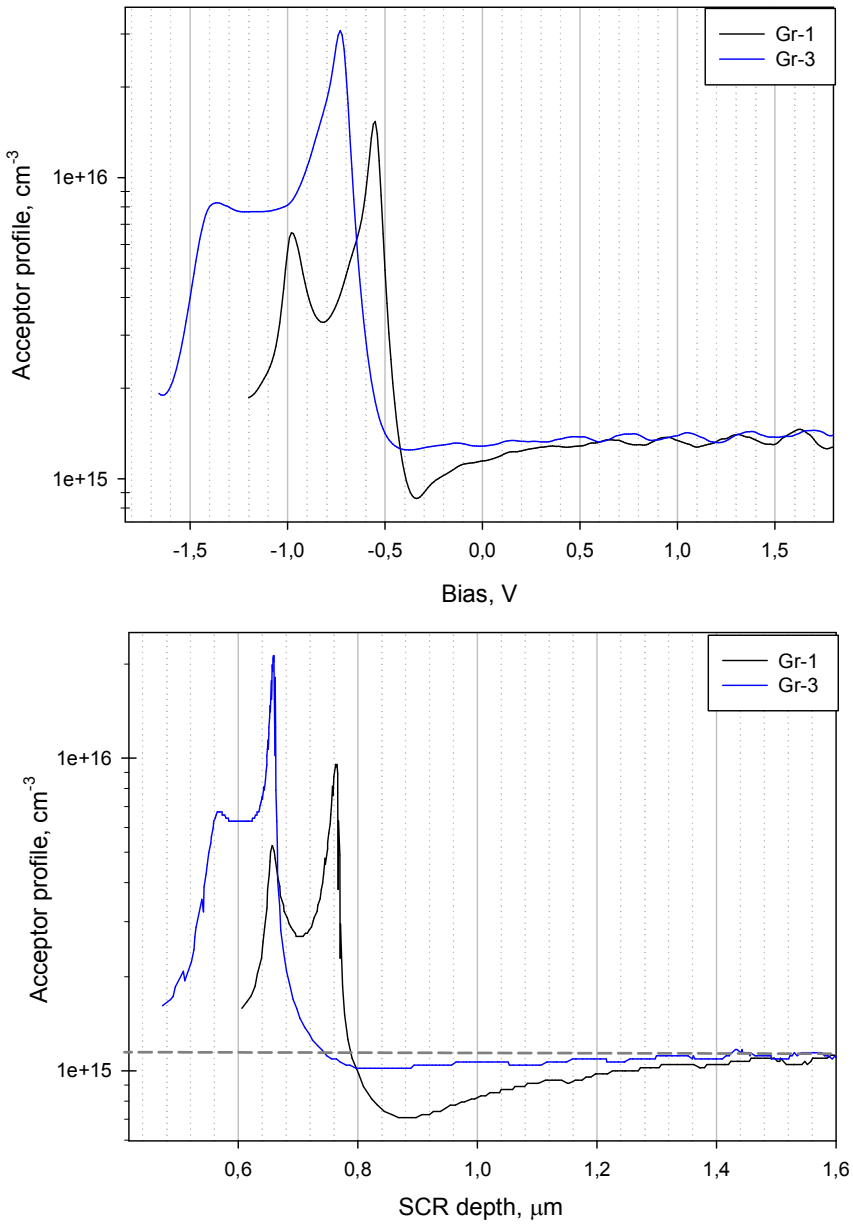

Figure 6.11. Acceptor profiles of Gr-1 and Gr-3 samples versus applied bias (upper plot) and SCR depth (lower plot) as derived from the CV curves measured at 40K.

However, it should be pointed out, that these peaks on the N_a profiles do not reflect the variation (i.e. increasing) in the distribution of the doping impurity, but simply correspond to the regions of the constant capacitance on the corresponding CV. Instead, these peaks

prohibit the determination of exact acceptor concentration close to the DN position, which is expected to be considerably lower than in the bulk – note the considerable N_a dip on the profile of Gr-1 sample around *0,9 μm* (on the other hand, if the boron atoms are indeed accumulated in the vicinity of the DN as it was suggested in paragraph 6.6, then the N_a profile close to the front sample surface could be significantly non-monotonic).

Since CV curves at 40K were recorded with the smallest possible voltage increment step of *10 mV* (in order to record the capacitance steps as precisely as possible), the dip on the N_a profile of Gr-1 sample at 40K appeared to be more pronounced – up to $\sim 0{,}7 * 10^{15}$ cm^{-3} at the SCR depths $<1{,}0$ *μm* – than it was observed at higher temperatures T_{MEAS}= 80K and 300K, as those CV curves were recorded with larger voltage increment step. Acceptor profile of the Gr-3 sample at 40K remains practically invariable, showing only the minor N_a decreasing around *~0,8-1 μm* relative to the bulk value.

In principle, as the depth position of the DN in the bonded samples is known, it is possible to calculate the DN barrier heights φ_{DN} at the moment of 1st and 2nd capacitance steps appearance, knowing the distance between the depth w corresponding to the position of N_a peaks in Fig. 6.11 (lower plot) and exact position of DN x_d as (see Eq. 1.18) [Schmalz 1994]

$$\lambda = w - x_d = \sqrt{\frac{2\varepsilon\varepsilon_0}{eN_a}\Delta E} \tag{6.25}$$

with the ΔE being equal to

$$\Delta E = V_{DN} + E_V - E_F \tag{6.26}$$

the sum of the potential V_{DN} and the Fermi level position inside the band gap in the neutral region outside the barrier $E_V - E_F$ (Fig. 6.8). However, as one can see, the results will depend strongly on the exact value of acceptor concentration N_a used for the calculations in Eq. 6.25, which for the depths of interest – less than *0,8 μm* – remains unknown.

However, by looking on to Eq. 6.25 it becomes qualitatively clear, that due to the considerable decreasing of the acceptor concentration in the near surface region of Gr-1 sample, the pinning of the Fermi level by the shallow states should occur at smaller forward biases in this sample (in spite the fact that ST1 traps are more shallow than ST3 traps in Gr-3), thus being in agreement with the measured CV curves.

6.7. Built-in voltages and DN charges in Gr-1 and Gr-3 samples at T_{MEAS}=300K.

Additional important information about the DN charges in Gr-1 and Gr-3 samples can be obtained from the comparison of the built-in voltages V_b in these samples (see Eq. 1.2 and description in paragraph 1.1).

Built-in voltage V_b can be derived as the extrapolated intersection with the bias axis of the corresponding $1/C^2$ curve, see Eq. 1.10. Generally speaking, there are two ways to derive the built-in voltage from the $1/C^2$ curves shown in Fig. 6.1: either by drawing a straight line up to the intersection with the bias axis along that part of $1/C^2$ curve falling at the range of the reverse bias voltages higher than *~0,7 V* – where the near surface decreasing of acceptor concentration has no sense yet, or instead – to draw a line just along that part of $1/C^2$ curve falling into the region of small close-to-zero reverse bias voltage and further onto the forward bias voltages range (just as it is shown by the thin dash lines in Fig. 6.1) where the decreasing of acceptor concentration occurs (especially in case of Gr-1 sample). Thus, two different sets of built-in voltages could be obtained – which will be notated as "small V_b" and "large V_b". The values of built-in voltages in Gr-1 and Gr-3 samples as obtained from the corresponding $1/C^2$ curves measured at 300K (Fig. 6.1) are collected in Table 6.2.

It appeared, that the "large V_b" value for Gr-1 sample is approximately *0,25 V* larger, than the "small V_b" value. Obviously, such a big difference is explained by the considerable lowering of acceptor concentration in the near surface region in this sample. According to Poisson equation, the total band bending voltage is given by (see Eq. 1.5)

$$U_R + V_b = \frac{w^2 e N_a}{2\varepsilon} \tag{6.27}$$

if there is no acceptor lowering in the near surface region and by

$$U_R + V_b = \frac{w^2 e N_a}{2\varepsilon} - \frac{x^2 e \Delta N_a}{2\varepsilon} \tag{6.28}$$

if the lowering of acceptor concentration in the near-surface region of the width x by the value ΔN is supposed (in the context of simple approximation of rectangle-like N_a profile). Looking on the N_a profiles shown in Fig. 6.10 and 6.11, for Gr-1 sample x and ΔN values could be estimated as $x=1,1\mu m$ and $\Delta N \sim 0,3*10^{15}\ cm^{-3}$, which will give (second term in the Eq. 6.28) the addition of *0,27 V* to the real built-in voltage V_b in Gr-1 sample, thus showing a good agreement with the corresponding V_b difference (note, that in the frame of rectangular model it is enough to consider the approximate value of ΔN_a lowering, whereas in Eq. 6.25 the exact concentration is needed in order to get the reliable ΔE values). In Gr-3 sample the difference between "small V_b" and "large V_b" values is considerably smaller (of only *0,05 V*), thus being in agreement with less prominent lowering of acceptor concentration in this sample, as it could be visible on the N_a profiles shown in Fig. 6.10 and 6.11.

Table 6.2. Built-in voltages V_b as derived from the CV characteristics (in form of $1/C^2$ curves) measured at 300K (values corresponding to the large V_b and small V_b are shown, see comments in the text).

	Gr-1 sample	Gr-3 sample
large V_b	0,65 *V*	0,45 *V*
small V_b	0,4 *V*	0,4 *V*

The same reason (considerable N_a lowering in Gr-1 sample and more uniform profile in Gr-3 sample) is responsible for the *~0,2 eV* difference between the "large V_b" values of Gr-1 and Gr-3 sample at T_{MEAS}= 300K (as also for the voltage shift between the $1/C^2$ curves of Gr-1 and Gr-3 samples – see the mark in Fig. 6.1). Whereas the "small V_b" values, which were determined from the pieces of $1/C^2$ curves corresponding to the region of N_a lowering, are equal in both samples at 300K. Hence, it could be concluded, that the DN charges in Gr-1 and in Gr-3 sample are the same at room temperature in spite of different traps concentrations in these samples.

An alternative concept – to explain the *ΔU~0,2 eV* difference between the "large" built-in voltages at T_{MEAS}= 300K (when the majority carrier traps are empty) by supposition of higher negative charge in Gr-3 sample (which would make the barrier height in Gr-3 sample lower than in Gr-1 sample) – demands, that the concentration of ionized negatively-charged acceptors in Gr-3 sample should be (see Eq. 6.3) by

$$N_s = \frac{\Delta U \varepsilon}{e x_d} \approx 1*10^{11} cm^{-2}$$

higher, than in Gr-1 sample. This is rather high concentration. Taking in mind that the total concentration of all traps detected by DLTS in Gr-3 samples is nearly *~1,7*10^{11} cm^{-2}*, while in Gr-1 sample – only *~0,8*10^{11} cm^{-2}* (see Table 5.1), this estimation requires, that all traps detected in Gr-1 and Gr-3 samples should be acceptors. This conclusion contradicts to the experimental results which will be discussed in the following paragraphs as well as to the results of the previous investigations [Kisielowski 1991]. Therefore, it should be admitted that this explanation is incorrect. Thus, it could be concluded that in Gr-1 and Gr-3 samples no acceptor states in the lower half of band gap (at least in the significant concentration) whose concentration would be scaled with DN density are presented.

6.8 Discussion on the charge state of the detected traps.

Now it is interesting to specify, in which part of band gap the positive DN charge is stored? Indeed, two different variants are possible, see the sketch in Fig. 6.12. It was revealed by MCTS measurements that in the investigated SA-samples the shallow level(s) near the edge of the conduction bands exists, making a pair for the shallow level located near the edge of the valence band [Isakov 2011]. Both of these levels are shown in the Fig. 6.12. Supposing ST1/ST3 peaks are due to shallow 1D dislocation-related bands, one can write (from the symmetry reason)

$$N_{shallow}(C-zone) \equiv N_{shallow}(V-zone), \tag{6.29}$$

i.e. their concentrations should be equal. Besides, the charge states of the shallow 1D bands located in the different parts of band gap should be opposite, also from the symmetrical reason. However, if the ST1/ST3 peaks are related with shallow stacking fault states (which do not have a twin-level near the edge of conduction band), when the concentration of the shallow levels located in the lower part of band gap should be higher. Though there is no clarity about the exact origin of ST1/ST3 peaks at the moment, this uncertainty will not influence much the following consideration.

Furthermore, some deep levels in the upper part of band gap could be also expected. Unfortunately, much less is known about their origin and concentration. However, it could be supposed that the equality similar to the Eq. 6.29 for the shallow traps absolutely not necessary has to be fulfilled for the deep levels as well, since the origin of the deep levels appearing in the upper and in the lower parts of band gap could be completely different (no symmetry reason in this case). Instead,

$$N_{deep}(C-zone) \neq N_{deep}(V-zone) \tag{6.30}$$

ought to be assumed. For instance, in plastically deformed samples a higher concentration of deep levels in the lower part of band gap was observed [Kisielowski 1991]. As for the charge states of the deep traps – they should not be obligatory of the different types in the upper and lower halves of band gap. The sets of the deep traps in the upper and lower parts of band gap are also shown in Fig. 6.12.

A question then arises – how to determine at which half of band gap which charge (positive/neutral, i.e. donors/acceptors) is stored?

Traps in the upper part of band gap remain filled at any temperature and at any applied bias, since it is not possible to change the occupancy of the minority carriers traps in the DLTS experiments (i.e. by applying the filling voltage pulses, see Chapter 1). In case of acceptor-like character, the charge of these traps will be zero, whereas in case of donor-like – traps will be positively charged. Both cases of donors and acceptors together with the particular charge carrying by a trap (positive, negative or neutral) are depicted in Fig. 6.10. Charge of the traps located in the lower half of band gap could be modified by temperature and by the applied forward bias.

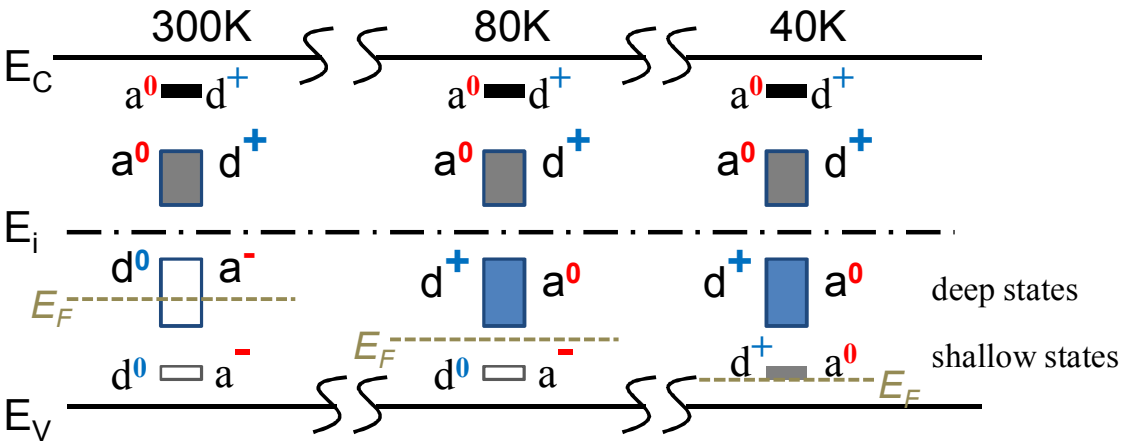

Figure 6.12. Sketch of the band diagram showing the pairs of shallow and deep sets of traps located in the opposite parts of band gap. Three different temperatures – 300K, 80K and 40K are considered. Charge states (donors – **d** and acceptors – **a**, with the sign +, – or 0 corresponding to the charge carrying by the trap), traps occupancy (empty rectangles mean empty traps, filled rectangles – occupied traps) and Fermi level positions are also indicated in the drawing.

So, at T_{MEAS}= 300K all traps located in the lower part of band gap should be empty due to high thermo-emission rate. This implies negative charge in case of acceptor like-traps and zero charge for donor-like traps (marked as $\mathbf{a}^-$ and $\mathbf{d}^0$ in Fig. 6.12, respectively). At T_{MEAS}= 80K after the freezing of all deep states out, their overall charge should change from negative to zero in case of acceptors, or from zero to positive in case of donors. Thus, in the former case the uncompensated positive charge will be carried by the donor-like traps in the upper half of band gap, whereas in the later – by the donors in the lower part. The similar changes are expected for the charges carried by the shallow traps at lower temperature of 40K when the forward bias voltage high enough to fill the traps is applied.

The key point for the following discussion – is the equal built-in voltage (hence - barrier heights) at room temperature in both Gr-1 and Gr-3 sample in spite of two times higher DN-traps concentration in Gr-3 sample, as it was established in paragraph 6.8. Secondly, the forward current through the Schottky diode on Gr-1 and Gr-3 samples – as also on the Ref one – at 300K appear just at the same voltage of ~0V, as it clearly visible in Fig. 6.5, thus testifying the absence of the non-compensated positive charge at the DN at room temperature. As a consequence, it should be concluded that at T_{MEAS} =300K the total charge at DN is zero in both bonded samples $\sum Q_{DN}(300K) = 0$. This automatically excludes the possibility that deep traps located in the opposite parts of band gap are of the same charge state.

The most probable suggestion then is that the acceptor-like traps are located in the upper part of band gap – thus being neutral at all temperatures, while donor-like traps are spaced in the lower part of band gap, being also neutral at 300K. This conclusion is in agreement with the observations made by Kisielowski and Weber [Ksielowski 1991], who also have ascribed the donor-characters to the dislocation-related deep traps detected in p-type Si plastically deformed samples (i.e. located in the lower part of band gap) and the acceptor-like behaviour to the traps detected in the n-type Si plastically deformed samples (i.e. in the upper part of band gap). Since the considerable correlation was revealed between the Arrhenius plots for the H.33 DLTS peak detected in the plastically deformed p-type sample in [Kisielowski 1991] and that for the DLTS peak appearing near 170K in the investigated Gr-1 and Gr-3 samples, the same charge state of these traps could be assumed as well.

Another possibility – that the acceptor-like traps locate in the lower part of band gap (negatively charged at 300K) and donor-like traps in the upper part of band gap (being positively charged at 300K) and their concentrations are exactly equal – seems to be less probable, since it was already discussed above that the equal concentrations in the opposite parts of band gap may be expected for the shallow 1D states but not for the deep states (Eq. 6.29 and 6.30).

However, supposing the equal concentration of the shallow traps in the different parts of band gap and their opposite charges – for the case of shallow 1D states (Eq. 6.29), it is not so easy to come to the certain conclusion about the exact charge state of the shallow traps in the upper and the lower parts of the band gap: uncompensated positive charge could be stored by donors in either band gap halves. According to some experimental evidences [Sauer 1986] [Steinman 2005], the D1 radiative transition occurs between donor-like and acceptor-like traps located in the opposite parts of band gap: considering the deep levels in the lower half of band gap as donors, it should be supposed in turn the acceptor-like behaviour for the shallow traps located in the upper half of band gap and vice versa. Summarising, donor-like character could be ascribed to the deep and shallow traps located in the lower half of band gap, whereas acceptor-like – to the traps in the upper part.

6.9. Summary for Chapter 6.

As a result of detailed examination of CV and IV characteristics of Gr-1 and Gr-3 bonded samples as also from the comparison with the data obtained for the reference sample, the following statements could be concluded:

- At low temperatures, when DN-related states become frozen out, the variations of DN charge render a particular influence on the shapes and behavior of corresponding CV and IV curves.
- Energy-band diagram and the model, comprising the combined influence of both Schottky diode and DN barriers on the current flowing through the double-barrier structure, capable to explain the observed features of IV curves (absence of the direct current up to the certain forward bias voltage) and CV characteristics (capacitance steps), were proposed.
- The concentrations of the DN-related defect states as obtained from the analysis of CV and IV curves (in form of factor-*n* dependences) were found to be in a good agreement with the respective concentrations derived from the magnitudes of DLTS peaks for both Gr-1 and Gr-3 samples.
- DN-states detected in the lower half of band gap were identified as donors, whereas those DN-states located in the upper part of band gap – as acceptor-like traps, respectively.
- Considerable lowering of the acceptor concentration in the near surface region of Gr-1 sample, do not relate with the contacts preparation procedure, was revealed. Less pronounce N_a decreasing was also observed in Gr-3 sample. Boron out-diffusion during prolonged high-temperature annealing and collecting in the vicinity of the DN was supposed as a possible reason.

Chapter 7
Field-enhanced emission from the shallow dislocation-related states

Shallow dislocation-related states appeared to be a “tough nut” for the experimental investigations. During long period of time only the indirect evidences concerning these shallow bands were obtained from various physical experiments, such as dependence of the EBIC (electron-beam-induced current) contrast at dislocations on temperature and injection dose [Kveder 2001], microwave conductance, electric-dipole spin resonance, and photoluminescence (see paragraph 2.5). Whereas the numerous efforts to detect and characterize the shallow dislocation-related states by means of DLTS measurements – the direct method designed for studying the electrically active defects in semiconductor – were mostly unsuccessful: just the deep levels were revealed by DLTS in the dislocated samples. Only once DLTS peak due to the shallow 1D dislocation related states was observed on the specially prepared samples containing the system of very regular array of parallel 60^0 dislocations subjected to the additional heat treatment yielding to the oxygen segregation along the dislocations [Castaldini 2005b].

As a result, relatively scanty information concerning the characteristics and inner properties of the shallow dislocation states in silicon exists. Specifically, nothing is known about the influence of external electric field on the carrier emission from these shallow states, though the interaction of electric field in the depletion region of the Schottky diode with the dislocation deformation potential may lead to the appearance of the new and unexpected phenomena, promoting the better understanding of the dislocation properties and behaviour in Si. However, in the work of Castaldini et al [Castaldini 2005b] no special attention was drawn on to the possible influence of external electric field on the carrier emission from the shallow 1D states.

Thus, in the present chapter the results of experimental investigations of the electric field influence on the majority carrier emission from the shallow states ST1 and ST3 are presented and the particular mechanism responsible for the observed phenomena is described. Additionally, the origin of ST1/ST3 DLTS peaks broadening will be considered and some facts about the second shallow level SN3 will be presented as well.

7.1 DLTS spectra measured with different reverse biases.

During DLTS measurements of Gr-1 and Gr-3 samples it was noticed that the temperature positions of the low-temperature ST1 and ST3 peaks detected in these samples were shifting towards the lower temperatures with the increase of the applied reverse bias U_r, i.e. with the increase of the external electric field in the depletion region of Schottky diode.

There are two factors limiting the range of reverse bias voltages for which the informative DLTS spectra could be measured. First one – is that at high enough reverse bias voltages the magnitudes of the capacitance transients fall below the detection limit of our DLTS spectrometer (as the eN_s / $e \cdot wN_a$ ratio in Eq. 5.8 becomes too small with the increasing of the SCR width w). The second factor – the low-temperature peaks of interest while shifting towards the lower temperatures with the increasing of U_r come closer to the limiting temperatures achievable in our cryostat, as well as approach the critical temperatures at which the freezing out of the shallow acceptors (boron) takes place. So, the limiting reverse voltages with which the reasonable and informative DLTS spectra still could be recorded are $U_r \sim 4\text{-}5\ V$ and $U_r \sim 10\ V$ for the case of Gr-1 and Gr-3 sample, respectively – see Fig. 7.1 and 7.2.

After the application of C^3 normalization to the set of DLTS spectra measured on Gr-1 sample with different reverse bias voltages, their magnitudes became exactly equal – see Fig 7.1. This confirms the correctness of our model described in paragraph 5.1 concerning the calculations of the interface traps density (Eq. 5.10). The small variations of amplitudes of the DLTS peaks located at 150-220K visible in Fig. 7.1 is due to the fact that for DLTS spectra normalization the stationary capacitance values C measured at temperature of 40K – at which the dominating ST1 peak appears – were used. And as the stationary capacitance increases with temperature, it should be expected *ab origin* that the amplitudes of the DLTS peaks appearing at higher temperatures of 150-220K would be not coinciding precisely after the normalization by the C values corresponding to $T_{MEAS}= 40K$. But in case of using the stationary C values measured at around 200K for normalization – the amplitudes of these peaks turned out to be exactly the same.

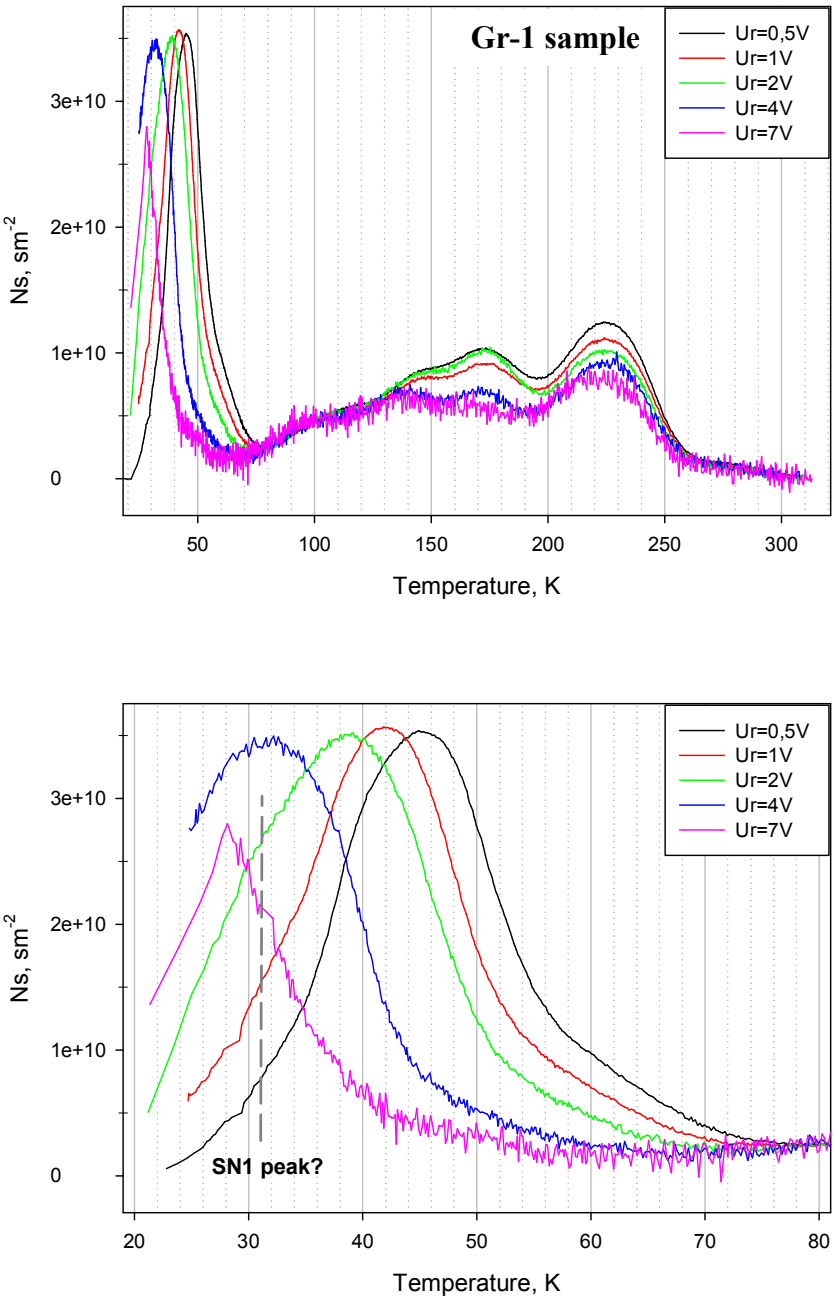

Figure 7.1. Set of DLTS spectra of Gr-1 sample measured with different reverse bias voltages. Ordinate axes reflect the surface trap density calculated according to the Eq. 5.9 after the normalization to C^3 values. Upper plot – whole temperature diapason 20-320K, lower plot – detailed view of low-T peak. Grey dashed line shows the approximate temperature position of the low-temperature shallow SN1 peak. DLTS-scan parameters: filling pulse duration t_p=100μs, filling pulse voltage U_p= –1V, rate window t_w=20ms, reverse bias voltages U_r are shown in legends.

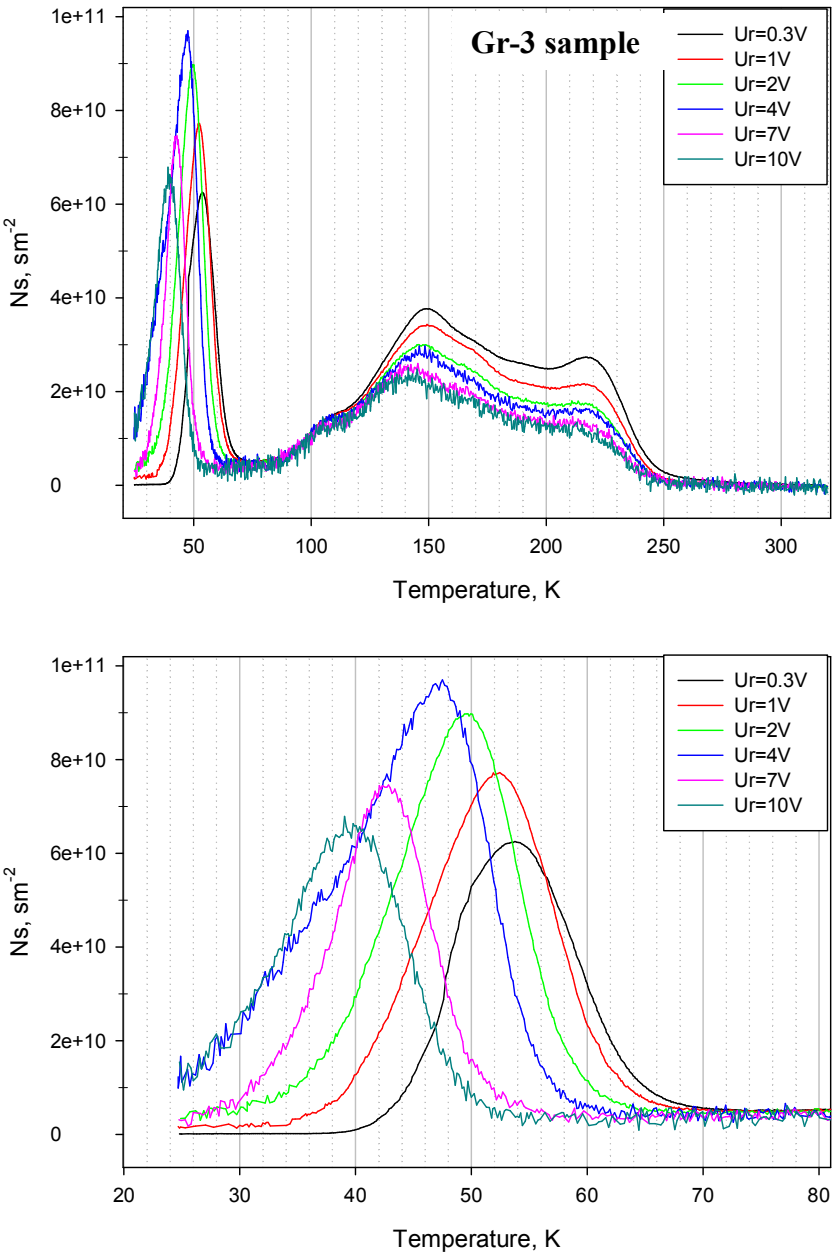

Figure 7.2. Set of DLTS spectra of Gr-3 sample measured with different reverse bias voltages. Ordinate axes reflect the surface trap density calculated according to the Eq. 5.9 after the normalization to C^3 values. Upper plot – whole temperature diapason 20-320K, lower plot – detailed view of low-T peak. DLTS-scan parameters: filling pulse duration t_p=100μs, filling pulse voltage U_p= –1V, rate window t_w=20ms, reverse bias voltages U_r are shown in legends.

For Gr-3 sample – on the contrary – the C^3 normalization (applying the stationary capacitance values measured at temperature of 50K) didn't lead to the similar magnitudes of ST3 DLTS peaks measured with different U_r voltages, see Fig 7.2. More likely, the set

of DLTS spectra revealed a "pyramid-looking" trend – the gradual increase of the peak amplitude with the increasing of the reverse bias up to $U_r=4V$ which is replaced then by subsequent decrease of the peak amplitude at higher reverse biases.

Obviously, such kind of variation of the peak heights after normalization is related with two different effects. First one – is the signal due to the second shallow level SN3 (more shallow than ST3 one), which becomes well visible as the shoulder on the low-temperature side of the main ST3 peak when measuring the DLTS spectra with $U_p=-1,5V$ see Fig. 5.4. Note that the ST3 peak on the DLTS spectrum measured with $U_r=4V$ is rather broadened and contains noticeable low-temperature shoulder as compare with the spectra measured with another reverse bias voltages U_r, see Fig.7.2. This is due to the second effect related with the instability of the pulse generator functioning on Accent spectrometer – the parasitic voltage oscillations in the initial period of every filling pulse (see details in the paragraph 4.3) which appeared to be of the maximal amplitude just when the reverse bias voltage is in order of $U_r=4...5V$. As a result, the signal from the SN3 shallow level arises being excited by these oscillations, thus giving rise to both the broadening of ST3 peak and increasing of its magnitude when the reverse bias voltage is set at $U_r=4V$.

A small effect of the bias voltage increase is also visible for the position of SD DLTS peak located nearly 150K. However, due to the strong overlapping with its neighbors, this effect could not be unambiguously interpreted and we leave the appropriate explanation for future investigations.

7.2 Voltage dependence of the activation enthalpies of ST1/ST3 traps. Simulation of ST1 and ST3 peaks shape.

The activation enthalpies for the hole thermo-emission E_a and capture cross sections σ – as retrieved from the Arrhenius graph data for the low-temperature ST1 and ST3 DLTS peaks at different reverse bias voltages are reported in Table 7.1. As one can see, the activation enthalpies for ST1 and ST3 traps decrease with the increasing of reverse bias. In other words, the field enhanced emission from the shallow traps in Gr-1 and Gr-3 samples takes place.

The values of capture cross sections for both ST1 and ST3 peaks as obtained from the corresponding DLTS spectra measured with different U_r voltages are in the range of $6*10^{-16}$ - $5*10^{-15}$ cm^2, which is more typical for the capture to neutral point-like defect. Similar values of the capture cross section were registered for many other dislocation-related defects [Omling 1985], including ascribed to the shallow 1D bands in p-Si [Castaldini 2005b].

The results of numerical simulations of DLTS peak shapes using trap parameters listed in the Table 7.1 are presented in Fig. 7.3, showing that both ST1 and ST3 low-temperature peaks are considerably broader than that expected for point-like defects with similar activation energies and capture cross sections.

Whereas for every particular reverse bias voltage the adequately correspondence between the temperature positions of real and simulated peaks is observed, the real peaks are noticeably broader than the simulated ones, see Fig. 7.3. It also should be noted, that both ST1 and ST3 peaks could not be decomposed into 2 (or more) peaks due to the common point-like defects, thus the broadening of the ST1 and ST3 peaks is not a result of overlapping of several closely-spaced peaks but is the broadening indeed. However, the fact of ST1 and ST3 peaks magnitudes independence on the rate window period T_C (see Fig. 5.5 and 5.6 and discussion in paragraph 5.4), imply another mechanism of broadening for these peaks, distinctive from Gaussian broadening suggested by Omling [Omling 1983] which arises as a result of dislocations densities and point defects fluctuations and which was typically observed for DLTS peaks in plastically deformed samples previously (see Chapter 2). Discussion about the possible origin of ST1 and ST3 peaks broadening will be continued in the paragraph 7.8.

Careful examination of the spectra of Gr-1 and Gr-3 samples presented in Fig. 7.3 reveals that another one DLTS peak is presented on the low-temperature side of the ST1 peak. This peak is strongly overlapped with the main ST1 peak and could be also recognized in Fig. 5.5 as the small shoulder on the low-temperature side of ST1 peak at the temperatures of *30-35 K*.

Table 7.1. Activation enthalpies E_a and capture cross sections σ as evaluated from the Arrhenius plots of low-temperature ST1 and ST3 DLTS peaks in Gr-1 and Gr-3 samples measured with different reverse bias voltages U_r.

U_r, V	ST1 peak, Gr-1 sample		ST3 peak, Gr-3 sample	
	E_a, eV	σ, cm^2	E_a, eV	σ, cm^2
0,3			0,085	1,55e-15
0,5	0,067	8,2e-16		
1	0,062	7,6e-16	0,081	1,2e-15
2	0,055	3,96e-16	0,074	6,5e-16
4	0,051	3,77e-15	0,070	9,3-16
7			0,061	6,24e-16
10			0,058	8,64e-16

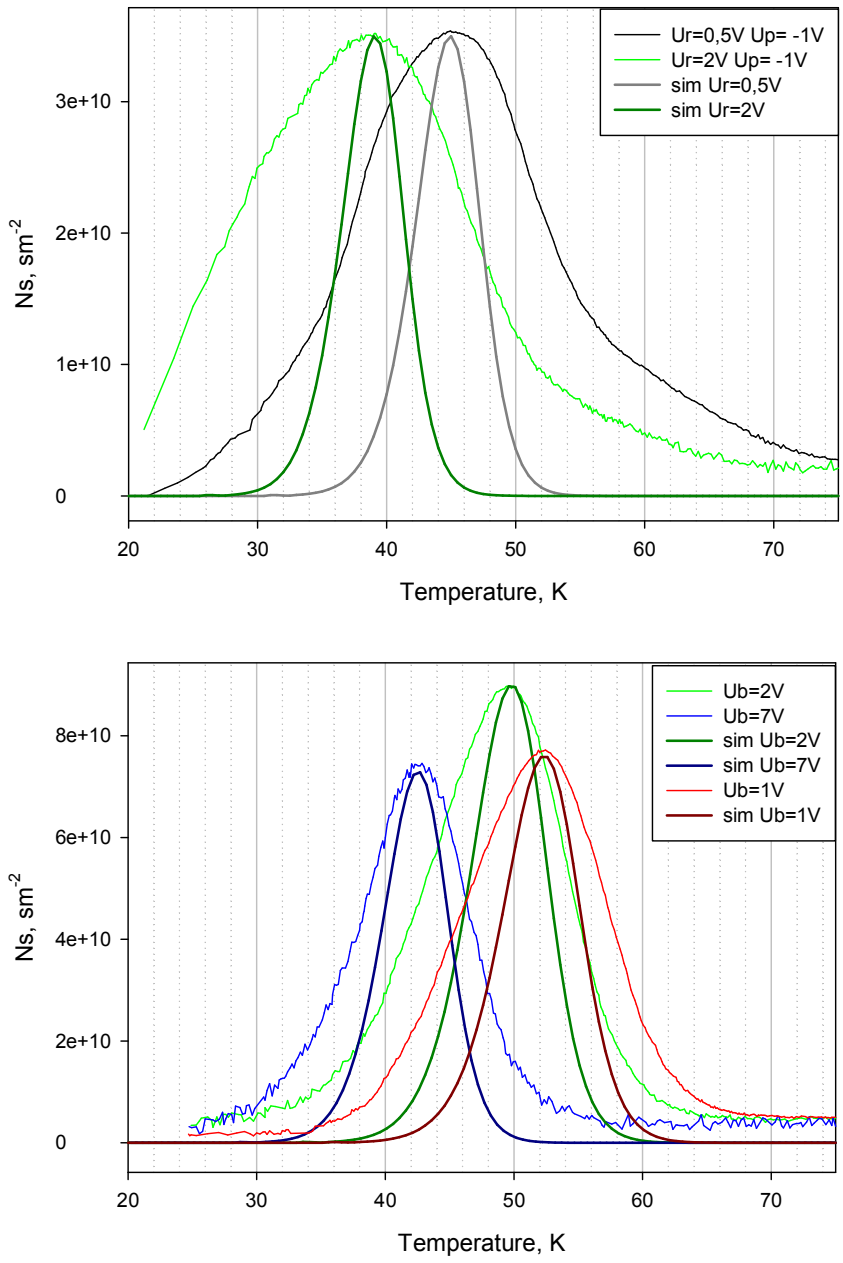

Figure 7.3. Comparison of the measured (real) low-temperature DLTS peaks ST1 and ST3 with the simulated ones for several values of reverse bias voltage U_r. Upper plot – examples for the Gr-1 sample and the lower plot – for Gr-3 sample. E_a and σ values used for simulation are listed in Table 7.1.

By analogy with Gr-3 sample, where the second shallow level (shallower than the main ST3 level) was marked as SN3, the second shallow level in Gr-1 sample will be denoted as SN1. Obviously, due to the lower DN-barrier height in Gr-1 sample, the SN1 level can be filled with holes when measured with U_p= *-1 V* already. Properties of SN1/SN3 shallow traps will be discussed below in paragraph 7.9.

7.3 Possible mechanisms for the field enhanced emission.

Generally speaking, there are three possible mechanisms of emission enhancement by the electric field: (i) the Poole-Frenkel effect, where the electron climbs over a barrier lowered by the presence of electric field F, (ii) pure tunnelling, and (iii) phonon-assisted tunnelling, where the electron absorbs thermal energy from lattice and then tunnels through the barrier at a higher energy. These mechanisms are illustrated in Fig. 7.4. Since pure tunnelling is unlike for electric fields below about 10^7 *V/cm* (which is much higher than the fields accessible in our experimental conditions), it could be excluded from the further consideration.

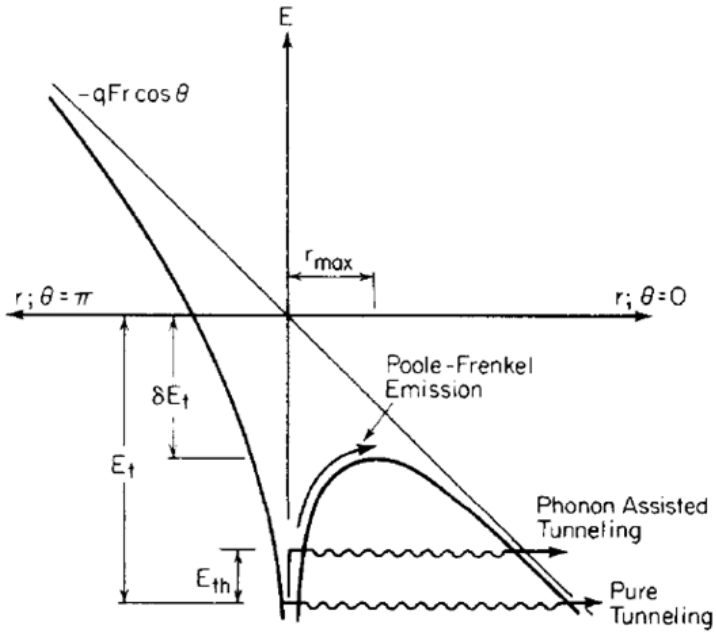

Figure 7.4 One-dimensional representation of the potential at a defect state E_t in the presence of an electric field F. Modification of the carrier emission process by the Poole-Frenkel effect (barrier lowered by δE_t), by tunnelling, and by phonon-assisted tunnelling (phonon energy E_{th}) are indicated as well (after [Martin 1981]).

- Poole-Frenkel effect

The Poole-Frenkel effect is the simplest process in which the electron is thermally emitted over the top of a potential barrier which has been lowered by the presence of an electric field. Therefore, the emission rate from the defect state E_t to the conduction (valence) band will be increased according to

$$e_n = N_c \sigma_n \langle \upsilon_n \rangle \exp\left\{-\frac{(E_c - E_t) - \delta E_t}{kT}\right\} \tag{7.1}$$

which may be rewritten as

$$e_n = e_{n0} \exp\left\{\frac{\delta E_t}{kT}\right\} \tag{7.2}$$

where e_{no} is the emission rate in zero-field. Here δE_t is the barrier lowering due to electric field (see Fig. 7.4), N_c – is the density of states in the corresponding band, σ_n capture croass section and $<\upsilon_n>$ is thermal velocity at the actual temperature (compare with Eq. 1.15).

Calculations of δE_t were performed first in one-dimensional model by Frenkel [Frenkel 1938] and later extended in to three-dimensions by Hartke [Hartke 1968]. For a Coulombic potential in an electric field F aligned in the $-z$ direction, potential could be written as:

$$V(r) = -\frac{e^2}{4\pi\varepsilon r} - eFr\cos\theta \tag{7.3}$$

where r and θ are spherical coordinates. For $0<\theta<\pi/2$ there is a well defined potential minimum which could be obtained by setting $\partial V/\partial r = 0$ at $r=r_{max}$, see Fig. 7.4. This gives

$$r_{\max} = \left(\frac{e}{4\pi\varepsilon F\cos\theta}\right)^{1/2} \tag{7.4}$$

and

$$\delta E_t = V(r_{\max}) = -e\left(\frac{eF\cos\theta}{\pi\varepsilon}\right)^{1/2} \tag{7.5}$$

Frenkel's one-dimensional result is obtained by setting $\theta=0$, hence

$$\delta E_{t1D} = -e\sqrt{\frac{qF}{\pi\varepsilon}} = \sqrt{F} * 2.2*10^{-4} V^{-1/2} cm^{1/2} \tag{7.6}$$

Thus, in general form Eq. 7.2 could be rewritten as

$$e_n = e_{n0}\exp\left\{\frac{\beta\sqrt{F}}{kT}\right\} \tag{7.7}$$

where β is the resulting constant describing the lowering of the barrier for carrier emission, so-called Poole-Frenkel constant.

However, the experimental results (see short review below) often gave the resulting constant β somewhat smaller than value predicted by Eq. 7.6 for 1-D case. Obviously, the one-dimensional analysis overestimates the lowering of the barrier by calculating it only at the maximum point $\theta=0$.

To clarify this discrepancy, Hartke [Hartke 1968] has extended 1-D model of Frenkel to three dimensions and performed the exact calculation of emission rate. In three-dimensional calculations an integration over θ because of the spatial variation of δE_t (determined by Eq. 7.5) is required:

$$\frac{e_{n3D}}{e_{n0}} = \frac{1}{4\pi}\left(\int_0^{2\pi} d\phi \int_0^{\pi/2} d\theta \sin\theta \exp[\frac{\delta E_t}{kT}] + \int_0^{2\pi} d\phi \int_{\pi/2}^{\pi} d\theta \sin\theta \right) =$$
$$= \frac{1}{4\pi}\left(\int_0^{2\pi} d\phi \int_0^{\pi/2} d\theta \sin\theta \exp[-\frac{e\left(eF\cos\theta/\pi\varepsilon\right)^{1/2}}{kT}] + \frac{1}{2} \right) \tag{7.8}$$

For hemisphere $\pi/2<\theta<\pi$ it is assumed that no barrier lowering takes place there (see Fig. 7.4), hence the electric field does not change the emission rate in this hemisphere. The first integral in the Eq. 7.8 could be evaluated by substituting $y=cos\theta$, with the result being

$$\frac{e_{n3D}}{e_{n0}} = \left(kT/\gamma\sqrt{F}\right)^2 \{1+[(\gamma\sqrt{F}/kT)-1]\exp(\gamma\sqrt{F}/kT)\} + \frac{1}{2} \tag{7.9}$$

where the coefficient γ is defined as

$$\gamma = e\left(\frac{e}{\pi\varepsilon}\right)^{1/2} \tag{7.10}$$

By plotting this equation as a function of electrical field F, temperature values around 40-50K (corresponding to the ST1 and ST3 peaks appearance) and Si dielectric constant ε, the slope constant of the resulting curve (i.e. Poole-Frenkel coefficient β) was found to increase consistently from *1,1* for low electric field up to *2,2* for the high field. For our range of electric fields and temperatures the resulting constant β could be estimated approximately as $\beta=1,8–2*10^{-4}\ V^{1/2}\ cm^{1/2}$.

- Phonon-assisted tunnelling

Second possible mechanism of the emission enhancement by the electric field is the phonon-assisted tunnelling. In a simple way this process could be regarded as a thermal emission of the electron from the defect level E_t into the pseudolevel E_{th} with the subsequent tunnelling through the triangular barrier, see Fig.7.4. The most extensive numerical studies of this process were carried out by Makram-Ebeid and Lanoo [Makram-Ebeid, 1982]. For the present study it is sufficient to show briefly their general results.

For the case of phonon-assisted tunnelling emission rate increases exponentially with the square of the electric-field strength according to

$$\frac{e_n}{e_0} = \exp(\frac{F^2}{E_c^2}) \tag{7.11}$$

where E_c is a characteristic field strength, given by

$$E_c = \sqrt{\frac{3m^*\hbar}{e\tau_2^3}} \tag{7.12}$$

where m^* is the effective mass of charge carriers and τ_2 is the tunnelling time which is given by

$$\tau_2 = \frac{\hbar}{2kT} \pm \tau_1 \tag{7.13}$$

Here, the plus and minus signs correspond to the adiabatic potential structures of substitutional impurities and autolocalized centres, respectively. The time constant τ_1 is in the order of the inverse local impurity vibration frequency.

- Criterion to distinguish between Poole-Frenkel and phonon-assisted tunnelling mechanisms.

A comparison of Eq. 7.7 with Eq. 7.11 suggests a simple way to distinguish between Poole-Frenkel and the phonon-assisted tunnelling mechanisms of carrier enhanced emission [Ganichev 2000]. Namely, in case of Poole-Frenkel effect the dependence of emission rate on electric field could be expressed as (according to Eq. 7.7)

$$\ln(e_n) = \ln(e_{n0}) + \frac{\beta}{kT}\sqrt{F} \tag{7.14}$$

Similar expression could be also written for dependence of activation enthalpy on the electric field. Following the Eq. 7.1 and 7.7 one will get

$$E_a = E_{a0} - \beta\sqrt{F} \tag{7.15}$$

Whereas for the case of phonon assisted tunnelling the emission rate and activation enthalpy dependences on the electric field will be given by (Eq. 7.11)

$$\ln(e_n) = \ln(e_{n0}) + \frac{1}{E_c^2}F^2$$

$$E_a = E_{a0} - kT\frac{F^2}{E_c^2} \tag{7.16}$$

Hence, the simple way to distinguish these two mechanisms is to plot the logarithm of emission rate (or simply the activation enthalpies) against F^2 and $\sqrt{F}$ and to compare which of the two plots can be fitted by a straight line. In order to do this, it is necessary to calculate precisely the electric field value at the position of the DN for every particular reverse bias voltage U_r.

An important supplement which should be mentioned here is that for the Poole-Frenkel effect to occur, the defect must acquire a net charge upon emission of the carrier (i.e. become ionized). For the neutral impurities Poole-Frenkel lowering of the emission barrier doesn't occur, since in this case there is no Coulomb potential around the defect. Thus, a donor-like (acceptor-like) centre which is initially neutral and becomes positively (negatively) charged upon emission of an electron (hole) in n-type (p-type) semiconductor is expected to display the Poole-Frenkel effect. Whereas for the phonon-assisted tunnelling the charge state of the defect level plays no role at all.

7.4 Calculation of the electric field at the position of DN.

DN represents a charged plane lying inside the SCR of Schottky diode at every reverse bias voltage U_r used for DLTS measurements. To calculate correctly the electric field values at the position of the DN, it is necessary to solve Poisson equation taking into account the charge collected by the DN states. Thus, remembering the Eq. 5.4 obtained in paragraph 5.1 one can write the corresponding solution of the Poisson equation as

$$\varepsilon V = \frac{eN_A}{2} w^2 - Q_s x_d \ . \tag{7.17}$$

In order to calculate the electric field F at the depth x_d, i.e. at the position of the dislocation network, equation 7.17 should be subjected to the differentiation according to

$$F(x_d) = \left. \frac{dV(x)}{dx} \right|_{x=x_d} \tag{7.18}$$

Thus, the electric field will be equal to

$$F(x_d) = \frac{eN_A(w - x_d)}{\varepsilon} - \frac{Q_s}{2\varepsilon} \tag{7.19}$$

The factor 2 in the denominator of the second term in Eq. 7.19 arises due to the fact that electric field at the right F_R and left F_L sides from the DN are summarized to give

$$F_R - F_L = -Q_s / \varepsilon \tag{7.20}$$

and we are interested only in the half of this field, since at the left side from the DN the potential is raised by the external field of Schottky diode and no emission occurs in this direction (just as it was discussed for the 3D Poole-Frenkel effect, see paragraph 7.3).

Calculations of the first term in the equation 7.19 are straightforward - necessary values of N_a and w could be obtained from the CV curves measured at the temperature corresponding to the appearance of the particular DLTS peak, while a problem arises with the estimation of the dislocation network charge Q_s, which should be used in the calculations.

At the temperatures of 35-55K corresponding to the appearance of ST1/ST3 peak, the DN charge Q_s could be written as the sum of two components

$$Q_S = Q_{deep} + Q_{shallow} \exp(-e_p t) \, , \tag{7.21}$$

where Q_{deep} is the sum of the charges of all deep levels $Q_{deep} = e \sum N_{deep}$ (see Table 5.1), which are completely frozen out at the temperatures of interest, i.e. their occupation could not be changed by filling pulses at such temperatures. But the occupation of the shallow traps could. Thus, the second component due to the charge of the shallow traps is determined by the amount of the holes remaining at the trap after the switching off the filling pulse, i.e. at the moment when the capacitance transient is recorded and the correlation procedure is applied (here e_p is the emission rate from the shallow trap).

In paragraph 6.8 deep levels in both Gr-1 and Gr-3 samples were identified as donors, so they should be positively charged when filled with holes. As a result, both charge components – due to deep and due to shallow traps – have the same sign "plus" in Eq. 7.21, thus leading to the decreasing of electric field as it follows from the substitution of this charge Q_s in the Eq. 7.19 for the electric field at the position of DN. At the very beginning of the emission process the shallow traps are filled with holes, hence the total electric field is minimal and when it growths up gradually as holes emit from the shallow traps, thus reducing the total DN charge Q_s.

So, the question arises which charge of the shallow traps should be taken for the electric field calculations – either at the very beginning of the emission process, when the states are filled with holes (it means the charge $Q_{shallow}= eN_{shallow}$, where $N_{shallow}$ is derived from the magnitude of the corresponding DLTS peak) or at the end of the emission process when most of holes have left the traps (which corresponds to the $Q_{shallow}=0$) or some value in-between?

In the next paragraph it will be shown, that the correction of the electric field for the charge $Q_{shallow}$ is rather small and insignificant for the whole calculations of the electric field, but to be completely sure, both limiting cases of completely filled and completely empty shallow traps will be considered in the following paragraphs.

- Influence of N_a lowering onto the electric field.

As it was described in the previous chapter (paragraph 6.2), a significant lowering of the acceptor concentration in the near surface region of Gr-1 sample was revealed. Since the strong N_a lowering will also influence on the electric filed, it should be necessarily taken into account. Following the discussion in paragraph 6.3, let us consider a simple approximation of rectangle-like N_a profile in the near surface region of Gr-1sample, i.e. regarding that the bulk acceptor concentration N_a in the near-surface region of the thickness x is reduced by ΔN_a value. In paragraph 6.3 the thickness of the region of reduced acceptor concentration was estimated as $x=1,1\ \mu m$ and the magnitude of acceptor lowering as $\Delta N_a \sim 0,3*10^{15}\ cm^{-3}$ for Gr-1 sample. Thus, one get $x>>x_d$. The SCR depth w corresponding to the $U_r=0,5\ V$ – the minimal reverse bias voltage used for the DLTS spectra measurements on Gr-1 sample (see Fig. 7.1) is equal to $1,3\ \mu m$, hence the inequality $x<w$ is always fulfilled for all measured DLTS spectra. Then, the electric field at the depth of x (implying that at the depth between w till x acceptor concentration is equal to N_a, while closer to the surface at the depths less than x concentration is $N_a - \Delta N_a$) will be equal to

$$F(x) = eN_A(w-x)/\varepsilon \qquad (7.23)$$

Keeping in mind the linear behaviour of the electric field inside the space charge region of the Schottky diode (Eq. 1.4), the following equations for the electric field at the dislocation network could be written

$$\begin{aligned} F(x_d) &= F(x) + e(x - x_d)(N_A - \Delta N_A)/\varepsilon = \\ &= eN_A(w - x)/\varepsilon + e(x - x_d)(N_A - \Delta N_A)/\varepsilon = \\ &= \frac{e}{\varepsilon}(N_A w - \Delta N_A x - (N_A - \Delta N_A)x_d) \end{aligned} \tag{7.24}$$

This expression could be further simplified to give

$$F(x_d) \approx \frac{e}{\varepsilon}(N_A w - \Delta N_A x) \tag{7.25}$$

as the depth of the dislocation network x_d is rather small and the third term in the Eq. 7.25 will be too small to make a big influence on the total electric field and could be neglected. Thereby, the lowering of the acceptor concentration in the near surface region will simply lead to the decreasing of the electric field by the additive quantity $\Delta N_a x$ independent on the applied bias. Consequently, the final formula for the electric field at the DN in Gr-1 sample could be obtained by the combination of Eq. 7.19 and 7.25 to give

$$F(x_d) = \frac{e}{\varepsilon}(N_A w - \Delta N_A x - \frac{Q_s}{2}) \tag{7.26}$$

For Gr-3 sample due to much more uniform acceptor distribution such correction for N_a lowering is not essential, thus Eq. 7.19 could be directly used.

Now, all necessary components for electric field calculations at the position of DN are known: Eq.7.19 and Eq.7.21 describe the electric field taking into account the charge collected by the interface traps, and Eq. 7.26 – N_a lowering in Gr-1 sample in addition.

7.5 Electric field dependence of E_a energies derived from DLTS.

Using the values of activation enthalpies for ST1 and ST3 traps corresponding to the different reverse bias voltages as listed in Table 7.1, the dependences on the squared electric field F^2 and square root of electrical field $\sqrt{F}$ were plotted for the two limiting cases of completely filled and completely emptied shallow levels. As a result, linear dependences appeared for the plots of E_a versus $\sqrt{F}$ for both ST1 and ST3 traps and for both considered charges of shallow traps, thus following a Poole-Frenkel law (Eq. 7.15), see Fig. 7.5. The obtained dependences of activation enthalpies on the square root of electric field could be well approximated by the straight lines and, by analogy with Eq.

7.15, the slope of obtained straight lines should correspond to the coefficient β (Poole-Frenkel coefficient) while the cutoff values – to the activation enthalpies expected at the zero electric field E_{a0}. Derived values of E_{a0} and β are summarized in Table 7.2.

As one can see from the data presented in Table 7.2, the exact value of the shallow traps charge $Q_{shallow}$ has only minor influence on the Poole-Frenkel coefficient determination: the corresponding β values derived for two limiting cases of completely filled and empty shallow states differ only by ~10%. Even less influence the particular charge of the shallow states has on to E_{a0} energies. Partly, this is due to the necessity of extracting of the square root from the electric field – this additionally minimizes the possible uncertainties related with the determinations of w, N_a and Q_S. Obviously, the real β and E_{a0} are laying somewhere in-between the values obtained for the limiting cases of completely filled and empty shallow traps, which are presented in Table 7.2.

And yet, the obtained results appeared to be rather unexpected and unusual. First of all – different Poole-Frenkel coefficients in Gr-1 and Gr-3 samples, namely the coefficients β obtained for the ST1 peak in Gr-1 sample are larger than those obtained for ST3 peak in Gr-3 sample irrespective on the occupancy state of the shallow traps. Second unusual fact is that – in spite of perfectly linear E_a vs. $\sqrt{F}$ dependences justifying the Poole-Frenkel effect performance – the obtained coefficients β appeared to be significantly higher (especially those for Gr-1 sample) than the theoretically predicted value

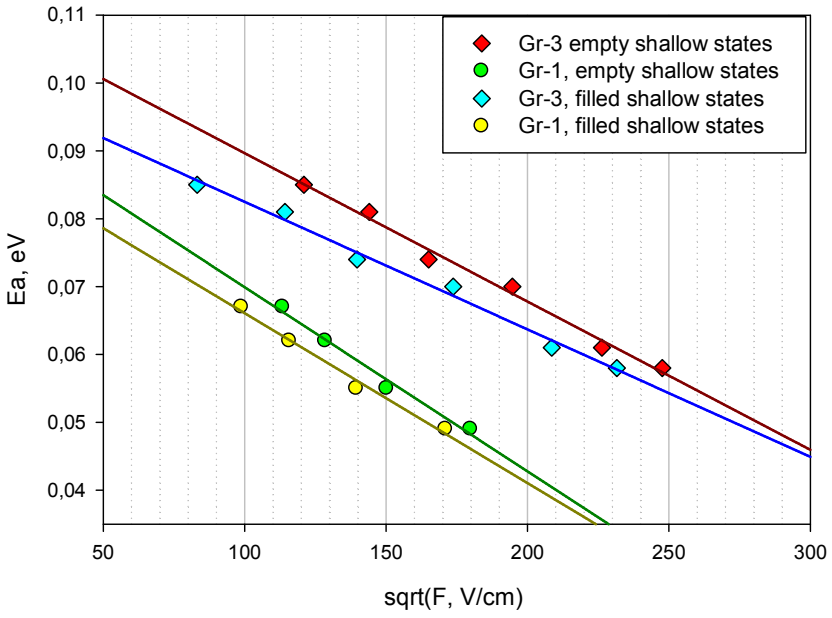

Figure 7.5. Activation enthalpies for hole thermo-emission from ST1 and ST3 shallow traps in Gr-1 and Gr-3 samples versus the square root of electric field, corrected for the DN charge (two cases of completely filled and emptied shallow states are considered) and for N_a lowering in Gr-1 sample. Solid lines correspond to the best linear fit for experimental data.

$\beta_{theor} \approx 1{,}8–2*10^{-4}\ cm^{1/2}\ V^{-1/2}$ for our range of electric fields (see paragraph 7.3) as well as higher than the Poole-Frenkel coefficients ever observed before. Moreover, as it was discussed in the paragraph 7.3, Poole-Frenkel effect in p-type semiconductor is expected to occur only for acceptor-like traps, whereas the shallow levels ST1 and ST3 were identified as donors (in paragraph 6.6)!

At the same time, the obtained values of activation enthalpies E_{a0} for ST1 and ST3 levels at zero electric field are in the outline with the previous results: as it was suggested in paragraph 5.8 from the different energy positions of D1 line in these samples, the shallow level E_{D1s} participating in D1 radiative recombination (i.e. ST1 level) should be *~25 meV* shallower in Gr-1 sample than in Gr-2. And, as one can see in Table 7.2, the obtained zero field energy E_{a0} for ST1 trap is by *10-15 meV* smaller than the E_{a0} energy for ST3 trap, thus showing the reasonable agreement with the energy difference obtained from the PL spectra presented in Fig. 5.10.

Before the looking for the appropriate explanation for the detected peculiarities of E_a vs. $\sqrt{F}$ dependences in general and the derived coefficient β in particular, it is necessary to be sure that all procedures for β evaluations were performed correctly. Specifically, the following moment arouses suspicion – the conformity of the E_a values listed in Table 7.1 and which were used to plot the graph in Fig. 7.5 to the positions of the real shallow levels in bandgap. In principle, as the both ST1 and ST3 DLTS peaks are broadened (see Fig. 7.3), they should be analyzed with the appropriate model instead of using the procedure developed for the analysis of point-like defects and which for such traps could give no clear relation with the real position of defect level.

Table 7.2 β coefficients and E_{a0} values for the shallow traps ST1 and ST3, derived for two limiting charges of the shallow levels. For Gr-1 sample, the correction for the N_a lowering in the near surface region was also considered in the calculations.

	Gr-1 sample		Gr-3 sample	
	$Q_{shallow}=0$ empty shallow states	$Q_{shallow}=e\ N_{shallow}$ filled shallow states	$Q_{shallow}=0$ empty shallow states	$Q_{shallow}= e\ N_{shallow}$ filled shallow states
$\beta,\ cm^{1/2}\ V^{1/2}$	2,7e-4	2,5e-4	2,2e-4	1,9e-4
$E_{a0},\ eV$	0,095	0,09	0,11	0,1

In order to clarify this question – experiments of Isothermal Spectroscopy Measurements (ITS) were performed (see description of the method in paragraph 1.3). The advantage of the ITS method over DLTS is that by measuring the ITS spectra at different reverse bias voltages it is possible to trace the variation of holes emission rate e_p on the electric field strength directly, without necessity of plotting Arrhenius graphs and E_a energies determination.

7.6 Poole-Frenkel coefficient as obtained from the ITS measurements.

For ITS measurements it is especially important to select the proper temperature in order to record the successful spectra. With the increasing of the applied reverse bias, i.e. with the increasing of external electric field, the barrier for majority carriers emission decreases, leading to the increasing of the emission rate. As a result, position of the ITS peak would also shift towards the lower values of τ (emission time constant) with the increasing of the reverse bias voltages.

The usable time range of our transient recorder (period width T_w, see paragraph 1.4) for time-dependent measurements (transients) is of $2*10^{-4}$ *s – 4 s*. In reality, upper limit could be even smaller, due to the low-frequency noise arising when the vibration of the working close-cycled cryostat comes in to a resonance with the electrode connected to the Ti dot of the Schottky contact. Consequently, the measurement temperatures for ITS investigations should be chosen so as to record as much as possible informative ITS spectra with different U_r voltages as long as trap emission rates fall inside the usable time interval indicated above. Another limitation factor – at the temperatures lower than approximately 35K, our measurement system could not provide the required temperature stability during the recording of ITS spectrum (better than *0,1 K*). This is especially essential for Gr-1 sample, where the ST1 peak appears at the close temperatures at sufficiently high reverse biases U_r.

The examples of ITS spectra of Gr-1 and Gr-3 samples measured with different reverse bias voltage U_r, but with the same filling pulse voltage U_p = *-1 V* are presented in Fig. 7.6. Measurement temperatures were 40K for Gr-1 sample and 53K for Gr-3 sample. Activation energies and capture cross sections derived from the temperature dependences of the ITS peaks measured with constant reverse bias voltage appeared to be the same as those derived for ST1/ST3 traps from the DLTS spectra measured with the same U_r voltages, thus confirming the identity of the trap levels studied by DLTS and ITS. Measured spectra appeared to be somewhat noisy (especially in the interval of τ close to *0,1-1 s*, where the strong resonance effect occurred), so the smoothing procedure was applied.

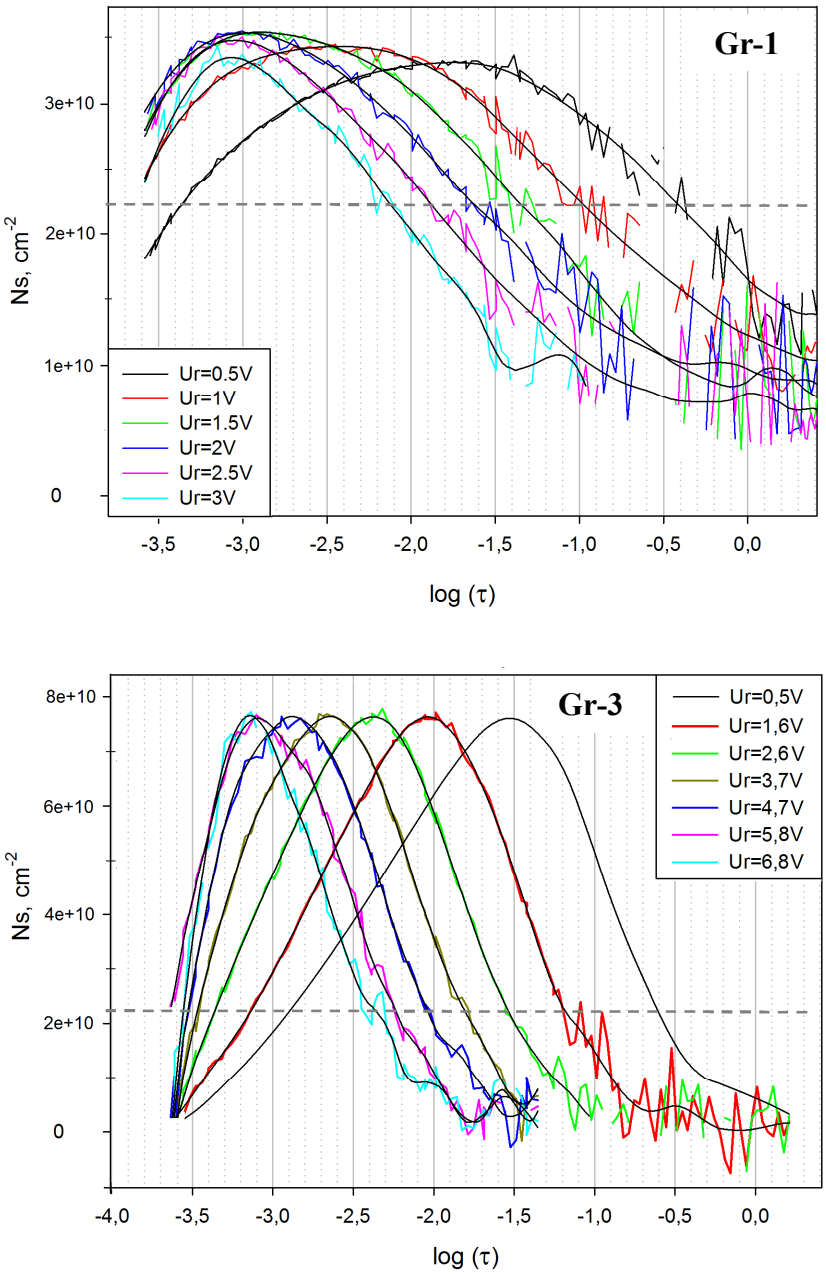

Figure 7.6. Set of ITS spectra of Gr-1 sample (upper plot) and Gr-3 sample (lower plot) showing the ITS peaks due to ST1 and ST3 shallow traps, respectively, measured with different reverse bias voltages. Ordinate axes show the surface trap density concentration, abscissa axes – common logarithm of the emission time constant τ. ITS-scan parameters: measurement temperatures were 40K for Gr-1 sample and 53K for Gr-3 sample, filling pulse duration t_p=*100 μs*, filling pulse voltage U_p= *–1 V*, reverse bias voltages U_r are shown in the legends. Straight horizontal dashed lines denote the τ points on the right-side shoulders of the ITS peaks which were used for β coefficient determination (see Fig. 7.8 and comments in the text).

As in case of DLTS measurements, the magnitudes of the ITS peaks were recalculated according to Eq. 5.10 to represent the surface trap densities, showing the concentrations comparable to that obtained for the corresponding ST1/ST3 DLTS peaks in Gr-1 and Gr-3 samples.

The impact of the electric field on the emission processes is evident from the ITS spectra shown in the Fig. 7.6. Hereof it could be concluded, that for the reverse bias voltages $U_r \geq 3V$ for Gr-1 sample and $U_r \geq 7V$ for Gr-3, the characteristic emission time from the defect level at the relevant measurement temperature becomes too small to fit into the usable time range of our transient recorder, thus the real maximum of ITS peak is expected to appear outside of the measurable diapason and only the right (long-τ) shoulder of the ITS peak was recorded correctly.

Again, like it was noted for DLTS spectra, the ITS peaks due to both ST1 and ST3 shallow traps are broadened – especially the ITS peaks in Gr-1 sample. Nevertheless, both the smoothened peaks due to ST1 trap and more sharpened peaks due to ST3 trap could not be deconvoluted to a number of the standard peaks due to the point-like defects.

For the determination of β coefficients from the ITS spectra it is necessary – following the Eq. 7.14 – to plot the dependences of the kT-corrected logarithm of emission rates $kT^* \ln(e_p)$ on the square root of electric field $\sqrt{F}$. And the emission rates could be obtained from the position of the ITS peaks maxima, as at the maximum the periodwidth T_w fits best to the emission time constant τ. But due to such broadened and smoothened ITS peaks (especially in case of Gr-1 sample), it is difficult to define the exact positions of the maxima. In principle, differentiation of the ITS peaks could withdraw this problem: zero-crossing point of the obtained derivative curve must correspond to the exact position of ITS peak maximum.

However, it is even not necessary to look for the certain positions of the ITS peaks maxima in order to determine the coefficient β. It is sufficient to plot the dependence of $\ln(e_p)$ on the square root of electric field using the e_p values taken at the same height on the left- or right-side shoulder of the ITS peaks recorded with the different reverse bias voltages. Since the response of the DLTS correlator is the function of the product of the emission rate e_p and the correlator period T_w (see Eq. 1.24, which was written with the periodwidth of the correlation function T_C, but here $T_C = T_w$ may be considered, see paragraph 1.4) the dependence of τ on the electrical field as obtained at every certain level of ITS signal (i.e. keeping the product $e_pT_w = const$ for the ITS peaks recorded with different U_r) will be shifted relatively to the analogous dependence derived for the points corresponding to ITS peaks maxima τ_{max}, preserving the slope which gives the β constant. This procedure when applied to the right-side (i.e. to the slower-e_p side) shoulders of the ITS peaks recorded with the different reverse biases voltages allows one to set more informative dots on the graph, as whereas the ITS peak maximum at high enough reverse

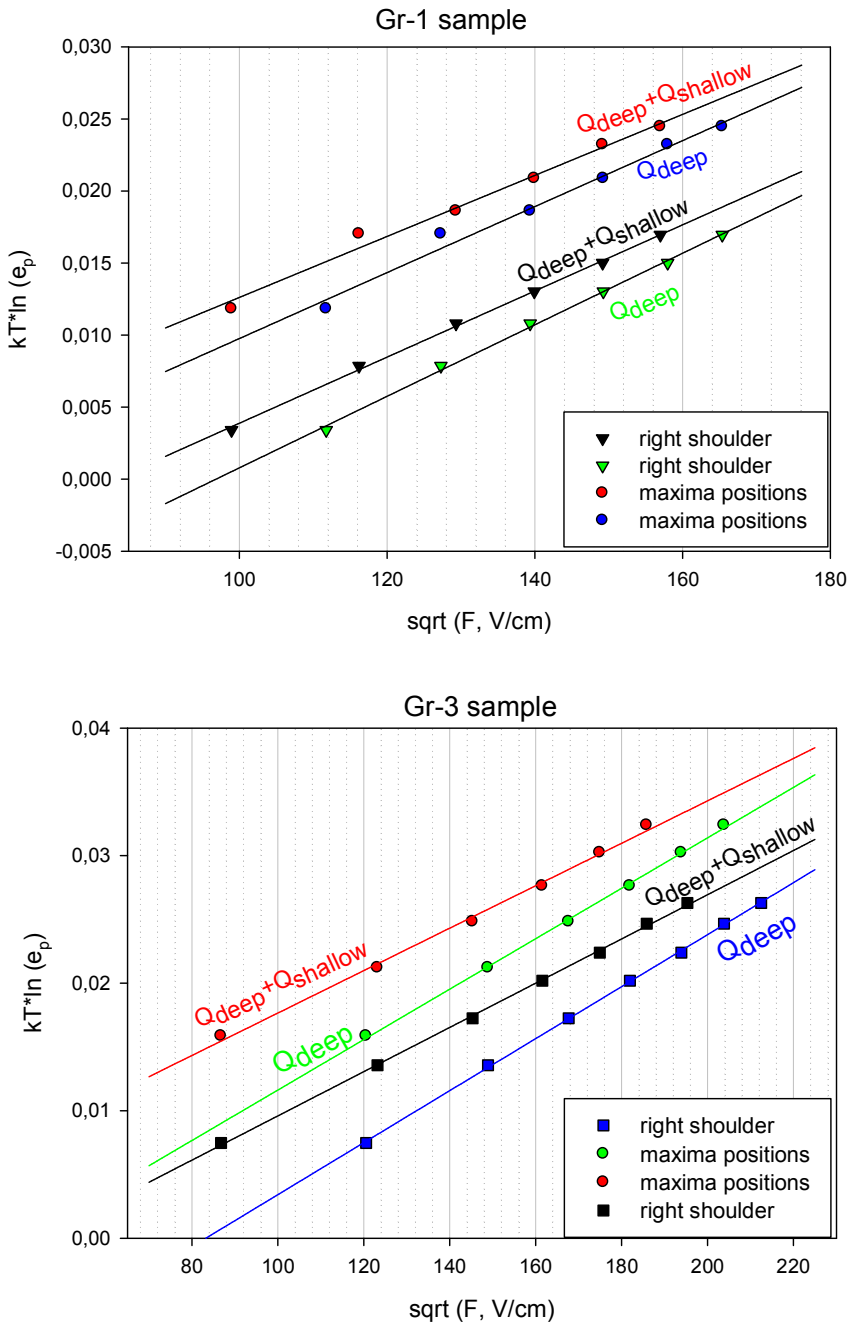

Figure 7.7. *kT*-corrected logarithms of emission rates as a function of the square roots of electric field for Gr-1 (upper plot) and Gr-3 sample (lower plot) considered for the two limiting DN charges of Q_{deep} and $Q_{deep}+Q_{shallow}$ as also for the lowering of acceptor concentration in case of Gr-1 sample. Points are the present experimental data as obtained from the position of the ITS peaks maxima and from the e_p values taken at the same height on the right-side shoulders of ITS peaks (see marks in Fig.7.6), solid lines are the data best fits.

bias voltages runs out of usable time interval, the right-side shoulder is still measured correctly. This is just the case for the ITS spectra recorded with $U_r=3\ V$ on Gr-1 sample and with $U_r=6,8\ V$ on Gr-3 sample.

Moreover, since at the every specified ITS measurement temperature (40K and 53K) the emission rate from the more shallow traps SN1/SN3 will be higher than that from the dominant ST1/ST3 levels $e_p(SN)>e_p(ST)$ (i.e. $\tau(SN)<\tau(ST)$), thus the ITS signal due to the second shallow traps SN1/SN3 should also appear at the lower-τ side (left side) of the main ITS peak corresponding to ST1/ST3 trap. Probably, this is the reason for the extremely broad ITS peaks of GR-1 sample, as in this sample emission from the SN1 trap could be already initiated after the applying of $U_p=-1V$ filling pulses (see paragraph 7.2 and Fig. 7.1), thus leading to the appearance of the additional signal on the lower-τ side. Consequently, it becomes possible to 'filter out' effectively the unwanted contribution from the SN traps by considering the e_p points on the right-side (higher-τ side) shoulders.

The obtained graphs confirm the linear dependences of $ln(e_p)$ on $\sqrt{F}$ - i.e. the presence of Poole-Frenkel lowering of the barrier for emission from the shallow ST1/ST3 levels in both Gr-1 and Gr-3 samples, as this is reported in Fig. 7.7. Corrections of the electric field for the two limiting cases of DN charges Q_{deep} and $Q_{deep}+Q_{shallow}$ were done and the lowering of the acceptor concentration in the near surface region of Gr-1 sample was also taken into account (see Eq. 7.19, 7.21 and 7.26).

For Gr-1 sample 5 points corresponding to the ITS peaks maxima could be obtained after application the differentiation procedure, whereas 6 points – when using the e_p values on the same height on the right-side shoulders of ITS peaks (see dashed line in Fig. 7.6). As one can see from the Fig.7.7, the points corresponding to the ITS peaks maxima fall into the straight line not exactly – consequence of the inaccuracy in the determination of ITS peaks maxima positions. Instead, those points derived from the emission values on the right-sides of ITS peaks could be well approximated by the straight line. Poole-Frenkel coefficients, obtained from the positions of peaks maxima and from the certain level on the right-side shoulders are slightly different from each other – see the results collected in Table 7.3, and it could be supposed that the last method gives the more reliable results.

According to the ITS spectra of Gr-3 sample shown in Fig.7.6, it is possible to derive 6 points of the emission rate considering the ITS peaks maxima positions. By plotting the horizontal line at the level shown by the dashed line in the Fig. 7.6, it is possible to mark 7 informative intersection points at the right-side shoulders of the ITS peaks measured with different reverse biases. Both sets of points excellently fall into the straight lines which are going exactly parallel, thus showing the same slope coefficient β, see the data in Table 7.3.

Table 7.3. Poole-Frenkel coefficients β (in $cm^{1/2}\ V^{-1/2}$) for the shallow levels ST1 and ST3 as derived from the consideration of ITS peaks maxima positions and from the certain position on the right-side shoulders, corresponding to the two limiting cases of DN charges of Q_{deep} and $Q_{deep}+Q_{shallow}$.

	Gr-1sample, ST1 peak		Gr-3 sample, ST3 peak	
	$Q_{DN} = Q_{deep}$ empty shallow states	$Q_{DN} = Q_{deep}+Q_{shallow}$ filled shallow states	$Q_{DN} = Q_{deep}$ empty shallow states	$Q_{DN} = Q_{deep}+Q_{shallow}$ filled shallow states
maxima positions	$2{,}3*10^{-4}$	$2{,}1*10^{-4}$	$2{,}0*10^{-4}$	$1{,}7*10^{-4}$
right-side shoulders	$2{,}5*10^{-4}$	$2{,}3*10^{-4}$	$2{,}05*10^{-4}$	$1{,}7*10^{-4}$

7.7 Comparison of Poole-Frenkel coefficients derived from ITS and DLTS measurements.

As one may note from the comparison of the data presented in Table 7.2 and Table 7.3, Poole-Frenkel coefficients obtained from DLTS measurements are slightly higher than that obtained from the analysis of ITS spectra. While the main general trend remained unchanged, namely – the Poole-Frenkel coefficients obtained for the ST1 peak in Gr-1 sample are larger than that for ST3 peak in Gr-3 sample β(Gr-1) > β(Gr-3) for both considered cases of shallow traps charges and irrespective from measurement method.

The small discrepancy between the β values obtained from DLTS and ITS methods might be caused by a systematic error in temperature measurements affecting mostly the determination of the activation energies E_a from Arrhenius plots. So, it is worth to make a direct comparison of the received linear dependences by plotting them in one graph.

As we could not derive the values of activation energies E_{a0} expected at zero electric field from the analysis of ITS data directly (only the e_{p0} values could be obtained from the approximation to the zero electric field – see Fig. 7.7), however there is a way to estimate them by plotting the straight line using the β values from Table 7.3 (obtained from the ITS method) as the slope coefficients and regarding the cutoff values as a free parameter to obtain the best fit with the experimental E_a vs. $\sqrt{F}$ dependences derived from the DLTS measurements – see the graphs in Fig.7.8.

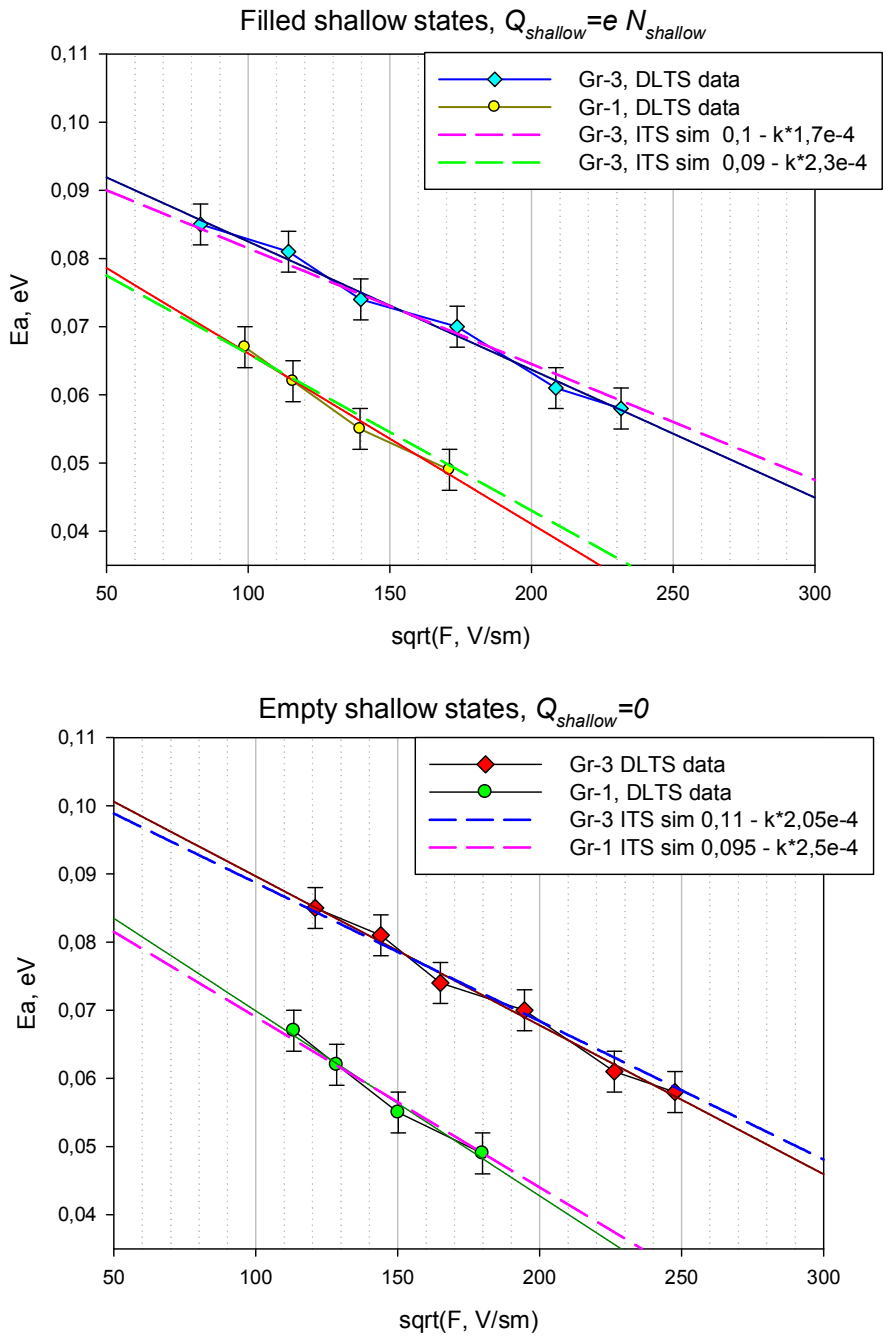

Figure 7.8. Dependences of the activation enthalpies for hole thermo-emission E_a on the square root of electric field for Gr-1 and Gr-3 samples: dots - derived experimentally from the DLTS measurements (vertical error bars correspond to ± *2,5 meV*), thin solid lines – are the data best fits, whereas the thick dashed lines were calculated using β coefficients from the Table 7.3 and regarding the E_{a0} value as a free parameter. Obtained linear equations (where $k \equiv \sqrt{F}$) are shown in the legends.

As a result, the experimental dependences of E_a on $\sqrt{F}$ resulting from the analyses of DLTS spectra could be well adjusted by the straight lines, calculated by using the β coefficients derived from the ITS method, if taking into account the possible errors in the determination of the activation energies E_a from Arrhenius plots, which could be estimated in order of *±2,5 meV*. Moreover, the values of activation energies at zero electric field E_{a0} selected for the best fit – *0,1* and *0,11eV* for Gr-3 sample and *0,09* and *0,095eV* for Gr-1 sample (see the lines equations shown in the legends in Fig. 7.8) – are just the same as those listed in Table 7.2 obtained from the electric field dependences of DLTS spectra, thus confirming that the discrepancy between the β values obtained from DLTS and ITS methods is small and insignificant.

Consequently, the ITS method confirmed the conclusions drawn in paragraph 7.5 from the consideration of the Poole-Frenkel coefficients obtained from DLTS spectra analysis:

- we are dealing with Poole-Frenkel effect
- however, Poole-Frenkel coefficients obtained for ST1 and ST3 traps (at least the β value for the ST1 trap) appeared to be larger than the value β_{theor} predicted theoretically for the interaction of Coulomb centre with electric field
- $\beta(ST1) > \beta(ST3)$. Different Poole-Frenkel coefficients in Gr-1 and Gr-3 samples suggest that the DN-structure has a particular influence onto the Poole-Frenkel coefficients for the shallow ST1 and ST3 levels in these bonded samples.

Combining and averaging the results obtained from DLTS and ITS methods as well as for the two limiting DN charges of Q_{deep} and $Q_{deep}+Q_{shallow}$, the final estimations of the most reliable values of Poole-Frenkel coefficients β and activations energies approximated to zero electric field E_{a0} for the shallow ST1 and ST3 traps in Gr-1 and Gr-3 samples could be made – see Table 7.4.

Table 7.4. Averaged values of the β coefficients and E_{a0} energies as derived from the comparison of the results obtained from DLTS and ITS methods.

	E_{a0}, *eV*	$\beta*10^{-4}$, $cm^{1/2} V^{-1/2}$
Gr-1 sample, ST1 trap	~0,09…0,095	~2,4 ± 0,3
Gr-3 sample, ST3 trap	~0,10…0,11	~1,9 ± 0,2

7.8 Previously observed events of field-enhanced emission.

Poole-Frenkel effect was observed and described for a number of point-like defects in silicon – for example for oxygen thermo-donors (TD) [Kimmerling 1981] and carbon-hydrogen donor $(C\text{-}H)_I$ [Andersen 2002] in n-type Si, Tl acceptors [Brotherton 1978] and Pt acceptors [Brotherton 1979] in p-type Si. Values of Poole-Frenkel constants reported for these defects are varying in wide range from $0{,}5*10^{-4}\ V^{-1/2}\ cm^{1/2}$ for Pt acceptor till $1{,}9*10^{-4}\ V^{-1/2}\ cm^{1/2}$ for Tl acceptor, whereas for both TD and $(C\text{-}H)_I$ donors $\beta \sim 1.0*10^{-4}\ V^{-1/2}\ cm^{1/1}$. So, as one can see, the Poole-Frenkel coefficients obtained for ST3 and – especially – for ST1 trap are significantly higher than those observed before for point-like defects.

Up to now, there were no definite facts about the electric field influence on the emission from the dislocation related states. Only in the early work of Kveder et al [Kveder 1982] a certain evidence of electric field influence on the emission processes from the deep dislocation-related states was observed as decreasing of the activation enthalpy with electric field growth (however only for two values of reverse bias voltages and without specification about possible mechanism – Poole-Frenkel effect or phonon-assisted tunnelling). It was also supposed in that work [Kveder 1982], that the interaction of the electric field with the Coulomb potential around the dislocations could lead to the considerable broadening of the corresponding DLTS peak.

7.9 Possible reasons for ST1/ST3 DLTS and ITS peaks broadening.

As it was already mentioned, DLTS and ITS peaks in Gr-1 and Gr-3 samples corresponding to the ST1 and ST3 defect levels, respectively, are broadened (see Fig. 7.3 and discussion in paragraph 7.2). Neither the shapes of DLTS peaks nor of ITS ones could be simulated by 2 or more point-like levels with the close energies (activation enthalpies) using the simple model developed for point-like defects.

By discovering the effect of strong electric field influence on the emission process from the shallow levels, it seems reasonable to try to explain the observed broadening of corresponding DLTS and ITS peaks just by this original effect. Indeed, when considering the Poole-Frenkel effect, the thermal emission rate is enhanced by the electric field as (see Eq. 7.7)

$$e_p(T) = \gamma T^2 \sigma_{pa} \exp\left(-\frac{E_{a0} - \delta E_t}{kT}\right) = e_{p0} \exp\left(\frac{\beta\sqrt{F}}{kT}\right) \qquad (7.27)$$

with the electric field F being dependent on the DN charge Q_s as (see Eq. 7.19 and 7.21)

$$F = \frac{eN_A}{\varepsilon}(w - x_d) - \frac{Q_S}{2\varepsilon} = \frac{eN_A}{\varepsilon}(w - x_d) - \frac{1}{2\varepsilon}\left(Q_{deep} + Q_{shallow}\exp(-e_p t)\right) \qquad (7.28)$$

Hence, the electric field will continuously grow up with the emission process, leading in turn to the continuously lowering of a barrier for emission E_{a0}–δE_t. In other words, in the beginning of the emission process the trap will be more "deep", becoming "shallower" as the holes are emitted from the trap. Thus, continuously increasing of the emission rate e_p may yield to the broadening of DLTS and ITS peaks. Moreover, in this case the peak broadening will strongly depend on the value of Poole-Frenkel coefficient – the higher the coefficient β, the broader should be the peak. This is also in agreement with the broader ITS and DLTS peaks observed in Gr-1 sample for ST1 trap.

However, this theory did not find any experimental confirmation. First of all, if the peak broadening was really caused by the electric field variations, the values of the β coefficients derived from the positions of ITS peaks maxima τ_{max} and from the e_p values taken at the right-side shoulders would be different, i.e. coefficients β would vary depending on the particular ITS signal level (more strictly, β values derived from the maxima positions should be somewhat higher than those derived on the right-side shoulder, as the electric field is expected to be higher when considering the right-side shoulder). However, β-values as obtained from ITS-data at different signal levels are the same within the measurements errors for both ST1 and ST3 traps (see Table 7.3), indicating the absence of the noticeable effect of the electric field variation. Thus, another mechanism of the peaks broadening should be suggested, which is not related with the electric field variations as well as with the Gaussian-type of broadening (see discussion in paragraph 7.2), but which is able to explain the invariability of the DLTS peaks magnitude with the decreasing of the rate window period T_w – see Fig. 5.5 and 5.6.

By attributing the ST1/ST3 traps to the density of states inside the band gap with the fast inter-level exchange, i.e. by ascribing the "band-like" character to ST1/ST3 traps (see paragraph 2.4 and Fig. 2.5), all observed phenomena can be explained. Indeed, in such a case DLTS and ITS peaks would be broadened, whereas the fast inter-level transition rate makes the emission to occur mainly from the upper filled level(s), thus promoting the invariance of corresponding DLTS peaks magnitude on the rate window period T_C. Moreover, when the broadening of DLTS peak is caused by the widening of the electronic spectrum, the dependence of $ln(e_p)$ on the square root of electric field would have the same slope β for all ITS signal level. According to the previous experimental results [Vyvenko 2005], band-like behaviour was also established for the dislocation-related trap level *F-dis* in the uncontaminated p-type $Si/Si_{0.98}Ge_{0.02}/Si$ hetero-structures, which was ascribed to the hole trap state at the stacking fault between partial dislocations (see paragraph 2.4). On the other hand, Castaldini et al [Castaldini 2005b] revealed the "localized" behaviour for their low-temperature DLTS peak ascribed to the dislocation 1D bands. Obviously, additional

investigations are needed to verify the assumption about the band-like character of the ST1/ST3 traps in Gr-1 and Gr-3 bonded samples.

7.10 Electric field influence on the emission from the shallowest SN1/SN3 traps.

The field enhanced emission was not revealed for the shallowest levels SN1/SN3 as it follows from an inspection of the set of DLTS spectra of Gr-1 sample measured with the different U_r voltages presented in Fig. 7.1 lower plot: one can note that SN1 peak is not moving with the increasing of the reverse bias voltage, but rather gives rise to the growth of the shoulder on the low- temperature side of ST1 peak.

Even more compelling evidence was obtained for the pair SN3-ST3 levels in Gr-3 sample. The dependence of DLTS spectrum on the reverse bias voltages U_r for this sample was also measured with the filling pulse voltage U_p=*-1,5 V*, see Fig. 7.9 (compare also with the similar set measured with U_p=*-1V* shown in Fig. 7.2). Now it is clearly visible, that only ST3 peak is shifting towards the lower temperature with increasing of the electric field, whereas SN3 peak remains at the same temperature position, thus leading to the broadening of the joint overlapped peak on the low-temperature side. Finally, when the strongest overlapping of SN3 and ST3 peaks at U_r=*7V* is achieved, the joint peak with the very smoothed top arises.

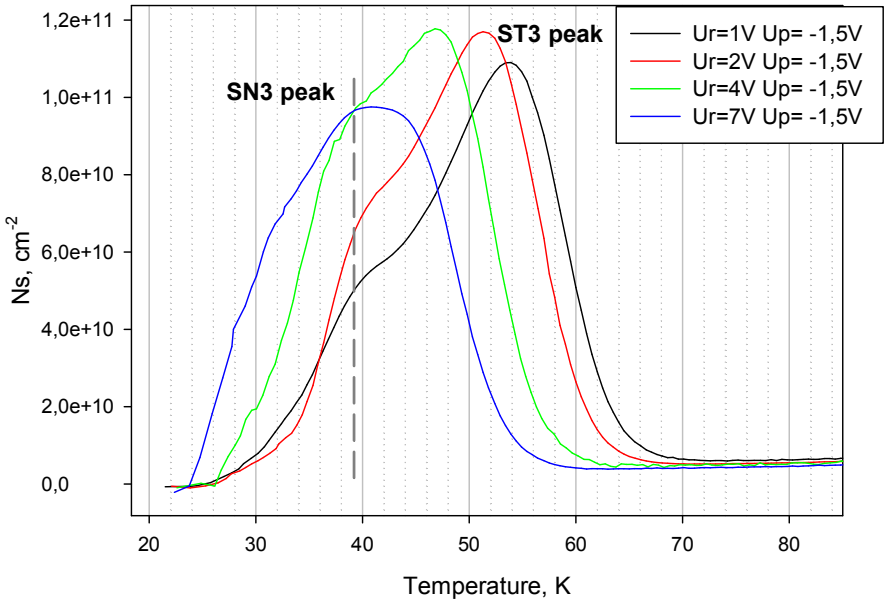

Figure 7.9. Set of DLTS spectra of Gr-3 sample measured with different reverse bias voltages and with the filling pulse voltage U_p=*-1,5 V*. Other DLTS-scan parameters: filling pulse duration t_p=100μs, rate window T_w=20ms, reverse bias voltages U_r are shown in the legends. Vertical dashed line shows the approximate temperature position of SN3 peak.

A strong overlapping of SN3 and ST3 peaks (as well as of SN1 and ST1 peaks) made it impossible to obtain the reliable emission parameters for the shallowest levels SN1/SN3. Thus, at the moment it is not clear, whether the SN-traps have the same parameters in Gr-1 and Gr-3 samples or not. However, as it could be supposed from the comparison of the approximate temperature positions of SN1 and SN3 peaks – which could be estimated as ~30K for SN1 peak and ~40K for SN3 peak (marked by the grey dashed lines in Fig. 7.1 and 7.9), the SN1 level seems to be shallower than SN3 one. Some considerations concerning the origin of these traps will be discussed in Chapter 8.

7.11 Summary of the Chapter 7.

As a result of detailed investigations of ITS and DLTS spectra measured with different reverse bias voltages U_r, the following particular features of the shallow levels ST1/ST3 and SN1/SN3 were revealed:

- field enhanced emission following the Poole-Frenkel law was observed for the main ST1/ST3 levels, but not for the shallower levels SN1/SN3;
- Poole-Frenkel coefficients β obtained for ST1 and ST3 traps appeared to be larger than that predicted theoretically for the interaction of Coulomb centre with electric field (3D-model). Moreover, Poole-Frenkel coefficient obtained for the ST1 trap in Gr-1 sample was found to be larger than that for ST3 trap in Gr-3 sample;
- donor-like character of the ST1/ST3 traps together with the particular dependence of the coefficient β value on the DN structure suggest another mechanism of the field enhanced emission in Gr-1 and Gr-3 samples, which has nothing in common with the classical model of J. Frenkel [Frenkel 1938];
- activation enthalpy of ST3 trap approximated toward the zero electric field appeared to be *~10-15 meV* higher than the corresponding enthalpy of ST1 trap, thus showing a general agreement with the PL results;
- “band-like” character was supposed for ST1 and ST3 traps in order to explain the observed broadening of the respective DLTS and ITS peaks.

Chapter 8
Theory of Poole-Frenkel effect due to elastic strain field of dislocations.

In the previous chapter a distinctive feature of the shallow DN-related ST1/ST3 traps was described – electric field enhanced emission complying with the Poole-Frenkel law. It was also shown, that the discovered effect could not be explained in the framework of the classical theory developed by J. Frenkel (Eq. 7.5), which describes the trap with Coulomb attractive potential in the presence of a uniform electric field. The fact of particular dependence of the derived Poole-Frenkel coefficients on the DN structure in Gr-1 and Gr-3 sample has led us [Trushin 2011b] to the assumption about the dislocation-strain-related origin of the observed phenomenon.

In the present chapter the details of theoretical calculations of Poole-Frenkel effect due to the strain fields of screw and 60° dislocations for the valence band (i.e., for the levels located in the lower half of band gap) in silicon are presented, resulting in a good agreement with the experimental findings. Furthermore, theoretical calculations allowed us to throw more light on the origin of the shallow ST1/ST3 and SN1/SN3 traps detected in SA-samples, pointing to the particular element of the dislocation network responsible for the shallow traps appearance.

8.1. Theory of Poole-Frenkel effect due to elastic strain fields of isolated screw and 60° dislocations.

- generalization of the Poole-Frenkel theory

Generally speaking, Poole-Frenkel lowering of the potential barrier for thermoemission of the captured carriers reflects the fact that the defect potential is inversely proportional to the distance from the defect *r*, i.e. the potential is of *1/r* type. Thus, Eq. 7.3 describing the interaction of defect potential with an electric field *F* aligned in the *–z* direction, could be rewritten in more general form as

$$V(r) = -e(\frac{\Psi}{r} + Fr\cos\theta), \tag{8.1}$$

where Ψ is the particular shape of an actual defect potential and θ is the angle between *F* and *r* (see Fig. 7.5 in previous Chapter 7). The resulting potential *V(r)* has a maximum at the distance

$$r_{\max} = \sqrt{\frac{\Psi}{F\cos\theta}}, \tag{8.2}$$

giving rise to the reduction of the emission activation energy by the value of

$$\delta E_T = -e\beta\sqrt{F} \tag{8.3}$$

where

$$\beta = 2\sqrt{\Psi\cos\theta} \tag{8.4}$$

is the Poole-Frenkel coefficient (compare with the Eq. 7.4 and 7.5). For Coulomb potential

$$\Psi = \frac{e}{4\pi\varepsilon} \tag{8.5}$$

that gives the Poole-Frenkel constant $\beta_{1D}=2,2*10^{-4}\ V^{1/2}\ cm^{1/2}$ for 1D case and, after the integration over spatial angles, $\beta_{3D}=1,8\text{-}2*10^{-4}\ V^{1/2}\ cm^{1/2}$ for 3D case, see discussion in paragraph 7.3.

Beside Coulomb potential, deformation potential of dislocations is also inversely proportional to the distance *r*, i. e. exhibit a symmetry of *1/r* type [Hirth and Lothe 1970]. Thus, qualitatively similar field effect on the thermal emission of the carriers from the electronic states located close to the dislocation cores can be expected. In the following, calculations of Poole-Frenkel effect will be performed for the hole thermoemission from the dislocation-related level to the valance band (*Γ-point*) in silicon. For this zone point, theory [Bir and Pikus 1974] predicts that both uniaxial and shear components of dislocation deformation tensor can contribute to the deformation potential.

- deformation tensor in natural crystal coordinates

The components of the dislocation deformation tensor are usually expressed in the own dislocation coordinate system, where x direction coincides with the dislocation line which is [110] for both screw and 60° dislocations in silicon. Two other coordinates directions are arbitrary and could be considered as z direction along [001] and y direction along $[\bar{1}10]$ directions, see Fig. 8.1.

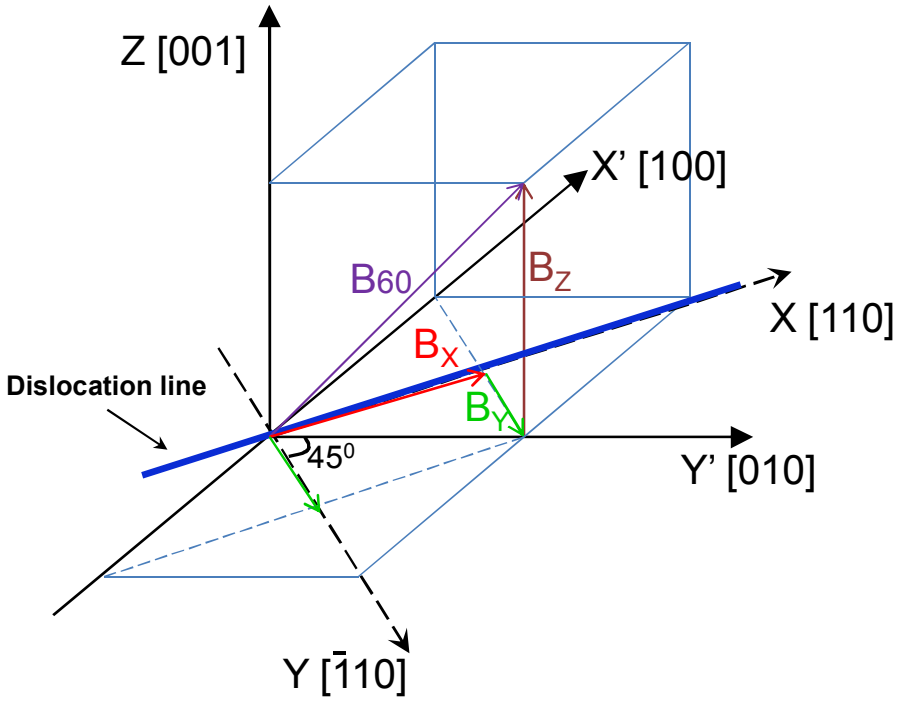

Figure 8.1 Rotation of dislocation coordinate system around the z axis by the angle of 45° in order to fit the natural crystal coordinate system. Dislocation line and the projection of Burgers vector of 60^0 dislocations B_x, B_y and B_z on the corresponding axes are shown. Electric field F is directed along z axis.

In this coordinate system the deformation tensor for screw dislocation consist of two non-zero components ε_{xy} and ε_{zx} [Hirth and Lothe 1970], those explicit form is given by

$$\begin{aligned} \varepsilon_{xz} = \varepsilon_{zx} &= -\frac{Br_y}{4\pi r^2} = -\frac{B}{4\pi r}\sin\theta \\ \varepsilon_{xy} = \varepsilon_{yx} &= \frac{Br_z}{4\pi r^2} = \frac{B}{4\pi r}\cos\theta \end{aligned}, \qquad (8.6)$$

where B is Burgers vector, r is the distance from dislocation and the angle θ is count out from z axis (as the electric field is also directed along z axis). Then, the deformation tensor for screw dislocations written in the matrix form will contain only non-diagonal components

$$\begin{pmatrix} 0 & \varepsilon_{xy} & \varepsilon_{xz} \\ \varepsilon_{yx} & 0 & 0 \\ \varepsilon_{zx} & 0 & 0 \end{pmatrix}. \tag{8.7}$$

For edge dislocation deformation tensor consists of three components including also hydrostatic deformation component ε_{xx}:

$$\begin{aligned}
\varepsilon_{yy} &= -\frac{B_y}{4\pi r(1-\nu)}\left(\cos\theta\left\{(1-2\nu)+2\sin^2\theta\right\}\right)+\frac{B_z}{4\pi r(1-\nu)}\left(\sin\theta\left\{(1-2\nu)-2\cos^2\theta\right\}\right) \\
\varepsilon_{zz} &= -\frac{B_y}{4\pi r(1-\nu)}\left(\cos\theta\left\{(1-2\nu)-2\sin^2\theta\right\}\right)+\frac{B_z}{4\pi r(1-\nu)}\left(\sin\theta\left\{(1-2\nu)+2\cos^2\theta\right\}\right) \\
\varepsilon_{zy} &= \frac{B_y}{4\pi r(1-\nu)}\left(\sin\theta\left\{1-2\cos^2\theta\right\}\right)-\frac{B_z}{4\pi r(1-\nu)}\left(\cos\theta\left\{1-2\sin^2\theta\right\}\right) \\
\varepsilon_{xx} &= Sp(\varepsilon_{ii}) = \frac{(1-2\nu)}{2\pi r(1-\nu)}\left(B_z\sin\theta - B_y\cos\theta\right)
\end{aligned} \tag{8.8}$$

where B_x, B_y and B_z are the projections of the Burgers vectors along corresponding directions and ν is the Poisson ratio (ν=*0,27* for Si). Thus, the deformation tensor for edge dislocation in the matrix form

$$\begin{pmatrix} \varepsilon_{xx} & 0 & 0 \\ 0 & \varepsilon_{yy} & \varepsilon_{yz} \\ 0 & \varepsilon_{zy} & \varepsilon_{zz} \end{pmatrix} \tag{8.9}$$

contains non-zero diagonal components.

The calculations of the dislocation deformation potential have to be performed in the natural crystal coordinate system that for cubic lattices is *x'=[100]*, *y'=[010]* and *z=[001]*, in which the deformation potential constants were defined. This can be done by 45° rotation of the dislocation coordinate system around *z* axis, see Fig. 8.1. The rotation matrix will be [Hirth and Lothe 1970]

$$\begin{pmatrix} \frac{\sqrt{2}}{2} & \frac{\sqrt{2}}{2} & 0 \\ -\frac{\sqrt{2}}{2} & \frac{\sqrt{2}}{2} & 0 \\ 0 & 0 & 1 \end{pmatrix} \tag{8.10}$$

Dislocation deformation tensor in natural crystal system could be obtained then following the rule of second-rank tensor and the resulting deformation tensor will be:

$$\begin{pmatrix} \varepsilon_{yy}/2+\varepsilon_{xy} & \varepsilon_{yy}/2 & \frac{\sqrt{2}}{2}(\varepsilon_{zy}+\varepsilon_{zx}) \\ \varepsilon_{yy}/2 & \varepsilon_{yy}/2-\varepsilon_{xy} & \frac{\sqrt{2}}{2}(\varepsilon_{zy}-\varepsilon_{zx}) \\ \frac{\sqrt{2}}{2}(\varepsilon_{zy}+\varepsilon_{zx}) & \frac{\sqrt{2}}{2}(\varepsilon_{zy}-\varepsilon_{zx}) & \varepsilon_{zz} \end{pmatrix}, \tag{8.11}$$

where for screw dislocations only the strain components specified in Eq. 8.6 should be considered (since all other components are zero), while for edge dislocation – components which are derived in Eq. 8.8. Since 60° dislocation is a dislocation of the mixed type with the angle between its Burgers vector *b* and dislocation line equal to 60°, the corresponding strain tensor for such kind of dislocations could be obtained using the combination of strain components of screw and edge dislocations taken with the appropriate projections of Burgers vector onto the particular axes, see the sketch in Fig. 8.1.

- ***dislocation deformation potential***

Following the deformation potential theory [Bir and Pikus 1974] the valence band in silicon at Γ*-point* exhibits a shift due to hydrostatic component and a splitting into two sub-bands due to the shear components of deformation tensor

$$V_{1,2} = \alpha\varepsilon_{x'x'} \pm \pm\left(\frac{b^2}{2}[(\varepsilon_{x'x'}-\varepsilon_{y'y'})^2+(\varepsilon_{z'z'}-\varepsilon_{y'y'})^2+(\varepsilon_{x'x'}-\varepsilon_{z'z'})^2]+d^2(\varepsilon^2{}_{x'y'}+\varepsilon^2{}_{x'z'}+\varepsilon^2{}_{y'z'})\right)^{1/2}$$

where the particular element of strain tensor ε_{ij} is the *ij* component of the matrix Eq. 8.11.

Considering the explicit form of deformation tensor Eq. 8.11, the resulting deformation potential of the dislocations can be written as:

$$V_{1,2} = aSp(\varepsilon_{ii}) \pm \pm\left(\frac{b^2}{2}[(2\varepsilon_{xy})^2+(\varepsilon_{zz}-\frac{\varepsilon_{yy}}{2}+\varepsilon_{xy})^2+(\varepsilon_{zz}-\frac{\varepsilon_{yy}}{2}-\varepsilon_{xy})^2]+\frac{d^2}{2}((\varepsilon_{zy}+\varepsilon_{zx})^2+(\varepsilon_{zy}-\varepsilon_{zx})^2+\frac{\varepsilon_{yy}^2}{2})\right)^{1/2} \tag{8.12}$$

where the numerical values of deformation potential constants for valence band in silicon are [Farvacque 2001]: $a=5{,}1eV$, $b=2{,}2eV$, $d=5{,}1eV$. For screw dislocations Eq. 8.12 includes only the shear components, since Sp(ε_{ii})=0 here. Whereas for edge dislocations - includes both shear and non-uniaxial components.

Potential $V_{1,2}$ expressed by Eq. 8.12 is per se the desired Ψ-factor introduced in Eq. 8.1. Therefore, using Eq. 8.12 together with explicit form of deformation components

presented in Eq. 8.6 and Eq. 8.8 Poole-Frenkel coefficient β can be calculated using Eq. 8.4. In the calculations electrical field was directed to *z,* corresponding to [001] axis. Thus, for pure screw dislocations one should take in Eq. 8.6 $B_x = B = 0{,}384$ *nm*. For 60° dislocation $B_x = B/2$, $B_z = 0{,}707B$ (see Fig. 8.1), whereas B_y is either $+B/2$ or $-B/2$ corresponding to those two possible orientations of 60° dislocation with respect to the (001) plane which are marked as *b1* and *b2* in Fig. 8.2, respectively [Trushin 2011b].

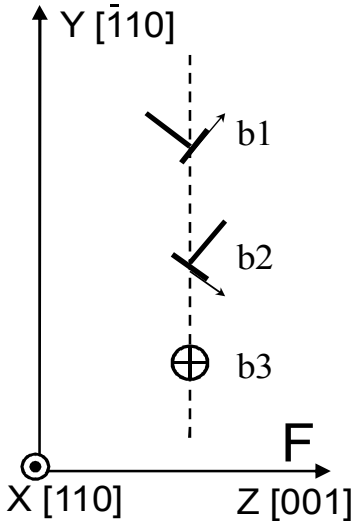

Figure 8.2 Orientations of 60° (b1, b2) and screw (b3) dislocations in the projection on (110) plane [Matare 1971]. Dashed line shows the projection of the (001) plane of dislocation network. Electric field *F* is directed along [001] direction.

Figure 8.3 represents the angle dependences of $V_{1,2}$ potential calculated for screw dislocations and for 60° dislocations with two possible orientations in DN plane (*b1* and *b2*, as depicted in Fig. 8.2). The main features of the obtained dependences are: 1) significant splitting of the valence band around the dislocations caused by shear deformations; 2) lower sub-band forms an attractive potential for the most directions that can cause Poole-Frenkel effect; 3) the shapes of the corresponding potentials for two possible orientations of 60° dislocation are similar to each other but shifted by the angle of about 70°.

Upper plot in Fig. 8.4 shows $\beta(\theta)$ dependence calculated for the lower valence band V_2 at screw, at both types of 60° dislocations as well as for 3D Coulomb potential (calculations for V_1 band give generally the same results, but due to $\cos\theta$ function under the square root in Eq. 8.4, the rational quantities will appear in the half-periods (-180; -90) and (90; 180) – i.e. $\beta(\theta)$ dependence will be broken in two parts; whereas in those half-periods no lowering of the barrier height occurs in the chosen coordinate system with the electric field *F* directed along [001]). As one can note in Fig. 8.4, dependence $\beta(\theta)$ for screw dislocation appeared to be rather similar to that for Coulomb potential, while for 60° dislocations of *b1* orientation it has a significantly larger maximum value.

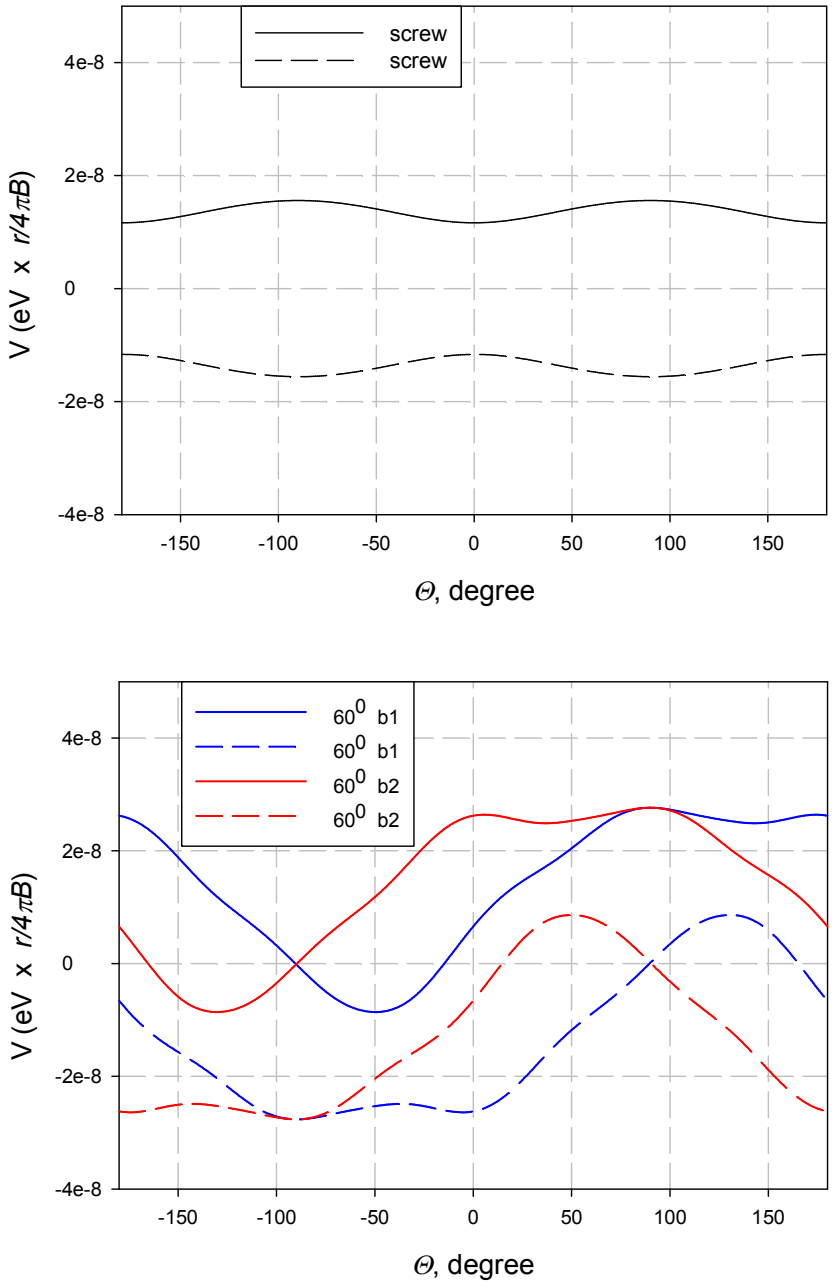

Figure 8.3 Calculated angle dependences of deformation potential (Ψ-factor) for screw dislocations (upper plot) and for 60° dislocations (lower plot) with the orientations *b1* and *b2* as shown in Fig. 8.1. Solid lines correspond to the sign "plus" in the Eq. 8.12, dashed lines – to the sign "minus". The angle is counted from [001] direction that coincides with the direction of electric field.

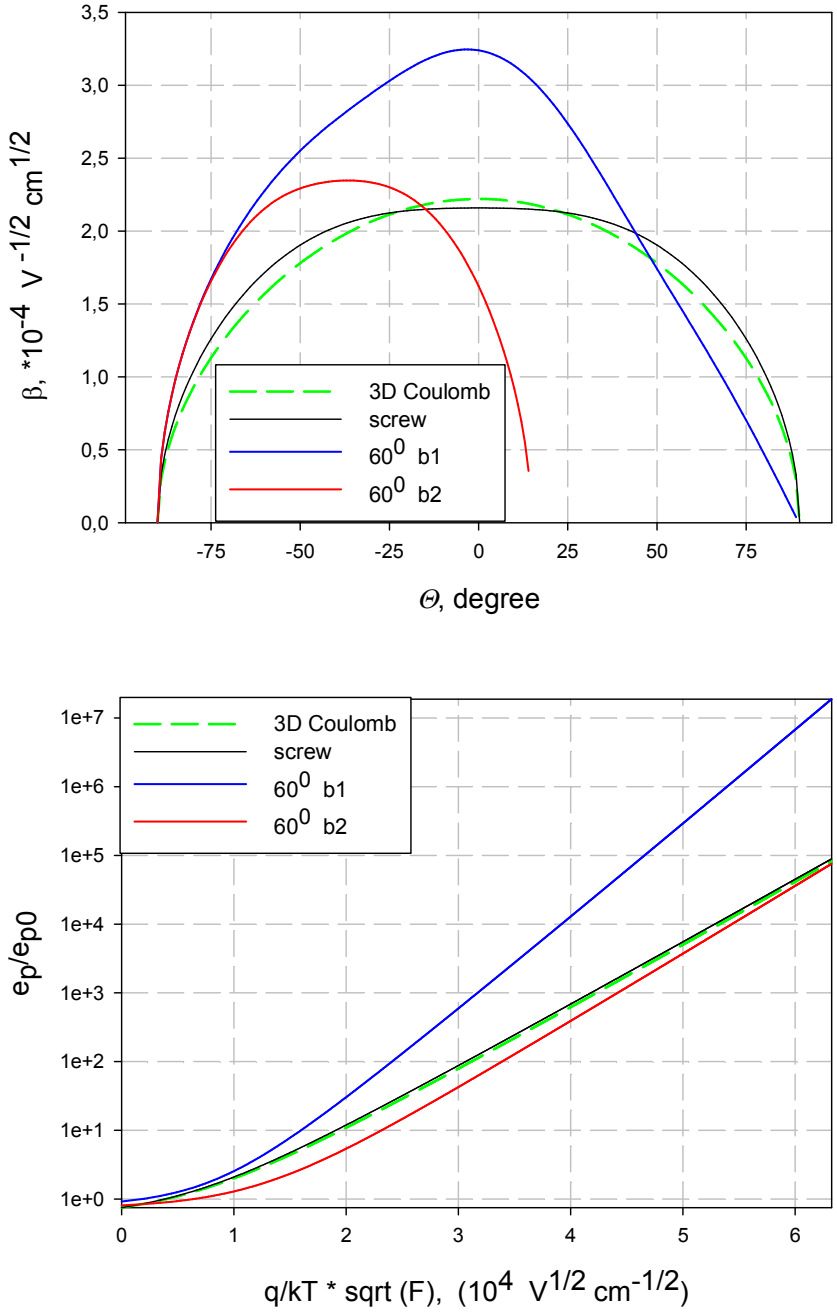

Figure 8.4 Angle dependence of Poole-Frenkel constant β (upper plot) and relative enhancement of the hole thermoemission under applied electric field (lower plot) for 3D Coulomb potential and for the deformation potentials of screw and 60 degree dislocation with two orientations *b1* and *b2* depicted in Fig. 8.1. Line assignments are shown in the legends.

The calculation of field enhanced emission rate, $\frac{e_p(F)}{e_{p0}}$, requires an integration over the space angle θ due to the spatial variation of δE_T. For 3D coulomb potential one obtain the integral similar to Eq. 7.8, which can be solved analytically [Hartke 1968] – see solution Eq. 7.9.

The calculation of the field enhanced emission rate for 2D strain field of dislocation is performed making use the integration according to:

$$\frac{e_p(F)}{e_{p0}} = \frac{1}{2\pi}\left(\alpha \int_{-\pi/2}^{\pi/2} d\theta \exp[\frac{\delta E_t(\theta)}{kT}] + 1 - \alpha \right) \tag{8.13}$$

where α is the ratio of the angles where enhanced emission takes place (α is 0,5 for screw and 60^0 dislocation of *b1* orientation, but is 0,289 for *b2* orientation). The integration of Eq. 8.13 succeeds only numerically.

The results of numerical integration of Eq. 8.13 for all dislocations as well as for 3D Coulomb potential as reported in [Hartke 1968] (Eq. 7.9) are presented in Fig. 8.4 lower plot. At sufficiently high electric fields all of the curves can be well fitted with Poole-Frenkel law $e_p(F)/e_{p0} = \exp(\beta_{eff}\sqrt{F})$ (electric field in the investigated samples at T_{MEAS}=40…50K corresponds to the interval just between *~2,3*10^4* and *~7*10^4* in Fig. 8.4). The curves for the Coulomb potential and for the screw dislocation deformation potential for the valence band coincide practically with each other giving $\beta_{eff} \approx 2{,}1\cdot 10^{-4}\, cm^{1/2}\, V^{-1/2}$. Poole-Frenkel coefficients obtained for 60° dislocation are $\beta_{eff}(b1) \approx 3{,}1\cdot 10^{-4}\, cm^{1/2}\, V^{-1/2}$ and $\beta_{eff}(b2) \approx 2{,}25\cdot 10^{-4}\, cm^{1/2}\, V^{-1/2}$.

8.2. Stress fields close to the dislocation network.

For the bonded samples were under investigation the interaction of the elastic strains between the dislocations composing the dislocation network must be taken into consideration, what generally results in the localization of dislocation strain field and deformation potential. Figure 8.5 represents the sketches of two dislocation structures observed experimentally in Gr-1 (predominantly the array of parallel 60^0 dislocations) and Gr-3 sample (square network of screw dislocations), respectively.

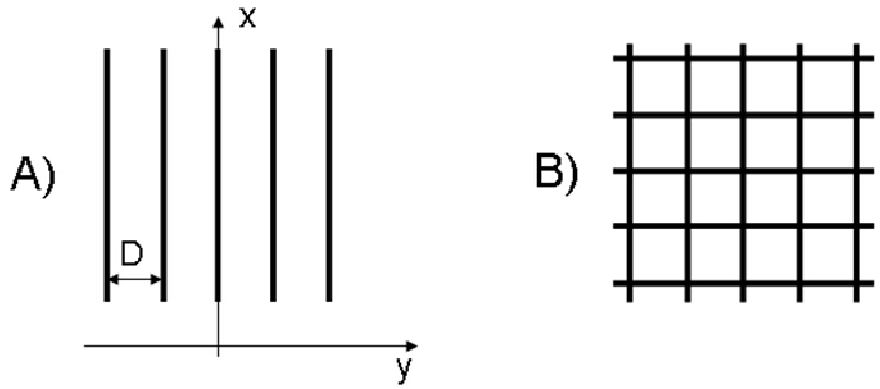

Figure 8.5 (A) Row of parallel dislocations and (B) square network of dislocations with the interdislocation distance *D*. *Z*-axis is going perpendicular to the pictures plane.

For the row of screw dislocation along *x* that expands in *y* direction (Fig. 8.5A), elastic strains are [Hirth and Lothe 1970]:

$$\varepsilon_{xz} = \frac{B}{4D}\frac{\sin 2\pi Y}{\cosh 2\pi Z - \cos 2\pi Y}$$
$$\varepsilon_{xy} = \frac{B}{4D}\frac{\sinh 2\pi Z}{\cosh 2\pi Z - \cos 2\pi Y} \qquad (8.14)$$

where $Z=z/D$, $Y=y/D$. Asymptotic behavior of expressions 8.14 at $Y=0$ (i.e. at the exact dislocation position in a row) when $Z \to 0$ corresponds to the strain of an isolated dislocation:

$$\varepsilon_{xy} \to \frac{B}{4\pi z}, \qquad (8.15)$$

whereas for $Z \to \infty$ ε_{xz} disappeared, but ε_{xy} reaches a stationary value of B/4D, indicating thereby the presence of long-rang stress field for a row of dislocations.

The deformation components for the dislocation network consisting of two rows of screw dislocations that are going along *x* and *y* (Fig. 8.5B) will be equal to

$$\varepsilon_{xz} = \frac{B}{4D}\frac{\sin 2\pi Y}{\cosh 2\pi Z - \cos 2\pi Y}$$
$$\varepsilon_{yz} = \frac{B}{4D}\frac{\sin 2\pi X}{\cosh 2\pi Z - \cos 2\pi X} \qquad (8.16)$$
$$\varepsilon_{xy} = \frac{B}{4D}\sinh 2\pi Z\left(\frac{1}{\cosh 2\pi Z - \cos 2\pi Y} - \frac{1}{\cosh 2\pi Z - \cos 2\pi X}\right)$$

The presence of the second dislocation row makes $\varepsilon_{xy} = 0$ far from the plane of the network ($Z \to \infty$) providing the pure rotation of the matrix in the vicinity of the network without any long-range fields. Besides, according to Eq. 8.16, ε_{xy} along the network diagonals (X=Y) is zero including the dislocation intersection points and remains practically constant along the most part of the segments between the knots, see Fig. 8.6.

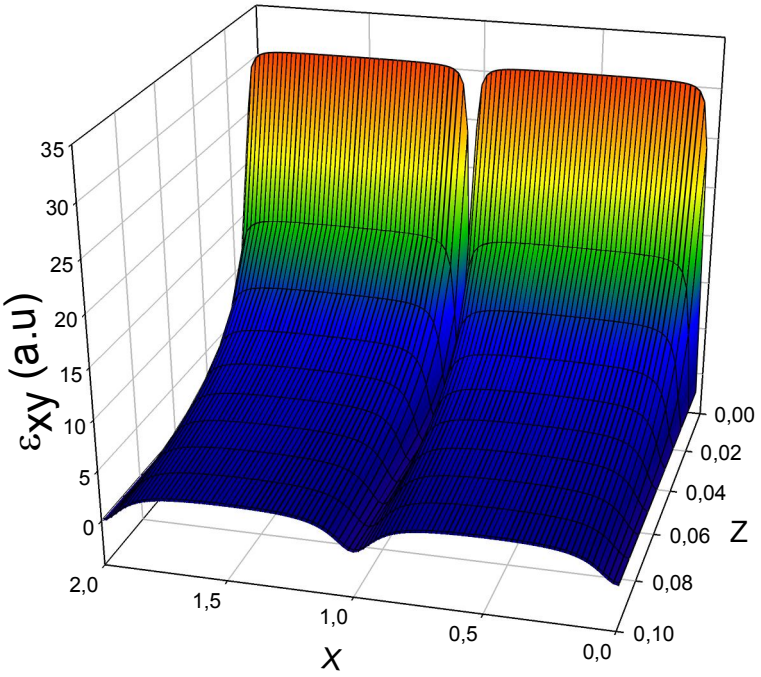

Figure 8.6 Decreasing of the strain field ε_{xy} while moving away from the DN plane which corresponds to *Z=0*. Integer numbers of *X* correspond to the positions of dislocation lines, according to the drawing Fig. 8.5.

The asymptotic behavior of ε_{xy} at the middle of regular segments (X=0, Y=0,5) when $Z \to 0$ is also similar to the case of single dislocation:

$$\varepsilon_{xy} = \frac{B}{4D} \frac{-2\sinh 2\pi Z}{(\cosh 2\pi Z)^2 - 1}\bigg|_{Z\to 0} \to -\frac{B}{4D} 2 \frac{2\pi Z}{(2\pi Z)^2} = -\frac{B}{4D\pi z}. \qquad (8.17)$$

Figure 8.7 compares the deformations ε_{xy} of an isolated dislocation, row of dislocations and of the square network of dislocations as a function of the distance from the DN plane (corresponding to Z=0). The main effect of the dislocation interaction is a significant shortening of the deformation field radius like the screening effect in electrostatics. At the distances from the dislocated interface of about *0,5D* (the half-period of the dislocations in a row or network) strain ε_{xy} reaches a spatially independent value

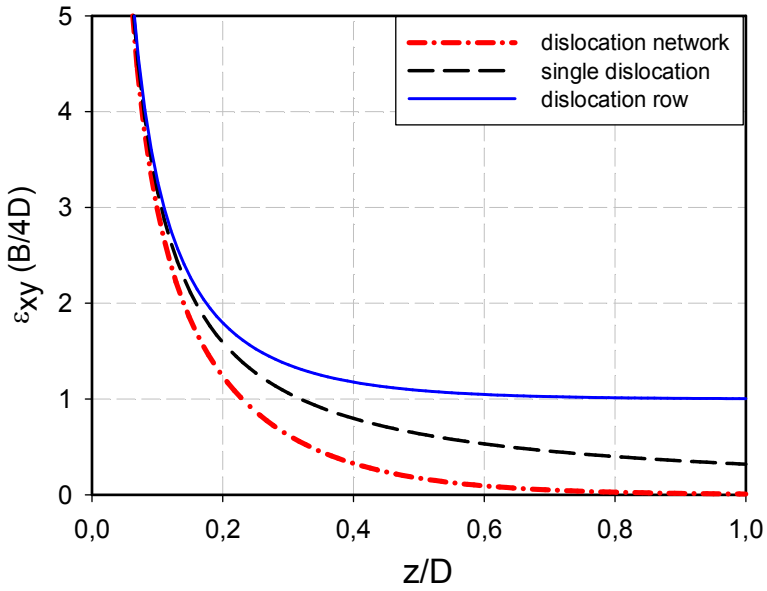

Figure 8.7 Deformations of an isolated dislocation (long dashed), the dislocations in the row (solid) and in the square network (dash-dot) as a function of the distances from the DN plane corresponding to Z=0. For DN Z-coordinate is going through the centre of dislocation segments between the nodes.

that is *B/4D* for dislocation row and nearly zero for dislocation network. One should also note, that for the dislocation network the significant difference of the deformation field from *1/r* law started at the distances of approximately *z=D/2,5*, whereas for the row of dislocation – at the distances of *z=D/4* [Trushin 2011b]. Obviously, Poole-Frenkel effect due to elastic strain field of dislocations can be observed under application of the electric field above the value F_{min} that corresponds to Poole-Frenkel radius r^* of about *D/2,5* or *D/4*, respectively.

The latter values can be used for estimation of F_{min} as the function of D by using the following relation (Eq. 8.2 and Eq. 8.4 with θ=*0*):

$$r^* = \frac{\beta}{2\sqrt{F_{\min}}} \tag{8.18}$$

$$F_{\min} > \left(\frac{(2,5 \div 4)\beta}{2D} \right)^2 \tag{8.19}$$

or estimate D_{min} for the given electric field ranges:

$$D_{\min} > \frac{(2,5 \div 4)\beta}{2\sqrt{F_{\min}}} = (2,5 \div 4) \cdot r^* \tag{8.20}$$

where the numbers 2,5 or 4 relate to network or to the row, respectively. Similar estimation is valid for the row of edge type dislocations as well (see [Hirth and Lothe 1970]).

Thus, following the theoretical calculations presented in this and in previous paragraphs it can be concluded that the β–coefficient value of dislocation-related Poole-Frenkel effect depends strongly on the type, on the orientation and on the density of dislocations in the DN.

8.3. Comparisons with the experimental results.

Considering the experimentally obtained Poole-Frenkel coefficients β (Table 7.4) and electric field values used in the experiments (see axis of abscissas in Fig. 7.6 or 7.8), the corresponding Poole-Frenkel radiuses (Eq. 8.18) could be estimated as $r^*(ST1) \approx$ *8-12 nm* and $r^*(ST3) \approx$ *5-10 nm* for the carrier emission from ST1 and ST3 traps, respectively. Comparing the obtained r_m values with the dissociation width d – which in equilibrium conditions is close to $d_0 \sim 5$ *nm* – one could see, that even minimal r^* values (corresponding to the highest electric field) are greater than the dissociation width d in both samples. Therefore, the direct comparison of the Poole-Frenkel coefficients β calculated theoretically for undissociated screw and 60° dislocations with those obtained from the DLTS and ITS experiments is correct, in spite of dissociation (as expected) character of the dislocations composing the networks in Gr-1 and Gr-3 samples.

- ***Gr-1 sample***

According to microscopic images in Fig. 5.11, DN in Gr-1 sample consists of a row of uni-directional 60° dislocations separated by the distances of about *60 nm*, which are disturbed by the curved 60° dislocation of II set. In other words, DN structure in this sample looks like a row of parallel dislocations rather than the square network.

Minimal interdislocation distance D_{min} (Eq. 8.20 with coefficient 4 for a row of dislocations) when the theory of isolated dislocation is still valid could be estimated as about *45 nm*, considering the minimal electric field as *~10 kV/cm* (see Fig. 7.5 or 7.7) and coefficient β taken from Table 7.4. Thus, the theory conditions are satisfied and predicted Poole-Frenkel coefficient value is expected to be of about $\beta_{eff}(b1) \approx 3{,}1 \cdot 10^{-4}\, cm^{1/2} V^{-1/2}$ for the case of most favourable orientation of 60° dislocation in DN or $\beta_{eff}(b2) \approx 2{,}25 \cdot 10^{-4}\, cm^{1/2} V^{-1/2}$ for the second possible orientation *b2* (see Fig. 8.2).

Experimentally obtained value $\beta_{exp}(ST1) = (2{,}4 \pm 0{,}3) \cdot 10^{-4}\, cm^{1/2} V^{-1/2}$ (see Table 7.4) seems to fall just between the values calculated for *b1* and *b2* orientations. Thus, one may suppose nearly equal amount of 60° dislocations with *b1* and *b2* orientation composing the DN in this sample, leading to the intermediate value of the Poole-Frenkel coefficient.

- ***Gr-3 sample***

The dislocation structure in Gr-3 sample consists of square mesh of perfectly straight screw dislocations and the rows of curved 60° dislocations that are inclined in average to the screw dislocation lines under the angle of about 30°, see Fig. 5.12. The interdislocation distances for screw dislocations are of about *8 nm* while for 60° varies from *30* to *50 nm*.

For the lowest electric field in this sample of *~7,3 kV/cm* (corresponding to the case of filled shallow states, see Fig. 7.5), the critical distances D_{min} as estimated from Eq. 8.20 were found to be of about *23 nm* for the mesh of screw and *~35 nm* for the row of 60° dislocations. Hence, the validity of the theory for isolated dislocation is satisfied for the row of 60° dislocations, but not for the square network of screw ones. This means that the screw dislocations have to be ruled out of the consideration as a possible origin for the observed Poole-Frenkel effect. The Poole-Frenkel coefficient value obtained from experiment $\beta_{\exp}(ST3) \approx (1,9 \pm 0,2) \times 10^{-4}\, cm^{1/2}\, V^{-1/2}$ (Table 7.4) corresponds to the theoretically predicted value for 60° dislocations with *b2* orientation.

- ***Probable reason for different Poole-Frenkel constants in Gr-1 and Gr-3 samples***

The difference between the experimental β-values for the shallow levels ST1 and ST3 in Gr-1 and Gr-3 sample, respectively, can be then explained by the different crystallographic orientations of the handle and of the top wafers. The predominant 60^0 dislocations orientation *b1* or *b2* could be realized due to an asymmetry of the tilt misorientation between the handle and the top wafers. For example, when the handle wafer has exact (100) orientation and the tilt between the bonded wafers appear due to misorientaion of the top wafer only or instead, when both wafers have had particular tilt misorientaion component before the bonding process. Since the tilt between the bonded wafers was not controlled during the bonding process and arose as the result of wafers polishing inaccuracy, such explanation seems to be reasonable.

Nevertheless, one can not exclude that the lower β in Gr-3 sample was due to the interaction of 60^o dislocations with screw dislocations giving rise to a zigzag configuration of resulting dislocations [Föll 1979]. Such configuration, obviously, could have the strain field that differs significantly from the strain field of a straight dislocation considered here.

8.4. Possible origins of the shallow traps.

- ST1/ST3 traps and D1 luminescence centres

Direct conclusion following from the above discussed statements – particular structural element responsible for the low-temperature ST3 peak in Gr-3 sample exhibiting Poole-Frenkel effect should be directly related with 60° dislocations and not with the mesh of screw ones. This correlates with the suggestions made in Chapter 5 that the origin of D1 luminescence centres in Gr-3 sample is related with the triple dislocation knots – intersections of 60° and screw dislocations and that the ST3 shallow level is just the level directly participating in D1 radiative transition. For Gr-1 sample it was of course obvious – origins of D1 luminescence as well as of shallow ST1 level are directly related with 60° dislocations and products of their reactions – triple dislocation knots arising at the intersection points of 60° dislocations of I and II sets (see Fig. 5.11).

On the contrary, intersection points of screw dislocations (four-fold dislocation knots) could scarcely serve as D1-sources: according to Eq. 8.16 and Fig. 8.6, strain field is zero in the intersection points therefore no shallow strain-related states could be expected there, whereas no deep states could be expected at the straight dislocation segments between the intersection points. Consequently, space delocalisation of deep and shallow states capable of participating in D1 recombination processes exists for the screw dislocation mesh, thus reducing the probability of radiative recombination of trapped carriers.

Notwithstanding, ST1 and ST3 levels have different activation enthalpies E_{a0} at zero electric field – ST1 level is shallower than ST3 one (see Chapter 7), although these both levels were have 60° dislocations as their origin. How this difference in shallow levels energies can be explained and how it can be related with different DN-structures in Gr-1 and Gr-3 sample?

According to Rouviere et al. [Rouviere 2000], the size of the stacking fault d bounded by two partials (Fig. 2.1) depends strongly on the distances between the neighbouring dislocations composing the DN (specifically, in the work of Rouviere et al. – on the distances between the screw dislocations, i.e. on the twist misorientation angle, see also paragraph 3.4). Whereas the stacking fault size d is known to have a significant influence onto the shallow dislocation-related 1D states: one may expect deeper positions of shallow bands E_{De}, E_{Dh} for dissociated dislocations with smaller d, since the higher strain arising due to the interference between the strain fields of partial dislocations pushes the shallow 1D bands deeper into the band gap [Kveder 1996]. Experimentally the influence of the stacking fault size on the energy position of dislocation-related shallow bands E_{De} and E_{Dh} was proved as the shift of energy position of D3/D4 luminescence lines towards the lower energies with the decreasing of the stacking fault size d [Sauer, 1986] [Kveder 1996], see also discussion in Chapter 2. Additionally, theoretical calculations of

Lehto [Lehto 1997] (see paragraph 2.2) showed, that the energy position of stacking fault shallow states near the edge of the valence band would be also shifted deeper into the band with the decreasing of the stacking fault size d (Fig. 2.3).

At the moment, there is no clarity about the exact values of the dissociation widths for dislocations in Gr-1 and Gr-3 samples. However, as it follows from the experimental results of Rouviere et al., it is necessary to consider closely the distances between the nearest neighbouring dislocations and to compare them with the equilibrium stacking fault width d_0 in order to surmise the probable dissociation width.

In Gr-1 sample, the distance between the uni-directional 60° dislocations is *60 nm* and the mean length of the straight dislocation segments between the two neighbouring triple dislocation knots (along the 60° dislocation lines of the II set) is also about *50-60 nm,* see Fig. 5.11. These distances are large enough to allow the dislocation dissociation with the equilibrium stacking fault width of d_0 *~5-6 nm*. In Gr-3 sample, the interdislocation distances for 60° dislocations vary from *30* to *50 nm*, but at the same time 60° dislocations are strongly perturbed by the dense network of screw dislocations with the mesh size of about *8 nm*, see Fig. 5.12. Thus, the dissociation width of 60° dislocations is expected to be smaller than the equilibrium one $d<d_0$, implying deeper position of ST3 level in silicon band gap (irrespectively whether this level is due to stacking fault states or dislocation related 1D states).

- SN1/SN3 traps

It seems reasonably to suppose that the particular structural element(s) of DN giving rise to the second shallow level SN1/SN3 which didn't reveal any field-enhanced emission should be located somewhere far from the 60° dislocations or, more exactly, far from the regions of high elastic strain field. In principle, SN3 traps in Gr-3 sample could be related with the square network of screw dislocations. However, the question arises concerning the origin of SN1 level, since the network of screw dislocations is absent in Gr-1 sample. Taking in mind the similar sets of defect levels revealed in Gr-1 and Gr-3 samples, and, as a consequence – the similarity of their origins, it may be also expected that the origin of SN1 and SN3 traps in both samples should be the same as well.

It is interesting to note, that in the recent work of Bondarenko et al. [Bondarenko 2011], who studied the cathodoluminescence (CL) spectra on the bonded sample similar to Gr-3 one studied in present work, two components of CL spectrum related with DN were registered in the vicinity of the D1 band. Authors have supposed, that shallow levels denoted in the present work as SN3 and ST3 are responsible for these two components of the broad CL line near *0,8 eV*, i.e. that both SN3 and ST3 levels are participating in the radiative recombination. Regarding, that the square network of screw dislocations in Gr-3

sample doesn't participate in radiative recombination in its own (as it was just discussed above), this observation of Bondarenko et al. may serve as additional confirmation that SN3 traps are not related with the screw dislocations.

Alternatively, the special places along the 60° dislocations (or zig-zag dislocations) of strong deformation potential localization could be supposed as structural elements responsible for SN1/SN3 traps. It is known, that localization of deformation potential may result in the significant changes of dislocation strain field (as an example – ε_{xy} strain component turns to zero in the intersection points of screw dislocation), thus leading to the disappearance of the dislocation-related Poole-Frenkel effect. Otherwise, it could be supposed that SN1/SN3 levels without Poole-Frenkel effect are related with some defects located outside the dislocation cores, for example – with small oxygen clusters (which are not visible by TEM). In such interpretation, the second CL component of the smaller energy is simply related with the radiative recombination on oxygen clusters or precipitates, which is known to give rise to the luminescence line of the energy *~0,78 eV* [Pizzini 2000]. Additional experiments are needed to clarify the origin of the shallowest SN1/SN3 states.

8.5. Comparison with other estimations of dislocation-related 1D bands energy position.

Now, having established the relation of ST1/ST3 shallow levels with 60° dislocations and knowing the activation energies of these levels at zero electric field $E_{a0}(ST1) \approx 90\text{-}95\ meV$ and $E_{a0}(ST3) \approx 100\text{-}110\ meV$ (Table 7.4) it is worth to compare the obtained energies with the results of other research teams.

First of all – with the results of Castaldini et al [Castaldini 2005b], who have also measured the DLTS spectra on the sample containing a regular array of 60° dislocations and found the shallow level STh with $E_a \sim 70\ meV$ (*68 meV* according to our estimation from Arrhenius graph in Fig. 8.8), which was ascribed to the shallow dislocation related states. Unfortunately, the electric field occurring during those DLTS experiments is unknown (as well as the presence of electric field enhanced emission in general). Moreover, as in the samples studied by Castaldini et al the dislocations were located not on the single surface inside the SCR of Schottky diode but instead – were distributed across the whole sample volume, one can expect different effect of electric field onto the dislocations located close to the metal / semiconductor interface and those located closer to the SCR edge. Comparing the Arrhenius plots for the STh shallow level detected by Castaldini et al [Castaldini 2005b] with the Arrhenius plots obtained for the shallow ST1/ST3 levels, a good coincidence can be observed with Arrhenius plot of ST3 level

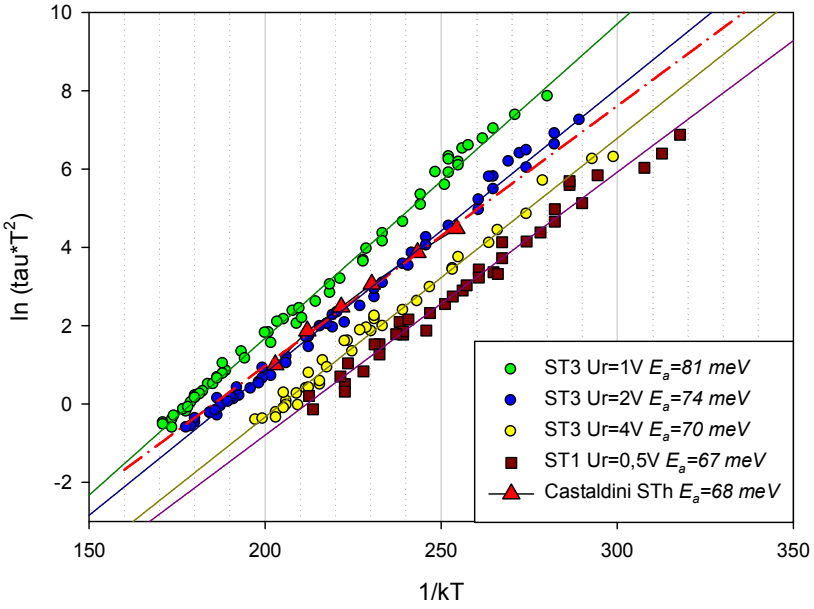

Figure 8.8. Arrhenius plots for the ST3 trap as derived from the DLTS spectra measured with reverse bias voltages *1 V*, *2 V* and *4 V* (circles), for ST1 trap as derived from the DLTS spectrum measured with U_r=*0,5V* (squares) and for the STh trap detected by Castaldini et al (triangles). Curves assignments and corresponding activation enthalpies are shown in legend. Points correspond directly to the experimental data, lines represent the best linear fits.

which derived from DLTS spectra measured with U_r=*2 V*, whereas the Arrhenius plots for ST1 level (even for the smallest reverse bias voltage U_r=*0,5 V*) locate at somewhat higher *1/kT* values (i.e. ST1 DLTS peak appears at lower temperatures than STh one) showing however quite similar activation enthalpies (slope coefficient), see Fig. 8.8. Thus, STh level detected by Castaldini et al indeed might have the same origin as ST1/ST3 traps detected in present work.

On the other side, energy positions of shallow dislocation-related levels which have been derived from the set of electroluminescence (EL) measurements can be considered as being obtained at zero electric field, thus allowing the direct comparison with E_{a0} energies of ST1/ST3 levels. In the experiments of Kveder et al [Kveder 1995b], rather deep energy position of shallow level E_{De}, E_{Dh} *~150 meV* was obtained from the temperature dependence of the D1 band intensity. Whereas the energy position of shallow levels E_{De}, E_{Dh} *~90 meV* derived by Kittler et al [Kittler 2009] from the temperature dependence of optimal current density through the diode with dislocations corresponding to the highest D1 intensity appeared to be rather similar with the zero field enthalpies found for shallow ST1/ST3 levels, especially with E_{a0} of ST1 level in Gr-1 sample, where the equilibrium stacking fault width is expected!

Energy position of the 1D-bands obtained by Kveder et al. [Kveder 1995a] from photo-EDSR measurements as E_{De}, E_{Dh} *~80-85 meV* is also close to the zero field activation energy of ST1 level, whereas an earlier result on temperature dependence of microwave conductivity of Brohl et al [Brohl, 1989] gave the location of the 1D band for holes at E_{Dh} *~70 meV*, what is slightly lower than the zero field energy of ST1 and ST3 levels.

As for theoretical calculations, the results of Farvacque et al. [Farvacque 2001] set the energy position of the shallow 1D band at E_V*+47 meV* for perfect screw and E_V*+37meV* for unsplitted 60° dislocation, which are considerably lower than the energies obtained for ST1/ST3 levels in the present work as well as works of other groups (see discussion in the paragraph 2.5). On the other hand, the results of theoretical calculations by Lehto [Lehto 1997] giving the energy level at E_V*+100 meV* for the stacking fault bounded by the partial dislocations (Fig. 2.3) appear to be very close to the E_{a0} energies of ST1/ST3 levels, thus giving an argument for the stacking fault origin of ST1/ST3 traps.

Thereby, the zero electric field activation enthalpies E_{a0} obtained for ST1 and ST3 traps correlate quite well with the energy of shallow dislocation-related level obtained by means of EL measurements [Kittler 2009], but E_{a0} energies seem to be slightly higher than the energy position of 1D bands estimated from EDSR and microwave conductivity methods (taking into account that deeper position of ST3 level is due to the stacking fault width that is smaller than equilibrium one). Considering, that two latter methods have measured the direct energy position of 1D bands (see details in paragraph 2.5), whereas the EL method in the work of Kittler et al – the energy position of shallow level participating in D1 recombination, it could be suggested that at the position of triple dislocation knots – structural elements responsible for D1 recombination – the shallow 1D bands become by approximately *20-30 meV* deeper, than they were along the straight unperturbed dislocation segments. Interaction and superposition of deformation potentials of dislocations composing the triple knot can be considered as being responsible for that.

Thus, the energy scheme of D1 radiative recombination may be constructed combining the models depicted in Fig. 2.11A and 2.11C: there exists a coupling of the shallow level participating in D1 recombination with shallow 1D bands, which serve as delivery channels for carriers towards the D1 recombination point, but the second - deep level participating in D1 transition is not coupled with any of shallow bands. In such scheme, the transition between the localized and somewhat “deeper” shallow level and the deep level in the opposite part of band gap (which have the same spatial location) would be more preferable than simply transition 1D band - deep level.

8.6. Summary for the Chapter 8.

The results of the theoretical calculations presented in this Chapter have demonstrated that:

- Poole-Frenkel effect due to elastic strain fields of screw and 60° dislocations for valence band is possible in silicon and the resulting Poole-Frenkel coefficients might be significantly higher than that for Coulomb-like potential of singly charged point defect
- in practice, dislocation strain-field related Poole-Frenkel effect depends strongly on the dislocations geometry in the sample: distances between the neighbouring dislocations, their type and orientation relative to the electric field
- comparisons with the experimentally obtained Poole-Frenkel coefficients allow to conclude that the Poole-Frenkel effect in Gr-1 sample is due to the combined influence of 60° dislocations of both possible orientations, whereas in Gr-3 sample – due to 60° dislocations of primarily *b2* orientation. The reason for the different dominating orientation of 60° dislocations in these samples is probably related with the different crystallographic orientations of the handle and the top wafers
- based on the results of theoretical calculation, it was concluded that the ST3 traps (as well as ST1 ones) are directly related with the 60° dislocations, and the higher activation energy of ST3 level as compared with ST1 one is related evidently with the dissociation width of 60° dislocations in Gr-3 sample, which seems to be somewhat smaller than equilibrium one.
- on the other hand, shallower SN1/SN3 traps should be located in the regions with the negligible influence of dislocation strain field. Probably, these levels are related with the oxygen precipitates or other defects outside the dislocations cores.
- quite well agreement was found between the ST1/ST3 trap activations enthalpies E_{a0} approximated towards the zero electric field and the energy of shallow dislocation-related level obtained from EL measurements [Kittler 2009], however E_{a0} energies appeared to be slightly higher than the energies of 1D bands estimated from EDSR and microwave conductivity. Thus, a new scheme of D1 transition – between the shallow level coupled with 1D bands and isolated deep level was suggested.

Chapter 9
Summary.

As a result of investigations of the bonded samples with the various structures of dislocation networks, the following facts were established:

a) DLTS measurements have revealed a great difference in the electronic structure of small-angle and large-angle bonded interfaces: dominating shallow level and a set of 6-7 deep levels were found in SA-samples Gr-1 and Gr-3, whereas the prevalent deep levels – in LA-samples Gr-6 and Gr-30. The critical twist misorientation angle separating SA- and LA- interfaces could be estimated as $\alpha_{TW}^{*} \approx 3{,}5 \pm 0{,}5°$, what agrees quiet well with the results of previous estimations performed on the basis of TEM [Rouviere 2000] and PL [Mchedlidze 2011] measurements.

b) Most of deep levels in SA-samples are probably caused by the interstitials and oxygen atoms (or clusters) segregated in the vicinity of 60° dislocations. Revealed correlations with the Arrhenius graphs of dislocation-related traps found previously in plastically deformed samples serve as a conformation. On the other side, deep levels detected in LA-samples arose most likely due to the large bond-angle and bond-length distortions expected for LA-interfaces of (100) orientation.

c) For the dominating shallow traps ST1/ST3 in SA-samples a new phenomenon – that is Poole-Frenkel effect of enhanced carrier emission due to dislocations elastic strain field was discovered and theoretically described for the first time. Theoretical calculations showed that the particular strength of this effect (and even its realizability) depends strongly on the dislocation type and – especially – on the interdislocation distance and on

the angle between the Burgers vector and electric field direction. As a result, the Poole-Frenkel effect observed for ST1/ST3 shallow traps allows to attribute them unambiguously to 60° dislocations. Whereas the absence of Poole-Frenkel effect for the shallower SN1/SN3 traps suggests a different spatial location and origin of ST- and SN- kinds of traps.

d) It was also established, that shallow ST1/ST3 traps participate in D1 radiative recombination and the intensity of D1 line correlates with the magnitude of corresponding ST1/ST3 DLTS peak. Broad distribution of electronic states with rapid inter-states exchange (band-like behaviour) was attributed to these shallow traps. In this respect, shallow traps ST1/ST3 can be identified either with shallow dislocation 1D bands (directly or as being coupled with them) or with shallow stacking fault states.

e) As the structural elements, responsible for D1 luminescence of small-angle dislocation networks, the triple knots along the 60° dislocations have been recognised. This result is in general agreement with the previous suppositions [Sekiguchi 1996] [Steinman 1999] that D1/D2 lines originate from the products of dislocation reactions. Whereas the four-fold knots of screw dislocations – instead – were found to be less probable candidates for D1 centres. It was also suggested, that superposition of dislocation strain fields at the position of triple knots might shift the energy position of shallow 1D deeper into band, resulting in the energy scheme of D1 luminescence where the radiative transition occurs between the shallow level coupled with 1D bands and isolated deep level.

f) In addition to the previous conclusions that for the highest D1 intensity the twist misorientation angle should be close to *3*° [Mchedlidze 2010], the obtained results give clear indication that tilt misorientation angle is also playing a significant role for D1 luminescence intensity and that the optimal tilt angle needs additional specification. Suppression of shallow traps magnitude as well as DRL intensity in the samples with twist misorientation angle higher than critical one may be explained – basis on the results of previous TEM investigations [Rouviere 2000] – by a distinct type of reaction between 60° dislocations and interfacial ones, which does not create the D1 luminescence centres.

g) Considering the results of CV and IV measurements, energy band diagram of the double-barrier ‘Schottky diode / charged DN’ structure was constructed and equations describing the majority carrier current flowing through such structure were developed. Moreover, DN-states located in the lower half of band gap were identified as donors, whereas acceptor-like DN-states are expected in the upper half of band gap.

References.

[Ahn 1989] K.-Y. Ahn, R. Stengl, T.Y. Tan, U. Gösele and P. Smith, J. Appl. Phys. 65, 561 (1989).

[Akatsu 2004] T. Akatsu, R. Scholz, U. Gösele, J. Mat. Sci. 39, 3031 (2004).

[Alexander 1991] H. Alexander and H. Teichler, in *Materials Science and Technology, Electronic Structure and Properties of Semiconductors 4*, edited by W. Schröter, VCH, New York, , p. 249 (1991).

[Alexander 2000] H. Alexander and H. Teichler: "Dislocations" in: Handbook of Semiconductor Technology, ed. K. A. Jackson and W. Schröter, WILEY-VCH Weinheim, vol. 1, p.291 (2000).

[Andersen 2002] O. Andersen, A. Peaker, L. Dobaczewski, K. Bonde Nielsen, B. Hourahine, R. Jones, P. Briddon, S. Oberg, Phys. Rev. B 66, 235205 (2002).

[Arguirov 2007] T. Arguirov, PhD thesis BTU Cottbus, Germany (2007).

[Aspar 1997] B. Aspar, M. Bruel, H. Moriceau, C. Maleville, T. Poumeyrol, A.M. Papon, A. Claverie, G. Benassayag, A.J. Auberton-Herve, and T. Barge, Microelectron. Eng. 36, 233 (1997).

[Bazhenov 1993] A. Bazhenov, V. Kveder, L. Krasilnikova, K. Rezchikov, phys. stat. sol. (a) 137, 321 (1993).

[Belov 1999] A. Belov, K. Scheerschmidt, Phil. Mag. Let. 79, 107 (1999).

[Benamara 1995] M. Benamara, A. Rocher, A. Laporte, G. Sarrabayrouse, L. Lescouzères, A. Peyre-Lavigne, M. Fnaiech and A. Claverie , Mat. Res. Soc. Symp. Proc. 378, 863 (1995).

[Benamara 1996] M. Benamara, A. Rocher, P. Sopéna, A. Claverie, A. Laporte, G. Sarrabayrouse, L. Lescouzères, A. Peyre-Lavigne, Materials Science and Engineering: B 42, 164 (1996).

[Bengtsson 1992] S. Bengtsson, G.I. Andersson, M.O. Andersson, O. Engstrom, J. Appl. Phys. 72, 124 (1992).

[Bethe 1942] H. Bethe, Theory of the Boundary Layer of Crystal Rectifiers, MIT Radiat. Lab. Rep., 43—12 (1942).

[Bir and Pikus 1974] G.L. Bir and G.E. Pikus, *Symmetry and deformation effects in semiconductors*, Wiley, New York, (1974).

[Blood 1992] P. Blood and J. W. Orton, *The Electrical Characterization of Semiconductors: Majority Carriers and Electron States*, Academic Press, London, (1992)

[Bollmann 1970] W. Bollmann, *Crystal Defects and Crystalline Interfaces*, Springer Verlag, New York, Heidelberg 1970.

[Bondarenko 1980] I.E. Bondarenko, V.G. Eremenko, V.I. Nikitenko and E.B. Yakimov, phys. stat. sol. (a) 60, 341 (1980).

[Bondarenko 2009] A. Bondarenko, O. Vyvenko, N. Bazlov, O. Kononchuk, Physica B 404, 4608 (2009).

[Bondarenko 2011] A. Bondarenko, O. Vyvenko, I. Isakov and O. Kononchuk, Journal of Physics: Conference Series 281, 012008 (2011).

[Brohl 1989] M. Brohl, H.Alexander, "Structure and Properties of Dislocations in Semiconductors", edited by S.G. Roberts, D. B.Holt and P.R. Wilshaw, IOP Conf. Proc. No. 104 (Institute of Physics, London, 1989), p.163.

[Brohl 1990] M. Brohl, M.D. Dressel, H.W. Helberg, H. Alexander, Phil. Mag. B 61, 97 (1990).

[Broniatowski 1987] A. Broniatowski, Phys. Rev. B 36, 5895 (1987).

[Brotherton 1978] S.D. Brotherton, A. Gill, Appl. Phys. Lett. 33, 953 (1978).

[Brotherton 1979] S.D. Brotherton, P. Bradley, J. Bicknell, J. Appl. Phys. 50, 3396 (1979).

[Castaldini 2005a] A. Castaldini, D. Cavalcoli, A. Cavallini, S. Binetti, S. Pizzini, Appl. Phys. Lett. 86, 162109 (2005).

[Castaldini 2005b] A. Castaldini, D. Cavalcoli, A. Cavallini, S. Pizzini, Phys. Rev. Lett. 95, 076401 (2005).

[Cavalcoli 1997] D. Cavalcoli, A. Cavallini, E. Gombia, Phys. Rev. B 56, 10208 (1997).

[Cavalcoli 2008] D. Cavalcoli, A. Castaldini, A. Cavallini, Applied Physics A 90, 619 (2008).

[Debbar 1989] N. Debbar, D. Biswas, P. Bhattacharya, Phys. Rev. B 40, 1058 (1989).

[Dimitrakis 1997] P. Dimitrakis, S. Hatzandroulis, D. Tsoukalas, J. Stoimenos and G.J. Papaioannou, ECS Proc. Vol. 97-23, Paris, 25 (1997).

[Drozdov 1976] N. Drozdov, A. Patrin and V. Tkachev *JETP Lett.* **23**, 597 (1976).

[Farvacque 2001] J.-L. Farvacque, P. Francois, phys. stat. sol. b 223, 635 (2001).

[Föll 1979] H. Föll, D. Ast, Phil. Mag. A 40, 589 (1979).

[Föll] Helmut Föll, *Defects in Crystals*, internet available textbook, http://www.tf.uni-kiel.de/matwis/amat/def_en/index.html

[Fonash 1983] S. J. Fonash, J. Appl. Phys. 54, 1966 (1983).

[Fournel 2002] F. Fournel, H. Moriceau, B. Aspar, K. Rousseau, J. Eymery, J.-L. Rouviere and N. Magnea, Appl. Phys. Let. 80, 792 (2002).

[Frenkel 1938] J. Frenkel, Phys. Rev. 54, 647 (1938).

[Gallagher 1952] C. Gallagher, Phys. Rev. 88, 721 (1952).

[Ganichev 2000] S.D. Ganichev, E. Ziemann, W. Prettl, I.N. Yassievich, A.A. Istratov, E.R. Weber, Phys. Rev. B 61, 10361 (2000).

[Hartke 1968] J.L. Hartke, J. Appl. Phys. 39, 4871 (1968).

[Higgs 1993] V. Higgs, E.C. Lightowlers, E.A. Fitzgerald, Y.-H. Xie, J. Silverman, J. Appl. Phys. 73, 1952 (1993).

[Hirth and Lothe 1970] J.P. Hirth and J. Lothe, *Theory of Dislocations*, New York:

McGraw-Hill. (1970).

[Hoang 2007] T. Hoang, J. Holleman, P. LeMinh, J. Schmitz, T. Mchedlidze, T. Arguirov, M. Kittler, IEEE Transactions on Electron Devices 54(8), 1860 (2007).

[Ikeda 2000] K. Ikeda, T. Sekiguchi, S. Ito, M. Takebe, M. Suezawa, J Cryst. Growth, Vol. 210, 90 (2000).

[Intel roadmap 2009]
http://download.intel.com/pressroom/kits/events/idffall_2009/pdfs/22nm_factsheet.pdf

[Isakov 2011] I. Isakov, A. Bondarenko, O. Vyvenko, V. Vdovin, E. Ubyivovk and O. Kononchuk, Journal of Physics: Conference Series 281, 012010 (2011).

[Istratov 1995] A. A. Istratov, and O. F. Vyvenko, Fizika i Tekhnika Poluprovodnikov, 29(4), 654 (1995).

[Istratov 1997] A. Istratov, Rev. Sci. Instrum. 68 (10), 3861 (1997).

[Ishikawa 2006] Y. Ishikawa, C. Yamamoto, M. Tabe, Appl. Phys. Let., 88 (2006) 073111.

[Izotov 1987] A. Izotov, E. Steinman, phys. ptat. sol. (a) 104, 777 (1987).

[Jalali 2008] B. Jalali, phys. stat. sol. (a) 205, 213 (2008).

[Jones 2000] R. Jones, B.J. Coomer, J.P. Goss, S. Oberg, P.R. Briddon, phys. stat. sol. (b) 222, 133 (2000).

[Kartalopoulos 2000]. S. W. Kartalopoulos, Introduction to DWDM technology, Wiley IEEE Press, New York (2000) p. 55

[Kimerling 1979] L. C. Kimerling and J. R. Patel, Appl. Phys. Lett. 34, 73 (1979).

[Kimerling 1981] L.C. Kimerling, J.L. Benton, Appl. Phys. Lett. 39, 410 (1981).

[Kittler 2007] M. Kittler, X. Yu, T. Mchedlidze, T. Arguirov, O. Vyvenko and W. Seifert, M. Reiche, T. Wilhelm, M. Seibt, O. Voss, W. Fritzsche, A. Wolff, Small Vol. 3, 963 (2007).

[Kittler 2008] M. Kittler, M. Reiche, T. Arguirov, T. Mchedlidze, W. Seifert, O.F. Vyvenko, T. Wilhelm, X.Yu, Solid State Phenomena Vols. 131-133, 289 (2008).

[Kittler 2009] M. Kittler, T. Mchedlidze, T. Arguirov, W. Seifert, M. Reiche, T. Wilhelm, phys. stat. sol. (c) 6, 707– 715 (2009).

[Kisielowski 1991] C. Kisielowski, E.R. Weber, Phys. Rev. B 44, 1600 (1991).

[Knobloch 1996] K. Knobloch and H. Alexander, Mater. Sci. Eng. B 42, 63 (1996).

[Knobloch 2003] K. Knobloch, M. Kittler and W. Seifert, J. Appl. Phys. 83, 1069 (2003).

[Koch 2002] C. Koch, PhD thesis Arizona State University, (2002).

[Kohyama 1994] M. Kohyama, R. Yamamoto, Phys. Rev. B 49, 17102 (1994).

[Kononchuk 1996] O. Kononchuk, V. Orlov, O. Feklisova and E. Yakimov Solid State Phenomena, Vols. 51-52, 15 (1996).

[Kononchuk 2008] O. Kononchuk, F. Boedt, F. Allibert, Sol. State Phen. Vol. 131-133, 113-118 (2008).

[Kreher 1993] K. Kreher, phys. stat. sol. (a) 135, 597 (1993).

[Kveder 1982] V.V. Kveder, Yu.A. Osipian, W. Schröter, G. Zoth, phys. stat. sol. (a) 72, 701-713 (1982)

[Kveder 1985] V.V. Kveder, Yu.A. Osipian, A.I. Shalynin, Sov. Phys. JETP 61(1), 182 (1985).

[Kveder 1989] V.V. Kveder, A.E. Koshelev, T.R. Mchedlidze, Yu.A. Osipian, A.I. Shalynin, Sov. Phys. JETP 68(1), 104 (1989).

[Kveder 1995a] V. Kveder, T. Sekiguchi, K. Sumino, Phys.Rev. B 51(23), 16721 (1995).

[Kveder 1995b] V.V. Kveder, E.A. Steinman, S.A. Shevchenko, H.G. Grimmeiss, Phys. Rev. B 51, 10520 (1995).

[Kveder 1996] V. V. Kveder, A. I. Shalynin, E. A. Steinman, and A. N. lzotov, *JETP* 83 (4), 829 (1996).

[Kveder 1997] V.V. Kveder, A.I. Shalynin, E.A. Steinman, A.N. Izotov, Solid State Phenomena 57-58, 299 (1997).

[Kveder 2001] V. Kveder, M. Kittler, and W. Schröter, Phys. Rev. B 63, 115208 (2001).

[Kveder 2005] V. Kveder, M. Badylevich, W. Schröter, M. Seibt, E. Steinman, A. Izotov, phys. stat. sol. (a) 202, 901 (2005).

[Kveder 2008a] V. Kveder, M. Kittler, Materials Science Forum, Vols. 590, 29 (2008).

[Kveder 2008b] V. Kveder, V. Orlov, M. Khorosheva, M. Seibt, Solid State Phenomena, Vols. 131-133, 175 (2008).

[Lang 1974] D. V. Lang, J. Appl. Phys. 45, 3014 (1974).

[Lehto 1997] N. Lehto, Phys. Rev. B 55, 15601 (1997).

[Lelikov 1992] Y. Lelikov, Y. Rebane, S. Ruvimov, D. Tarhin, A. Sitnikova and Y. Shreter, Materials Science Forum 83-87, 1321 (1992).

[Lemke 1981] H. Lemke, phys. stat. sol. (a) 65, 389 (1981).

[Libertino 2001] S. Libertino, S. Coffa, J. Benton, Phys. Rev. B 63, 195206 (2001).

[Liu 2004] A. Liu, R. Jones, L. Liao, D. Samara-Rubio, D. Rubin, O. Cohen, R. Nicolaescu, M. Pannicia, Nature 427, 615 (2004).

[Lodge 1989] K.W. Lodge, A. Lapiccirella, C. Battistoni, S.L. Altmann and N. Tomassini, Phil. Mag. A60, 643 (1989).

[Lourenco 2003] M.A. Lourenco, M.S.A. Siddiqui, R.M. Gwilliam, G. Shao, P. Homewood, Physica E 16, 387 (2003).

[Love 1927] A. E. H. Love, "*The Mathematical Theory of Elasticity*", Cambridge University Press, Cambridge, (1927).

[Marklund 1981] S. Marklund, phys. stat. sol. (b) 108, 97 (1981)

[Markram-Ebeid 1982] S. Markram-Ebeid and M. Lannoo, Phys. Rev. B ***25***, 6406 (1982).

[Martin 1981] P.A. Martin, B.G. Streetman, K. Hess, J. Appl. Phys. 52, 7409 (1981).

[Matare 1971] H. F. Matare, *Defect Electronics in Semiconductors*, Wiley, New York (1971).

[Mattheiss 1981] L.F. Mattheiss, J.R. Patel, Phys. Rev. B 23, 5384 (1981).

[McGonigal 1983] G. McGonigal, D. Thomson, J. Shaw, H. Card, Phys. Rev. B 28, 5908 (1983).

[Mchedlidze 1999] T. Mchedlidze, K. Matsumoto, E. Asano, Jpn. J. Appl. Phys. 38, 3426 (1999).

[Mchedlidze 2007] T. Mchedlidze, T. Arguirov, G. Jia and M. Kittler, phys. stat. sol. (a) 204 (7), 2229 (2007).

[Mchedlidze 2008] T. Mchedlidze, T. Wilhelm, X. Yu, T. Arguirov, G. Jia, M. Reiche, M. Kittler, Sol. State Phenom. 131-133, 503 (2008).

[Mchedlidze 2009] T. Mchedlidze, T. Wilhelm, T. Arguirov, M. Trushin, M. Reiche, M. Kittler, phys. stat. sol. (c) 6(8), 1817 (2009).

[Mchedlidze 2010] T. Mchedlidze, O. Kononchuk, T. Arguirov, M. Trushin, M. Reiche, M. Kittler, Sol. Stat. Phenom. 156-158, 567 (2010).

[Mchedlidze 2011] T. Mchedlidze, T. Arguirov, O. Kononchuk, M. Trushin, M. Kittler, phys. stat. sol. (c) 8 (3), 991 (2011).

[Nagai 1992] K. Nagai, H. Takato, Y. Hayashi, Japan. J. Appl. Phys. 31, L1529 (1992).

[Oehme 2006] M. Oehme, J. Werner, M. Jutzi, G. Wöhl, E. Kasper, M. Berroth, Thin Solid Films 508, 393 (2006).

[Omling 1983] P. Omling, L. Samuelson, H.G. Grimmeiss, J. Appl. Phys. 54, 5117 (1983).

[Omling 1985] P. Omling, E.R. Weber, L. Montelius, H. Alexander, J. Michel, Phys. Rev. B 32, 6571 (1985).

[Ono 1985] H. Ono and K. Sumino, J. Appl. Phys. 57, 287 (1985).

[Orowan 1934] E. Orowan, Z. Phys. 89, 605 (1934).

[Patel 1979] J.R. Patel, L.C. Kimerling, J. Physique 40, C6-67 (1979).

[Pavesi 2003] L. Pavesi, J. Phys.: Condens. Matter 15**,** R1169–R1196 (2003).

[Pike 1979] G. Pike, C. Seager, J. Appl. Phys. 50, 3414 (1979).

[Pike 1984] G. Pike, Phys. Rev. B 30, 3274 (1984).

[Pizzini 2000] S. Pizzini, M. Guzzi, E. Grilli and G. Borionetti, J. Phys.: Condens. Matter 12, 10131 (2000).

[Plößl 1999] A. Plößl, R. Scholz and T. Akatsu: in: *Semiconductor Wafer Bonding: Science, Technology and Applications V*, edited by C. E. Hunt, H. Baumgart, U. Gösele and T. Abe, PV 99-35, The Electrochem. Soc., Pennington 232 (1999).

[Polanyi 1934] M. Polanyi, Z. Phys. 89, 660 (1934).

[Read 1953] W. T. Read, *Dislocations in crystals*, McG Raw-Hill Book Company Inc., New-York (1953).

[Rebane 1990] Y. Rebane, Y. Shreter, Polycryst. Semicond II, ed. J. Werner and H. Strunk, Springer-Verlag, Berlin/Heidelberg/New York (1990).

[Reiche 1995] M. Reiche, Q. Tong, U. Gösele, J. Heydenreich 196-201, 1847 (1995).

[Reiche 1997] M. Reiche, K. Scheerschmidt, D. Conrad, R. Scholz, A. Plößl, U. Gösele, K.N. Tu, Inst. Phys. Conf. Ser. 157, 447 (1997).

[Reiche 2008] M. Reiche, Materials Science Forum Vol. 590, pp 57-78 (2008).

[Reznicek 2002] A. Reznicek; Thesis Techn. Univ. Berlin (2002).

[Reznicek 2003] A. Reznicek, R. Scholz, S. Senz and U. Gösele: Mater. Chem. Phys. Vol. 81, 277 – 280 (2003).

[Rousseau 2002] K. Rousseau, J.L. Rouviere, F. Fournel, H. Moriceau, Appl. Phys. Lett. 80, 4121 (2002).

[Rouviere 2000] J.L. Rouviere, K. Rousseau, F. Fournel, H. Moriceau, Appl. Phys. Lett. 77, 1135 (2000).

[Sakaki 1980] H. Sakaki, Jpn. J. Appl. Phys., Part 1, 19, 94 (1980).

[Sauer 1985] R. Sauer, J. Weber, J. Stolz, E.R. Weber, K.-H. Küsters, H. Alexander, Appl. Phys. A 36, 1 (1985).

[Sauer 1986] R. Sauer, Ch. Kisielowski-Kemmerich, H. Alexander, Phys. Rev. Lett. 57, 1472 (1986).

[Schmalz 1994] K. Schmalz, I. Yassievich, H. Rücker, H. Grimmeiss, H. Frankenfeld, W. Mehr, H. Osten, P. Schley, H. Zeindl, Phys. Rev. B 50, 14287 (1994).

[Schmalz 1996] K. Schmalz, I. Yassievich, E. Collart, D. Gravesteijn, Phys. Rev. B 54, 16799 (1996).

[Schober 1970] T. Schober and R.W. Baluffi: Phil. Mag. Vol. 21, 109 – 123 (1970).

[Schockley 1953] W. Shockley, Phys. Rev. 91, 228 (1953).

[Schröter 1995] W. Schröter, J. Kronewitz, U. Gnauert, F. Riedel and M. Seibt, Phys. Rev. B 52, 13726 (1995).

[Schröter 2002a] W. Schröter and H. Cerva, Sol. State Phenom. Vols. 85-86, 67 (2002).

[Schröter 2002b] W. Schröter, H. Hedemann ,V. Kveder, F. Riedel, J. Phys.: Condens. Matter 14, 13047–13059 (2002).

[Schönecker 2004] A. Schönecker, L. J. Geerligs, A. Müller, Solid State Phenomena 95-96, 149 (2004).

[Seager 1979] C. Seager, G. Pike, Appl. Phys. Let. 35, 709 (1979).

[Sekiguchi 1996] T. Sekiguchi, K. Sumino, J. Appl. Phys. 79, 3253 (1996).

[Sekiguchi 2002] T. Sekiguchi, S. Ito, A. Kanai, Mat. Sci. Eng. B 91-92, 244 (2002).

[Shen 1996] B. Shen, J. Jablonski, T. Sekiguchi, K. Sumino, Japan. J. Appl. Phys. 35, 4187(1996).

[Steinman 1999] E. A. Steinman, V. I. Vdovin, T. G. Yugova, V. S. Avrutin, N. F. Izyumskaya, Semicond. Sci. Technol. 14, 582 (1999).

[Steinman 2005] E.A. Steinman, Physics of the Solid State 47, 5 (2005).

[Suezawa 1983a] M. Suezawa and K. Sumino, Phys. Status Solidi A **78**, 639 (1983).

[Suezawa 1983b] M. Suezawa, Y. Sasaki, K. Sumino, phys. stat. sol. (a) 79, 173 (1983).

[Sze, 1981] S. M. Sze, *Physics of semiconductor devices*, Wiley-Interscience publications, New-York, (1981).

[Taylor 1934] G. I. Taylor, Proc. R. Soc. A 145, 362 (1934).

[Tittelbach-Helmrich 1993] K. Tittelbach-Helmrich, Semic. Sci. and Technol. 8, 1372-1376 (1993).

[Trushin 2009] M. Trushin, O. Vyvenko, W. Seifert, G. Jia, M. Kittler, Physica B 404, 4645 (2009).

[Trushin 2011a] M. Trushin, O. Vyvenko, T. Mchedlidze, M. Reiche and M. Kittler, phys. stat. sol. (c) 8(4), 1371-1376 (2011).

[Trushin 2011b] M. Trushin, O. Vyvenko, V. Vdovin, M. Kittler, Journal of Physics: Conference Series 281, 012009 (2011).

[Vdovin 2011] V. Vdovin, O. Vyvenko, E. Ubyivovk, O. Kononchuk, Solid State Phenomena Vols. 178-179, 253 (2011).

[Veth 1984] H. Veth and H. Teichler, Phil. Mag. B49, 371 (1984).

[Volterra 1907] V. Volterra, Ann. Ecole Norm. Super. 24, 400 (1907).

[Vyvenko 2004] O. Vyvenko, M. Kittler, W. Seifert, J. Appl. Phys. 96, 6425 (2004).

[Vyvenko 2005] O. Vyvenko, M. Kittler, W. Seifert, M. Trushin, phys. stat. sol (c) 2, 1852 (2005).

[Watson 1998] G.P. Watson, J.L. Benton, Y.H. Xie, E.A. Fitzgerald, J. Appl. Phys. 83, 3773 (1998).

[Wattenbach 1990] M. Wattenbach, C. Kisielowski-Kemmerich, H. Alexander, V.V. Kveder, T.R. Mchedlidze, Yu.A. Osipian, phys. stat. sol. (b), 158, K49 (1990).

[Weber 1990] J. Weber and M. Alonso*, Defect in Semiconductors,* ed. K. Sumino, Elsevier Science publishers B. V., North Holland 1453, (1990).

[Weber 1994] J. Weber, Solid State Phenomena 37-38, 13 (1994).

[Weronek 1992] K. Weronek, J. Weber, A. Hopner, F. Ernst, R. Buchner, R. Stefanniak and H. Alexander, Mat. Sci. For. 83-87, 1315 (1992).

[Wessel 1977] K. Wessel and H. Alexander, Philos. Mag. **35**, 1523 (1977).

[Wilhelm 2008] T. Wilhelm, T. Mchedlidze, X. Yu, T. Arguirov, M. Kittler, M. Reiche, Solid State Phenomena 131, 571 (2008).

[Winter 1978] S. Winter, phys. stat. sol. (b) 90, 289 (1978).

[Yu 2007] X. Yu, O. Vyvenko, M. Kittler, W. Seifert, T. Mtchedlidze, T. Arguirov, M. Reiche, Semiconductors 41, 458 (2007).

[Zakharov 2003] N.D. Zakharov, V.G. Talaev, P. Werner, A.A. Tonikikh, G.E. Cirlin, Appl.Phys.Lett. 83, 3084 (2003).

[Zheng 1994] B. Zheng, J. Michel, F.Y.G. Ren, L.C. Kimerling, D.C. Jacobson, J.M. Poate, Appl. Phys. Lett. 64, 2842 (1994).

Acknowledgments

First of all, I would like to express my largest gratitude to Prof. J. Reif and to Prof. H. Vierhaus for giving me the opportunity to study and to prepare my Ph.D. thesis in Brandenburg University of Technology.

I am deeply grateful to Prof. M. Kittler for his constant support, friendly encouragement and for his efforts in making a continuation of the experimental work possible, as well as for his valuable advices on manuscript correction.

I thank Prof. O. Vyvenko cordially for the ideas, which contributed very much to the progress of my work, for his constant accessibility for questions and also for thorough proof-reading of the drafts and for many useful discussion and comments on them.

My special thanks to SOITEC Company and especially to Dr. O. Kononchuk for kindly providing the bonded samples for the investigations and for performing the XRD measurements.

I would like to express my thanks to Dr. T. Mchedlidze for the interesting discussions and useful advices, as well as for providing the PL investigation results.

I would like to acknowledge the contribution of Dr. V. Vdovin for performing the TEM measurements.

I am very grateful to Dr. T. Arguirov and Dr. W. Seifert for their friendly and kind support.

Our secretaries Ms. M. Bormann and Ms. K. Starr are kindly acknowledged for their continuous help with all the small and big administrative problems.

Finally, I wish to express my gratitude to all my colleagues and friends for the nice working atmosphere and the cordial spirit which we have in our group. This made my stay and work in Cottbus really enjoyable.